Alma Mater Studiorum - Università di Bologna

DOTTORATO DI RICERCA IN

MONITORAGGIO E GESTIONE DELLE STRUTTURE E DELL'AMBIENTE - SEHM2

Ciclo 33

STUDY OF INNOVATIVE STEEL 3D-PRINTING PROCESS FOR STRUCTURAL ENGINEERING APPLICATIONS

Presentata da: Vittoria Laghi

Coordinatore Dottorato

Alessandro Marzani

Supervisore

Tomaso Trombetti

Co-supervisore

Stefano Silvestri

Esame finale anno 2021

ABSTRACT

The present study aims at providing a first exploration on the application of metal 3D printing technology in the construction field.

Over the last decade, Additive Manufacturing (AM) has gained wide importance on several industrial fields, from automotive to aerospace and biomedical, with however severe limitations in the dimensions on the outcomes, constrained to the limits imposed by the printer environment. As such, the applications of these innovative manufacturing technologies in construction have been limited to few explorations on small pieces, to be used as connection parts.

With the advent of a new weld-based AM process, referred to as Wire-and-Arc Additive Manufacturing (WAAM), the scale of the printed outcomes increased up to several meters span, thus becoming suitable for large-scale applications in marine and construction sectors. The high velocity and possibility to realize large-dimension parts, maintaining high structural performances at relatively good quality of the finishing, confirmed the advantages to apply this technology to realize innovative forms and new shapes for a new generation of structural members. On the other hand, the outcomes from the printing process result in non-negligible geometrical irregularities and marked anisotropic behavior, which should be properly characterized in order to perform structural design of WAAM-produced parts.

The study is focused on the characterization of WAAM-produced 308LSi stainless steel for structural applications and divided in three parts: Part A, Part B and Part C.

Part A is devoted to study the so-called "continuous printing" strategy, to realize planar elements. It is articulated as follows: from the specifics of the printing process, a suitable design approach is chosen for WAAM-produced elements. Then, the results from an intense experimental study are presented in terms of microstructural, material, geometrical and mechanical characterization. From these results, an ad-hoc orthotropic material model is calibrated to account for the inherent anisotropic behavior of the WAAM-produced plates. Then, first design guidelines are proposed from the calibration of design values and partial safety factors according to the European standard provision for steel structures. Finally, some first explorations on topologically-optimized structural members realized with WAAM are presented.

Part B is devoted to study the so-called "dot-by-dot printing" strategy, to realize lattice and rod-like elements. It is articulated as follows: based on the specifics design issues of this process, a

_____

design approach has been chosen, according to the studies performed in part A. The results from the experimental campaign are presented in terms of geometrical and mechanical characterization. From these, first design guidelines are drawn following the same approach as in part A. Finally, a first example of computational design of a WAAM-produced diagrid column is proposed.

Part C is devoted to present new technologies and future developments on WAAM applications in construction. It is articulated as follows: first, a new mobile 3D printing system is presented, able to move along the element while 3D printing it. Then, a future perspective in terms of real-time monitoring system is proposed for possible further research.

.

ACKNOWLEDGMENTS

To my family

Table of Contents

_____

_____

_____

_____

_____

_____

List of Figures

List of Tables

PART A: Wire-and-Arc Additive Manufacturing stainless steel – continuous printing

1. Introduction to Part A

1.1. BACKGROUND OF 3D PRINTING IN CONSTRUCTION

Along the centuries, the evolution in building construction has always been strictly linked to significant advancements in material science, technology, industrial processes and engineering. As the first Industrial Revolution marked the use of metals as structural members, the improvement in scientific knowledge and the introduction of concrete at the beginning of the 20th century paved the way for Reinforced Concrete (RC) constructions (Addis, 2007). Similarly, in the last 30 years the way structures are designed, planned and built has changed completely with the technological innovations offered by softwares for Computer-Aided Design (CAD), which replaced manual drawings, without however changing the resulting architectural shapes. Only in the early years of the 21st century, a new design approach to architecture resulting in novel forms started to emerge by the utilization of three-dimensional computer modelling and digital fabrication methods. More recently, with what has been called the "*digital turn*" (Carpo, 2013), innovative computerized tools for architecture, structural and civil engineering have gained influence, enabling the design and construction of buildings with complex, doubly-curved geometry, such as shell structures and other free-form designs (Adriaenssens et al., 2014).

The growth of automation since the beginning of 21st century has prevailed in almost all production domains with the exception of the building construction sector, in which the use of automatic tools is still challenging and at its first applications. The main challenge is due to some peculiar aspects of the construction industry: (i) building and civil constructions are very large-scale products requiring customization of conventional automated fabrication technologies; (ii) conventional design approaches are not tailored for automation; (iii) significantly smaller ratio of production quantity/type of final products as compared with other industries; (iv) limitations in the materials that could be employed by an automated system (Khoshnevis, 2004). Only in the last few years, the fast development in digital fabrication techniques is leading towards applications in Structural Engineering field as well, through Additive Manufacturing (AM)-based technologies, already commonly used in other sectors such as aerospace, automotive and biomedical engineering (Attaran, 2017; Giannatsis & Dedoussis, 2009; Y. Song et al., 2002; Thomas et al., 1998).

Recent developments of Additive Manufacturing (AM) process in construction have seen the application of 3D printing techniques to realize a new generation of structures in concrete, polymers and metals (Buchanan & Gardner, 2019). In applications for steel structures, Powder-Based Fusion (PBF) technology has been adopted to realize ad-hoc connections parametrically designed either for structural optimization purposes (Galjaard et al., 2015b) or to create free-form gridshells (Raspall et al., 2019). However, due to the intrinsic geometrical constraints of the printer environment (enclosed in a box of typically 250-mm side), the application of PBF process is limited to the realization of small-size connections and structural details (Buchanan et al., 2017). In order to realize real-scale structural elements without ideally any geometrical constraints either in size or shape, the most suitable manufacturing solution for metallic elements is the so-called Wire-and-Arc Additive Manufacturing (WAAM) process. This 3D printing technology uses off-the-shelf traditional welding equipment mounted on top of either numerically-controlled robotic arms or cartesian machines, able to realize large-scale elements of several meters of dimension. The main advantage presented by WAAM process relies on the possibility to create new shapes and forms following the breakthrough design tools for modern architecture as algorithm-aided design with in principle no constraints either in shape or size of the printed outcome. At the same time, the WAAM process ensures fast production with good quality outcome both in terms of geometrical precision and mechanical properties. On the other hand, two additional considerations must be considered when dealing with WAAM-produced elements. First, the inherent surface roughness proper of WAAM process could influence the mechanical response. Moreover, the marked anisotropy also evidenced from the material microstructure is to take into account when defining the main mechanical parameters. Different process parameters result in different surface finishing and microstructure, both affecting the mechanical response (Dinovitzer et al., 2019).

_____

1.2. OBJECTIVES OF PART A

Part A of the doctoral thesis focuses on the so-called "*continuous printing*" technology of WAAM process as developed by MX3D adopted to create 3D printed stainless steel structural elements, as for the case of the MX3D Bridge, the first proof-of-concept of the WAAM process in construction to realize free-form large-scale structures. Indeed, the research group at University of Bologna composed by prof. Tomaso Trombetti, P.E. Michele Palermo and myself are partner in the Bridge project held by MX3D to run experimental tests for the characterization of WAAM-produced specimens. The continuous printing strategy consists in fabricating planar elements through successive deposition in continuous of welded material, layer upon layer.

As the application of metal 3D printing to construction allows to explore new forms and shapes according to the concepts of computational design and topology optimization, it becomes crucial to first have a detailed characterization of the printed outcomes, in terms of mechanical properties and microstructure, in order to derive ad-hoc design guidelines for structural applications.

From the knowledge acquired through extensive experimental tests, first calibrations of the design values for application in structural engineering are derived. Moreover, from the anisotropic mechanical behavior, an ad-hoc orthotropic model for the elastic behavior of WAAM stainless steel material can be estimated. From this, advanced algorithms for topology optimization allow to create a first catalogue of optimized geometries based on the peculiar features of WAAM stainless steel.

1.3. ORGANIZATION OF THE TEXT

The first part of the doctoral thesis presents the comprehensive study related to continuous printing (Part A). Section 2 presents an overview of WAAM continuous printing and the design issues related to the geometrical irregularities and anisotropic mechanical behavior of the printed outcomes. Section 3 presents the design approach proposed for WAAM stainless steel structures. Section 4 presents the experimental characterization of WAAM-produced stainless steel planar elements, from the microstructure to both geometrical and mechanical investigations. The results from the experimental campaign are used to calibrate an ad-hoc elastic model for orthotropic material (Section 5) as well as ad-hoc design guidelines for structural design applications (presented in Section 6). Then, some first explorations on the topology optimization applied to WAAM are presented in Section 7. The results from the study are compared with current literature review on WAAM continuous printing in Section 8.

2. The continuous printing process

2.1. OVERVIEW

Unlike traditionally-manufactured steel elements, Wire-and-Arc Additively Manufactured steel is a completely new material characterized by a particular microstructure that affects its structural behavior and basic properties (Figure 2.1). Moreover, the 3D-printed elements result in inherent geometrical irregularities and different mechanical properties which must be fully characterized.

The present chapter provides an insight on Wire-and-Arc Additive Manufacturing process among different metal 3D printing technologies (Section 2.2), the printing process studied in the present work (Section 2.3) and the specific design issues related to WAAM planar elements (Section 2.4).

Figure 2.1: Example of WAAM continuous printing process (*MX3D Webpage*).

2.2. WIRE-AND-ARC ADDITIVE MANUFACTURING (WAAM)

2.2.1. Metal additive manufacturing (AM) in construction

The term Additive Manufacturing has been attempted to be standardized in ISO/ASTM 52900 (ASTM International, 2012), where such terminology has been adopted for all processes of making parts from 3D models and materials. Nowadays Additive Manufacturing (AM) refers to the technology (or additive process) of depositing successive thin layers of material upon each other, as opposed to the traditional subtractive manufacturing, producing a final three-dimensional object, realized either in plastic, resin, rubber, ceramic, glass, concrete and metal. Recent reviews of the metal Additive Manufacturing processes (Buchanan & Gardner, 2019; Everton et al., 2016; Lewandowski & Seifi, 2016; Sames et al., 2016; Wong & Hernandez, 2012) distinguish them into three major categories: (i) Powder Bed Fusion (PBF); (ii) Directed Energy Deposition (DED) and (iii) sheet lamination.

In recent years research effort has been intensively dedicated to the study of PBF material fabrication and its specifications concerning building orientation and mechanical characteristics (Buchanan et al., 2017; Guan et al., 2013; Niendorf et al., 2013; Skiba et al., 2009; Song et al., 2015; Yap et al., 2015). ASTM F2792-10 (ASTM, 2010) provides also an outline of metallic single-step Additive Manufacturing methods for this category of AM process. The PBF process, although presenting small geometrical imperfections and mechanical characteristics in the order of the traditional material, is limited by the build envelope of the equipment, which is typically a 250-mm cube (Buchanan et al., 2017).

Early uses of metal additive manufacturing (AM) in construction have primarily featured modest-scale components such as façade nodes and connections (Buchanan & Gardner, 2019).

One example of an AM-produced façade node is the Nematox façade node (Strauß & Knaack, 2016), developed to show how additive manufacturing process could be used to allow more optimized geometries. A full-size prototype (Figure 2.2) was built using PBF with aluminum powder.
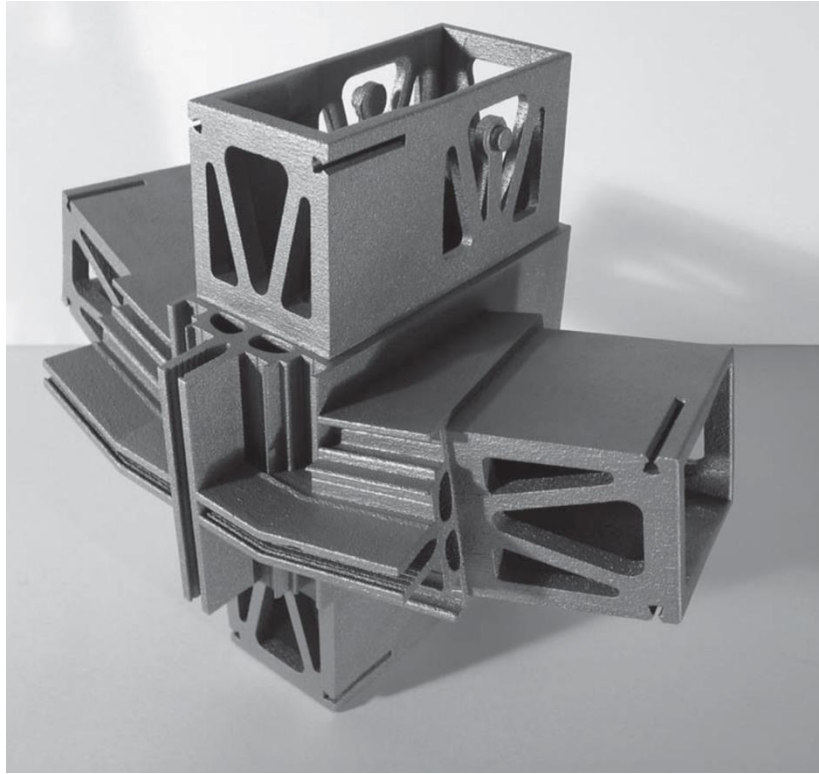
Figure 2.2: Full-size aluminium prototype Nematox façade node (Strauß & Knaack, 2016).

A tensegrity structure lighting node was redesigned by Arup to take advantage of the opportunities presented by additive manufacturing combined with topology optimization. The design has been first optimized according to the boundary conditions prescribed, and then rationalized for manufacture, i.e. reducing the amount of material used, minimize cost and speed up manufacture (Figure 2.3). The final design has been realized using PBF with ultra-high strength steel powder. However, it was noted in 2014 that the final node costed roughly three times that of a conventionally produced node, but it was expected to become cheaper through manufacturing development within five years.
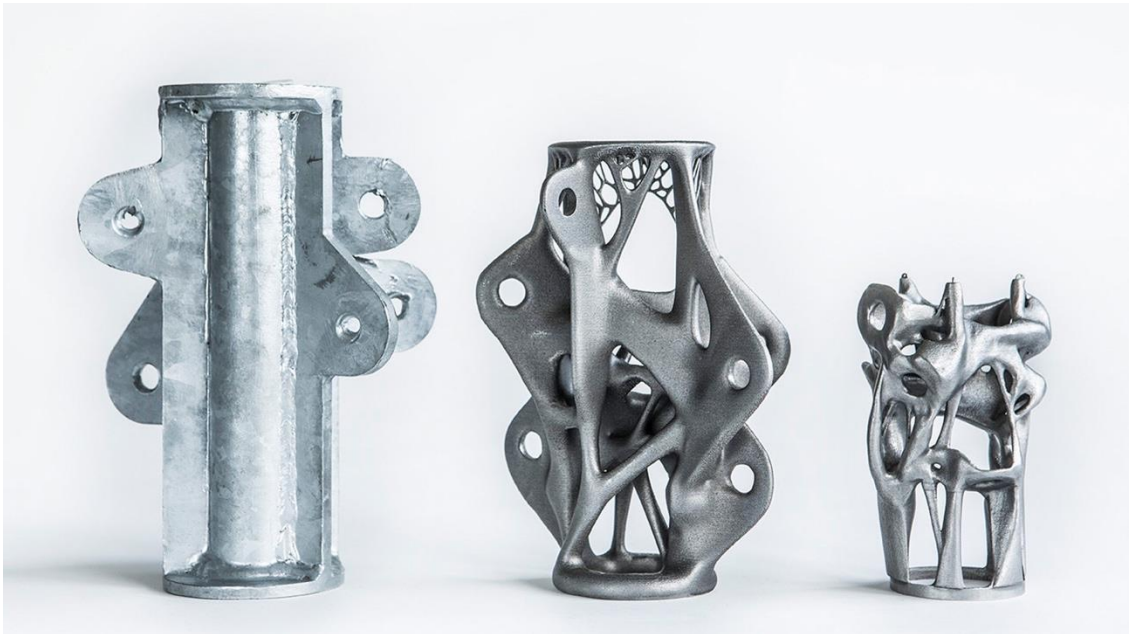
(a)

(b)

Figure 2.3: Arup lighting node: (a) progression from conventional to optimized node; (b) application of the geometrical optimized node (*ARUP - Additive Manufacturing*; Galjaard et al., 2015a).

More recently, metal 3D-printed nodes were adopted to create an ultra-light pavilion held in Singapore and developed by AirLab at Singapore University of Technology and Design (*AIRMESH Pavilion*). Geometric optimization processes based on force distributions have been applied to design the 54 unique nodes realized using PBF with stainless steel powder (Figure 2.4).

(a)

(b)

Figure 2.4: (a) AirMesh Pavilion; (b) 3D-printed stainless steel node (*AIRMESH Pavilion*).

2.2.2.   Wire-and-Arc Additive Manufacturing process

Among different AM processes, Wire-and-Arc Additive Manufacturing (WAAM) technology consists of a combination of an electric arc as heat source and wire as feedstock. It currently uses off-the-shelf welding equipment, such as welding power source, torches and wire feeding system, while motion is provided by either a robotic arm or computer numerical-controlled gantries. Such flexible building set-up allows for the realization of elements without theoretical dimensional constraints. Thus, it appears more suitable for structural engineering applications, for which the outputs requested are of the order of several meters (typically 3 to 5 m long).

WAAM's layer height is commonly in the range of 1 to 2 mm, resulting in an expected surface roughness of about 0.5 mm for single track deposits. As a result, this process is not considered net shape, as machining is required to finish the part, thus being better suited for low- to medium-complexity and medium- to large-scale elements, as those implemented in structural engineering (Haden et al., 2017; Ji et al., 2017; Uziel, 2016; Williams et al., 2016). Indeed, in order to obtain

pieces of large dimensions, higher printing velocities are required, resulting in larger geometrical imperfections with respect to the digital model. Therefore, much effort is needed for a proper assessment of both the geometrical and mechanical characterization of the outputs from Wire-and-Arc Additive Manufacturing (WAAM) process.

Nowadays there is limited amount of research work concerning the influence of WAAM process parameters on the material properties (Dinovitzer et al., 2019; Kim et al., 2003). Among WAAM-processed stainless steels, the available literature reports limited data about maraging steel (Xu et al., 2018), 2Cr13 martensitic stainless steel (Ge et al., 2018), 316L and 304 L austenitic stainless steels (Gardner et al., 2019; Gordon et al., 2018; Haden et al., 2017; Ji et al., 2017; Kyvelou et al., 2020), as well as 2209 duplex stainless steel (Hejripour et al., 2019). The presented results are focused on the assessment of the influence of the orientations with respect to the deposition layer on the tensile strength (yielding and ultimate tensile strengths) of WAAM metallic specimens, hence confirming the interest in studying the anisotropy of the printed outcomes. In the work done by Gordon and co-authors (Gordon et al., 2018), Young's modulus values are reported, indicating values around 130 to 140 GPa, significantly lower than the one registered by the conventional wrought material (about 190 GPa). Wu and co-workers (Wu et al., 2019) found a first correlation between the tensile strength and the specimens orientation, in terms of grain growth orientation.

The first full-size pedestrian bridge realized in metal 3D printing has been designed by MX3D (*MX3D Webpage*) and presented at the Dutch Design Weekend 2018 in Eindhoven (Figure 2.5). The bridge will be places in Amsterdam city center by the end of 2020.

MX3D, in partnership with engineers from Arup and researchers from Imperial College London, University of Technology Delft and University of Bologna, designed, modelled, built and tested the first additively-manufactured metal bridge. The bridge has a width of 2.5 m and a span of 10 m. The structure was printed using Wire-and-Arc Additive Manufacturing (WAAM) Directed Energy Deposition (DED) using stainless steel wire.

_____

Figure 2.5: MX3D footbridge realized with WAM process and presented at the Dutch Design Week 2018 in Eindhoven.

Recently, MX3D partnered with Takenaka to produce a structural steel connector (*MX3D - Takenaka Connector*) (Figure 2.6). The connector is designed by MX3D and Takenaka engineers with the help of topology optimization program, to show the progress in the production of highly customized and engineered steel connectors using WAAM. The connector is realized with WAAM process using Duplex stainless steel.

(a)
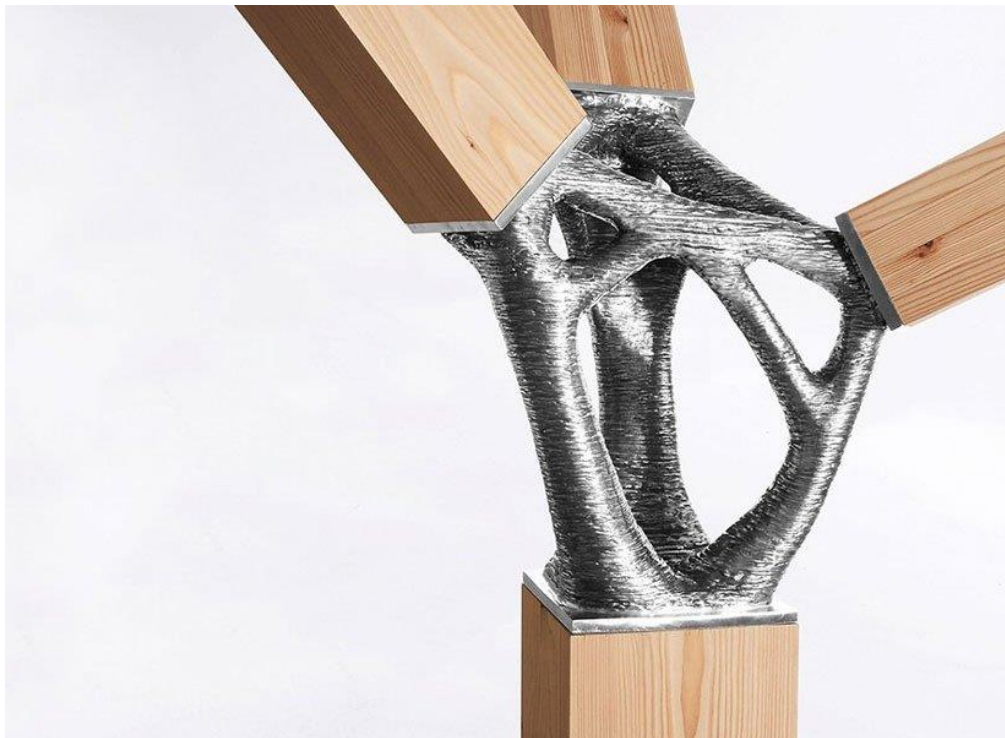
(b)

_____

Figure 2.6: MX3D Takenaka Connector: (a) render and (b) 3D-printed connector (*MX3D - Takenaka Connector*).

Another example on the application of structural optimization and WAAM technique has been proposed by a research group from TU Delft (Figure 2.7). The Glass Swing has been realized in structural glass and WAAM-produced steel nodes by the Dutch company RAMLAB (*RAMLAB*). The non-standard form of the swing was developed through ad-hoc optimization procedure for vector active glass structures (Snijder et al., 2020).
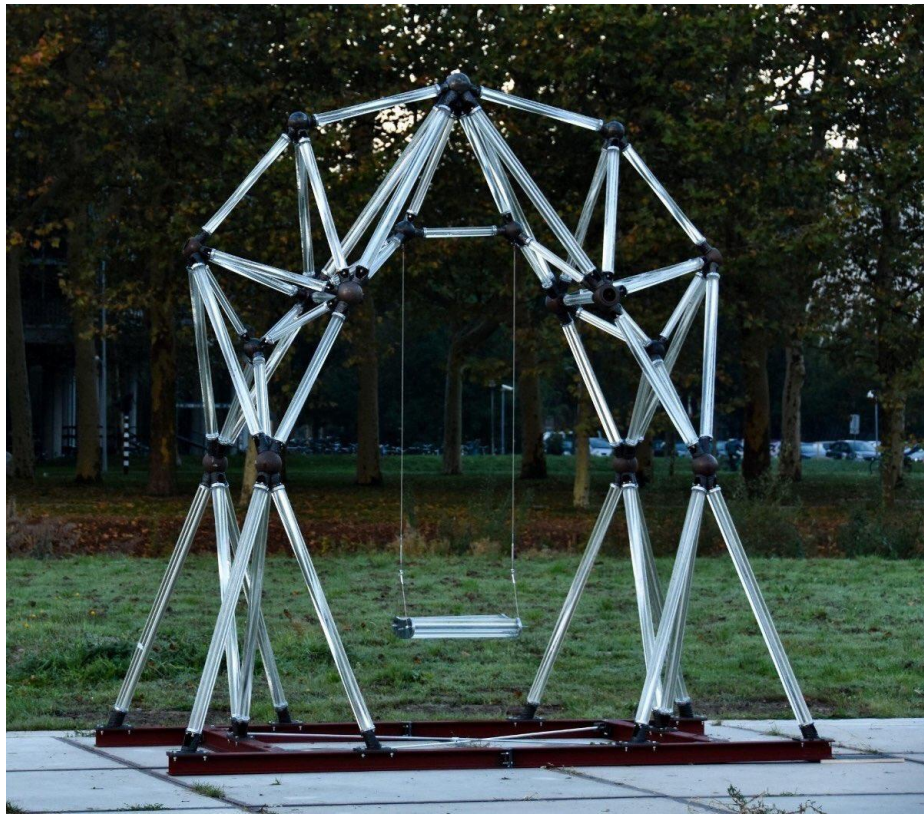
Figure 2.7: The Glass Swing realized at TU Delft in collaboration with the Dutch company RAMLAB (Snijder et al., 2020).

_____

2.3. WAAM CONTINUOUS PRINTING PROCESS

The study is focused on Wire-and-Arc Additive Manufacturing (WAAM) 308LSi stainless steel produced with continuous printing strategy, as adopted by MX3D to realize the MX3D Bridge (Figure 2.5). In particular, MX3D makes use of a Gas Metal Arc Welding (GMAW) process, characterized by a continuous wire electrode which is drawn from a reel by an automatic wire feeder. The wire is fed through the contact tip in the welding torch. The heat is transferred from the welding arc and the internal resistive power causes the wire to melt (Kim et al., 2003; Yilmaz & Ugla, 2017). The motion system adopted consists of industrial multi-axis ABB robots which, theoretically, are able to print from any angle.

The continuous printing strategy consists of depositing successive layers of welded metal one over the other to create planar or extruded elements with constant thickness. The fundamental process parameters are: (i) the current and its voltage, (ii) the wire diameter, (iii) the wire-feed rate, (iv) the welding speed and (v) the vertical printed layer height. The combination of such controlling parameters affects the printing quality (geometrical precision and surface roughness) as well as the material mechanical properties. The printing parameters used for the experimental studies are listed in Table 2.1.

The welding source used is Gas Metal Arc Welding (GMAW), with pulse arc metal transfer. No arc correction has been adopted during the printing process. The substrate is a printing plate of 1000 x 1000 x 30 mm, with H-type beams welded as support. Two different cooling strategies have been considered: (i) printing process with active cooling, consisting of blowing compressed air between two consecutive layers deposited to increase the printing velocity reducing the wait time between layers; (ii) printing process with uncontrolled cooling, through a wait procedure between layers to allow the material to cool down, until it reaches a temperature below the interpass temperature of 150°.

Table 2.1: Process parameters for WAAM continuous deposition process (Courtesy of MX3D (*MX3D Webpage*)).

Process parameters	Details	Value*
Deposition power	Current	100 - 140 A
	Arc voltage	18 - 21 V

Speed	Welding speed	15 - 30 mm/s
	Wire feed rate	4 - 8 m/min
	Deposition rate	0.5 - 2 kg/h
Distance and angle	Layer height	0.5 - 2 mm
	Electrode to layer angle	90°
Wire	Wire grade	ER308LSi
	Wire diameter	1 mm
Shield gas	Shield gas type	98% Ar, 2%CO_2
	Shield gas flow rate	10-20 L/min

values are provided within typical ranges. For more specific information, the interested reader may refer to MX3D (MX3D Webpage, n.d.).

The specimens considered have been manufactured by MX3D (*MX3D Webpage*, n.d.) using a commercially available standard stainless steel welding wire grade ER308LSi (1 mm diameter) supplied by *Oerlikon* (*Oerlikon*). Traditionally manufactured 308LSi stainless steel grade has both microstructure and mechanical properties close to 304L grade, whose nominal values are given by various standards (see Table 2.2).

Table 2.2: Summary of mechanical properties of grades 304LSi stainless steel for different standard provisions (*AS/NZS 4673: Cold-Formed Stainless Steel Structures*, 2001; *SEI/ASCE 08-02: Specification for the Design of Cold-Formed Stainless Steel Structural Members*, 1991; European Committee for Standardization (CEN), 2015).

Grade		AS / NZS (*AS/NZS 4673: Cold-Formed Stainless Steel Structures*, 2001)	SEI / ASCE (*SEI/ASCE 08-02: Specification for the Design of Cold-Formed Stainless Steel Structural Members*, 1991)	EC3 – 14 (European Committee for Standardization (CEN), 2015)

Austenitic 304 (EN 1.4301)	**E** [GPa]	195	193.1	200
	R$_{p,02}$ [MPa]	195 - 205	248.2 - 275.8	190 - 230
	UTS [MPa]	520	551.6 - 620.6	500 - 540

For structural engineering applications, the need of high welding velocity for a rapid realization of structural elements of such proportions plays a crucial role for the specific characteristics of the printed parts, as it induces geometric inaccuracy of the outcomes, both in terms of surface roughness and lack of straightness of the elements. For a given element to be printed, a digital model from which the printing head reads the coordinates of the points defining step by step the position of the welded layer is created with Rhinoceros software (*Rhinoceros 5*). However, due to intrinsic inaccuracy of the printing process, each point of the digital model has a real counterpart whose position is not exactly the one of the digital model, as it is affected by an error.

Therefore, when dealing with WAAM-produced structural elements it is necessary to first codify specific issues related to: (i) the set of process parameters; (ii) the wrought material; (iii) the printing strategy. Furthermore, given the novelty of the process especially for structural engineering applications, there is very limited database of experimental results to provide sufficient information for the structural response of WAAM-produced metallic structural elements.

As previously introduced, structural elements manufactured with current WAAM processes are characterized by peculiar geometrical irregularities and specific material mechanical properties that have to be properly taken into account in both analysis and design process.

_____

2.4. DESIGN ISSUES OF WAAM CONTINUOUS PROCESS

WAAM-produced planar elements are characterized by their inherent geometrical irregularities, proper of WAAM layer-by-layer printing process, and specific material behavior, governed by a marked anisotropy. Both issues need to be properly taken into account and fully characterized for structural design of WAAM-produced elements, as they are both sources of uncertainties which influence the structural response of the designed and printed elements.

2.4.1. Inherent geometrical irregularities of WAAM-produced planar elements

The first peculiar aspect when dealing with structural members realized with WAAM process is the geometrical irregularities of the printed outcome (Figure 2.8).

As far as the continuous printing strategy is concerned, the main issue related to the layer-by-layer deposition is the surface roughness which also causes variation in thickness of as-built specimens. From planar to tubular geometries, additional irregularities in terms of lack of straightness and out-of-roundness should also be studied.

Therefore, for ready-to-use elements and future applications of on-site metal 3D printing, it becomes crucial to study the geometrical irregularities of WAAM-produced structural elements. First of all, proper characterization of the geometry of WAAM printed outcomes should be carried out. From that, considerations upon the possible influence of these irregularities in the mechanical response of the printed specimens should be analyzed as well.

Figure 2.8: Close-up views of the surface irregularities proper of WAAM-produced specimens: surface roughness from continuous printing strategy (planar element).

In detail, for a given planar element to be printed, a digital model from which the printing head reads the coordinates of the points defining step by step the position of the welded layer is created with Rhinoceros software. However, due to the inherent geometrical irregularities proper of WAAM process, the real printed outcome results in general in different geometrical features.

With regards of planar elements realized with continuous printing strategy, the deposition of successive layers of welded metal results in a non-uniform undulating surface. Considering the uniform rectangular plate represented in Figure 2.9, the origin of coordinates system used to describe the geometry of the plate is assumed to be located at one edge. The x and y axes are taken parallel to the two main directions of the plate, while the z-axis is perpendicular to the x-y plane. The thickness of the plate is given by the amount of welded metal positioned by the printing head, whose nominal value in the digital model is constant all over the plate and equal to $t_n=4$ mm. On the other hand, the value of thickness in the printed plate is in general non constant and varies both with x and y, so that $t_{real}=t_{real}(x,y)$. Given that the plates have been produced with a certain printing direction, the thickness variation might have a different

influence on the mechanical behavior of specimens cut along the printing direction (*x*) with respect to those cut perpendicular to it (*y*).
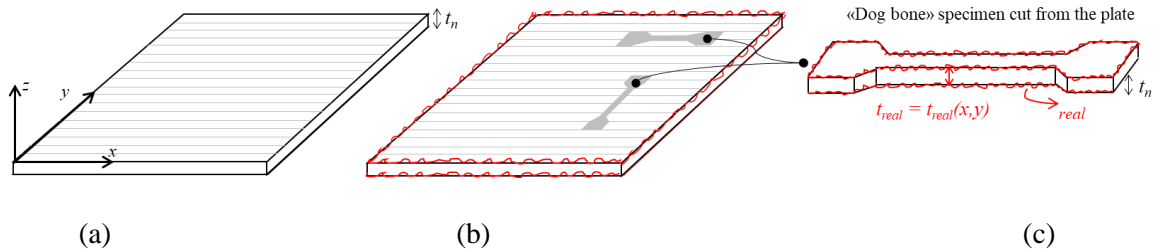
Figure 2.9: Digital model (a) and corresponding printed element (b) of a WAAM plate from which "dog-bone" specimens (c) are extracted.

2.4.2. Anisotropic material behavior of WAAM plates

The limited literature work focused on this innovative process slightly emphasizes the possible anisotropy induced by the process in the tensile properties of WAAM printed outcomes (Ge et al., 2018; Gordon et al., 2018; Haden et al., 2017; Ji et al., 2017; Kyvelou et al., 2020; Yilmaz & Ugla, 2017).

Since the manufacturing process may potentially induce an orthotropic behavior depending on the orientation towards printing direction and the presence of surface roughness resulting from the printing layers, the mechanical response should be investigated with reference to specimens having different orientation with respect to the deposition layers. Figure 2.10 qualitatively depicts three different orientations of specimens cut from printed plates: longitudinal direction (L) is taken along the deposition layers, transversal direction (T) is taken perpendicular to them, while diagonal direction (D) is taken at 45° from them.
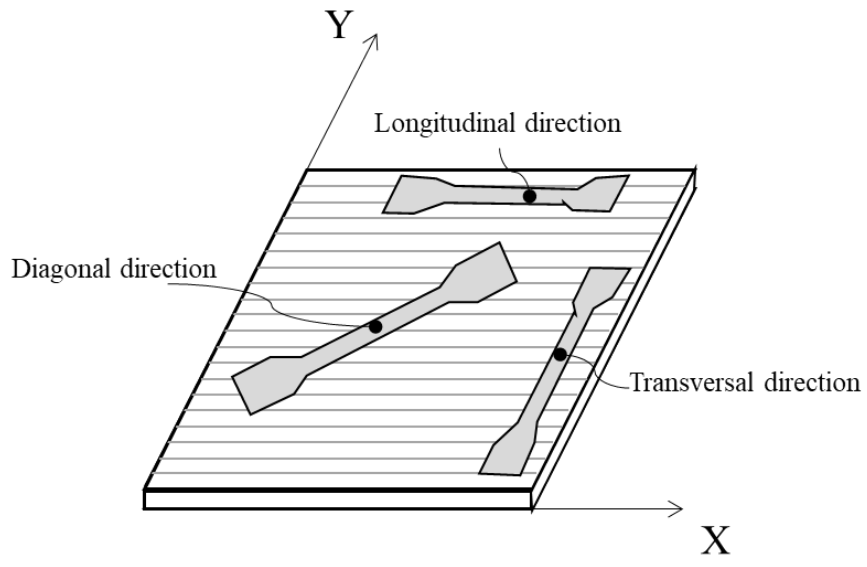
Figure 2.10: Orientation of the "dog-bone" shaped specimens cut from plates with respect to the deposition layer (grey lines).

_____

2.5. SUMMARY OF SECTION 2

The chapter briefly presents the Wire-and-Arc Additive Manufacturing process for continuous printing of planar elements. The specific printing process parameters adopted to realize the specimens for experimental characterization (as presented in Section 4) have been presented. Then, the main design issues for WAAM planar elements are described, in terms of both geometrical irregularities and anisotropic material behavior.

From these, an alternative design approach from the traditional one commonly adopted for structures should be considered, by taking into account the specific characteristics and issues proper of WAAM material (as presented in Section 3).

3. The design approach for WAAM structures

3.1. OVERVIEW

The design issues proper of WAAM stainless steel evidenced the need of ad-hoc guidelines and standards to design structures realized with this technology.

As such, different design approaches can be envisaged. Section 3.2 presents the traditional design approach commonly adopted for the design of traditionally-manufactured steel structures, while Section 3.3 proposes a design approach based on advanced numerical modelling. The proposed design approach adopted for the present study is described in Section 3.4.

3.2. THE TRADITIONAL DESIGN APPROACH

The design approach most widely adopted in international standard building codes, including Eurocodes, is the so-called design value method, also referred to as semi-probabilistic method (European Committee for Standardization (CEN), 2002; Holicky, 2009), as first introduced in ISO 2394: "General principles on reliability for structures" (*ISO 2394 - General Principles on Reliability for Structures*, 1998).

This method is based on the assumption that no limit state is exceeded when the design values of all basic variables are used in the models of structural resistance R and action effect E. Thus, if the design values E_d and R_d are determined considering the design values of all basic variables, then a structure is considered reliable if the following expression holds:

$$E_d < R_d \tag{3.1}$$

Both action effect and resistance are expressed in terms of their representative values, also denoted as characteristic, through the following expression:

$$E_k \cdot \gamma_E < R_k / \gamma_R \tag{3.2}$$

where γ_E and γ_R are denoted as partial safety factors. The computation of reliability remains deterministic, but the values of partial safety factors are calibrated to match a predefined probability of failure p_f (also referred to as target probability of failure). Hence, the approach is considered as semi-probabilistic.

The action effect depends on the loads and actions applied, while the structural resistance depends on the material properties. Both of them also depend on the geometrical properties and the model uncertainties:

$$E_d = E\left\{F_{d,i}, a_{d,i}, \theta_{d,i}\right\} \tag{3.3}$$

$$R_d = R\left\{X_{d,i}, a_{d,i}, \theta_{d,i}\right\} \tag{3.4}$$

Generally speaking, all these quantities are taken as random variables, and for design purposes their design values should be considered.

With reference to traditional structures, the material properties (as well as the actions) are taken as random variables, whose distribution is modelled with statistical analysis. On the other hand,

the geometrical properties are considered as deterministic values. This means that their value is not affected by any source of uncertainty. The model adopted to evaluate the structural response is by considering De Saint Venant's theorem, and assuming a linear elastic material behaviour. Hence, the structure is designed such that it remains elastic under the action effects.

3.3. THE DESIGN APPROACH BASED ON ADVANCED NUMERICAL MODELS AND TESTING

Within the design workflow of additive-manufactured parts and components, advanced numerical models should be adopted to account for the specific issues related to the printing process, as the levels of anisotropy, the geometrical imperfections, the residual stresses and so on.

As such, a new design approach referred to as "design by advanced analysis" has been developed to take the full advantages and characteristics of AM technology. The basic principle lies within the concept of the so-called "digital twin", i.e. the mirroring of a physical object created in a virtual environment by simulation-based engineering (Okita et al., 2019).

Theoretically speaking, the use of advanced simulation tools and digital twins would allow to model the geometrical imperfections of each single manufactured piece and to consider the actual orthotropic non-linear stress-strain material behavior such that all the potential modes of failure could be explicitly included in the model. Such complex and detailed Finite Element models would allow to even simulate loading tests, construction sequences, fatigue-related issues and other complex non-linear phenomena. These advanced analysis models may also be used along with structural monitoring systems for real-time control of the structural response. Pioneering research in this direction is currently under development by a research team led by Alan Turing Institute and MX3D in collaboration with Imperial College of London and Autodesk (*Alan Turing Institute to Turn the World's First 3D Printed Steel Bridge Into a "Living Laboratory" for Research*; Gardner et al., 2020) (Figure 3.1).
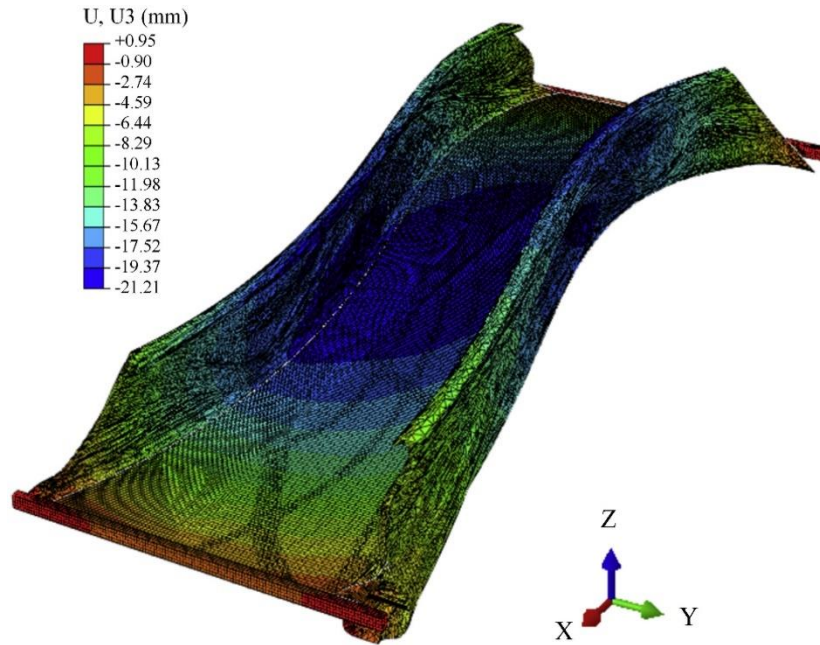
(a)
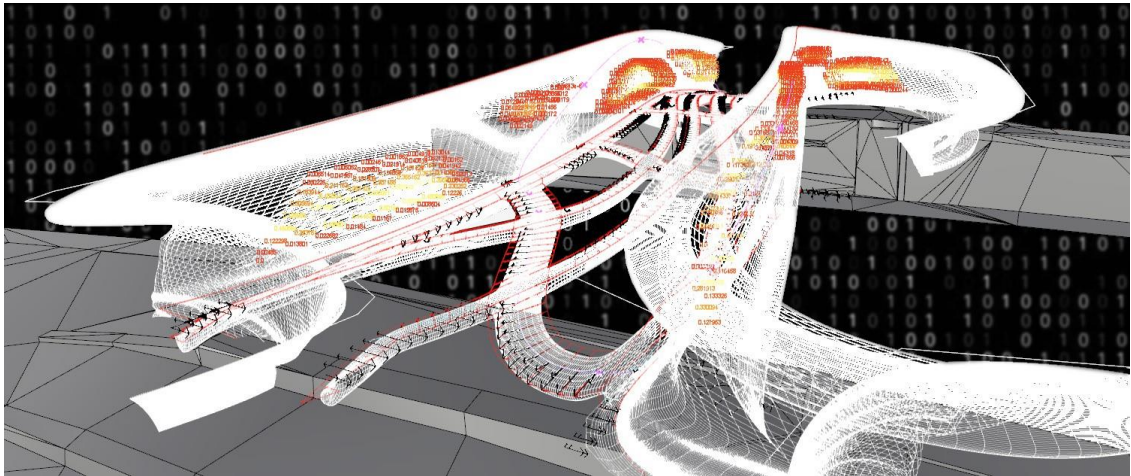
(b)

Figure 3.1: Advanced numerical model for the MX3D Bridge: (a) Finite Element simulation at test load; (b) "digital twin" for a smart monitoring network (Gardner et al., 2020).

The full development of a reliable digital twin requires detailed knowledge of the peculiar geometrical imperfections requiring use of random field approaches and uncertainties quantification techniques (Bae et al., 2004), as well as ad-hoc material models able to account for the specific features of WAAM. In order to properly manage such advanced simulation tools,

structural engineers need to become more computationally literate and acquire high level computational skills (Buchanan & Gardner, 2019).

3.4. THE PROPOSED DESIGN APPROACH FOR WAAM STRUCTURES

As an alternative to the advanced modelling of Section 3.3, the proposed design approach for WAAM structures adopted in the present study is adapted from the traditional design approach for structures (as presented in Section 3.2).

The method follows the semi-probabilistic approach to calibrate design values and partial safety factors for the material properties as for traditional structural elements. However, in order to properly consider the design issues for WAAM metals (presented in Section 2.4), additional considerations should be made. First of all, the key material properties should be defined along the three main directions with respect to the printing layers (see Section 2.4.2). Furthermore, additional considerations on the Young's modulus and Poisson's ratio, which are commonly taken as deterministic values, should be made. Indeed, as will be presented in the next Section, these parameters are also highly influenced by the orthotropic microstructure of the WAAM-produced part, thus being subjected to high uncertainty in their values.

As far as the geometry is concerned, generally speaking it is highly influenced by the inherent irregularities proper of the printing process (see Section 2.4.1). Thus, it should be properly characterized in order to derive the key material properties and the possible influence in their values.

As such, the geometrical characterization should provide two types of results:

1. general information on thickness and cross-sectional areas based on manual and volume measurement, to be used to obtain the values of effective stresses from the mechanical tests;

2. detailed information on the inherent geometrical irregularities in terms of surface roughness and thickness variation, based on 3D scan.

As far as results type 1 is concerned, one of the main purposes is the evaluation of the discrepancies between the *nominal* (associated to the digital model), the *real* (as manufactured) and the *effective* values (used to compute the effective stresses) of cross-sectional area. Figure 3.2 provides a qualitative comparison between nominal, real and effective thickness for a planar specimen manufactured through WAAM. It should be noted that, in general, the effective thickness takes an integral over the entire length of the specimen, thus considering both peaks and pits. For this reason, it could result higher or lower than the nominal thickness.
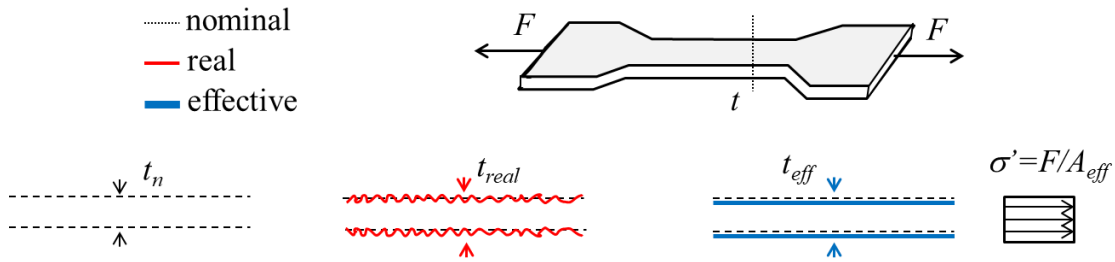
Figure 3.2: Nominal, real and effective thickness for WAAM planar specimen.

As far as the mechanical material properties are concerned, the mechanical tests are interpreted assuming that the cross-sectional area is constant along the member length so that the axial stresses can be computed according to simple beam theory:

$$\sigma_{eff} = \frac{F}{A_{eff}} \tag{3.5}$$

where:

- A_{eff} is an effective cross-sectional area of the structural member to be determined on the basis of the result type (1) of above.
- F is the tensile axial force (e.g. the force applied during a tensile test).

Clearly, the stress σ_{eff} can be interpreted as an effective stress which differs from the true material stress conventionally referred to as σ.

The effective stress σ_{eff} depends on A_{eff} and specific attention should be devoted to its choice.

Different criteria can be adopted to choose A_{eff}, based on scientific, technical and practical considerations related to significance, accuracy and reliability of the chosen value. Some possibilities are: (i) use of nominal values, (ii) use of a set of punctual values based on mechanical measurements, (iii) use of average values as obtained from volumetric measurements.

The use of nominal values as given by the manufacturer does not require any measurement, but, on the other hand, the absence of measurements may lead to lack of significance and poor reliability especially for non-standardized processes (like WAAM).

The use of few manual measurements (such as caliper measurements) is straightforward since such measurements can be easily executed even at the production site, but this type of measurements could be easily biased.

The use of average values as obtained from volumetric measurements (used in (Kyvelou et al., 2020; Laghi et al., 2020a) to obtain A_{eff}) has the advantage of providing an integral value based on equal weight criterion. It can also be adopted for a fast quality control during the production phase.

In the present study, the values of the effective cross-sectional areas are those derived from volume measurements.

This result leads to condense all uncertainties (geometrical and mechanical) in the mechanical parameters only. The simplified approach allows to treat the cross-sectional area as a deterministic value, while all the uncertainties are globally collected in the effective axial stress. In this way, the conventional format commonly adopted for the analysis and design of traditionally manufactured steel members, which considers the geometrical parameters as deterministic values and the material strength parameters as random variables, is maintained. Thus, the experimental mechanical parameters become dependent on both the specific geometrical and mechanical features related to the manufacturing process and not only on the material itself.

In order to derive the key material properties of WAAM stainless steel, experimental characterization has been carried out on machined specimens, from which the sources of variability of the geometry proper of WAAM process have been erased and only the uncertainties related to the mechanical properties of the material are present (see next Section 4.3). Then, experimental tests have been carried out on as-built specimens, to compare the mechanical response and provide first insights on the variability related to the geometrical irregularities of the printed outcomes (see next Section 4.5). For such reason, first a detailed geometrical characterization has been carried out (see next Section 4.4). The design approach followed in the present study is conceptually schematized in Figure 3.3.
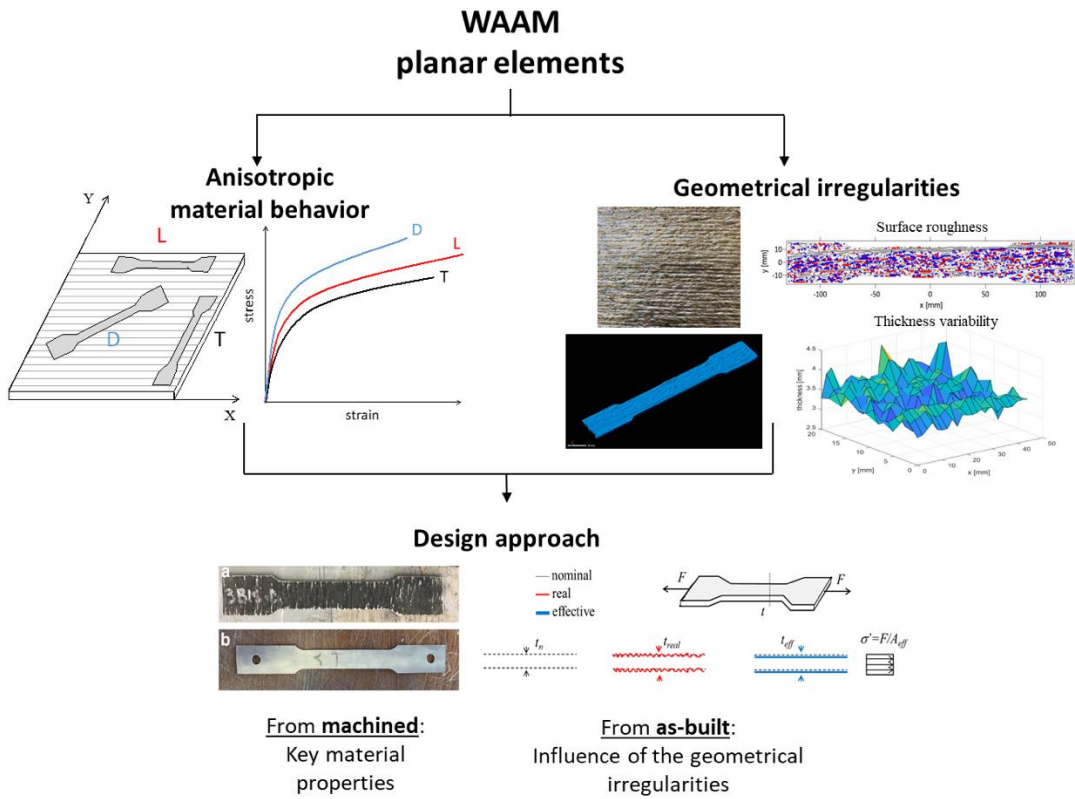
Figure 3.3: Conceptual flowchart of the proposed design approach for WAAM planar elements.

3.5. SUMMARY OF SECTION 3

The present Section proposes different design approaches to be applied for structural applications of WAAM-produced members.

Among different solutions to be used for the structural design of WAAM stainless steel elements, a simplified approach is adopted for the present study (Figure 3.4). The basic idea lies upon the decoupling of the two main sources of uncertainties, i.e. from the geometrical irregularities and from the inherent material properties. As such, two different types of specimens are considered in the experimental campaign (described in detail in the following Section): (i) machined specimens, from which the geometrical irregularities are erased and the only source of uncertainty is related to the material properties of WAAM stainless steel; (ii) as-built specimens, from which information related to the influence of the geometrical irregularities on the mechanical behavior of WAAM stainless steel elements is analyzed.
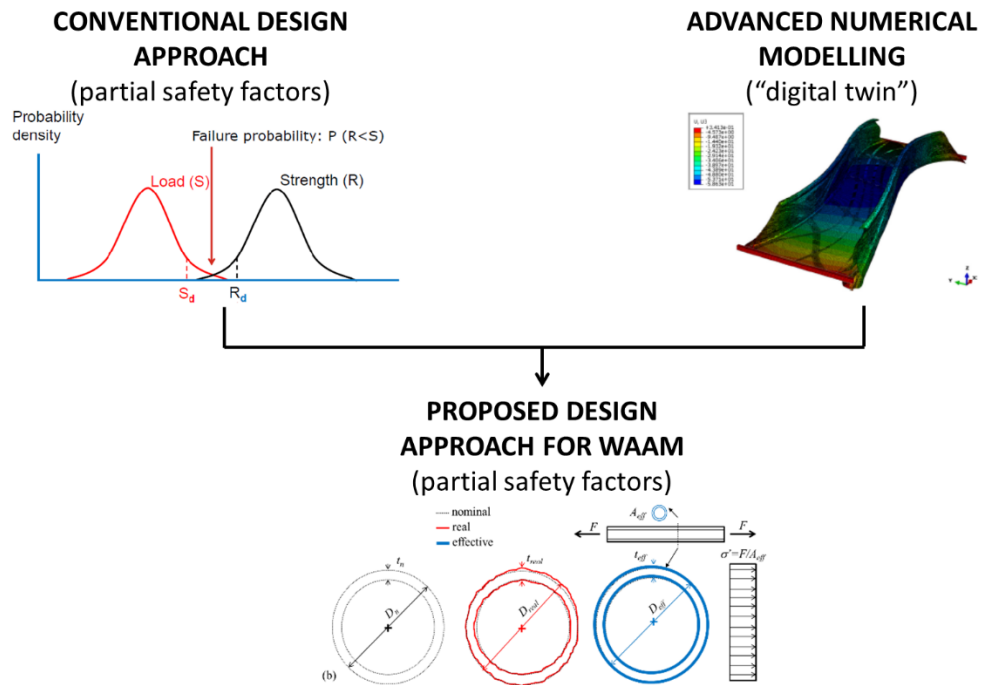
Figure 3.4: Conceptual flowchart of Section 3.

4. Experimental characterization of WAAM stainless steel plates

4.1. OVERVIEW

As presented in the previous Chapter, Wire-and-Arc Additive Manufacturing stainless steel elements present some design issues in terms of inherent geometrical irregularities and specific material behavior, especially related to its anisotropic nature. Thus, it becomes crucial to fully characterize WAAM-produced planar elements considering all these aspects.

For this reason, the experimental characterization has been carried out on two types of specimens: (i) machined specimens, from which information on the material properties is analyzed, and (ii) as-built specimens, from which information related to the geometrical irregularities and their influence on the mechanical behavior is studied.

From the tests on the machined specimens, first a microstructural analysis (presented in Section 4.2) has been carried out with the colleagues from the Metallurgic Department of University of Bologna. Then, the key material properties have been estimated from tensile tests on machined specimens (and presented in Section 4.3).

From the tests on the as-built specimens, a geometrical characterization has been carried out in two steps (Section 4.4). First, detailed investigation on the inherent geometrical irregularities in terms of surface roughness and thickness variation has been analyzed through 3D scanner of one planar specimen. Then, general information on the effective cross-sectional area of the planar specimens tested has been performed through manual and volume measurements. The mechanical behavior of as-built specimens (presented in Section 4.5) was studied through tensile tests to evaluate the influence of geometrical irregularities on the mechanical response of WAAM elements.

4.2. MICROSTRUCTURAL ANALYSIS ON MACHINED SPECIMENS

The chemical analysis of continuously printed WAAM machined pieces realized with commercial ER308LSi wire was carried out in collaboration with the Metallurgic department at University of Bologna. The main findings of this analysis have been presented in (Laghi et al., 2020b; Laghi et al., 2020c).

In detail, the analysis has been checked by Glow Discharge Optical Emission Spectroscopy (GDOES: GDA-650, Spectruma Analytik GmbH, Hof, Germany), with a sputtered burnt spot of 4 mm diameter, in order to determine the composition of the newly produced material compared with that of the feedstock wire.

To relate the mechanical behavior with specific microstructural features induced by the process, microstructural analyses were carried out by means of 3D-Digital Microscopy (Hirox KH-7700), Reflected Light Optical Microscopy (RLOM) and Scanning Electron Microscopy (SEM) equipped with energy dispersive X-ray spectroscopy (EDS) (Figure 4.1).

Figure 4.1: Optical Microscopy (Courtesy of Spectra Services).

Samples for microstructural characterization have been cut at different orientations with respect to the deposition layers. In detail, three different orientations have been considered (as presented in Section 2.4.2): (i) along the deposition layers, namely longitudinal direction L, (ii)

perpendicular to the deposition layers, namely transversal direction T, and (iii) at 45° from the deposition layers, namely diagonal direction D (see Figure 2.8). The samples were mounted in a phenolic resin, grounded with silicon carbide papers up to 2000 grits and finally polished according to ASTM E3 standard (ASTM International, 2017) with 1µm polycrystalline diamond suspension to obtain a mirror finish. In order to highlight any specific microstructural features induced by WAAM, chemical etching with 20s immersion in the Vilella's reagent (1 g picric acid, 5 mL hydrochloric acid and 100 mL ethanol) was performed (Vander Voort et al., 2004). Quantitative image analysis was carried out by ImageJ software (Bourne & Bourne, 2010) on low magnification micrographs (50x, 3D-Digital Microscope) over at least 15 images to evaluate the average thickness of the deposition layer.

After the tensile tests, specimens fracture surfaces were analyzed both at low magnification by 3D-Digital Microscopy and at higher magnification with SEM-EDS to investigate the specific failure mechanisms.

GD-OES compositional analysis was performed on the printed steel plates to verify whether their composition was different from that of the feedstock ER308LSi wire. The results are reported in Table 4.1, compared with the nominal chemical composition of the wire (given by the supplier), as well as of 308LSi (UNS-S-30800) and 304L (UNS-S-30403) austenitic stainless steels according to AWS A5.9 (*ANSI/AWS A5.9-93: Specification for Bare Stainless Steel Welding Electrodes and Rods*, 1993) and ASTM A276 (ASTM A276-16, 2016) respectively.

It can be inferred that the WAAM samples meet the requirements of UNS-S-30403 for an AISI 304L chromium-nickel austenitic stainless steel. Henceforth, all results on the WAAM stainless steel are compared to the properties of type 304L stainless steel.

Table 4.1: Results of the GD-OES composition analysis (wt.%) performed on the WAAM samples compared to the nominal chemical composition of the wire (given by the supplier), of 308LSi (UNS-S-30800) and 304L (UNS-S-30403) austenitic stainless steels according to AWS A5.9 (*ANSI/AWS A5.9-93: Specification for Bare Stainless Steel Welding Electrodes and Rods*, 1993) and ASTM A276 (ASTM A276-16, 2016) respectively.

	C	*Cr*	*Ni*	*Mn*	*Si*	*Co*	*V*	*Mo*	*Cu*	*P*	*S*	*Fe*
Wire	0.02	20	10	1.8	0.85	-	-	0.2	-	<0.025	<0.020	Bal.

ER 308LSi	<0.08	19.0-21.0	10.0-12.0	<2.0	<1.0	-	-	-	-	<0.045	<0.03	Bal.
WAAM Samples	0.009	19.495	9.583	1.73	0.634	0.471	0.111	0.015	0.015	0.0222	0.0113	Bal.
AISI 304L	<0.03	18.0-20.0	8.0-12.0	<2.0	<1.0	-	-	-	-	<0.045	<0.03	Bal.

A common issue for welding-related processes (like WAAM) is the controlled porosity. In this regard, no macroscopic defects (e.g. cracks, porosity, or lack of fusion) were evidenced by metallographic analyses in the majority of the as-printed samples between any two adjacent layers, demonstrating that the optimized WAAM processing parameters used in the present study ensure a substantially defect-free, dense structure. Further evidences of this aspect are found in the density measures of the printed plates, on average equal to 7930 ± 240 kg/m^3, determined by means of volume-based measures taken with a hydraulic scale according to the Archimedes' principle.

Additional investigations were performed to further analyze the crystallographic orientation of the WAAM stainless steel material. Microstructural analyses were carried out on samples extracted from grip regions of longitudinal (L), transversal (T) and diagonal (D) tensile specimens. Samples followed a complete metallographic preparation up to polishing to a mirror finish, as described in (ASTM International, 2017), then were chemically etched by immersion in the Vilella's reagent at room temperature for 20 s (1 g picric acid, 5 mL hydrochloric acid, and 100 mL ethanol (Vander Voort et al., 2004)). Microstructural characterization at low magnification was performed by means of an Hirox KH7700 3D digital microscope while for the observation at higher magnification a Zeiss Axio Imager A1 optical microscope was adopted.

X-Ray diffraction (XRD: X'Pert PRO diffractometer, PANAlytical, Almelo, NL) was used to determine phase composition of T, L and D representative samples. Spectra were acquired with a Ni-filtered Cu-Kα radiation source in the range $40° < 2\theta < 100°$, with a step size of $0.02°$ and 120 s/step dwell time, using a 1D array of solid-state detector (X'Celerator PANAlytical). Acquired spectra were elaborated with HighScorePlus software (PANAlytical) for phase identification and peaks characterization, texture coefficients were then obtained following the procedure described by (M. Liu et al., 2019; Saikia et al., 2013).

The microstructure of WAAM samples is shown in Figure 4.2 where 3D reconstructions obtained by low magnification analyses are reported for the L, T and D directions. From the micrographs, two peculiar features of additively manufactured parts can be recognized: (i) the layered macro-structure due to the subsequent depositions of molten material, and (ii) the epitaxial grains that have grown over the layers and whose direction is perpendicular to the deposition layer. In fact, due to the peculiar in-process solidification conditions, epitaxial growth occurs and grains grow following the crystallographic orientation of the previously solidified layer (Basak & Das, 2016), possibly leading to crystallographic texture. In Figure 4.2, layer boundaries and columnar grains are highlighted with yellow and red dashed lines, respectively. In the same figure, also the longitudinal direction of the specimen (coincident with the direction of the applied tensile load) is reported, so it can be clearly seen that layers and grains are differently oriented among L, T and D samples with respect to the direction of the applied tensile load. 3D reconstructions also evidenced that cross-sectional area of tensile specimens, in terms of grains and layer boundaries orientation, varies from one direction to another. These aspects, as also discussed in (Laghi et al., 2020), may play a significant role on the mechanical properties, thus leading to possible anisotropy.

Details of the layer boundary region, for the three directions, are reported in Figure 4.3 where two different grain morphologies can be recognized: a fine columnar structure in correspondence of the solidification of a newly deposited layer and a coarser one, where also secondary dendrites can be seen, at the bottom of the boundary due to heating of the previous layer, as also reported by (Wang et al., 2019). In the same figure, it can be also seen that growth of the aforementioned columnar grains did not stop at the boundaries, but proceeded across them without changing direction. This phenomenon is likely related to the epitaxial growth that may occur during the rapid solidification experienced by each deposited layer during AM process, where grains grow following the crystallographic orientation of the previously solidified layer (Basak & Das, 2016).
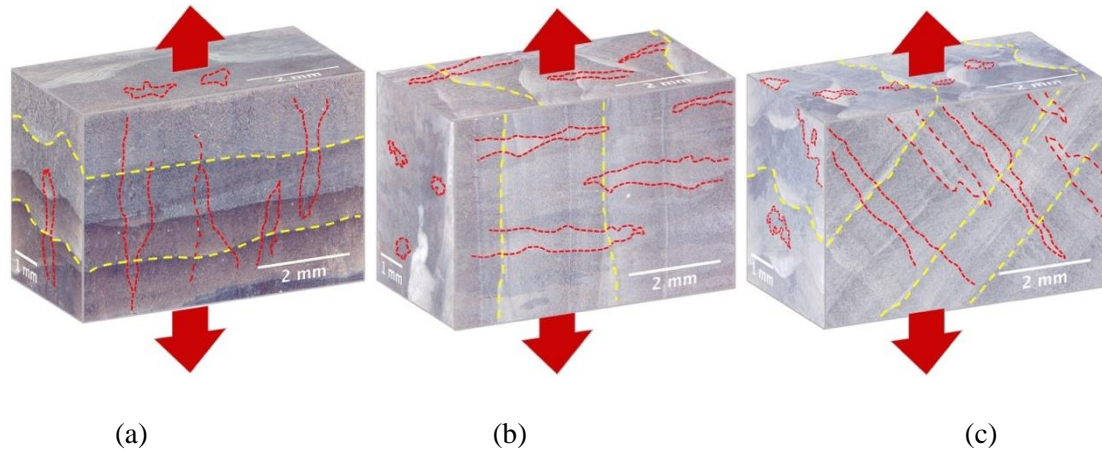
Figure 4.2: 3D reconstruction of low magnification optical micrographs of tensile specimens: a) longitudinal, b) transversal and c) diagonal specimen. Yellow dashed lines underline the deposited layers while the red ones highlight grain growth; red arrows indicate the loading direction during tests.
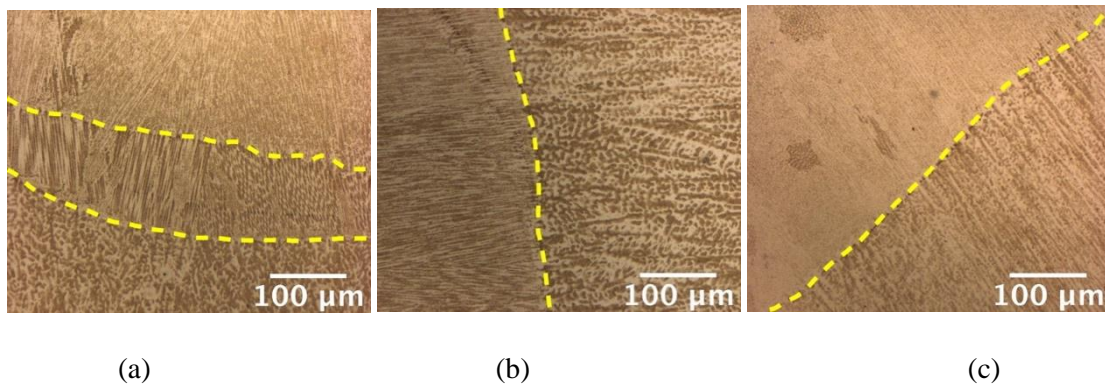
Figure 4.3: Optical micrographs showing sub-structure within epitaxial grains crossing over layers for: a) transversal, b) longitudinal and c) diagonal specimen. Layer boundaries are highlighted by yellow colour.

If this assumption is confirmed, WAAM plates may have developed (during the printing process) a preferential crystallographic orientation of grains and, as a consequence, tensile specimens extracted along T, L and D direction might exhibit different preferential orientations.

High magnification analyses also revealed a fine cellular sub-structure within the larger columnar grains, whose size is of the order of few microns, and consists of primary γ-austenite dendrites and δ-ferrite at the cell boundaries. It is known that solidification in austenitic stainless steel welds is related to the composition of the alloy. For the case studied, according to the GD-OES results reported in Table 4.1, since $Cr_{eq}=20.461\%$ and $Ni_{eq}=10.718\%$, according to the Schaeffler

diagram (Kou, 2003), the welds should solidify with the austenite being the primary or leading phase and the δ-ferrite located in the interdendritic spaces. Further details on this can be found in (V. Laghi et al., 2020).

In view of the above, crystal structure was analyzed with XRD, whose results are reported in Figure 4.4 for a set of representative samples. X-Ray diffraction (XRD: X'Pert PRO diffractometer, PANAlytical, Almelo, NL) was used to determine phase composition of T, L and D representative samples. Spectra were acquired with a Ni-filtered Cu-Kα radiation source in the range $40° < 2θ < 100°$, with a step size of 0.02° and 120 s/step dwell time, using a 1D array of solid-state detector (X'Celerator PANAlytical). Acquired spectra were elaborated with HighScorePlus software (PANAlytical) for phase identification and peaks characterization, texture coefficients were then obtained following the procedure described by (M. Liu et al., 2019; Saikia et al., 2013).

The same samples were also employed for electron backscatter diffraction (EBSD) analysis. The latter was carried out using the Nova NanoSEM 450 device, which was equipped with a QC-200 i (Bruker) EBSD system featuring an e−Flash1000 detector. Samples, placed at an inclination of 70° with respect to the electron beam axis, were scanned at 15 kV acceleration voltage under low-vacuum (40 Pa) conditions in order to avoid charging drift of their non-conductive surfaces.

XRD spectra (Figure 4.4a) showed that, for all samples, the predominant phase was austenite (γ), with minor traces of delta-ferrite (δ).

The reference pattern for austenite (ICDD 33-0379) shows five peaks corresponding to (111), (200), (220), (311), (222) crystallographic planes. However, as can be noticed by XRD results, none of the spectra exhibited the (222) austenite peak located at approximately 95.96° and, more importantly, samples showed different peaks characterized also by different peak intensities, suggesting the occurrence of a varied preferred orientation. Specifically, T, L and D directions showed two, four and three austenite peaks respectively.

_____
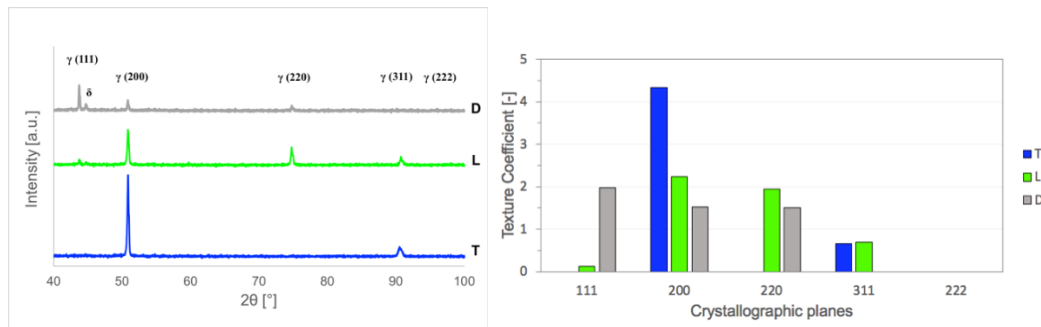
(a)   (b)

Figure 4.4: Results of XRD analyses: a) XRD spectra showing phase composition for transversal (T), longitudinal (L) and diagonal (D) specimens; b) texture coefficients for γ-austenite phase derived from spectra

With the aim of quantifying such preferred crystallographic orientation, texture coefficients (TC) for the dominant γ-austenite phase were calculated. The results are reported in Figure 4.4b. If no preferred orientation exists, TC is equal to 1 for all crystallographic planes, while in case that one or more orientations prevail, TC assumes value higher than 1 for the dominant orientations. Data reported in Figure 4.4b show that T direction is dominated by (200) orientation, while for L directions (200) and (220) are more predominant. It should be noticed that (111) peak was not revealed on T sample and was almost negligible for L one, while it prevails on D direction.

The presence of a marked crystallographic preferential orientation in the γ-austenite phase was also confirmed by EBSD analyses. According to the inverse pole figures (IPF) and maps reported in Figure 4.5 for sample D, a texture oriented along the <111> crystallographic direction exists. This outcome further supports the above discussion, relating the highest stiffness exhibited by D direction with the stiffest crystallographic direction of the fcc stainless steel lattice structure.
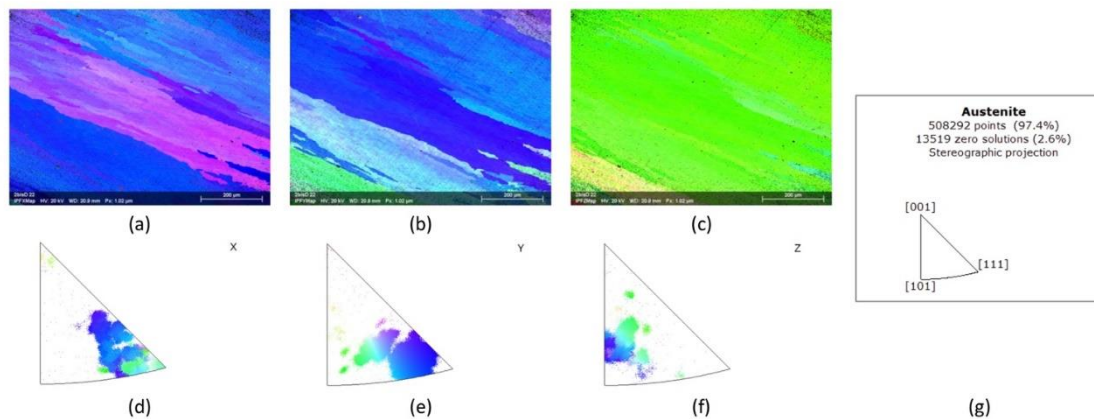
Figure 4.5: Inverse pole figures (IPF) from EBSD analyses on plane xy for a representative D sample: a) IPFx map; b) IPFy map; c) IPFz map; d), e), f) relative IPF; g) IPF key legend.

_____

4.3. MATERIAL CHARACTERIZATION FROM TENSILE TESTS ON MACHINED PLANAR SPECIMENS

4.3.1. Measurements and set-up

In order to assess the values of the key material properties of WAAM-produced stainless steel, a series of tensile tests have been performed on specimens cut from continuously-printed plates. To account for the possible anisotropic behavior of WAAM material, the specimens have been extracted along directions T, L and D (according to the scheme in Figure 2.8). In particular, a total of 26 tensile tests have been performed on the following samples: (i) 6 transversal T specimens, (ii) 8 longitudinal L specimens and (iii) 12 diagonal D specimens. From these, half of the specimens have been taken from plates printed with active cooling strategy, and half with uncontrolled cooling (as described in Section 2.3).

The specimens, extracted along the three main directions (following the scheme in Figure 2.8), were shaped according to ISO 6892-1 *(Metallic Materials — Tensile Testing — Part 1: Method of Test at Room Temperature*, 2009) (Figure 4.6). Table 4.2 provides an overview of the types of machined specimens tested under tensile action.

Table 4.2: Machined specimens details for tensile tests.

Surface type	Orientation	Printing process	Quantity	Specimen ID
Machined (M)	Transversal (T)	Active cooling (A)	3	M-T-A-1 to M-T-A-3
		Uncontrolled cooling (U)	3	M-T-U-1 to M-T-U-3
	Longitudinal (L)	Active cooling (A)	4	M-L-A-1 to M-L-A-4
		Uncontrolled cooling (U)	4	M-L-U-1 to M-L-U-4
	Diagonal (D)	Active cooling (A)	6	M-D-A-1 to M-D-A-6

		Uncontrolled cooling (U)	6	M-D-U-1 to M-D-U-6
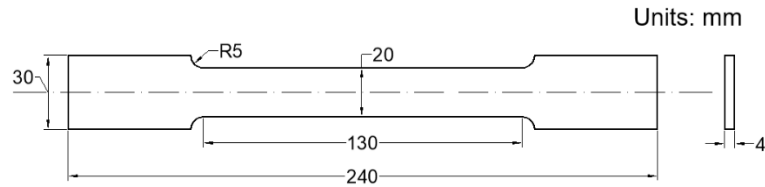
Figure 4.6: Geometry and dimensions (mm) of the flat tensile specimens according to ISO 6892-1.

Given the rough nature of the printed plates proper of the WAAM process (Laghi et al., 2019; Laghi et al., 2020a), in order to assess the material characteristics of WAAM-produced stainless steel, the surface of the tensile specimens has been polished by means of mechanical milling, reducing the final thickness to an average value of 2.5 to 3 mm, starting from the nominal 4-mm thickness of the plates. Images of the specimens before and after milling are shown in Figure 4.7.

Figure 4.7: Tensile specimen cut from WAAM plates: (a) as-printed and (b) after surface milling.

The tensile tests have been performed according to ISO 6892-1 on a Universal testing machine of 500 kN load capacity. The specimens have been tested in displacement-control having a loading rate of 2 MPa/s. Two types of monitoring systems have been adopted: a linear

deformometer of nominal dimension of 50 mm, to detect the linear deformation of the specimens up to yielding, and an optical-based system referred to as Digital Image Correlation (DIC), to acquire the full strain field during the whole test until failure. The tensile test set-up is presented in Figure 4.8.

Figure 4.8: Tensile test set-up for continuously-printed WAAM stainless steel elements.

4.3.2.   Tensile tests on machined specimens

Figure 4.9 provides the engineer stress-strain curves of the specimens tested and Figure 4.10 a zoom of them. For each orientation, both specimens realized with active (A) and uncontrolled (U) cooling are presented. From these, it clearly appears that T and D specimens have lower values of ultimate elongation with respect to the longitudinal ones. Moreover, D specimens result in higher stress values compared with the other two directions. From a closer look at the first part of the test (until 1% deformation), D specimens have stiffer behavior and result in higher values of yielding stress. Overall, from the stress-strain curves it seems that the cooling strategy does not highly influence the tensile response of WAAM stainless steel specimens.
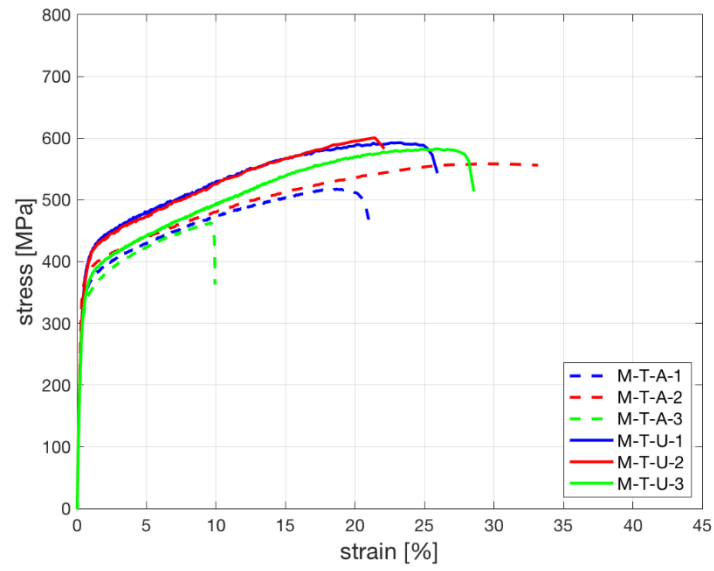
(a)
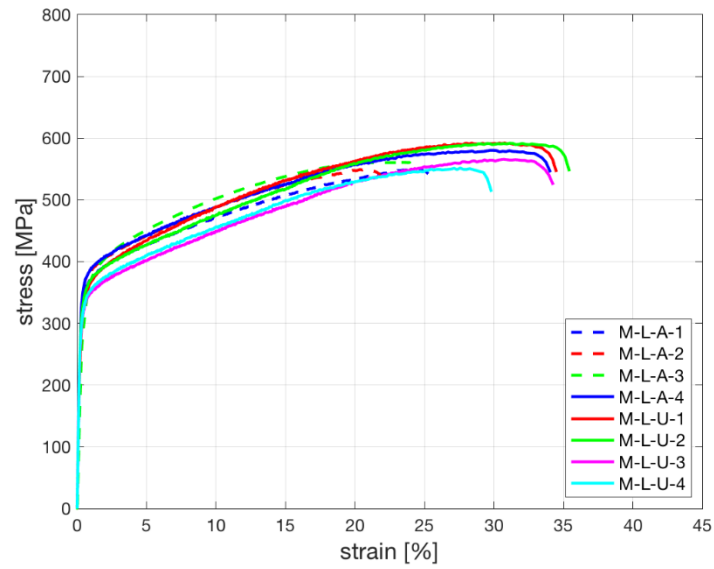
(b)
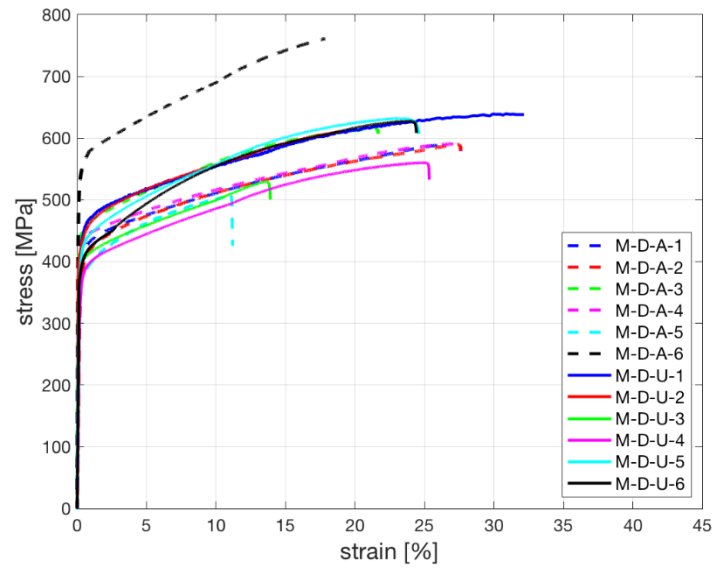
(c)

Figure 4.9: Stress-strain curves for tensile tests: (a) specimens T, (b) specimens L and (c) specimens D.

(a)
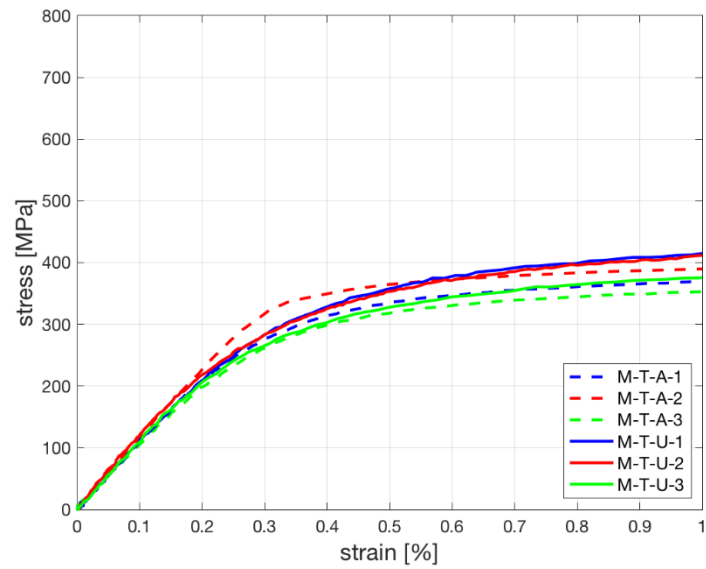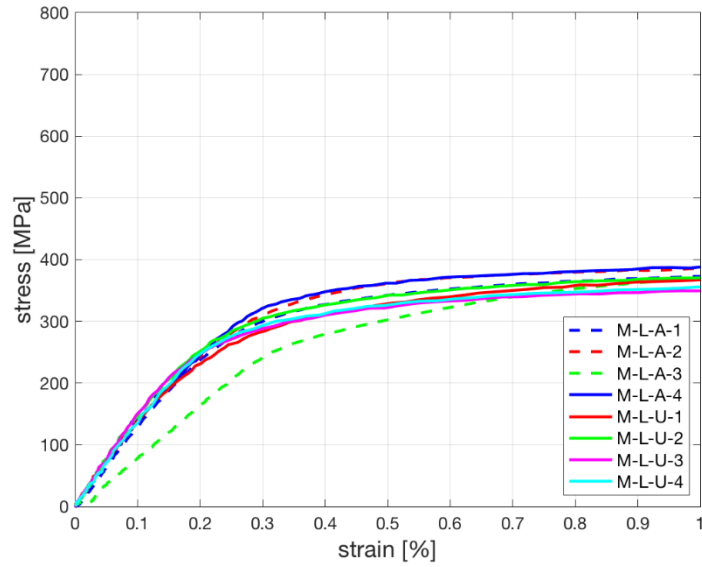
(b)
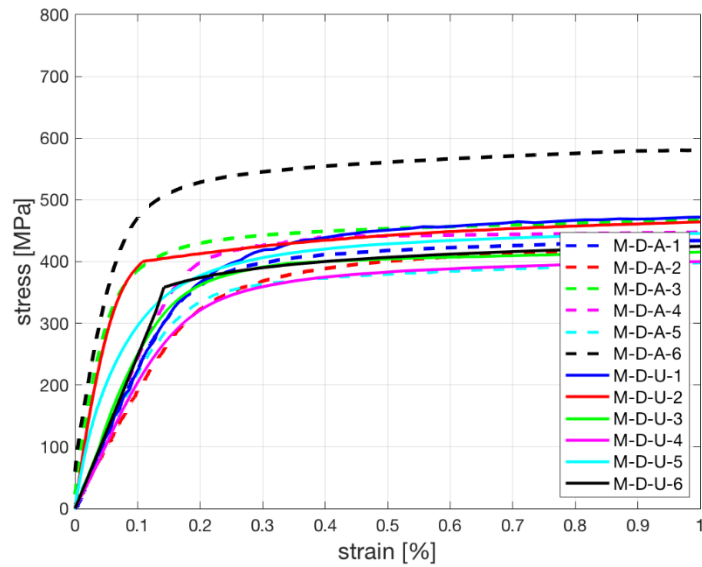
(c)

Figure 4.10: Zoom of stress-strain curves (at deformations <1%) for tensile tests: (a) specimens T, (b) specimens L and (c) specimens D.

Table 4.3 reports the values of the key material parameters computed from tensile tests according to EN ISO 6892-1 standards, in terms of Young's modulus (E), 0.2% proof stress ($R_{p0.2}$), ultimate tensile strength (UTS), elongation at rupture ($A_{\%}$) and yield to tensile strength ratio ($R_{p0.2}/UTS$).

Table 4.3: Summary of tensile tests results.

Specimen type	Printing strategy	Specimen ID	E [GPa]	$R_{p0.2}$ [MPa]	UTS [MPa]	$A_\%$ [%]	$R_{p0.2}$/UTS [-]
T	A	M-T-A	112 ± 7	351 ± 19	513 ± 39	21 ± 9	0.69 ± 0.03
	U	M-T-U	111 ± 1	354 ± 18	592 ± 7	26 ± 3	0.60 ± 0.03
L	A	M-L-A	133 ± 3	356 ± 10	560 ± 13	26 ± 5	0.64 ± 0.02
	U	M-L-U	142 ± 4	322 ± 11	575 ± 17	34 ± 2	0.56 ± 0.02
D	A	M-D-A	241 ± 38	420 ± 48	608 ± 77	22 ± 6	0.69 ± 0.03
	U	M-D-U	249 ± 30	408 ± 27	602 ± 41	24 ± 5	0.68 ± 0.05

4.3.3. Discussion on the key material properties

Figure 4.11 reports an overview of the mean values and variations of the key material properties for the three directions investigated (T, L and D) subjected to different cooling strategies (i.e. with active cooling or with uncontrolled cooling). Reference to traditional values of the key mechanical properties of 304L stainless steel according to European building code (European Committee for Standardization (CEN), 2015) is also provided.

As far as Young's modulus values are concerned (Figure 4.11a), they are highly affected by their relative orientation with respect to the deposition layers. L and T specimens have 30% to 50% reduced values with respect to the traditional value commonly adopted for stainless steel. This aspect is in line with the findings of (Gordon et al., 2018; Kyvelou et al., 2020; Van Bolderen, 2017). On the other hand, D specimens have 20% higher values than the traditional stainless

steel, as also reported by Kyvelou et al. (Kyvelou et al., 2020) and presented in (Laghi et al., 2020a). Overall, for all three orientations the specimens with uncontrolled cooling registered slightly higher values of Young's modulus.

For all three orientations, 0.2% proof stress values are much higher than the reference value for 304L steel (Figure 4.11b), with little difference between the two different cooling strategies.

As far as ultimate tensile strength values are concerned (Figure 4.11c), the values for all three orientations are slightly higher than the traditional reference for 304L steel. Only T specimens with active cooling strategy registered slightly lower values.

The highest discrepancy between specimens with different cooling strategy is encountered with the values of elongation at rupture (Figure 4.11d). Indeed, for all three orientations considered the specimens with uncontrolled specimens have higher values of elongation, with 10 to 25% increase.

(a)
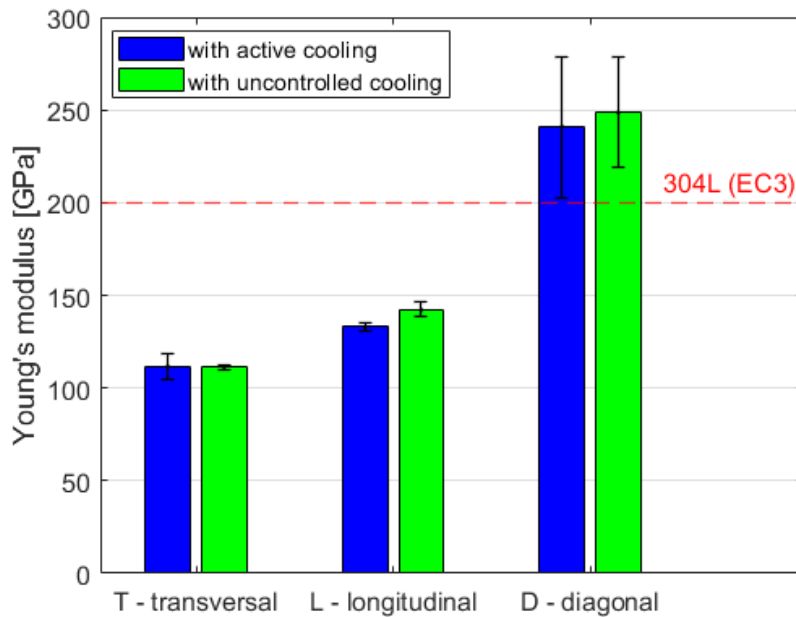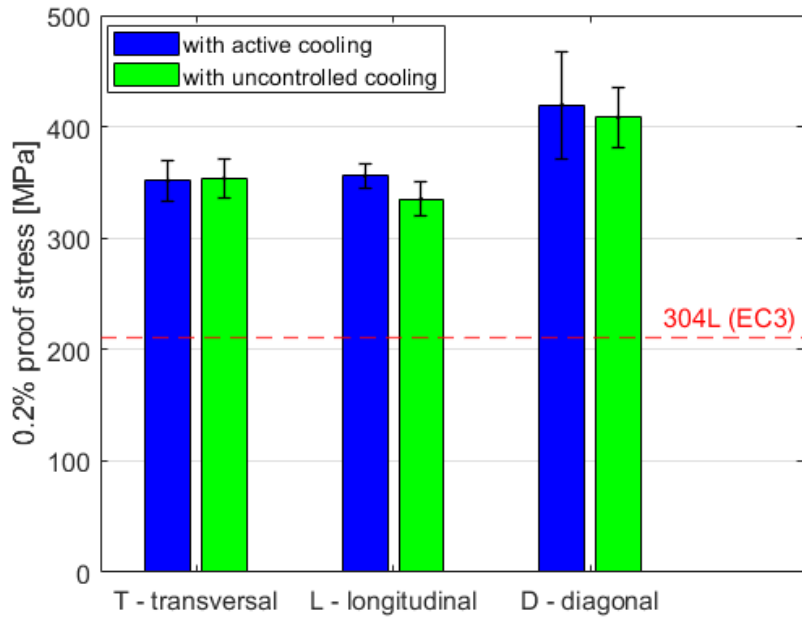
(b)
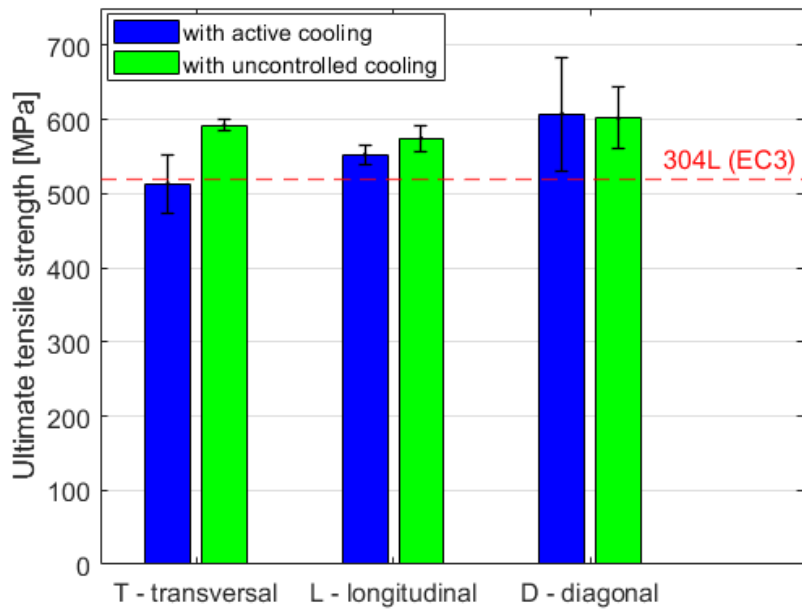
(c)
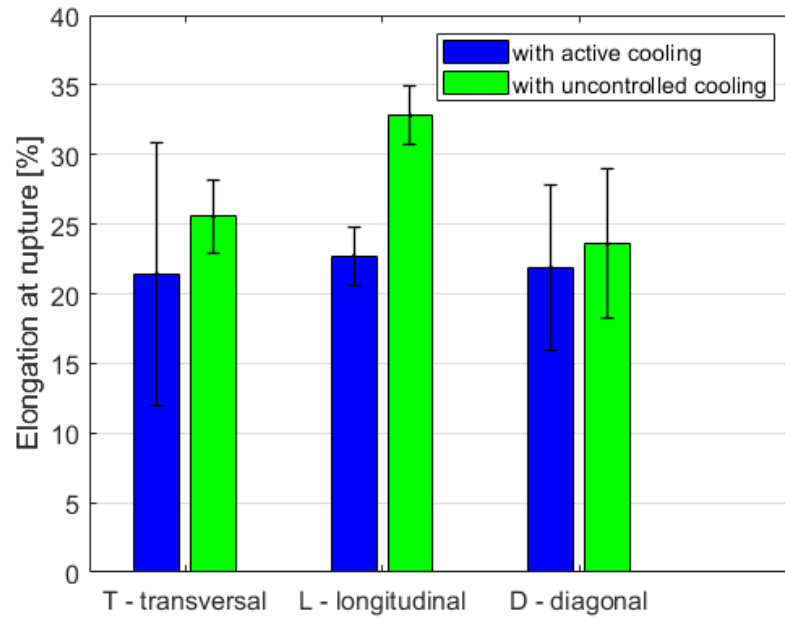
(d)

Figure 4.11: Results of the tensile tests on transversal, longitudinal and diagonal WAAM machined specimens: (a) Young's modulus; (b) 0.2% proof stress; (c) ultimate tensile strength; (d) elongation at rupture.

The ratios in Table 4.4 further evidence the anisotropic behavior of the WAAM stainless steel material. Indeed, the mechanical properties for specimens T are slightly lower than those for specimens L, which in comparison are significantly lower with respect to those for specimens D.

From the results of the analysis of texture coefficients (as reported in Section 4.2) it can be inferred that a relationship between the Young's modulus obtained with tensile tests at different orientations and the preferred crystallographic orientation among samples exists. In particular, the dominant orientation of the stiffest direction (D) differs consistently from both L and T ones, which showed instead a much lower Young's modulus. It is well known, indeed, that the fcc-cubic crystal structure of stainless steels is anisotropic and its elastic modulus varies in the range of 101-297 GPa on the basis of the crystal direction, being <111> the stiffest direction and <100> the least stiff one (Hutchinson, 2015), as also confirmed by experimental characterizations of lattice elastic constants for the AISI 304L stainless steels (Ledbetter, 1984, 1985). For the conventional polycrystalline material, with no preferred orientation, the average value of 190-200 GPa is commonly adopted. However, XRD results proved that WAAM plates studied in the

present work are characterized by a strong crystallographic texture that can justify the change in the elastic properties according to samples extraction direction. Further studies on this aspect are reported in the next Section 4.3.4.

Table 4.4: Relative ratios of the main mechanical properties with respect to the orientation of specimens.

	Relative ratio	E [-]	$R_{p0.2}$ [-]	UTS [-]	A% [-]	YS/UTS [-]
With active cooling (A)	**L / T**	1.19	1.01	1.09	1.19	0.93
	D / T	2.16	1.19	1.18	1.02	1.01
	D / L	1.81	1.18	1.09	0.86	1.09
With uncontrolled cooling (U)	**L / T**	1.27	0.91	0.97	1.32	0.94
	D / T	2.23	1.15	1.02	0.92	1.14
	D / L	1.75	1.27	1.05	0.70	1.22

Table 4.5 reports the relative ratio of the three orientations considered, with either active or uncontrolled cooling. Overall, the trends do not seem to be highly affected by the different cooling strategies. Indeed, the marked anisotropic behavior is equally registered by both types of specimens (A and U).

Table 4.5: Relative ratios of the main mechanical properties with respect to the cooling strategy.

Relative ratio	Relative ratio	E [-]	$R_{p0.2}$ [-]	UTS [-]	A% [-]	YS/UTS [-]
A/U	**T**	1.00	0.99	0.87	0.84	1.14
	L	0.94	1.11	0.97	0.76	1.15
	D	0.97	1.03	1.01	0.93	1.02

The observed anisotropy in the behavior of WAAM specimens might be related to the different grain orientations, with respect to the loading direction, as presented in Section 4.2.

It is well known that under uniaxial tensile loading, plastic deformation of metals preferentially occurs along slip planes oriented at 45° with respect to the loading direction, where shear stress reaches its maximum value (Dieter & Bacon, 1986). Hindering dislocation slip, which is responsible for plastic deformation, by strengthening mechanisms, allows increasing tensile strength. Several studies demonstrate that grain refinement is the one of the most effective strengthening mechanisms in SLM parts, enhancing both strength and elongation, due to the high solidification rate induced by the process (Hovig et al., 2018). In the hierarchical microstructure typical of additively manufactured parts, the first obstacle to dislocation slip is the cellular sub-structure (few micrometers in the present study). The observed anisotropy in the tensile properties of WAAM 304L stainless steel samples should be likely related to the different orientations of this fine cellular sub-structure among T, L and D specimens, schematically shown in Figure 4.2. The superior tensile properties in terms of yield and ultimate tensile strength observed in D samples can be related to the highest density of cells boundaries along the main slip direction oriented at 45° to the tensile loading. It is worth noting that specimens D also exhibited the highest elastic modulus, clearly related to crystallographic and mechanical fibering, that are widely reported as the main reasons for the elastic anisotropy of metals (Courtney, 2005; Dieter & Bacon, 1986).

4.3.4. Focus on the elastic parameters of WAAM-produced plates

The experimental tests carried out on machined specimens were further investigated to derive the elastic properties (i.e. Young's modulus and Poisson's ratio) for each tested plate (from which the specimens were extracted, see Section 4.3.1). A total of four plates are considered, and for each plate a dog-bone specimen has been cut along for each of the three main directions, i.e. T, L and D. The main findings of this study have also been presented in (Laghi et al., 2020c).

The elastic parameters of WAAM stainless steel were evaluated from the results of the monotonic tensile tests on the machined dog-bone shaped specimens, as described in Section 4.3.2. For each specimen, the values of Young's modulus E and Poisson's ratios ν were determined from the DIC measures on the average longitudinal ε_l (i.e. along the longitudinal direction of the dog-bone specimen) and transversal ε_t (i.e. along the transversal direction of the dog-bone specimen)

strains. The DIC system was in particular employed to provide highly accurate measurements of the surface strain field along the entire gauge length. The use of DIC is particularly important for WAAM material since the strain field under macroscopic uniaxial loading is not as uniform as for conventionally produced material, as also reported in (Kyvelou et al., 2020; Laghi et al., 2020b). The outputs of the DIC were processed using Vic3D software to obtain both the longitudinal (i.e. along the longitudinal direction of the dog-bone specimen) and transversal (i.e. along the transversal direction of the dog-bone specimen) surface strain fields (punctual values). From the two strain fields, longitudinal and transversal average deformations were evaluated by means of virtual extensometers (see Figures 4.12 and 4.13).

The values of the tangent Young's modulus were calculated from the stress-strain curves obtained from DIC measures on the longitudinal strains ε_l (Figure 4.12a) according to the method recently proposed by Kyvelou et al. (Kyvelou et al., 2020). Figure 4.12b provides a schematic representation of the tangent Young's modulus vs. longitudinal strain ε_l. In order to erase any possible experimental noise, the procedure consists in the identification of three regions (Figure 4.12b): (i) region I is characterized by the initial noise, (ii) region II is characterized by a pseudo-horizontal plateau, and (iii) region III is characterized by decreasing values of the tangent Young's modulus E with increasing values of ε_l. An ordinary least squares regression (OLSR) is then performed to identify the average E value considering only the values of region II. The procedure was applied on T, L and D specimens.
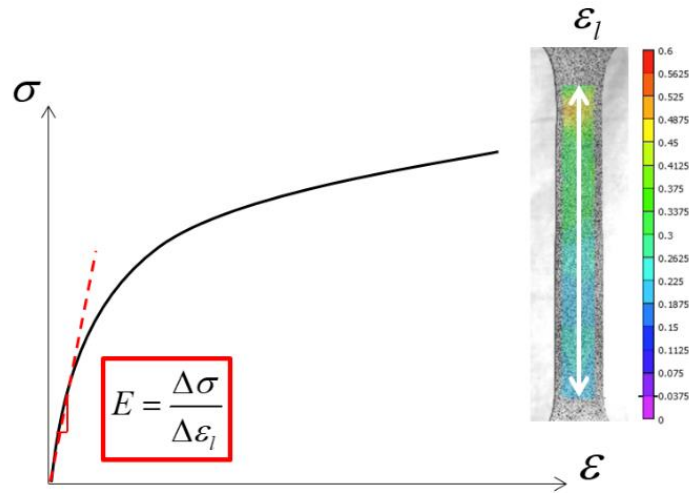
(a)
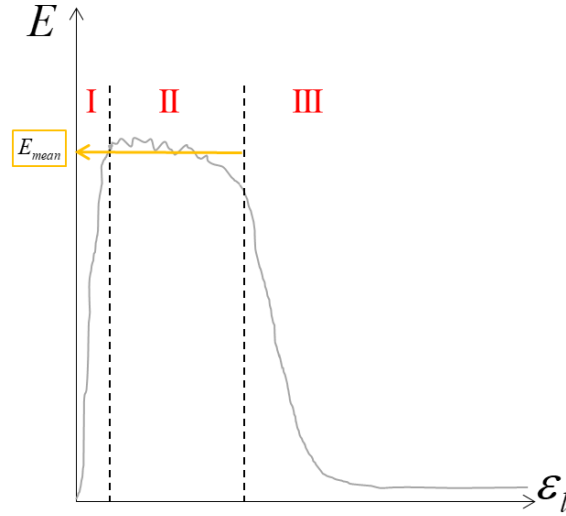
(b)

Figure 4.12: Conceptual schematization of the estimation of the tangent Young's modulus: (a) stress-strain curve, (b) E-strain curve.

The values of Poisson's ratio were estimated as ratios between average transversal and longitudinal strains $v = \dfrac{\varepsilon_t}{\varepsilon_l}$ at located cross-sections of L and T specimens (Figure 4.13a). In particular, in order to consider a possible uneven distribution of the transversal strains along the length of the specimen, the values of ε_t were taken as a mean over three measures taken at three different cross-sections, as presented in Figure 4.13a.

In particular, for specimens L (i.e. oriented parallel to the printing layers), the Poisson's ratio is computed as:

$$v_{TL} = \frac{\varepsilon_{t,T}}{\varepsilon_{l,L}} \tag{4.1}$$

where $\varepsilon_{t,T}$ refers to the transversal strain estimated along the direction T (i.e. perpendicular to the printing layers), while $\varepsilon_{l,L}$ refers to the longitudinal strain estimated along the direction L (i.e. parallel to the printing layers).

Likewise, for specimens T (i.e. oriented perpendicular to the printing layers), the Poisson's ratio is computed as:

$$v_{LT} = \frac{\varepsilon_{t,L}}{\varepsilon_{l,T}} \qquad (4.2)$$

where $\varepsilon_{t,L}$ refers to the transversal strain estimated along the direction L, while $\varepsilon_{l,T}$ refers to the longitudinal strain estimated along the direction T.

The method adopted to estimate the tangent Young's modulus was adopted also for the Poisson's ratio, through the definition of the region II of the v-ε_l curve (Figure 4.13b).
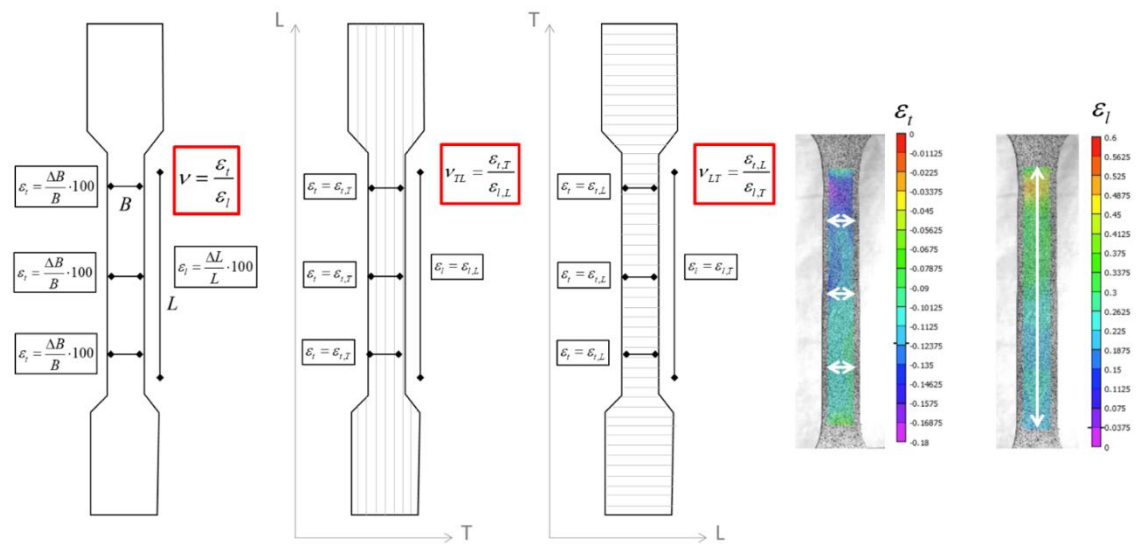
(a)
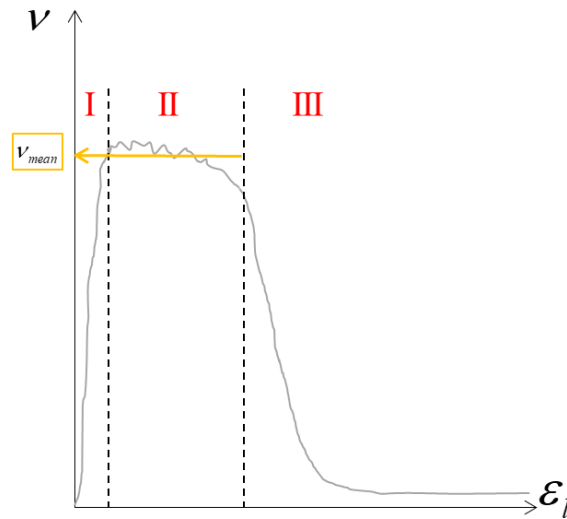
(b)

Figure 4.13: Conceptual schematization of the estimation of the Poisson's ratio: (a) stress-strain curve, (b) ν-strain curve.

Table 4.6 collects the values of the elastic parameters (e.g. Young's modulus and Poisson's ratios) for the specimens oriented along the three directions (T, L, D). On average, the different values of Young's modulus along the three direction confirms a marked anisotropy, as well described also in previous research (Kyvelou et al., 2020; Laghi et al., 2020a, 2020b; Laghi et al., 2020). Moreover, Poisson's ratio values seem to be also affected by the different orientations of the specimens with respect to the printing deposition. Indeed, for T specimens (having the longitudinal axis perpendicular to the deposition layers), ν values (ν_{LT}) are considerably lower than those (ν_{TL}) of L specimens.

Table 4.6: WAAM elastic parameters from tensile tests.

Plate	E [GPa]			ν [-]	
	T	L	D	LT	TL
1	116.45	135.54	242.06	0.352	0.384
2	109.64	147.31	252.09	0.354	0.494
3	112.27	137.94	228.54	0.356	0.457
4	111.99	137.27	255.31	0.374	0.434
mean	**112.59**	**139.52**	**244.50**	**0.359**	**0.442**
COV	**0.02**	**0.03**	**0.04**	**0.02**	**0.09**

Figure 4.14 provides the histograms of the elastic parameters of WAAM stainless steel along the different orientation as compared with those of a traditionally-manufactured stainless steel

_____

(E=200 GPa and ν=0.3 according to ASM Handbook (ASM Handbook, Volume 1)). As far as Young's modulus is concerned (Figure 4.14a), the trend for the three directions is the same for all four plates. In detail, the lowest values are registered for T specimens, while D specimens have almost 25% higher values than the one commonly adopted for 304L steel. Similar trend is registered for the Poisson's ratio (Figure 4.14b), for which both specimens T and L provided results 15% to 50% higher than the traditional reference (0.30).
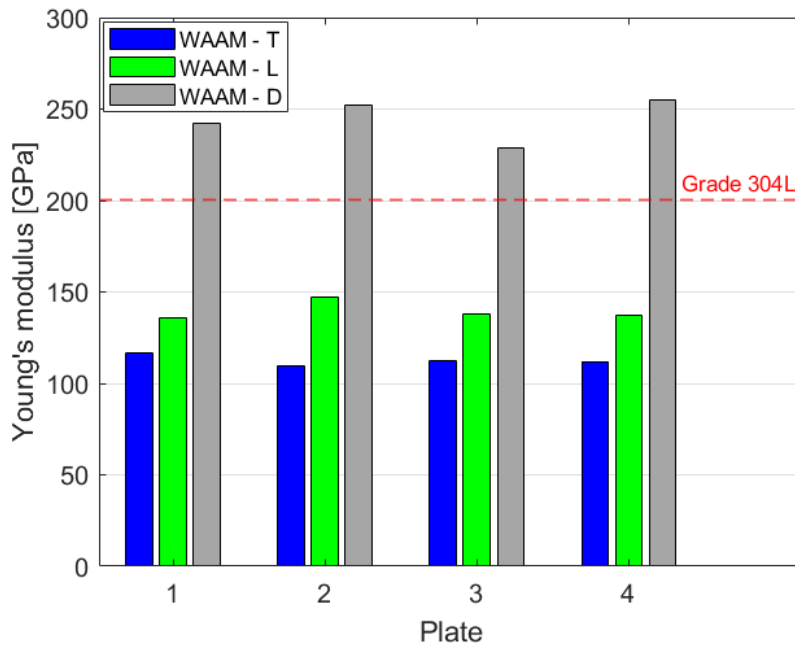
(a)
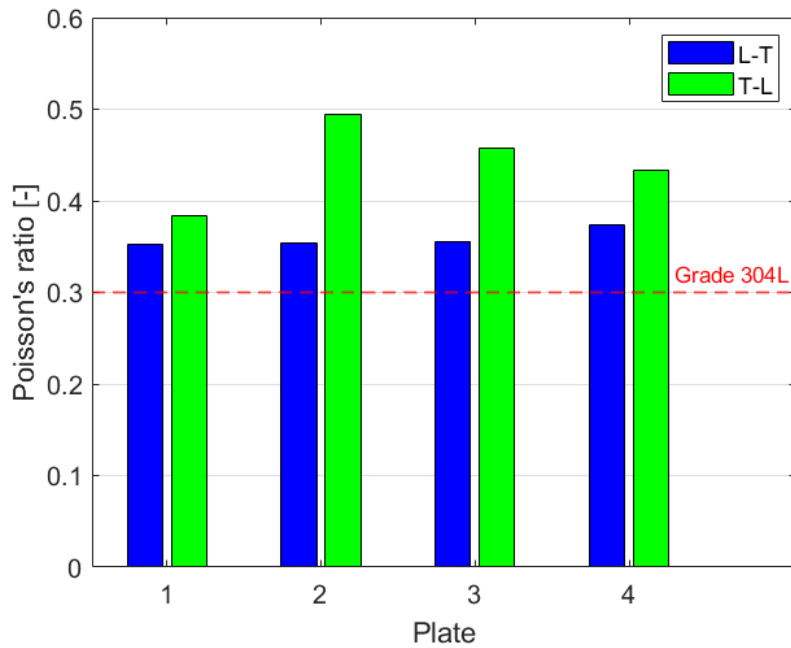
(b)

Figure 4.14: Histograms of (a) Young's modulus and (b) Poisson's ratio values for WAAM stainless steel.

It is of interest to compare the values of the products of the Young's moduli along one direction with the Poisson's ratio evaluated for the orthogonal one, namely $E_L \cdot \nu_{LT}$ and $E_T \cdot \nu_{TL}$. Those products are plotted in Figure 4.15. It can be noted that $E_L \cdot \nu_{LT} \simeq E_T \cdot \nu_{TL}$.

The symmetry condition $E_L \cdot \nu_{LT} = E_T \cdot \nu_{TL}$ is a clear indication of an orthotropic material behavior, see e.g. (Kaw, 2005).
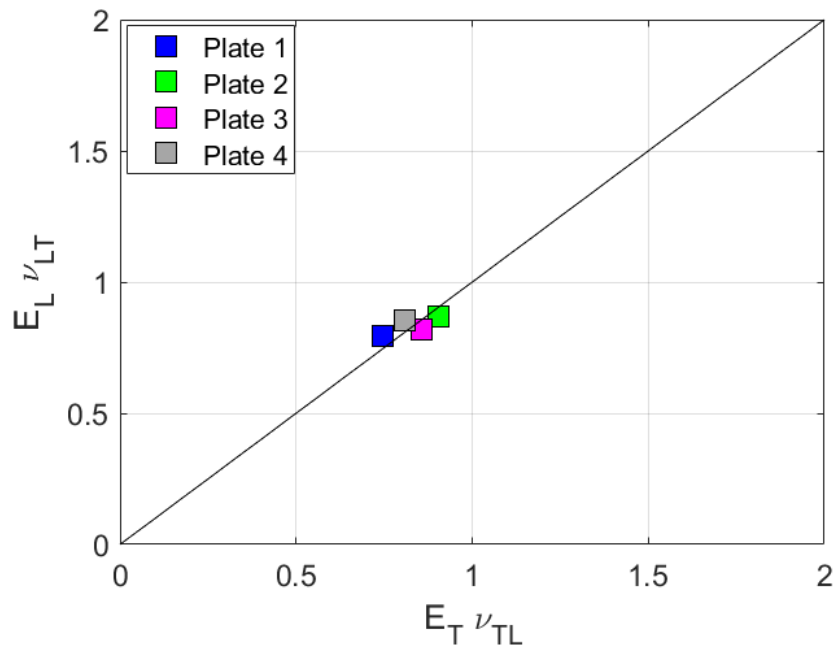
Figure 4.15: Comparison of Young's moduli and Poisson's ratios along T and L directions.

4.4. GEOMETRICAL CHARACTERIZATION ON PLANAR SPECIMENS

4.4.1. Measurements and equipment

In order to characterize the thickness and cross-sectional area of as-built dog-bone shaped specimens, different types of measures have been performed.

A detailed investigation on the surface roughness and distribution of thickness proper of the WAAM process has been performed on one specific specimen (not tested in tension) using 3D scanning technique. The specimen is taken along the longitudinal direction (L), and printed with active cooling (A). The surface has been left as-built (R) to properly characterize its roughness. From the whole 3D model, the point-clouds of the two surfaces (upper and lower ones) have been processed individually in terms of their roughness, treating their heights (z coordinates) as two individual random variables, whose main descriptors have been estimated according to ISO 25178-2 (ISO, 2012). Then, from the whole 3D model a series of cross-sections along both directions (x and y, i.e. along the deposition layers and perpendicular to them) has been extracted and the thickness has been analyzed according to random process theory. The main findings of this study have been presented in (Laghi et al., 2020b).

The instrument adopted for the 3D scan acquisition is a structured-light projection Artec Spider 3D scanner (*Artec 3D Webpage*), an optical non-contact system for measuring the 3D surface of objects using a projector of blue light pattern and a camera. The projected light pattern on the object surface evidences distortions due to the specimen's surface shape, while the camera captures these distortions and permits the reconstruction of the surface 3D model by means of topographic triangulation principles. The instrument acquires full-field scans of a volumetric area and is able to collect millions of points per scan. More in detail, the specific instrument used in the present work is characterized by an acquisition speed of 1 mln points/sec for metrology applications. The obtained 3D resolution is 100 points/mm^2, with a 3D point accuracy of 0.05 mm for a medium field size of 90x70 mm and a working distance of 0.25 m. The 3D model of the scanned planar specimen consists of around 40 millions triangular elements, with a medium points spacing of about 0.10 mm. Figure 4.16 shows a view of the entire mesh (blue model) and a zoom of it.

(a)   (b)
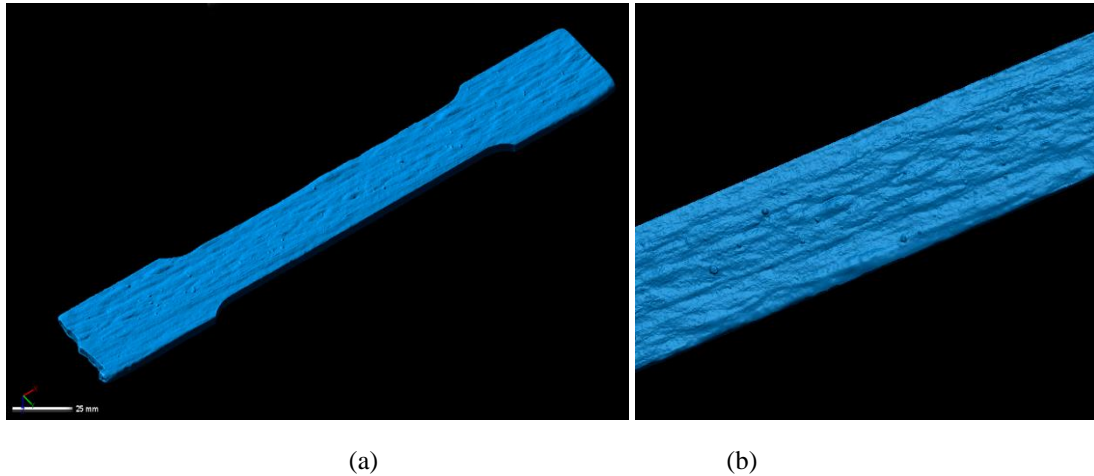
Figure 4.16: (a) 3D model of one specimen cut along longitudinal (L) direction and (b) a zoom of it.

From a global perspective, the effective cross-sectional area A_{eff} of as-built specimens has been characterized by means of volume measurements, based on the Archimedes' principle (Gardner et al., 2019; Laghi et al., 2020a), while the machined specimens have been characterized through multiple measurements with digital caliper (having a nominal precision of 0.01 mm) considering 20 cross-sections for each specimen.

4.4.2. Surface roughness of planar specimens

The 3D model obtained from 3D scanning has been first analyzed in terms of surface roughness, considering separately the two point-clouds of the upper and lower surfaces. For each surface the origin of the reference axis (z-axis) has been placed in order to obtain an ensemble of z_i points having zero-mean (i.e. the mean value of the z_i coordinates is zero for both surfaces). The set of z coordinates of each surface can thus be considered as an individual random variable, namely Z_{US} (for the upper surface) and Z_{LS} for the lower surface. In general, the two random variables could be correlated therefore they are not treated as independent random variables.

Data analysis has been carried out with an open-source GIS environment to gather information about the surface roughness in terms of peaks and pits (Figure 4.17). For this aim, the heights z of the points of each of the two surfaces (upper, z_{US}, and lower, z_{LS}) have been measured with respect to a horizontal plane x,y located at either the upper or the lower mean height. In this way, peaks and pits are identified as local maxima or minima of the function z directly by the software.

(a)   (b)
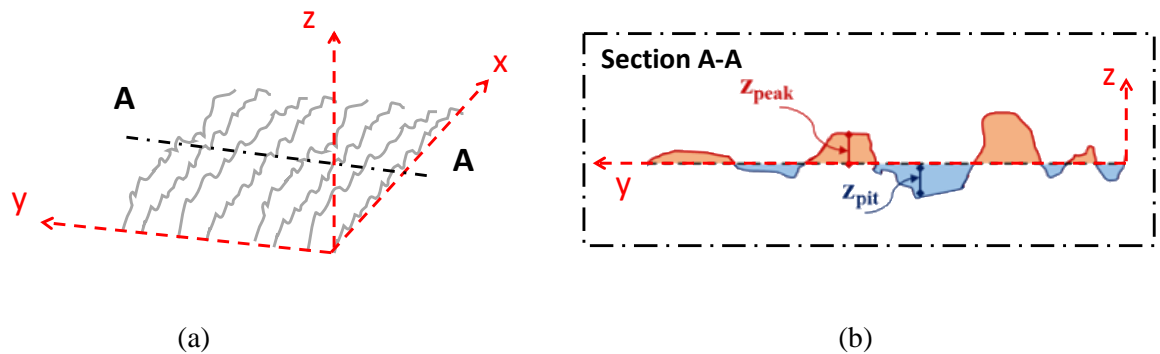
Figure 4.17: (a) Qualitative graphical representation of the surface roughness; (b) section A-A from surface profile and evaluation of peaks and pits from z coordinates.

Figure 4.18 shows the locations of peaks (small red dots) and pits (small blue dots) on both the upper and lower surface. The ten largest values of peaks and pits are indicated with big dots. The location of peaks and pits allows to appreciate the path following the deposition layers, as the crests of the printing layers correspond to the peak lines while among each two successive printing layers lie the pit lines. These lines clearly mark the orientation of the specimen scanned, which is taken longitudinally (L), i.e. having the longitudinal axis along the direction of the printing deposition layers.
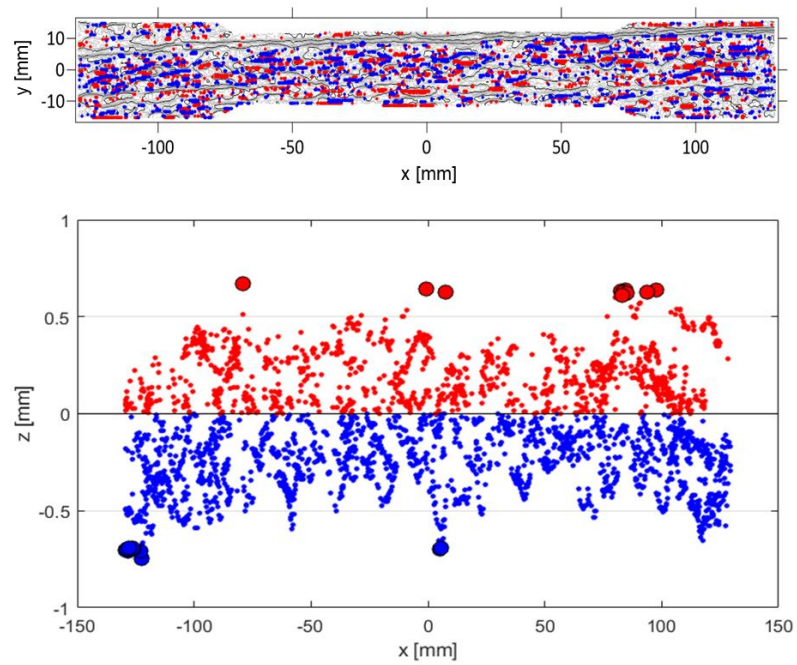
(a)
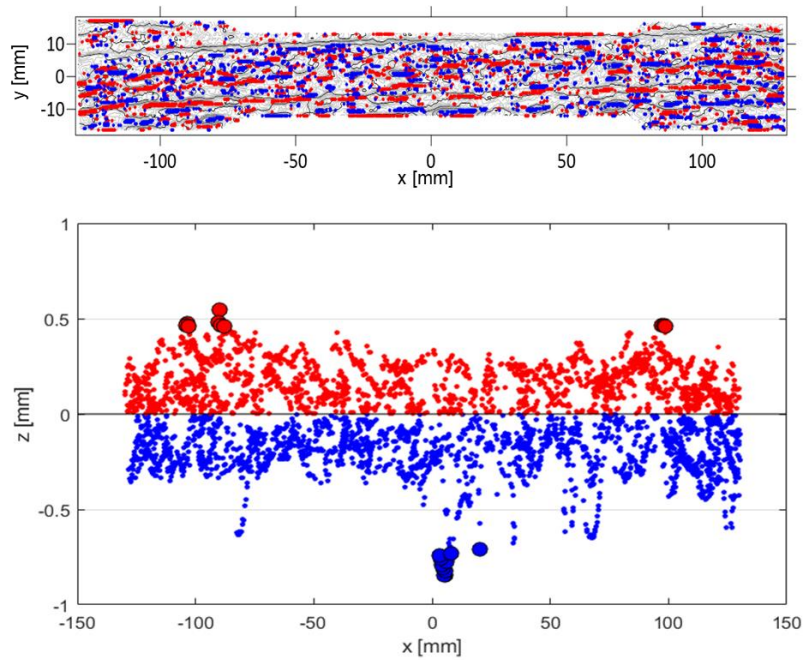
(b)

Figure 4.18: Distribution of peaks (red) and pits (blue) along the (a) upper and (b) lower surface of the 3D-scanned specimen.

The main features of the surface roughness can be quantitatively described in terms of the main descriptors identified by the standard ISO 25178-2 (ISO, 2012): maximum peak height (S_p), maximum pit height (S_v), arithmetical mean height (S_a), root mean square height (S_q), skewness (S_{sk}) and kurtosis (S_{ku}). The values of the main descriptors are collected in Table 4.7. The values labelled *US* refer to the upper surface, whereas those labelled *LS* refer to the lower surface.

Table 4.7: Surface roughness parameters evaluated according to ISO 25178-2.

Roughness parameters	Formulation (according to (ISO, 2012))	Value (mm)	
Maximum peak height (S_p)	$S_p = \max_A \left[z(x, y) \right]$	US	0.67
		LS	0.54
Maximum pit height (S_v)	$S_v = \min_A \lvert z(x, y) \rvert$	US	0.74
		LS	0.85
Arithmetical mean height (S_a)	$S_a = \dfrac{1}{A} \iint_A \lvert z(x, y) \rvert \, dx dy$	US	0.19
		LS	0.14
Root mean square height (S_q)	$S_q = \sqrt{\dfrac{1}{A} \iint_A z^2(x, y) dx dy}$	US	0.27
		LS	0.20
Skewness	$S_{sk} = \dfrac{1}{S_q{}^3} \left[\dfrac{1}{A} \iint_A z^3(x, y) dx dy \right]$	US	0.03
		LS	-0.14
Kurtosis	$S_{ku} = \dfrac{1}{S_q{}^4} \left[\dfrac{1}{A} \iint_A z^4(x, y) dx dy \right]$	US	2.73
		LS	3.38

Maximum peaks and pits heights are in the range of 0.54-0.85 mm with no significant differences between the two faces. The values of the arithmetic mean heights and root mean square heights are between 0.14 and 0.27 mm. The skewness values are close to zero thus indicating a quite symmetrical distributions of peaks and pits. Although due to the groove-like surface the relative distributions of peaks and pits would be expected to be asymmetric, the results show that the skewness is close to zero for both upper and lower surfaces. This suggests the need for further

investigations on the specific nature of the resulting roughness. The values of kurtosis are slightly larger or smaller than 3, suggesting a flatness similar to that of a Normal Gaussian distribution.

4.4.3.   Thickness from 3D scanning acquisition

From the full 3D model generated by 3D scanning acquisition (consisting of 40 millions of points), an in-depth characterization of the thickness has been carried out as well. The average (effective) thickness of the specimen as taken from volume measurements (according to the Archimedes' principles, as also used in (Kyvelou et al., 2020; Laghi et al., 2020a)) is 3.42 mm.

Given the marked orientation of WAAM planar elements due to the successive layers of deposited material, first a statistical analysis of the thickness distribution along the two directions x and y has been carried out. For this purpose, selected values of thickness $t(x_i, y_i)$ have been extracted from the 3D models discretizing a portion of specimen of 69 mm length as a grid (see Figure 4.19) with 3 mm spacing along the longitudinal direction (x) and 1.4 mm along the transversal direction (y) leading to N_x=23 measurements along x for a fixed value of y and N_y=14 measurements along y for a fixed value of x. The total number of measurements is therefore N_{tot}=322. Clearly, the thickness measurements indirectly provide also information on the correlation between the surface roughness of the upper and lower surfaces, even though based on a smaller dataset.

(a)

(b)
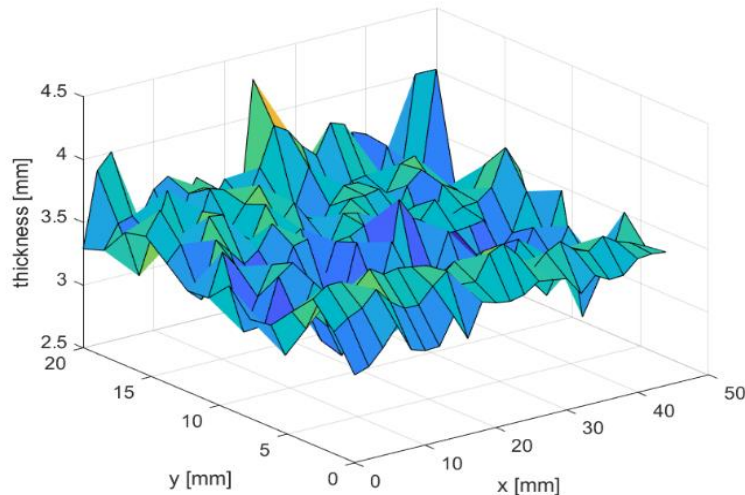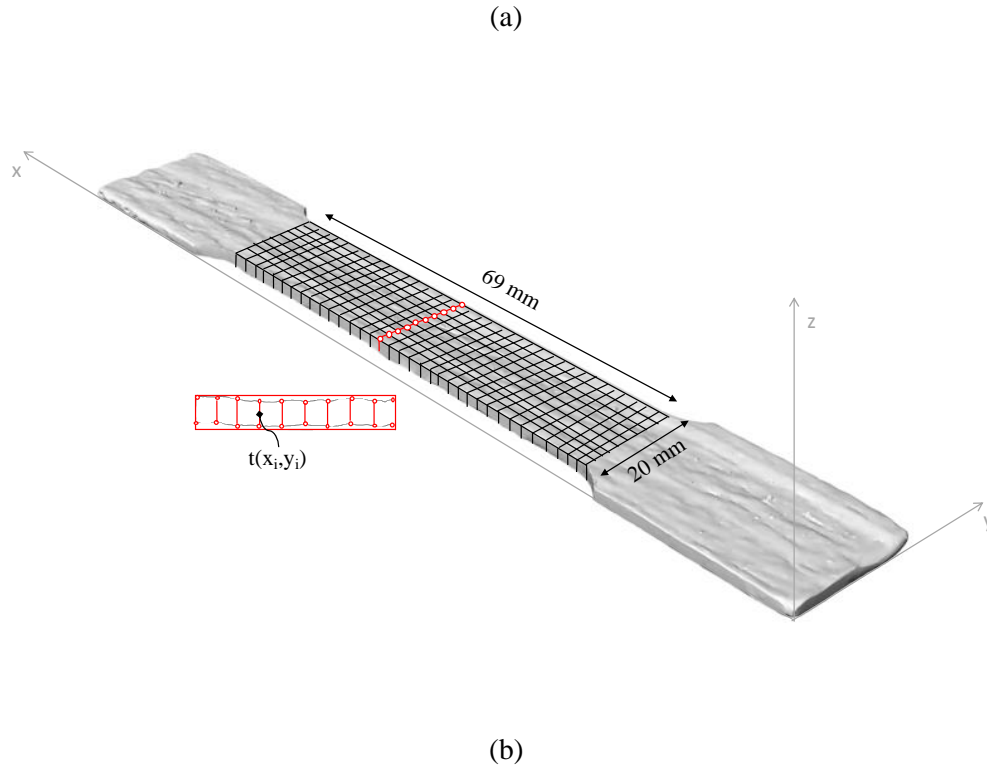
Figure 4.19: (a) 2D plot thickness distribution; (b) extraction of the thickness values $t(x_i,y_i)$ from 3D model.

For a fixed value of y_i, the set of measurements along the length (i.e. along the longitudinal direction x) $t(x/y_i)$ can be interpreted as the single realization of a random process $t(x)$. The set of all realizations $t(x/y_i)$ is typically called ensemble (Figure 4.20).
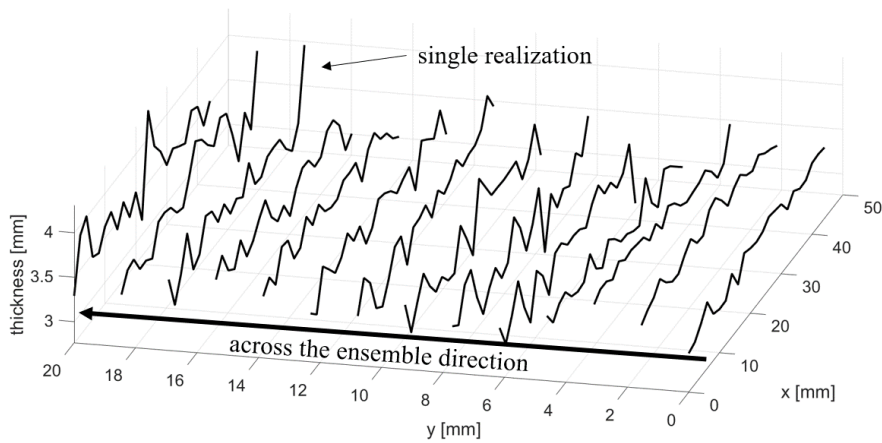
Figure 4.20: Plot of thickness measurements for fixed y values $t(x \rfloor y_i)$.

The main properties of the random process can be analyzed computing the statistics both across the ensemble (for a specific value x_i) and along the length (i.e. considering a single realization for a specific y_i) as reported in Table 4.8.

Table 4.8: Statistical properties of thickness modelled as a random process.

Statistical parameters	Definition	Range	Mean +/- st.d
Across-the-ensemble mean	$\mu_{t(x)} = \dfrac{1}{N_y} \sum\limits_{i=1}^{N_y} t\left(x_j \mid y_i\right)$	[3.35 - 3.58]	3.48 ± 0.05
Across-the-ensemble standard deviation	$\sigma_{t(x)} = \sqrt{\dfrac{\sum\limits_{i=1}^{N_y}\left(t\left(x_j \mid y_i\right) - \mu_{t(x)}\right)^2}{N_y - 1}}$	[0.11 - 0.38]	0.20 ± 0.06
Along-the-length mean	$\mu_{t(y)} = \dfrac{1}{N_x} \sum\limits_{j=1}^{N_x} t\left(x_j \mid y_i\right)$	[3.26 – 3.63]	3.48 ± 0.12
Along-the-length standard deviation	$\sigma_{t(y)} = \sqrt{\dfrac{\sum\limits_{j=1}^{N_x}\left(t\left(x_j \mid y_i\right) - \mu_{t(y)}\right)^2}{N_x - 1}}$	[0.09 – 0.25]	0.18 ± 0.05
Overall mean	$\mu_t = \dfrac{1}{N_y} \mu_{t(y)} = \dfrac{1}{N_x} \mu_{t(x)}$	3.48	
Overall standard deviation	$\sigma_t = \sqrt{\dfrac{\sum\limits_{i=1}^{N_{tot}}\left(t(x_i, y_i) - \mu_t\right)^2}{N_{tot} - 1}}$	0.21	

Across-the-ensemble means and standard deviations are functions of x ($\mu_{t(x)}$, $\sigma_{t(x)}$), while along-the-length mean and standard deviations are functions of y ($\mu_{t(y)}$, $\sigma_{t(y)}$). Their trends, together with the related coefficient of variations, are represented in Figure 4.21.
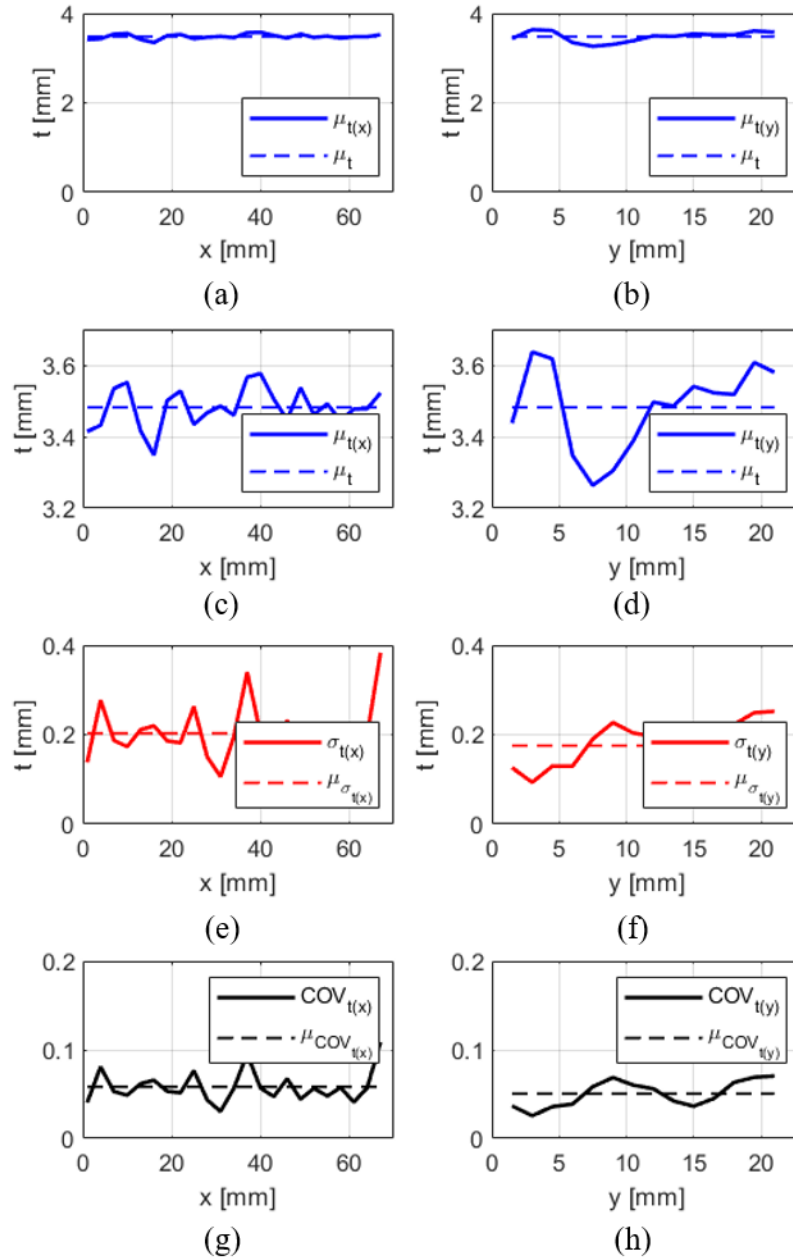
Figure 4.21: Main descriptors of the thickness: mean values across-the-ensemble (a) and along-the-length (b), and a zoom of them (c and d, respectively); standard deviation values across-the-ensemble (e) and along-the-length (f), coefficient of variation values across-the-ensemble (g) and along-the-length (h).

The across-the-ensemble mean values $\mu_{t(x)}$ oscillate around 3.35 mm and 3.58 mm with small variability. This condition ($\mu_{t(x)} \cong \mu_t$) indicates that the process can be considered stationary in average sense, since the thickness does not vary significantly moving along the longitudinal direction (e.g. the printing direction). Indeed, the succession of peaks and pits across the ensemble is quite regular moving along direction x. The across-the-ensemble standard deviation values $\sigma_{t(x)}$ exhibit a relatively large variability (values between 0.10 mm to almost 0.40 mm) with an average value equal to 0.20 mm. This large variability is partially due to the variation of the mean value among different realizations (i.e. succession of peaks and pits).

The along-the-length mean values $\mu_{t(y)}$ have a larger variability (from 3.26 to 3.64 mm.) than the across-the-ensemble mean $\mu_{t(x)}$, thus indicating that the process cannot be considered ergodic in a average sense. Indeed, each realization (i.e. corresponding to specific values of y_i) may be taken either in the proximity of the deposition layers (i.e. peak values) or between two consecutive layers (i.e. pit values). The along-the-length standard deviation values $\sigma_{t(y)}$ do not vary significantly for different realizations and have an average value of 0.18 mm. Such value can be considered a measure of the intrinsic variability of the thickness, within a specific layer, thus related to the precision of the deposition process. Coefficients of variation are, on average, around 0.05-0.06, with maximum values around 0.1.

A correlation analysis has been also carried out computing the correlation coefficient between all realizations $\rho(t(x|y_i))$ and between all sections taken across the ensemble $\rho(t(x_j|y))$.

For illustrative purposes, Figure 4.22 shows selected statistical distributions of thickness across the ensemble and along the length for a pair of consecutive or either far-located y or x points, together with their scatter graphs. In general, the distributions along x are quite random and tend to follow Gaussian-type distributions. The distributions along y tend to be more uniform with few peaks, possibly related to the consecutive distribution of peaks and pits.
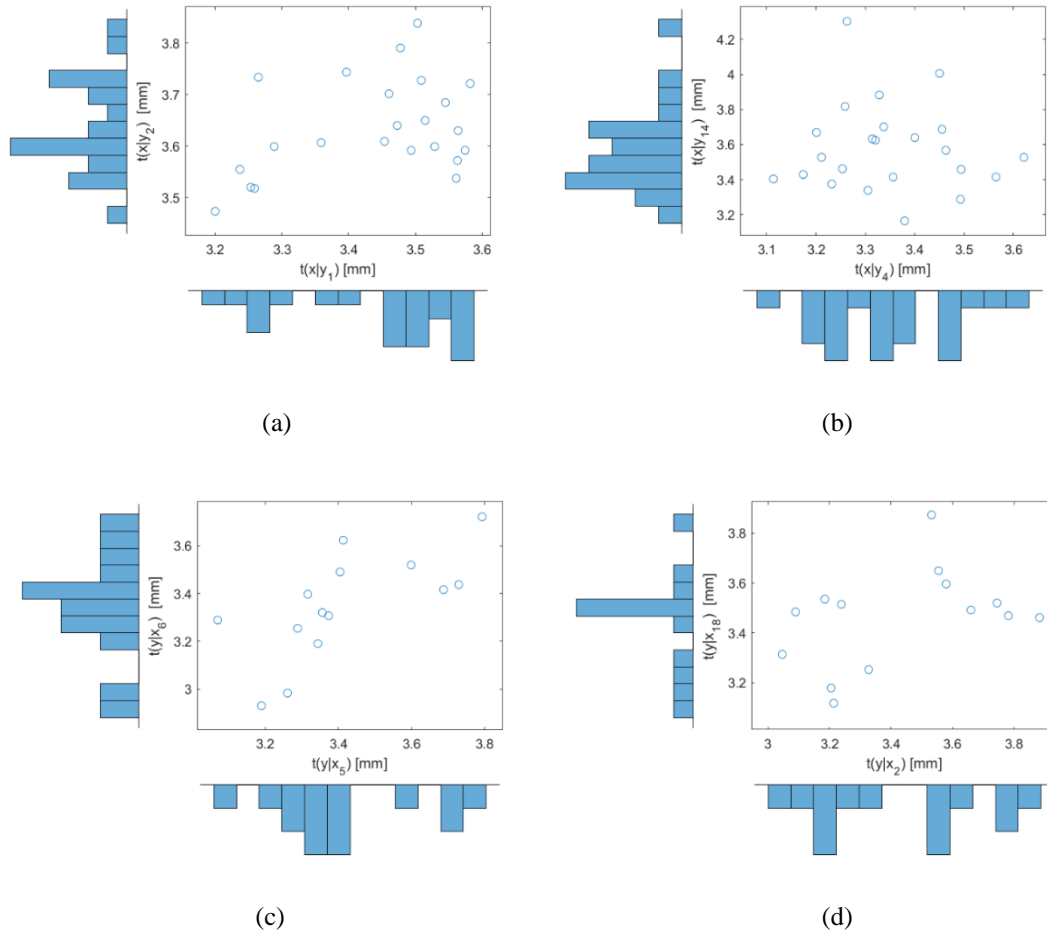
Figure 4.22: Distribution of thickness – (a) and (b) along x direction; (c) and (d) along y direction.

The overall statistical distribution considering all measured thickness values $t(x_i, y_i)$ is reported in Figure 4.23, in terms of both empirical cumulative distribution and relative frequency histograms. The estimations of the mean and standard deviation from the data are of 3.48 mm and 0.21 mm, respectively, resulting in a coefficient of variation equal to 0.06. The skewness coefficient is equal to 0.07. In the same graph also the best fit Normal and Lognormal statistical distributions have been plotted. Their main parameters (mean value, standard deviation and skewness coefficient) are provided in Table 4.9. It can be noted that the best-fit Lognormal is practically coincident with a Normal distribution, thus indicating that the statistical distribution is almost symmetric (the corresponding skewness value for the best-fit Lognormal is equal to 0.18) with respect to the mean value. Table 4.9 also provides the KS values of the Kolmogorov-Smirnov test associated to the two bet-fit distributions. The critical value for a significance level α=0.05 is equal to 0.07. Since both KS values are smaller than the critical one, both distributions

_____

can be considered a good fit of the experimental distribution. Since the data are all positive and have a small asymmetry, the Lognormal distribution could be preferred.
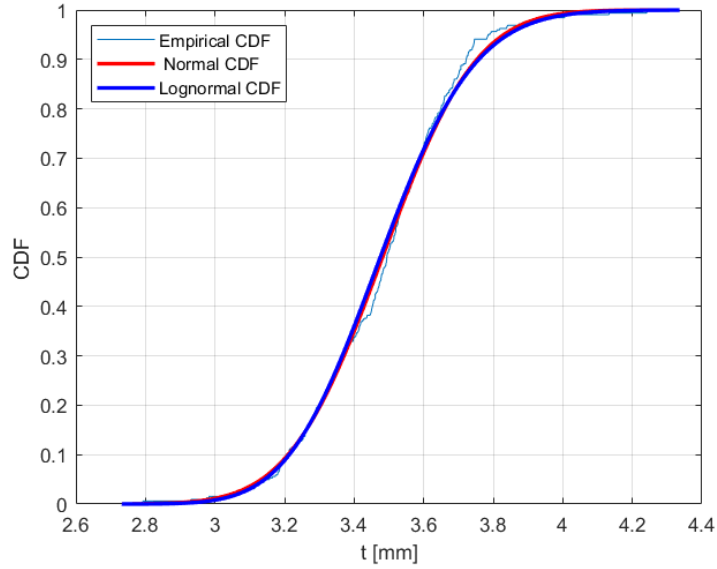
(a)
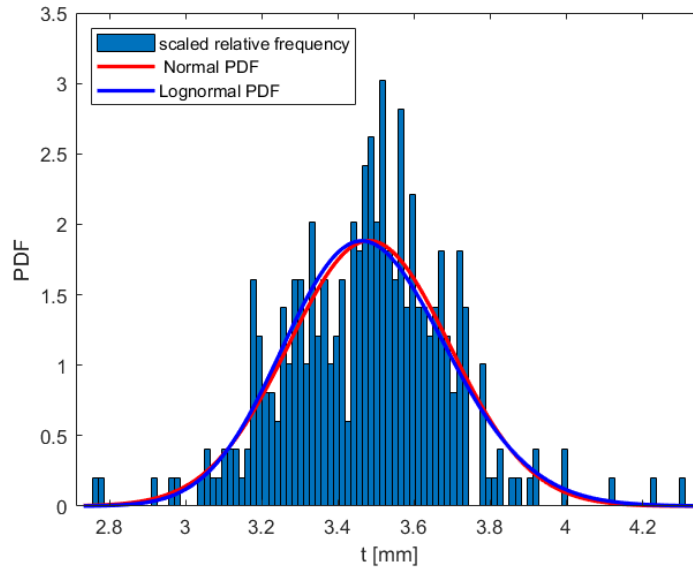
(b)

Figure 4.23: Distribution of thickness for the 3D-scanned specimen: (a) CDF; (b) PDF.

Table 4.9: Statistical parameters of the best-fit distribution of thickness along the 3D-scanned

_____

specimen.

Specimen Type	Surface Type	Measurement type	Distribution type	μ_t [mm]	σ_t [mm]
L	R (as-built)	3D scanning	Normal	3.48	0.21
			Lognormal	3.48	0.21

4.4.4. Thickness from manual measurements of planar specimens

As explained in Section 2.4.1, the effective thickness and cross-sectional area of the as-built specimens (labelled as R) were obtained from volume measurements. Table 4.10 presents an overview of the mean thickness values for longitudinal (L) and transversal (T) directions of the as-built specimens (that are going to be presented in Section 4.5).

Table 4.10: Average values of thickness for the 2D as-built specimens tested.

Specimen type	Surface type	Measurement type	t_m [mm]
Longitudinal	As-built	Volume	3.58
Transversal			3.76

The average effective thickness ($\mu_{t_{eff}}$) of the as-built specimens is equal to 3.58 mm for specimens oriented along the longitudinal direction (L) and 3.76 mm for specimens oriented along the transversal direction (T), thus resulting slightly lower that the nominal thickness $t_n=4$ mm. This result provides a first indication on the systematic difference between the effective as-built thickness and the nominal one, used as input from the printing process. Indeed, from volume-based measurements the difference $\Delta_{t,eff}$ is of 0.42 mm for L specimens and 0.24 mm for T specimens. The corresponding relative error between effective and nominal thickness (evaluated as (*effective- nominal) / nominal*) is of the order of -10% for L specimens and -6% for T specimens. The values of the standard deviations ($\sigma_{t_{eff}}$) are practically equal along the two

directions (0.13 mm for specimens along L and 0.14 mm for specimens along T) and correspond to a coefficient of variation of around 0.04.

The discrepancy between the nominal thickness set as digital input in the printing process (4 mm) and the average effective one of the printed outcomes (3.58 mm for L specimens, 3.76 mm for T specimens) is highly affected by the set of process parameters adopted. Different sets of parameters would result in general in a different surface finishing.

4.4.5. Discussion of results from planar specimens

The detailed characterization of the geometrical irregularities of the cross-section from the surface roughness and thickness of the single specimen from the 3D scanning (Sections 4.4.2 and 4.4.3) and the thickness measurements on different samples (Section 4.4.4) allows to make some interesting considerations on the main features of the printing process in terms of its accuracy and discrepancy between nominal geometry and as-printed one.

The detailed representation of the upper and lower surfaces through the point-clouds may allow a first estimation of the variability of the thickness from the variability of the two surfaces, represented as random variables (Z_{US} and Z_{LS}). In this way, the standard deviation of the thickness can be estimated from the standard deviation of the two surfaces, whose values have been evaluated in terms of root mean square height ($S_{q,US}$ for the upper surface and $S_{q,LS}$ for the lower surface) using the SRSS combination rule, i.e. $\sigma_t = \sqrt{S_{q,US}^2 + S_{q,LS}^2}$ (thus assuming that Z_{US} and Z_{LS} are statistically independent random variables), or a more complex combination accounting for the correlation coefficient ρ_{US} between Z_{US} and Z_{LS}, i.e. $\sigma_t = \sqrt{S_{q,US}^2 + S_{q,LS}^2 + 2 \cdot \rho_{UL} \cdot S_{q,US} \cdot S_{q,LS}}$. Those estimates can be then compared with the values of $\sigma_{t(x)}$, $\sigma_{t(y)}$ and σ_t obtained from the subset of measures as discribed in Section 4.4.3.

The values of the standard deviations of the thickness distribution along x and y ($\sigma_{t(x)}$, $\sigma_{t(y)}$) as well as the overall standard deviation σ_t are reported in the histogram of Fig. 4.24. The values of the root mean square height ($S_{q,US}$ and $S_{q,LS}$) are reported in the histogram of Fig. 4.24b together

with the SRSS estimate of the thickness standard deviation σ_t. As far as the thickness is concerned, the values of standard deviations along the two perpendicular directions $\sigma_{t(x)}$ and $\sigma_{t(y)}$ are of around 0.20 mm leading to a coefficient of variation of around 0.05. Also the value of the overall standard deviation σ_t is of around 0.20 mm thus leading to coefficient of variation of around 0.05.
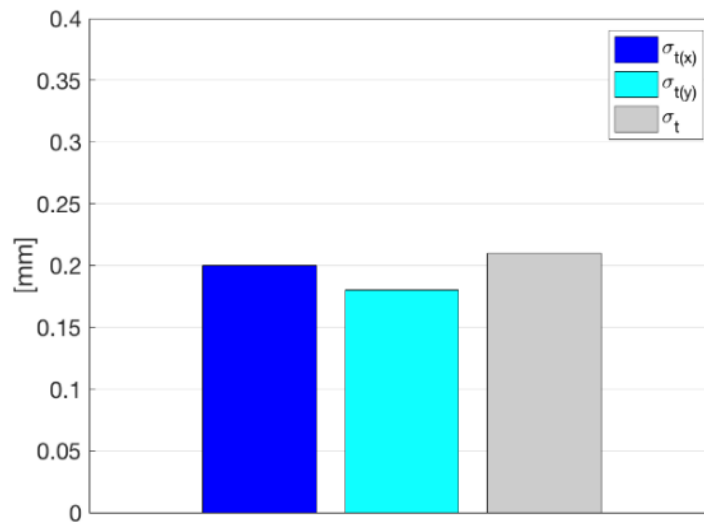
(a)

_____
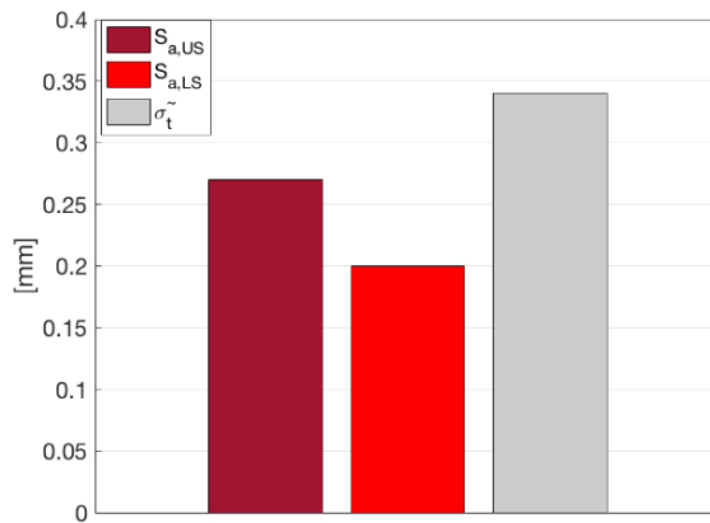
(b)

Figure 4.24: (a) comparison of standard deviations from thickness values; (b) comparison of root mean square values and estimation of standard deviation from roughness values;

The standard deviation values of the surface roughness (estimated in terms of root mean square height) are around 0.20 mm, while the values of σ_t (SRSS estimate of the thickness standard deviation) is of around 0.35 mm. This value appears quite higher than the value of σ_t (obtained from direct measures of thickness on a sub set of values), thus indicating, as expected, a non-negligible correlation between Z_{US} and Z_{LS}. A first estimation of the correlation coefficient ρ_{UL} may be obtained by imposing $\sigma_t = \sigma_t$, leading to a positive correlation of around 0.6. This finding further confirms that the main source of variation in thickness is the result of the roughness caused by the deposition of successive layers of material, that creates peaks (i.e. maximum thickness) and pits (i.e. minimum thickness).

The main source of information obtained from the measures of the effective thickness taken on all as-built specimens (as presented in Section 4.4.4) is summarized in the histograms of Figure 4.25, reporting the values of the standard deviation $\sigma_{t,eff}$ and the systematic difference $\Delta_{t,eff}$ along L and T (taken as difference between the mean effective thickness $\mu_{t,eff}$ and the nominal thickness t_n).

_____

(a)

(b)
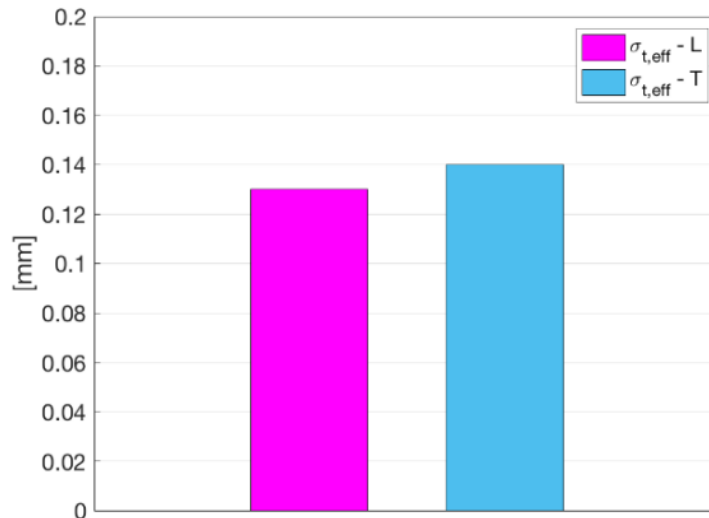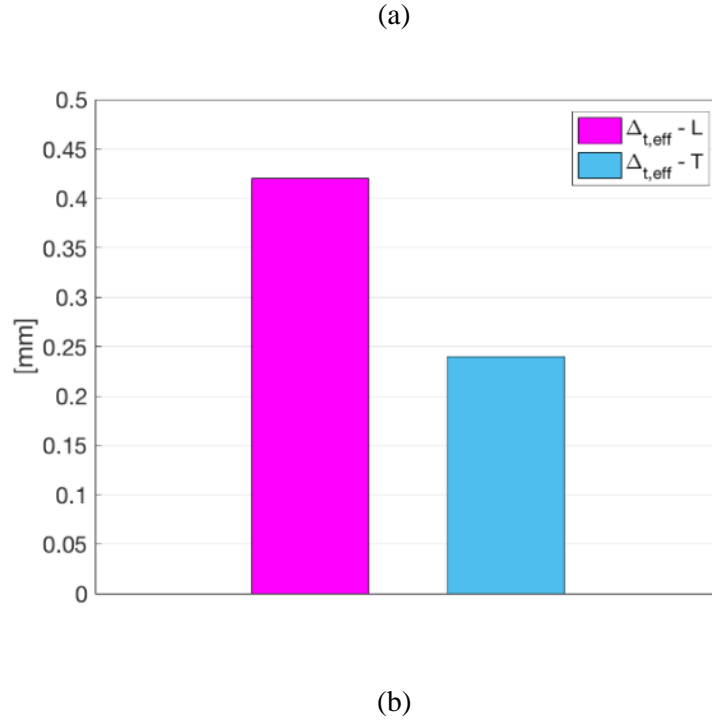
Figure 4.25: (a) comparison of standard deviation and (b) systematic difference of effective thickness.

The values of $\sigma_{t,eff}$ along L and T are almost the same (0.13 mm and 0.14 mm, respectively), corresponding to a coefficient of variation of around 0.03-0.04. On the other hand, the values of $\Delta_{t,eff}$ are larger for specimens L (around 0.40 mm) than for specimens T (slightly higher than 0.20 mm). The corresponding relative errors are between 5% (for specimens T) and 10% (for specimens L), with an average of 7.5%. In other terms, the mean value of the ratio between the effective and nominal thickness is equal to 0.90. These results related to the discrepancy between effective and nominal thickness could be properly considered at manufacturing stage. For design purposes, the effective values of thickness and corresponding effective cross-sectional area are suggested to be used.

4.5. MECHANICAL CHARACTERIZATION FROM TENSILE TESTS ON AS-BUILT PLANAR SPECIMENS

4.5.1. Measurements and set-up

The mechanical characterization on continuously printed WAAM plates have been carried out by performing uniaxial monotonic tensile tests on "dog-bone" shaped specimens according to ISO 6892-1 (see Figure 4.5).

The stress-strain curves for the as-built (R) specimens have been evaluated considering an effective homogeneous cross-sectional area taken from volume equivalency, as presented in Section 1.4 and previously adopted by (Kyvelou et al., 2020; Laghi et al., 2020a).

A total number of 32 specimens have been tested: 16 specimens oriented longitudinally (L) and 16 transversally (T), as for the scheme provided in Figure 4.26. In order to account for the possible influence of the cooling process in the mechanical behavior, half of the specimens were taken from plates printed with active cooling (A) and half from those printed with uncontrolled cooling (A). The plates were printed with the same set of process parameters as presented in Section 2.3. Table 4.11 provides an overview of the types of as-built specimens tested under tensile action.
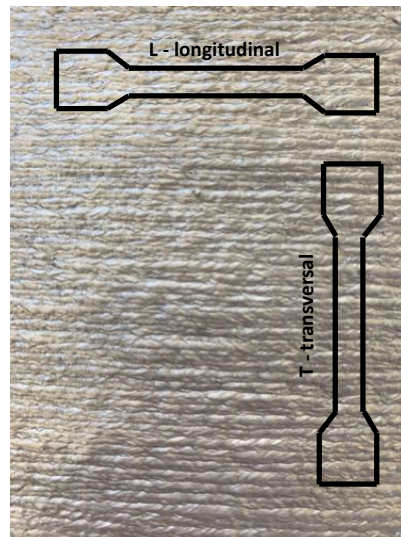
Figure 4.26: L and T as-built specimens cut from continuously-printed WAAM stainless steel plates.

Table 4.11: As-built specimens details for tensile tests.

Surface type	Orientation	Printing process	Quantity	Specimen ID
As-built "rough" (R)	Transversal (T)	Active cooling (A)	8	R-T-A-1 to R-T-A-8
		Uncontrolled cooling (U)	8	R-T-U-1 to R-T-U-8
	Longitudinal (L)	Active cooling (A)	8	R-L-A-1 to R-L-A-8
		Uncontrolled cooling (U)	8	R-L-U-1 to R-L-U-8

The tensile tests have been performed according to ISO 6892-1 on a Universal testing machine of 500 kN load capacity. The tensile test set-up is the same one adopted for the tensile tests presented in Section 3.3. The specimens have been tested in displacement-control with a loading rate of 2 MPa/s. The strain values have been obtained from optical system adopting Digital Image Correlation (DIC) technique to monitor the full strain field during the entire test. Additional Linear Variable Displacement Transducer (LVDT) with 50 mm gauge length has been adopted for comparison of strain measures up to yielding.

Elastic Modulus (E), 0.2% proof stress ($Rp_{0.2}$), ultimate tensile strength (UTS) and elongation at rupture ($A_{\%}$) were evaluated from the engineering stress-strain curves.

4.5.2. Tensile tests on as-built specimens

Figures 4.27 and 4.28 present the whole engineering stress-strain curve of WAAM-produced as-built (R) specimens tested under monotonic tensile action and a zoom of them. Overall, for all three orientations considered the variations in tensile response is quite high within each single orientation.

Overall, when comparing the two different orientations, it can be noticed that the curves of specimens oriented transversally (T) are smoother with a less sudden transition between the elastic and plastic phase. This is particularly evident from the zoom showed in Figures 4.27. Moreover, specimens oriented along transversal direction evidence, on average, smaller values of ultimate strength and elongation at rupture. The major difference, when comparing specimens realized with active cooling (A) and with uncontrolled cooling (U), is, also noticed in the values of elongation at rupture. Indeed, specimens with active cooling have elongation at rupture of around 20%, while those realized with uncontrolled cooling reach values up to 30-40%.
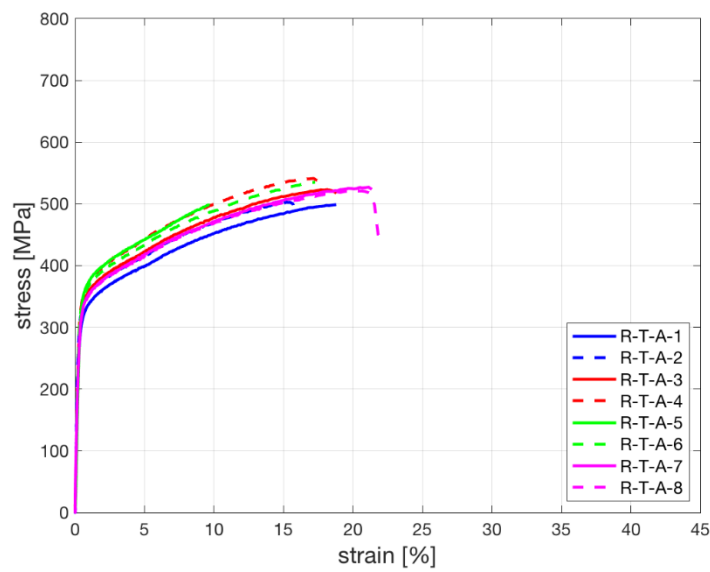
(a)
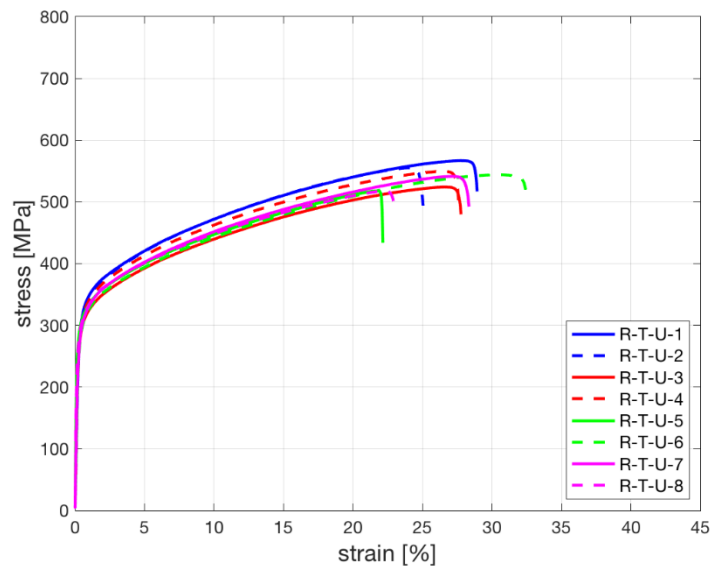
(b)
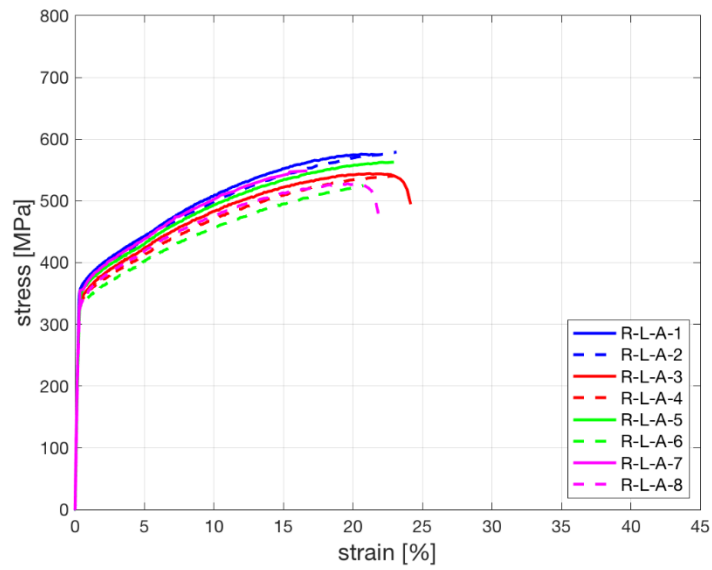
(c)
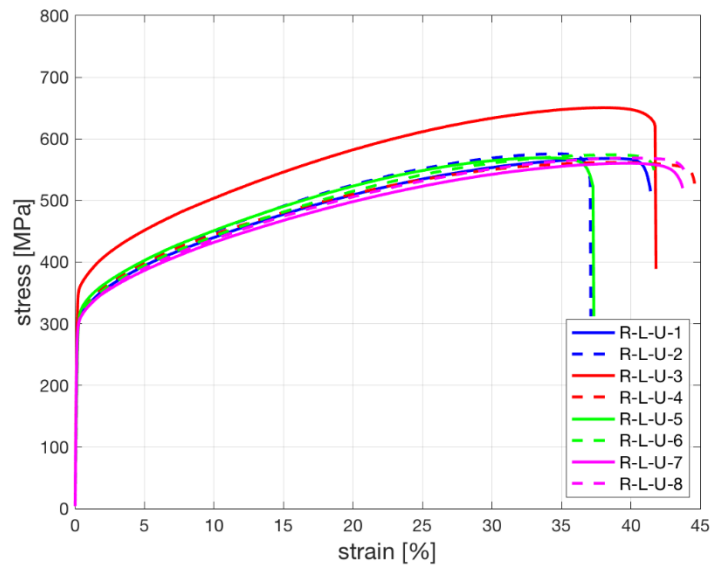
(d)

Figure 4.27: Stress-strain curves for tensile tests on WAAM planar specimens: (a) T specimens with active cooling and (b) with uncontrolled cooling; (c) L specimens with active cooling and (d)

with uncontrolled cooling.
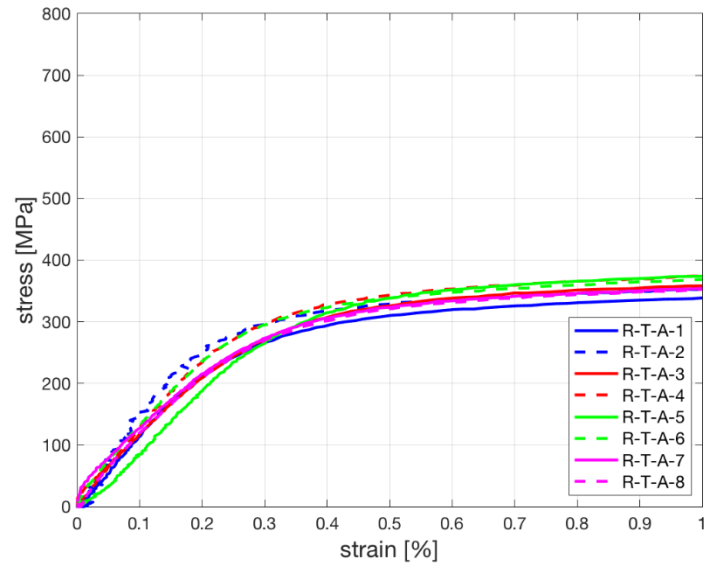
(a)
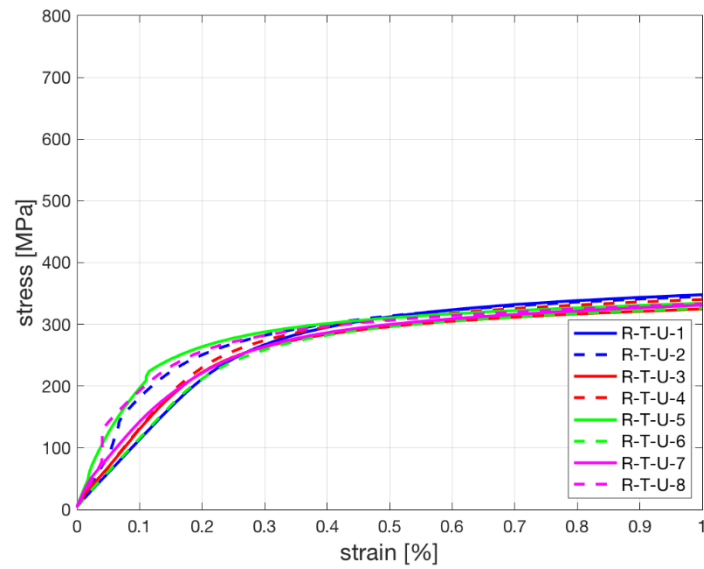
(b)
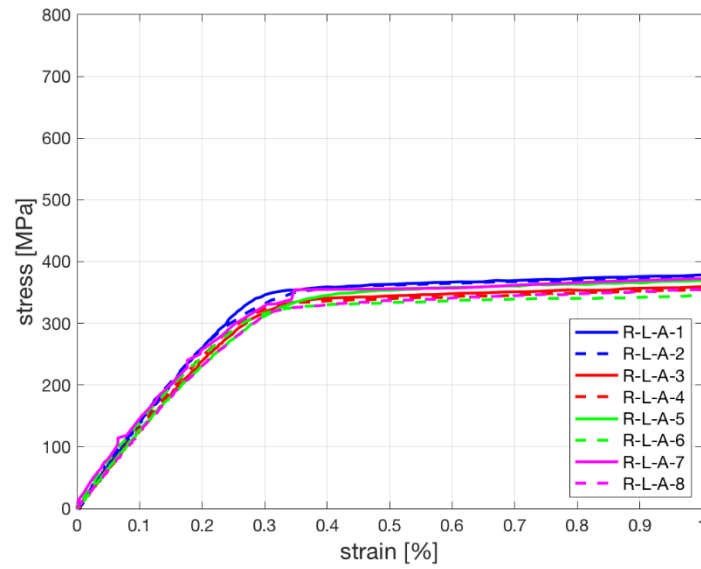
(c)
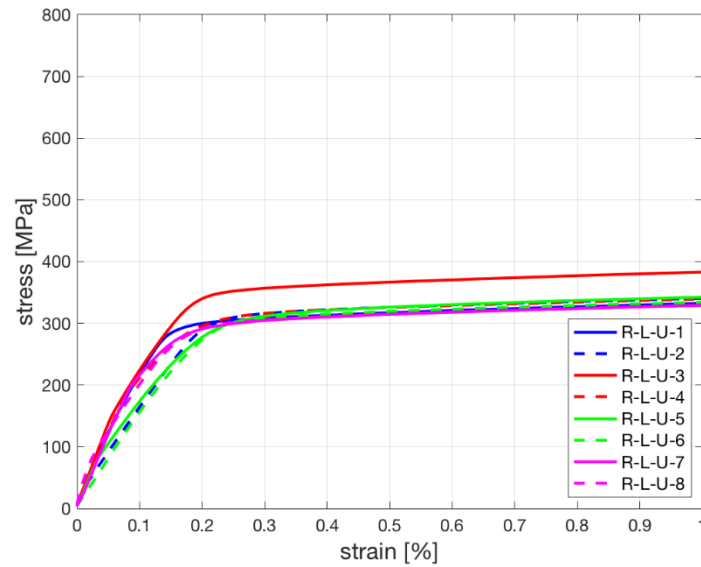
(d)

Figure 4.28: Zoom of stress-strain curves (at deformations <1%) for tensile tests on WAAM planar specimens: (a) T specimens with active cooling and (b) with uncontrolled cooling; (c) L specimens with active cooling and (d) with uncontrolled cooling.

Table 4.12 reports the mean values plus/minus one standard deviation of the key material parameters, i.e. Young's modulus (E), 0.2% proof stress ($R_{p0.2}$), ultimate tensile strength (UTS), elongation at rupture ($A_\%$) and yield to tensile strength ratio ($R_{p0.2}/UTS$) as obtained from tensile

_____

tests according to EN ISO 6892-1 standards. In order to accurately evaluate the Young's modulus values overcoming the experimental noise typical of the stress-strain curves as depicted in Figures 4.27 and 4.28, the ordinary least squares regression (OLSR) analysis was employed, as proposed by (Kyvelou et al., 2020) (see Section 4.3.4).

Overall, the values of Young's modulus are slightly higher as for those resulted from the mechanical characterization of machined specimens (presented in Section 4.3), especially for L specimens, with values also of around 170 GPa for specimens printed with uncontrolled cooling (U).

Those findings are in line with the results presented by Kyvelou et al. The values of 0.2% proof stress and ultimate tensile strength are on average similar to the ones found with the mechanical characterization of machined specimens (presented in Section 4.3). Slightly higher values of elongation at rupture are registered instead for as-built specimens with respect to the material properties of the machined ones presented in Section 4.3, with values on average for L specimens with uncontrolled cooling (U) of over 40%.

Table 4.12: Overview of the tensile test results from as-built continuously-printed 2D specimens.

Surface type	Specimen orientation	Printing strategy	Specimen ID	E [GPa]	$R_{p0.2}$ [MPa]	UTS [MPa]	$A_\%$ [%]	$R_{p0.2}/$ UTS [-]
R	T	A	R-T-A	117 ± 13	325 ± 13	518 ± 16	18 ± 4	0.63 ± 0.03
		U	R-T-U	125 ± 24	296 ± 6	540 ± 17	27 ± 3	0.55 ± 0.02
	L	A	R-L-A	133 ± 7	346 ± 9	547 ± 26	22 ± 2	0.63 ± 0.02
		U	R-L-U	174 ± 39	318 ± 19	579 ± 28	42 ± 3	0.55 ± 0.01

_____

4.5.3. Focus on the strain fields planar specimens

In order to investigate the influence of the geometrical irregularities on the strain field, DIC monitoring system is applied for planar specimens with either as-built surface (R) or with machined surface (M). For the sake of conciseness, the results for each of the four types of specimens are presented: one L specimen with machined surface (M), one T specimen with machined surface (M), one L specimen with as-built surface (R), one T specimen with as-built surface (R). The four specimens considered were realized with active cooling strategy. However, a similar response was obtained for the specimens realized with uncontrolled cooling. For each specimen considered, the whole strain field has been analyzed by comparing the local peak strain (ε_p) with the average strain (ε_m) evaluated along the gauge length ($\varepsilon_m = \dfrac{\Delta L}{L} \cdot 100$), see Figure 4.29. The results of this analysis are reported in Figure 4.30 for 10 relevant stages encompassing the whole range of behavior from the elastic field up to failure. The figure also represents colored maps of strain fields at selected stages with indication of the location of the peak strain. For all specimens, the location of the peak strain remained stable after reaching the first yielding up to failure. Table 4.13 reports the values of ε_p and ε_m and their relative discrepancies. On average, local peak strains are 50-60% larger than average strains. No appreciable differences are noticed when comparing as-built and machined responses. Thus, overall the geometrical irregularities seem to not significantly alter the strain distribution during tensile tests. It should be noted that the position of rupture for all specimens lie within the gauge length, and does not suggest particular evidence of defects or rougher parts affecting the failure of specimens.
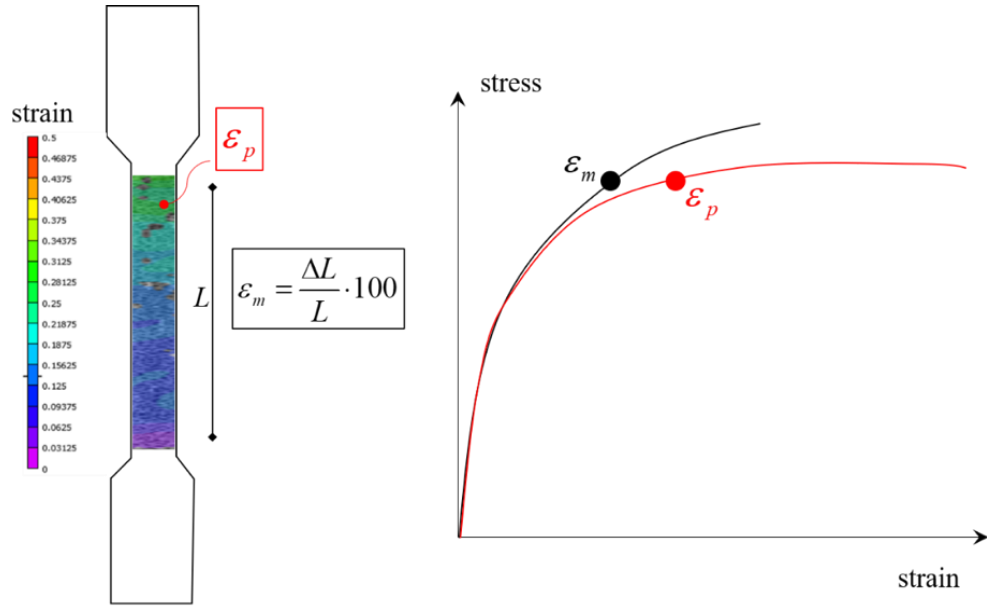
Figure 4.29: Qualitative representation of stress-strain curves from peak and average strains.
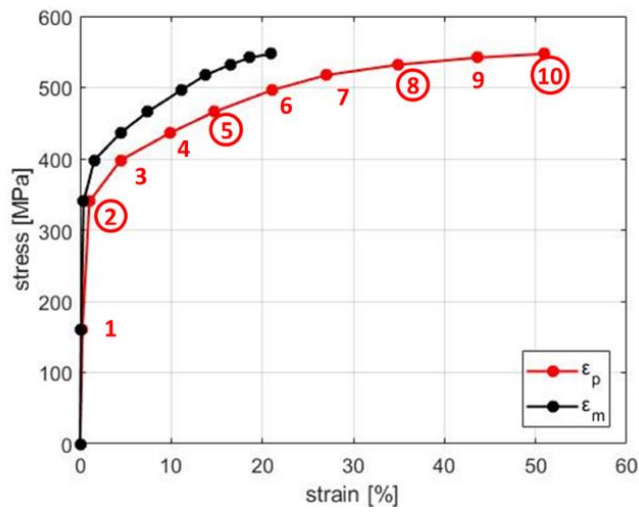
(a)
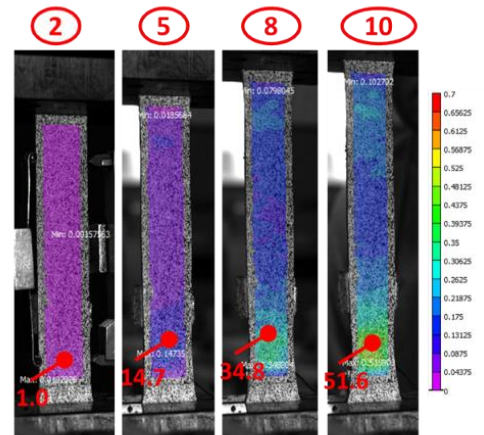
(b)

(c)

_____
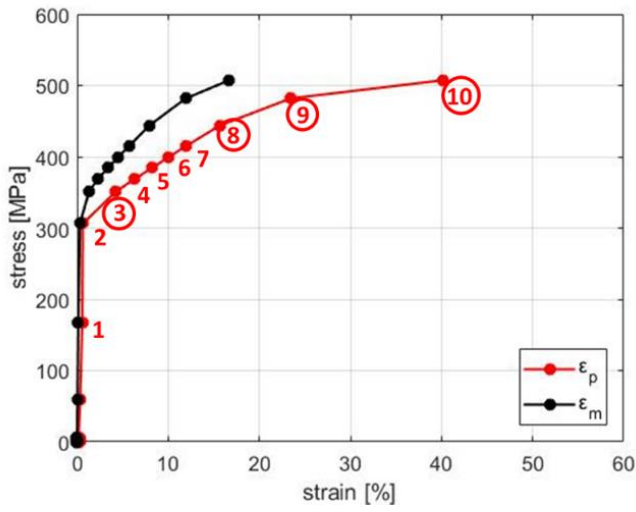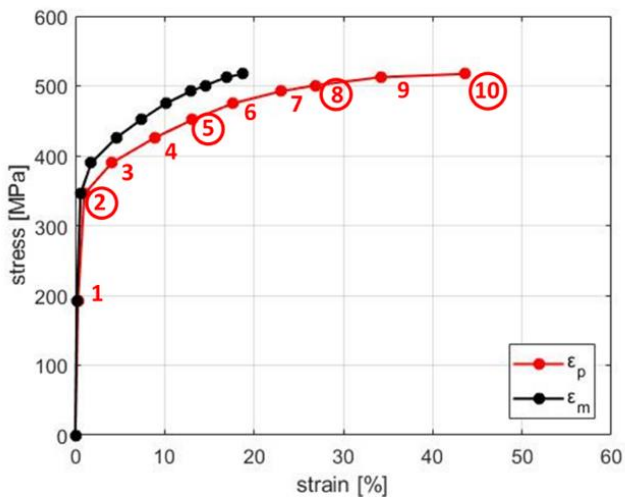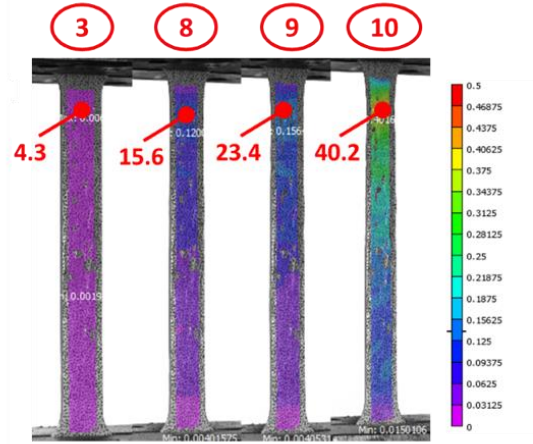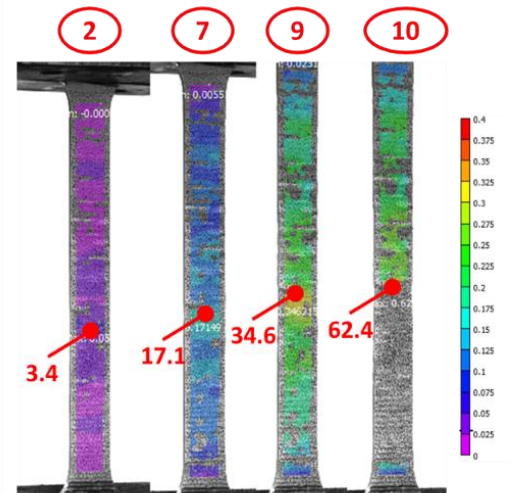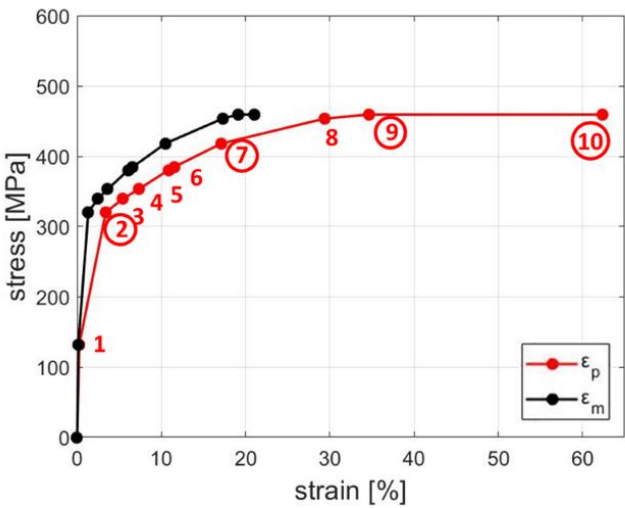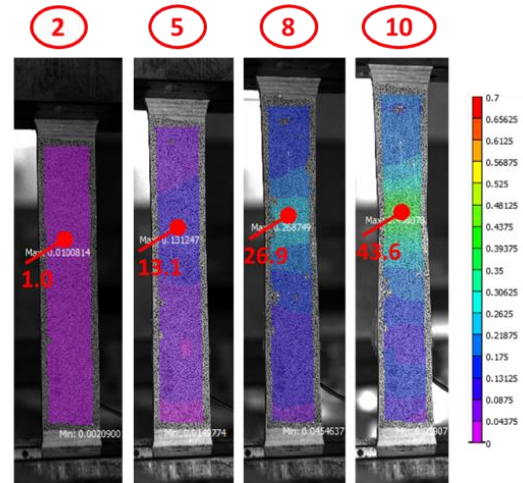
(d)

Figure 4.30: DIC results (stress-strain curves on the left-hand side and strain contour plots on the right-hand side) for specimens: (a) M-L-A-2, (b) R-L-A-8, (c) M-T-A-1, (d) R-T-A-8.

Table 4.13: Comparison of elongations for machined (M) and as-built (R) transversal (T) specimens.

Specimen ID	Step	ε_m [%]	ε_p [%]	$(\varepsilon_p - \varepsilon_m)/\varepsilon_p$ [%]
M-L-A-2	2	0.39	1.02	62
	5	7.42	14.74	50
	8	16.47	34.88	53
	10	20.96	50.88	59
				+56%
R-L-A-8	3	1.32	4.29	69
	8	7.92	15.65	49
	9	11.93	23.44	49
	10	16.70	40.16	58
				+56%
M-T-A-1	2	0.58	1.01	43
	5	7.36	13.12	44
	8	14.59	26.87	46
	10	18.73	43.61	57
				+48%
R-T-A-8	2	1.33	3.41	61
	7	10.49	17.15	39
	9	19.08	34.62	45
	10	21.09	62.63	66

_____

		+53%

4.5.4. Discussion on mechanical properties of WAAM stainless steel planar elements

The interpretation of the mechanical response from tensile tests focuses on the comparison of the results in terms of orientation (longitudinal vs. transversal) and surface finishing (machined vs. as-built). In particular, the results of the machined specimens are those presented in Section 4.3 and used to characterize WAAM stainless steel material. The comparison between machined and as-built specimens allows to make some considerations upon the influence of geometrical irregularities proper of WAAM process (as described in Section 4.4) on the mechanical response of the printed elements.

Figure 4.31 presents an overview of the mechanical properties of WAAM specimens realized with active cooling, comparing the response of those with machined surface with respect to those with as-built (rough) surface. Table 4.14 quantifies the relative differences between the mechanical parameters comparing both machined vs as-built ("rough") specimens (for the same orientation) and transversal vs longitudinal orientations.

Overall, the variations of the mechanical properties from as-built and machined specimens oriented longitudinally (L) are negligible. Specimens oriented transversally (T) instead present 5% increase in Young's modulus when tested as-built with respect to the machined values, as well as 8% reduction in yielding (0.2% proof stress). For both directions, the elongation at rupture decreases for the as-built specimens (-8% for L specimens and -17% for T specimens). It should be noted that these variations lie within the standard deviations of the distribution of the test results, thus suggesting that the influence of the geometrical irregularities in the as-built specimens is rather small.

Kyvelou et al. (Kyvelou et al., 2020) reported similar comparisons between as-built and machined specimens realized with WAAM stainless steel. The trends for 0.2% proof stress and elongation at rupture are similar to the ones obtained in the present work. However, the registered decrease in Young's modulus of as-built material relative to the machined one as reported in (Kyvelou et al., 2020) cannot be appreciated in the results reported here. The higher discrepancies

of the machined vs. as-built mechanical properties reported in (Kyvelou et al., 2020) might be affected by the layer thickness of the printed plates. Thus, further explorations on this aspect should be developed in detail. Moreover, given the limited number of samples analyzed, further studies should be developed in order to better investigate the possible influence of the geometrical irregularities.
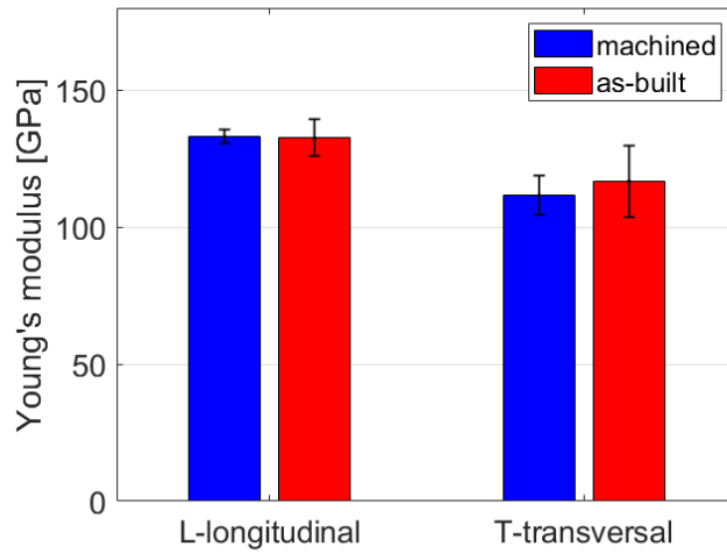
(a)
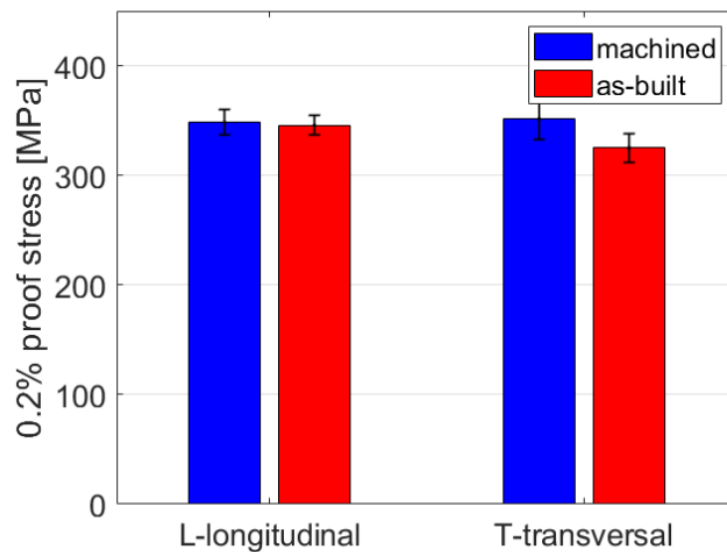
(b)
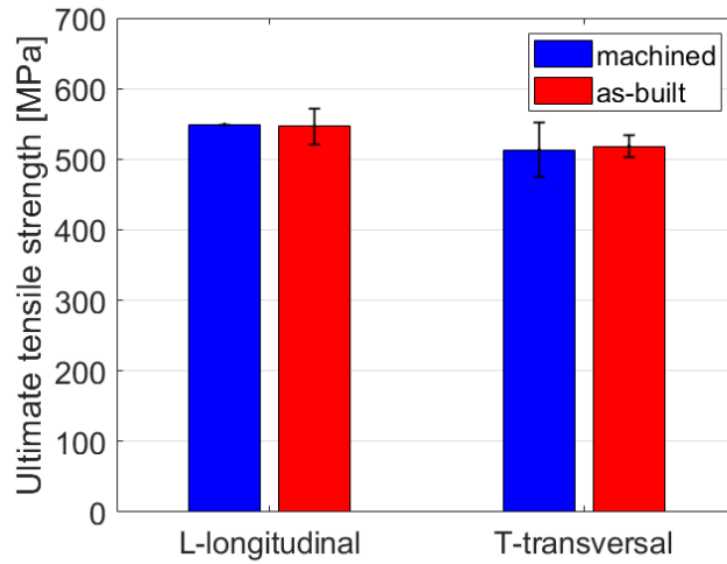
(c)
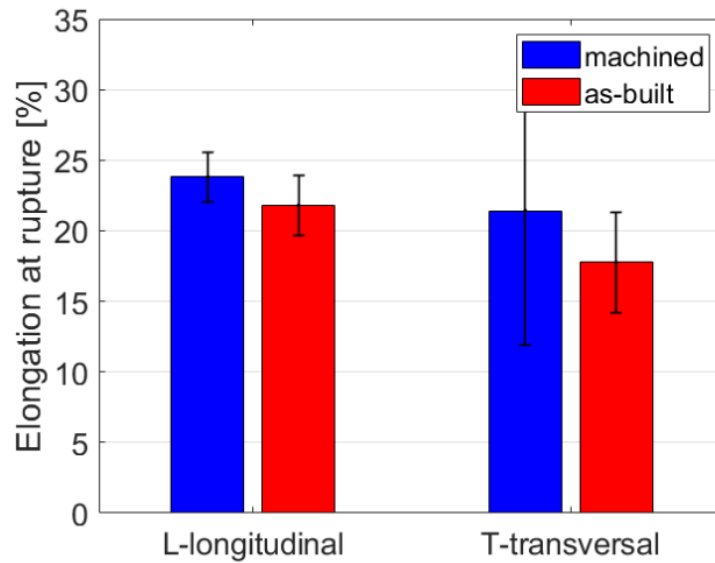
(d)

Figure 4.31: Comparison of WAAM mechanical properties for machined and as-built continuously-printed 2D elements with active cooling: (a) Young's modulus, (b) 0.2% proof stress,

_____

(c) ultimate tensile strength, (d) elongation at rupture.

Table 4.14: Comparison of mechanical properties for specimens with active cooling.

		E [GPa]	$R_{p0.2}$ [MPa]	UTS [MPa]	$A_{\%}$ [%]	$R_{p0.2}/$ UTS [-]
(R-M)/M	L	0%	-1%	0%	-8%	0%
	T	+5%	-8%	+1%	-17%	-9%
(L-T)/T	M	+19%	-1%	+7%	+11%	-8%
	R	+14%	+6%	+5%	+23%	+1%

Comparing the mechanical properties for the two directions, it appears that:

- In general, the longitudinal specimens (L) have higher values of all mechanical properties than the transversal ones (T), both in case of machined and as-built specimens.

- The main differences are observed for the Young's modulus values (+19% for machined specimens and +14% for as-built ones) and for the elongation at rupture (+11% for machined specimens and +23% for as-built ones).

These results further confirm the evidence also presented in Section 4.3 regarding the intrinsic anisotropy of WAAM stainless steel through mechanical tests on machined specimens, resulted from the microstructural characterization, with no distinct reference to the geometrical irregularities of the printed outcomes. This is also evidenced in (Gardner et al., 2019; Ji et al., 2017; Laghi et al., 2020a; Laghi et al., 2020).

Figure 4.32 presents the mechanical properties of specimens with uncontrolled cooling on both orientations comparing the results for machined and as-built specimens. In Table 4.15 the relative

_____

differences are proposed both between machined and as-built specimens, for the same orientation, and between the two different orientations.

Differently from the specimens printed with active cooling, the variations computed for the specimens with uncontrolled cooling are higher and with no clear pattern. This might also be due to the higher variability of the mechanical properties of the base material within each type of specimen (as also described in Section 4.3.2), which also affects the comparison. Thus, further studies would be required to deeply analyze the influence of cooling strategy in the material characteristics from both the microstructural and mechanical point of view.
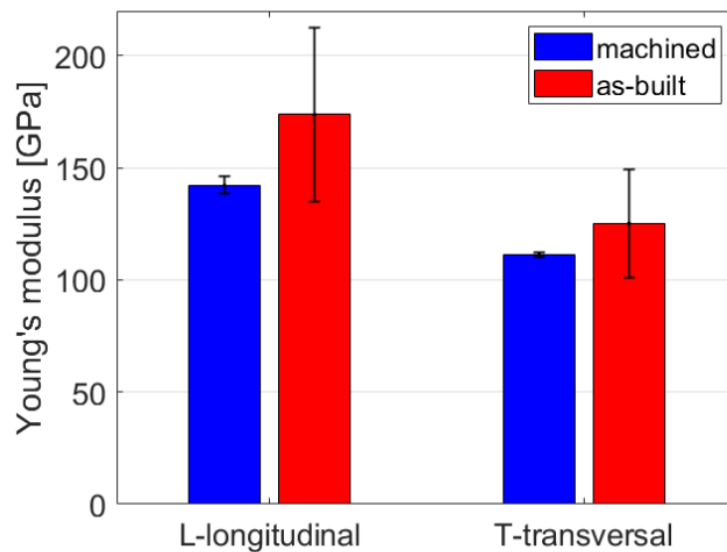
(a)
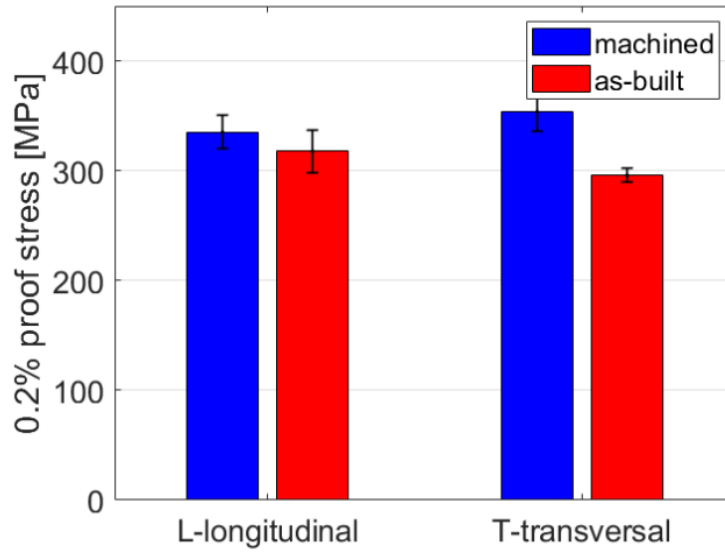
(b)
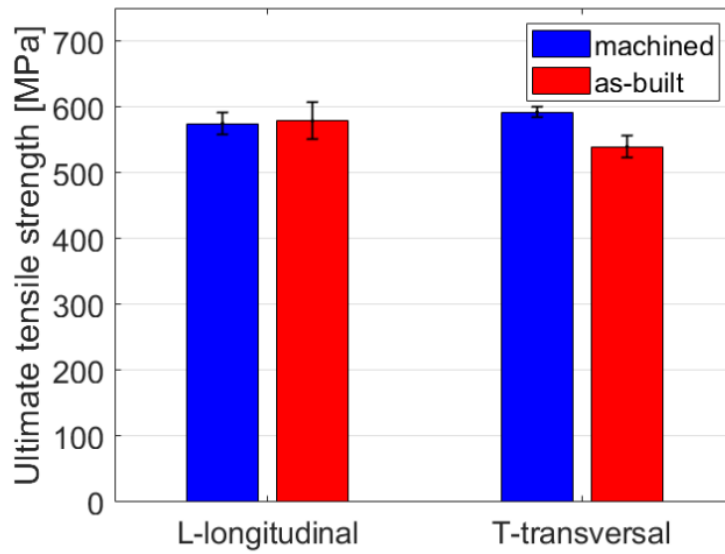
(c)
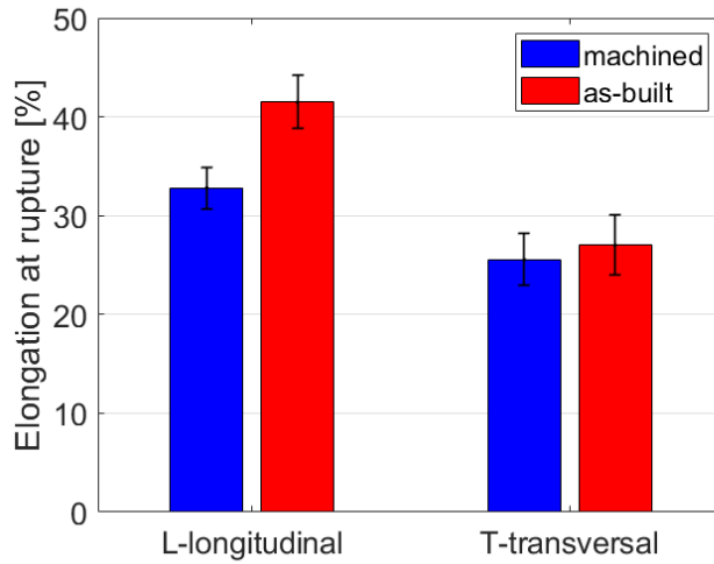
(d)

Figure 4.32: Comparison of WAAM mechanical properties for machined and as-built specimens with uncontrolled cooling: (a) Young's modulus, (b) 0.2% proof stress, (c) ultimate tensile strength, (d) elongation at rupture.

Table 4.15: Comparison of mechanical properties for specimens with uncontrolled cooling.

		E [GPa]	$R_{p0.2}$ [MPa]	UTS [MPa]	$A_\%$ [%]	$R_{p0.2}/$ UTS [-]
(R-M)/M	L	+22%	-5%	+1%	+26%	-6%
	T	+13%	-16%	-9%	+6%	-8%
(L-T)/T	M	+28%	-5%	-3%	+28%	-2%
	R	+39%	+7%	+7%	+54%	0%

4.6. FRACTURE SURFACES

Representative images of the tensile fracture surfaces, obtained by multi-focus microscopy at relatively low magnification (as described in Section 4.2), are shown in Fig.4.33, highlighting that no macroscopic defects were present in the tested samples.

High magnification analyses were also carried out by SEM-EDS to better highlight specific microstructural features of the failure. Representative SEM micrographs of fracture surface are reported in Fig. 4.34. All samples, regardless cooling condition and extraction direction, exhibited a ductile fracture mechanism. A ductile fracture is characterized by nucleation and growth of microvoids, called dimples, clearly visible at high magnification analyses (Fig. 4.34). Because of the very fine microstructure, dimples were still very fine, with an average dimension in the order of few micrometers. The fineness of the dimples is clearly related to the corresponding very fine microstructure induced by the WAAM process in the stainless steel. As a confirmation of the microstructural and tensile results above-discussed, no major differences in dimples size and shape were evidenced neither among specimens obtained with and without the active cooling system nor extracted along different directions, as also discussed in (Laghi, et al. 2020).
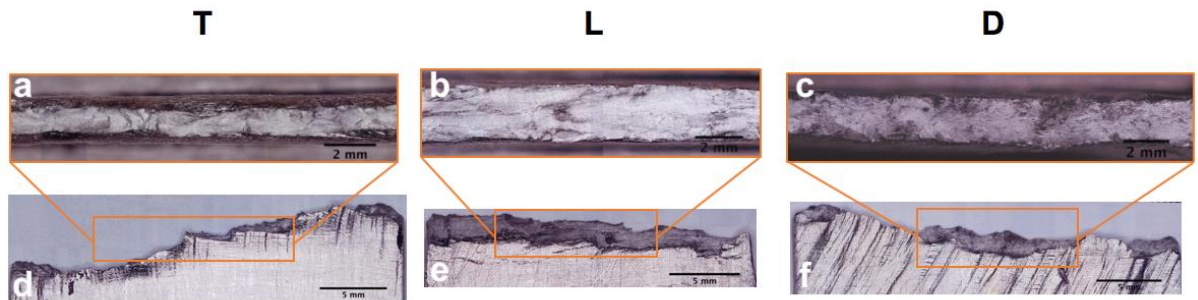
Figure 4.33: Low magnification micrographs obtained by 3D multifocus microscopy of the top and lateral view of the fracture region: a) and d) transversal, b) and e) longitudinal, c) and f)

diagonal tensile samples

(a)

(b)

(c)

(d)
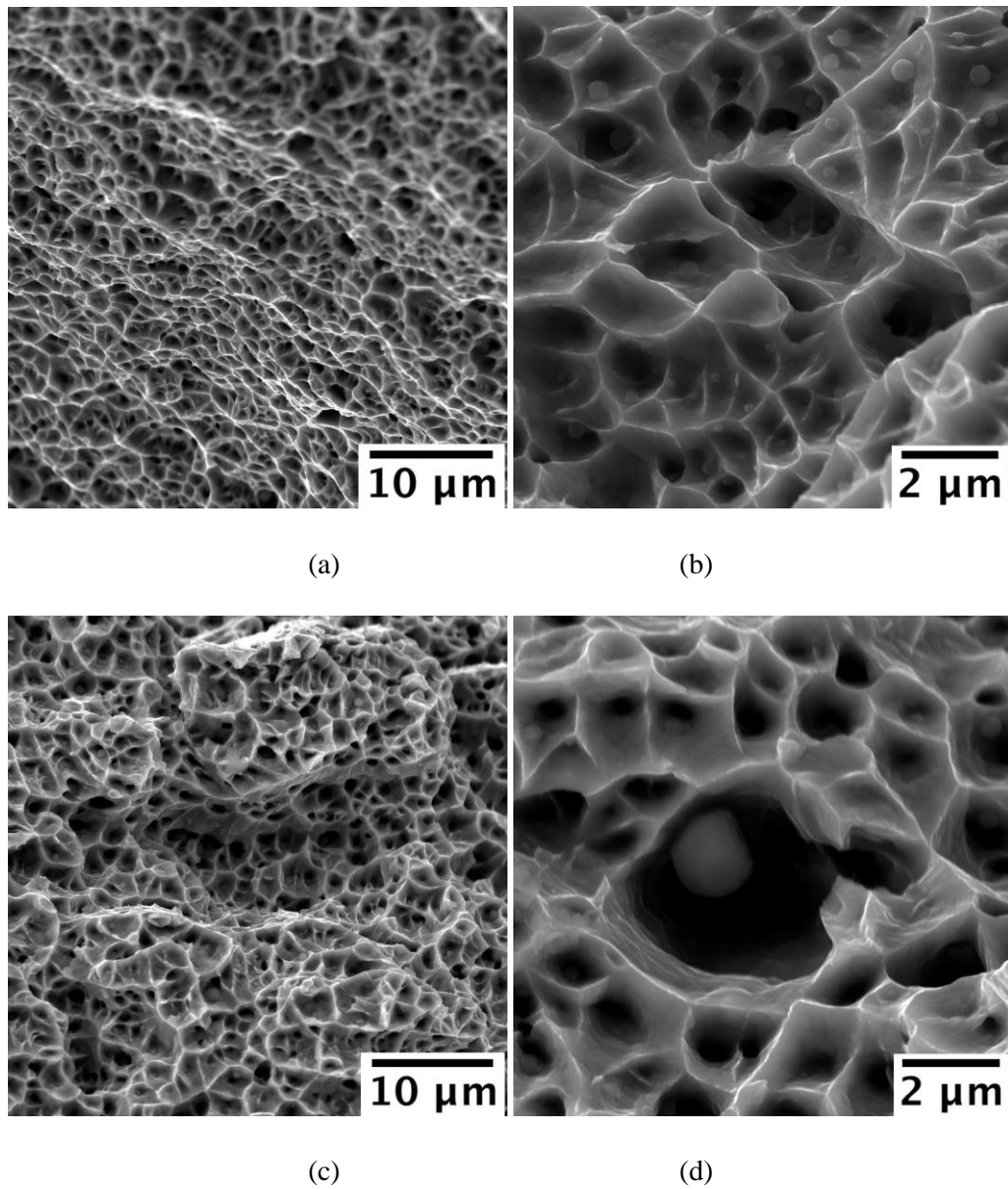
Figure 4.34: Low and high magnification FEG-SEM analyses of fracture surfaces of representative samples obtained: a), b) with and c), d) without active cooling system.

4.7. SUMMARY OF SECTION 4

From the results on the experimental characterization of WAAM-produced stainless steel planar elements, some important results have been evidenced:

- From the investigations on the material, the marked anisotropy also registered on the mechanical tests derives from the epitaxial growth of columnar grains with a preferential texture along the printing direction of the plate. As a result, the material properties are highly influenced on the relative orientation of the element with respect to the printing direction.

- The key material properties from mechanical tests on machined specimens are significantly affected by the anisotropic microstructure, and register values of Young's modulus varying from 60% reduction to 30% increase with respect to the traditional value for stainless steel, depending on the main orientation of the printed element. The elastic parameters (Young's modulus and Poisson's ratio) further prove the orthotropic nature of the WAAM-produced stainless steel plates.

- From the experimental characterization of as-built planar specimens, detailed investigation on the surface roughness allowed to provide some considerations on the distribution of thickness variability which depends on the relative orientation of the element with respect to the printing direction. The geometrical irregularities proper of WAAM process result in non-uniform cross-sectional area which might affect the mechanical response of the printed elements.

- The mechanical tests on as-built specimens confirmed a slight influence of the geometrical irregularities on the mechanical response, especially for transversal specimens. In particular, the highest discrepancies were registered for values of Young's modulus and elongation at rupture.

Thus, for structural design purposes, the calibration of the main material properties needs to be performed for the three main directions investigated (longitudinal, transversal and diagonal with respect to the printing deposition layers). The orthotropic nature of the WAAM plates also suggests the need of a proper material model to be calibrated from the elastic parameters experimentally evaluated. Moreover, additional considerations of the geometrical influence on the mechanical response of WAAM elements should be made at preliminary design stage.

5. Orthotropic material model for WAAM stainless steel planar elements

5.1. OVERVIEW

From the experimental tests carried out on WAAM-produced stainless steel plates (Section 4), the continuously-printed WAAM elements resulted in an intrinsic anisotropic behavior, which should be considered for structural design.

Following the traditional procedure for calibrating the design values of strength, in the previous chapter experimental values of the key material properties were proposed for the three main directions of WAAM plates (i.e. transversal, longitudinal and diagonal with respect to the printing deposition layers).

Concerning the stiffness of WAAM-produced stainless steel planar elements, a more accurate way of considering this material is by means of an orthotropic material constitutive model. Thus, the present Section proposes a calibrated orthotropic model for WAAM stainless steel plates. From the theory of the orthotropic material model (Section 5.2), a calibrated constitutive law is proposed for different WAAM-produced stainless steel plates (Section 5.3).

The calibrated orthotropic material model will be then used to create structurally optimized designs of new-generation steel members realized with WAAM technology.

5.2. THE ELASTIC CONSTITUTIVE MODEL FOR ORTHOTROPIC MATERIALS

In nature several materials present different mechanical properties based on their directions in space, and thus are considered as anisotropic. From these, different categories are formed based on the presence of material symmetrical axes or planes.

One example is for the class of orthotropic materials, characterized by two material symmetrical planes orthogonal to each other. Typical orthotropic materials are wood, fiber-reinforced composites with orthogonal pattern, as well as aligned fiber composites. Indeed, any WAAM lamina may be regarded as an aligned layer composite.

The principal axes of these materials are the intersections between the planes of symmetry. For 3D orthotropic materials, the independent elastic constants of the compliance matrix are 9, as identified by three elastic moduli (E_x, E_y, E_z), three independent Poisson's ratios (v_{xy}, v_{yz}, v_{zx}) and three shear moduli (G_{xy}, G_{yz}, G_{zx}).

For the case of a layered lamina undergoing a plane stress state in the plane x,y, the constitutive equations in the inverse form reduces to (Taliercio, 2020):

$$\begin{Bmatrix} \varepsilon_x \\ \varepsilon_y \\ \gamma_{xy} \end{Bmatrix} = \begin{bmatrix} 1/E_x & -v_{xy}/E_y & 0 \\ -v_{yx}/E_x & 1/E_y & 0 \\ 0 & 0 & 1/G_{xy} \end{bmatrix} \begin{Bmatrix} \sigma_x \\ \sigma_y \\ \tau_{xy} \end{Bmatrix} \tag{5.1}$$

Thus, the material constitutive law is expressed in terms of only 5 elastic constants, namely E_x, E_y, v_{xy}, v_{yz}, G_{xy}. Nonetheless, the major symmetries of the elastic tensor call for the symmetry of the compliance matrix, i.e.:

$$E_x \cdot v_{xy} = E_y \cdot v_{yx} \tag{5.2}$$

Hence, the number of independent elastic constants reduces to 4.

_____

5.3. ORTHOTROPIC MATERIAL MODEL FOR WAAM STAINLESS STEEL

5.3.1. Calibration of the elastic model for WAAM orthotropic material

As far as WAAM stainless steel material is concerned, the two main directions of the orthotropic material x and y should be, reasonably, coincident with the directions L and T, going parallel and perpendicular to the printing deposition layers, respectively (Figure 5.1). Therefore, in the calibration process the WAAM material will be assumed to behave as on orthotopic material with the axes of symmetry x and y coincident with directions L and T. As already remarked in Section 4.3, the experimental data are also consistent with the symmetry condition expressed by Eq. 5.2. The main findings of this research have also been reported in (Laghi et al., 2020c).
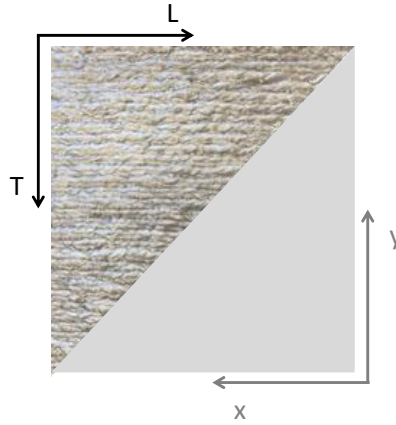
Figure 5.1: The two directions considered for the real material (L and T) vs. the axes of symmetry (x and y) of an orthotropic model.

From Eq. 5.1, the compliance matrix C for WAAM stainless steel is:

$$C = \begin{bmatrix} 1/E_x & -v_{xy}/E_y & 0 \\ -v_{yx}/E_x & 1/E_y & 0 \\ 0 & 0 & 1/G_{xy} \end{bmatrix} \tag{5.3}$$

In Eq.5.3, E_x and E_y are the Young's moduli along x and y, respectively, v_{xy}, and v_{yx} the Poisson's ratios, and G_{xy} the shear modulus. The Young's moduli E_x and E_y are assumed to be coincident

to the values obtained from the experimental tests on the four plates (as presented in Section 4.3) along L and T, respectively, so that: $E_x = E_L$ and $E_y = E_T$. Additionally, given the experimental values for Young's modulus along direction D, it is also assumed that the value of the Young's modulus found through transformation of the compliance matrix at an angle $\alpha = 45°$ corresponds to E_D.

On the contrary, the values of the Poisson's ratios cannot be, rigorously speaking, simply taken equal to those obtained from the experimental results but should instead be calibrated to achieve the (full) symmetry of the compliance matrix. Therefore, the following minimization problem can be used to calibrate the values of Poisson's ratios ν_{xy}, ν_{yx}, ensuring to satisfy Eq. 5.2:

$$\begin{cases} \min_{\nu_{xy}, \nu_{yx}} \quad (\nu_{xy} - \nu_{LT})^2 + (\nu_{yx} - \nu_{TL})^2 \\ s.t. \qquad \nu_{yx} \cdot E_y = \nu_{xy} \cdot E_x \end{cases} \tag{5.4}$$

with ν_{xy} and ν_{yx} unknowns. From Eq. 5.4 ν_{xy} and ν_{yx} can be expressed as follows:

$$\begin{cases} \nu_{xy} = \dfrac{E_x}{E_x + E_y} \cdot (\nu_{LT} + \nu_{TL}) \\ \nu_{yx} = \dfrac{E_y}{E_x + E_y} \cdot (\nu_{LT} + \nu_{TL}) \end{cases} \tag{5.5}$$

From the value of the Young's modulus measured along the diagonal direction E_D (see Section 4.3), the shear modulus G_{xy} can be found through transformation of the compliance matrix for $\alpha = 45°$ (see e.g. (Staab, 2015)) with the following formula:

$$G_{xy} = \left(\frac{4}{E_D} - \frac{1 - \nu_{xy}}{E_x} - \frac{1 - \nu_{yx}}{E_y} \right)^{-1} \tag{5.6}$$

Table 5.1 collects the values of the elastic parameters of the orthotropic model for WAAM stainless steel calibrated from the experimental results (as presented in Section 4.3) on the four plates making use of Eqs. 5.5 and 5.6.

Table 5.1: Elastic parameters of the orthotropic model for WAAM stainless steel.

Plate	E_x [GPa]	E_y [GPa]	G_{xy} [GPa]	ν_{yx} [-]	ν_{xy} [-]
1	135.54	116.45	156.34	0.396	0.339
2	147.31	109.64	152.47	0.486	0.362
3	137.94	112.27	127.52	0.448	0.365
4	137.27	111.99	168.48	0.445	0.363
mean	**139.52**	**112.59**	**151.20**	**0.444**	**0.357**
COV	**0.03**	**0.02**	**0.10**	**0.07**	**0.03**

It is of interest to notice that the values of the shear modulus are, on average equal to 150 GPa, which is twice the value commonly adopted for 304L steel (around 77 GPa assuming a Young's modulus equal to 200 GPa and a Poisson's ratio equal to 0.3).

Table 5.2 collects the discrepancies from experimental and calibrated Poisson's ratios. The values evidence a good agreement between the experimental measures and the calibrated values for almost all plates, for which a difference of around +/-3% is registered. This result is a further confirmation of the orthotropic nature of WAAM stainless steel plates.

Table 5.2: Discrepancy of experimental and calibrated Poisson's ratios.

Plate	$(\nu_{yx}-\nu_{TL})/\nu_{TL}$ [%]	$(\nu_{xy}-\nu_{LT})/\nu_{LT}$ [%]
1	+3.1%	-3.4%
2	-1.6%	+2.2%
3	-1.9%	+2.4%

4	+2.6%	-3.1%

Figure 5.2 shows the normalized polar diagrams of the Young's modulus and shear modulus, as computed through transformation of the compliance matrix of Eq. 5.3, see e.g. (Kaw, 2005). The diagrams are normalized with respect to the standard Young's modulus and shear modulus values for 304L stainless steel (i.e. 200 GPa and 77 GPa, respectively) according to ASM Handbook. The orientation α is measured from x (i.e. $\alpha = 0°$ corresponds to L direction on the real printed material, while $\alpha = 90°$ corresponds to T direction on the real printed material).
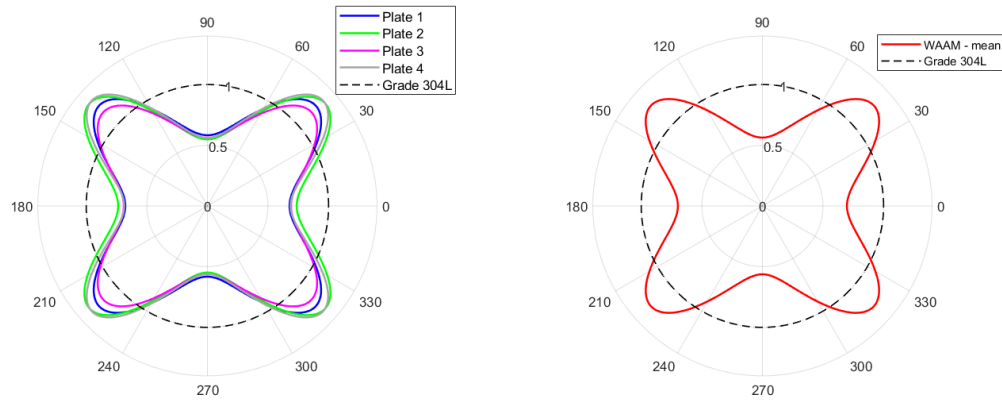
(a)
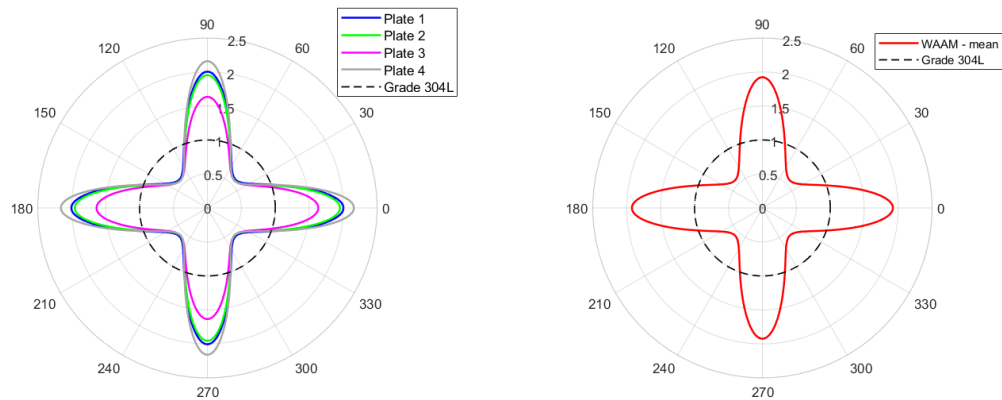
(b)

Figure 5.2: Normalized polar diagrams: (a) Young's modulus and (b) shear modulus of WAAM-produced stainless steel and of Grade 304 stainless steel depending on the orientation of the reference system with respect to x.

Tables 5.3 and 5.4 collect the maximum and minimum values and the corresponding orientations α of Young's modulus and shear modulus calibrated from the values of the four plates tested.

Table 5.3: Maximum and minimum values of Young's modulus and corresponding orientations for the four plates tested.

Plate	E_{max} [GPa]	$\alpha_{E,max}$ [°]		E_{min} [GPa]	$\alpha_{E,min}$ [°]	
1	243.44	± 43°	± 137°	116.45	± 90°	± 270°
2	257.61	± 41°	± 139°	109.64	± 90°	± 270°
3	230.98	± 42°	± 138°	112.27	± 90°	± 270°
4	257.95	± 42°	± 138°	111.99	± 90°	± 270°
mean	**247.50**	**± 42°**	**± 138°**	**112.59**	**± 90°**	**± 270°**

Table 5.4: Maximum and minimum values of shear modulus and corresponding orientations for the four plates tested.

Plate	G_{max} [GPa]	$\alpha_{G,max}$ [°]		G_{min} [GPa]	$\alpha_{G,min}$ [°]	
1	156.44	± 90°	± 180°	45.88	± 45°	± 135°
2	152.46	± 90°	± 180°	44.42	± 45°	± 135°
3	127.48	± 90°	± 180°	44.14	± 45°	± 135°
4	168.46	± 90°	± 180°	44.06	± 45°	± 135°
mean	**151.21**	**± 90°**	**± 180°**	**44.63**	**± 45°**	**± 135°**

5.3.2. Discussion and future research

Inspections of the graphs reported in Figure 5.2 and of Tables 5.3 and 5.4 allow to draw interesting observations.

Concerning the Young's modulus (Figure 5.2a), the minimum values, as expected, are for $\alpha = \pm90°$ and $\pm180°$, along the x coordinate of the material model, or else along the T direction of the real printed plate. On the other hand, the maximum values are not found exactly at $\pm45°$ and $\pm135°$, as might be expected from the experimental tests, but instead for α values on average around $\pm42°$, and $\pm138°$. Reasonings to this are related to the slightly different values of Young's modulus found along the two principal directions of WAAM stainless steel, i.e. longitudinal L (on average of 140 GPa) and transversal T (on average of around 110 GPa). Thus, the orthotropic elastic model calibrated from experiments gives a maximum value which is not exactly at 45° (as would be expected if the values of Young's modulus were equal along both T and L), but instead 42°. Examples of other anisotropic materials with similar behavior were studied in (Vannucci, 2018).

Comparing the average results obtained on WAAM stainless steel with the traditionally-manufactured 304L steel, the former one presents in general lower values of Young's modulus, especially for $\alpha = \pm90°$ and $\pm180°$, while it presents higher values than the traditional stainless steel for angles between $\pm25°$ and $\pm60°$ (and respectively $\pm120°$ and $\pm155°$). The ratio between maximum and minimum values of E for WAAM stainless steel is of around 2.

As far as shear modulus diagrams are concerned (Figure 5.2b), maximum values are registered for $\alpha = \pm90°$ and $\pm180°$, with values on average twice the one commonly adopted for 304L steel. Minimum values are, instead, quite below (almost halved) the standard value considered for 304L steel, at $\alpha = \pm45°$ and $\alpha = \pm135°$. In general, WAAM stainless steel presents higher values than the traditional stainless steel for angles between $\pm70°$ and $\pm110°$ (and respectively $\pm160°$ and $\pm200°$), while it is 50% higher for angles between $\pm80°$ and $\pm100°$ (and respectively $\pm170°$ and $\pm190°$). The ratio between maximum and minim values of G for WAAM stainless steel is of around 3.5.

The above outcomes, concerning both Young's and shear moduli, point out a quite marked orthotropy suggesting further experimental investigations to verify these theoretical predictions and to explore the material behavior at different orientations with respect to those already tested. For instance, additional axial tests at different orientations are needed to verify the model

prediction, both in terms of Young's modulus and relevant Poisson's ratios. This means measuring the axial elongation and evaluating a transverse contraction coefficient in each test. Directions for which maximum values of the elastic modulus are predicted should be experimentally assessed. Results of off-axis tension tests can be processed as well to provide an exact determination of the shear modulus, instead of resorting to more complex tests on tubes and plates (see e.g. (Morozov & Vasiliev, 2003)).

The presented results, enriched with further experimental investigations, will then allow to draw a full experimentally-validated orthotropic material model for WAAM stainless steel, including both the elastic and post-elastic behavior.

Moreover, the calibration of an orthotropic model for WAAM stainless steel also allows to draw unexplored design possibilities in structural design. In details, new design strategies could be explored through the exploitation of the different structural response by changing the printing directions. Possible topology optimization tools could be driven by deformation constraints which can be accurately matched at specific printing orientations (Bruggi et al., 2021). In general, high structural performances could be reached using the same feedstock, if the crystallographic orientation is well engineered, i.e. if the printing directions are set in order to follow the stress paths arising under a prescribed load. For example, considering the simple truss system of Figure 5.3, an efficient solution to reduce the deformability can be achieved by setting the printing direction of each truss element so that its longitudinal axis is aligned with the orientation of maximum axial stiffness. Also, periodic patterns could be printed to enhance the overall structural performance while saving material.

Finally, advanced materials could also be engineered to realize optimized WAAM-produced structures, through ad-hoc correlation studies on the influence of the printing parameters on the mechanical orthotropic response.
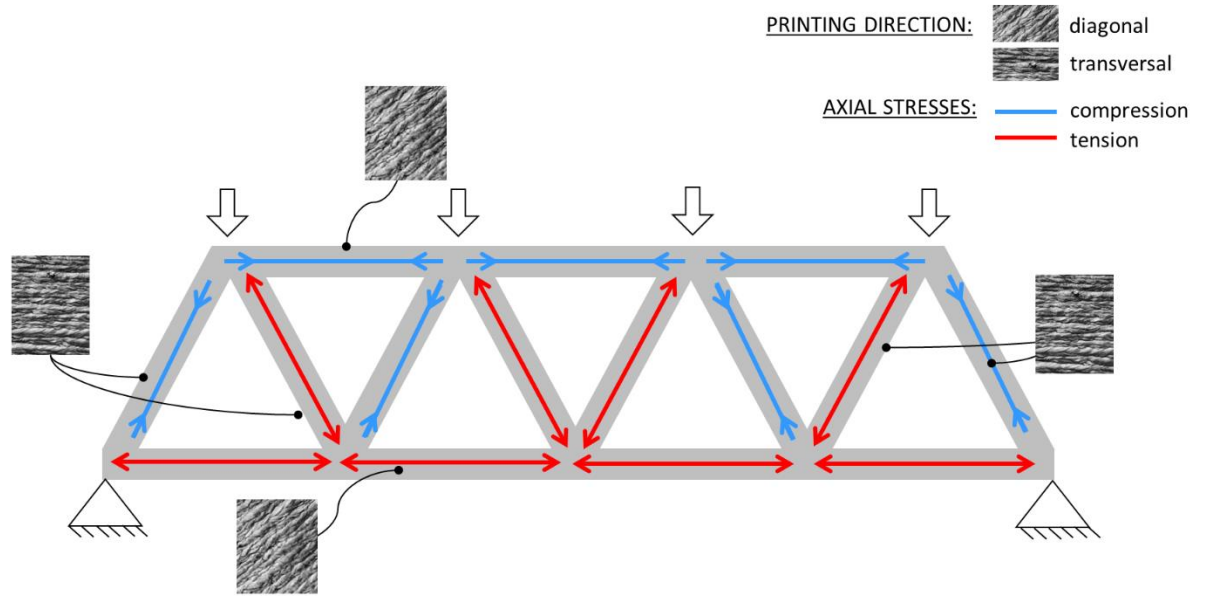
Figure 5.3: Graphical example of how to vary the printing directions in order to follow the orientation of highest axial stiffness in a WAAM planar truss system.

5.4. SUMMARY OF SECTION 5

In order to accurately account for the intrinsic anisotropy of WAAM plates, in the present chapter an ad-hoc orthotropic material model has been calibrated from experiments.

From the theory of orthotropic materials, the estimated elastic parameters from the model approximate well the experimental results for all four plates. The maximum value of Young's modulus is on average of around 245 GPa, registered for orientations θ on average of around $\pm 42°$. The minimum value is on average of 110 GPa, for θ of $\pm 90°$. The maximum value of shear modulus is on average of around 150 GPa, registered for orientations θ of $\pm 90°$. The minimum value is on average of 45 GPa, for θ of $\pm 45°$.

In order to use WAAM-produced material in structural engineering, proper calibration of the design values and partial safety factors should be carried out along the three main directions, to consider the orthotropic nature of the printed outcome.

_____

6. Design guidelines for WAAM stainless steel planar elements

6.1. OVERVIEW

The results from the experimental characterization of WAAM stainless steel planar elements suggest the need for proper guidelines for the design of WAAM structural elements, with considerations regarding the orientation of the element with respect to the printing deposition.

Therefore, the present Section illustrates a first calibration of the design mechanical properties and partial safety factors of WAAM stainless steel elements for structural purposes. Section 6.2 presents some concepts of structural reliability as adopted in European code provisions. Then, statistical distributions of the key material properties are presented in Section 6.3, from which the design values and partial safety factors are calibrated (Section 6.4).

_____

6.2. STRUCTURAL RELIABILITY THEORY

6.2.1. Basis of reliability

The concept of reliability is used in structural design as the ability of a structure to comply with given requirements under specified conditions during the intended life for which it was designed (according to ISO 2394 (*ISO 2394 - General Principles on Reliability for Structures*, 1998)).

The fundamental task of the theory of structural reliability is the analysis of the requirement that the action effect E is smaller than the structural resistance R:

$$E < R \tag{6.1}$$

Thus, the so-called limit state is the condition having: $E - R = 0$. Generally, both variables E and R are considered as random variables, meaning that they follow a certain distribution and thus the condition imposed by the structural reliability is affected by a certain probability of failure p_f:

$$p_f = P(E > R) \tag{6.2}$$

E and R are random variable generally distributed, therefore the exact solution of the probability of failure can be obtained by integration. However, simplifications such as the ones made by Eurocodes are commonly accepted to derive some basic probabilistic principles for developing the design quantities.

In Eurocodes, structures shall be designed and executed according to different levels of reliability, within the context of a given probability of failure p_f.

For the purpose of reliability differentiation, Eurocode 0 (EN 1990) establishes reliability classes (RC), also called consequence classes (CC). In particular, three classes are defined in accordance with consequences of failure or malfunction of the structure as follows:

- Reliability class RC3: high consequence for loss of human life, or economic, social or environmental consequences very great;

- Reliability class RC2: medium consequence for loss of human life, economic social or environmental consequences considerable;

_____

_____

- Reliability class RC1: low consequences for loss of human life, and economic, social or environmental consequences small or negligible.

Three categories of methods corresponding to three different levels of probability are considered in standard code provisions:

- Level I: semi-probabilistic methods;

- Level II: first order reliability methods (FORM);

- Level III: full probabilistic methods.

In both Levels II and III methods the measure of reliability should be identified with the survival probability:

$$p_s = 1 - p_f \qquad (6.3)$$

where p_f is the failure probability for the considered failure mode and within an appropriate reference period.

In Level II procedures, an alternative measure of reliability is considered by taking the reliability index β such that:

$$p_f = \phi(-\beta) \qquad (6.4)$$

where ϕ is the cumulative distribution function of the standard Normal distribution.

Eurocode 0 provides the basis of structural design, detailing in particular in Annex C and Annex D the basis for partial factor design and reliability analysis, as well as providing guidelines for design assisted by testing.

In Annex C precise reference on the calibration of partial safety factors is explained, specifying that this is possible either on the basis of calibration to a long experience of building tradition, or else on the basis of statistical evaluation of experimental data and field observations, within the framework of probabilistic reliability theory.

Probability reliability methods are based on the comparison of the failure probability p_f with its target value or the reliability index β with its target value β_t. It is generally required to design the

_____

_____

structures in such a way that the determined values of the basic variables are close to the target values specified in appropriate code provision.

The target reliability index β_t stated in Eurocodes derives from a number of previous reliability studies of structural members made from different materials, therefore having a great scatter, but however consists of a reasonable average value of the reliability level to be considered.

In particular, EN 1990 provides the recommended minimum values for the target reliability index β_t (associated with the probability of failure p_f) based on the reliability class for the structure to be designed. Typically, reliability class RC2 is considered for residential and office buildings, with an associated $\beta_t = 3.8$ for a reference period of 50 years. However, the probability of failure and its corresponding reliability index are only notional values that do not necessarily represent actual failure rates, which instead depend mainly on human error (Holicky, 2009). They are used as operational values for code calibration purposes and comparison of reliability levels of structures.

6.2.2. Reliability basis of the partial factor method

Partial factor methods provide operational design procedures adopted in many national and international standards, including Eurocodes (ISO 2394, Eurocode 0).

The design value method, also referred to as "semi-probabilistic method (Level I)" in Eurocode 0 (European Committee for Standardization (CEN), 2002), is a fundamental step from probabilistic design method towards operational partial factors method. The method is directly linked to the basic principle of Eurocode 0, for which it should be verified that no limit state is exceeded when the design values of all the basic variables are used in the models of structural resistance R and action effect E (Figure 6.1). Therefore, if the design values R_d and E_d are determined considering the design values of all basic variables, then a structure is considered reliable if:

$$E_d < R_d \tag{6.5}$$

_____
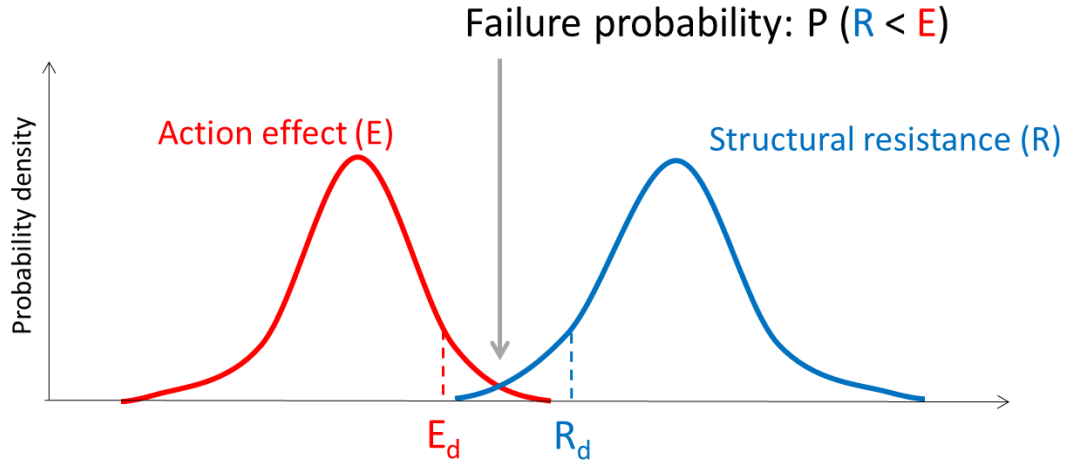
Figure 6.1: Conceptual schematization of the design value method.

It should be noted that E denotes a function describing the action effect and R a function describing the structural resistance as follows:

$$E_d = E\left\{F_{d,i}, a_{d,i}, \theta_{d,i}\right\} \tag{6.6}$$

$$R_d = R\left\{X_{d,i}, a_{d,i}, \theta_{d,i}\right\} \tag{6.7}$$

E depends on the actions (F) while R on the material properties (X), and they both depend also on the geometrical properties (a) and the model uncertainties (θ). All quantities are generally considered as random variables, thus the suffix "d" refers to their design values.

If only two variables are considered, the design values of E_d and R_d might be computed as:

$$P(E > E_d) = \phi(+\alpha_E \beta_t) \tag{6.8}$$

$$P(R < R_d) = \phi(-\alpha_R \beta_t) \tag{6.9}$$

where α_E and α_R are the FORM sensitivity factors, and β_t is the target reliability index. Suggested values for the FORM sensitivity factors are $\alpha_E = -0.7$ and $\alpha_R = 0.8$.

_____

Elementary methods of structural reliability can be used to assess the partial factors and other reliability elements in the fundamental case of two random variables when the limit state function is formulated as the difference between the resulting structural resistance and the load effect. More sophisticated theoretical principles of the First Order Reliability Method (FORM) are applicable to a general case of more basic variables, which can be adopted to estimate design points and partial factors of basic variables.

According to the partial factor methods presented in Eurocodes, the design values of the basic variables (generally denoted as X) are usually not introduced directly into the design equations, but expressed in terms of their representative values (X_{rep}), which should then be divided or multiplied by the appropriate partial factor. All partial factors should include model uncertainties, which may significantly affect the reliability of the structure.

6.2.3. Fractiles of random variables

General reliability analysis applied for structural design purposes derives from the statistical theoretical methods. In particular, the basic concepts of characteristic and design values of the variables governing actions and resistances are related to certain fractiles of such random variables.

The fractile of a random variable X is the value of the random variable such that the values less or equal to that occur with a given probability:

$$P(X < x_p) = \phi(x_p) = p \tag{6.10}$$

By making use of the tabulated values for the standardized random variable U (which follows the standard Normal distribution), the following transformation is given:

$$x_p = \mu + u_p \cdot \sigma = \mu \cdot (1 + u_p \cdot w) \tag{6.11}$$

where μ is the mean value, σ the standard deviation and w the coefficient of variation of the random variable X. For a standardized random variable with a general three-parameter Lognormal distribution (as for the general case of material properties), the value u_p of the standardized random variable is dependent also on the skewness. In case of Lognormal distribution with lower bound to zero, the fractile can be evaluated from the value of the standardized random variable computed for a Normal distribution with the following expression:

$$x_p = \frac{\mu}{\sqrt{1+w^2}} \exp(u_{norm,p} \sqrt{\ln(1+w^2)}) \tag{6.12}$$

where $u_{norm,p}$ is the fractile of the standardized random variable with a Normal distribution. An approximation of the Eq.6.12 is often applied in the form of:

$$x_p \approx \mu \cdot \exp(u_{norm,p} \cdot w) \tag{6.13}$$

whose accuracy is satisfying for $w<0.2$.

The commonly used fractiles adopted in structural design are the fractile corresponding to a probability of 5% ($p=0.05$), usually applied for the assessment of the characteristic value of material properties, and the fractile corresponding to a probability of 0.1% ($p=0.001$), usually applied for the assessment of the design value of dominant variables (Holicky, 2009).

In case the assessment of the fractiles of a random variable is taken from a limited amount of experimental values, from mathematical statistics it is possible to refer to three different methods of estimation theory for estimation of the population fractile: (i) coverage method; (ii) prediction method; (iii) Bayesian method.

The coverage method is based on the value of confidence γ adopted, which corresponds to the probability (usually 75% or 90%) that the estimated value covers the population fractile (from which the name is taken).

The estimation of the lower fractile x_p is:

_____

$$P(x_{p,\text{cover}} < x_p) = \gamma \tag{6.14}$$

Thus, the estimator is lower (on the safe side) with respect to the unknown fractile.

Considering a population with unknown standard deviation (the most general case), the estimation is:

$$x_p = m - k_p \cdot s \tag{6.15}$$

Where s is the sample standard deviation (i.e. an estimation of the standard deviation σ), m the average of the population (i.e. an estimation of the mean μ) and k_p is the coefficient of estimation. In general, it depends on the skewness of the population, on the probability p corresponding to the evaluating fractile, the confidence γ and the sample size n.

The prediction method is based on the estimation of the lower p-fractile x_p by the so-called "prediction limit" $x_{p,pred}$, for which it holds that a new value x_{n+1} randomly drawn from the population will be lower than the estimator only with probability p:

$$P(x_{n+1} < x_{p,pred}) = p \tag{6.16}$$

For increasing values of n, the estimator approaches the unknown fractile. Moreover, the estimator corresponds approximately to the estimator obtained by the coverage method for a confidence of γ=0.75.

In case of unknown standard deviation of the population (the most general case), the estimator is calculated as:

$$x_{p,pred} = m + t_p \left(\frac{1}{n} + 1\right)^{1/2} \cdot s \tag{6.17}$$

where t_p is the p-fractile of the generalized Student's t-distribution for v=n-1 degrees of freedom, with given skewness.

_____

_____

Comparison between the coverage and the prediction methods show that for a large number of sample size n, both coefficients k_p and $-t_p\left(\dfrac{1}{n}+1\right)^{1/2}$ approach the value of 1.64, which is valid for a theoretical model of the Normal distribution.

For the coverage method, the coefficient k_p increases with increasing confidence γ, and for the prediction method the relevant estimators of the lower fractile are decreasing on the safe side.

The Bayesian method is applied to the case of available previous experience for a random variable, for example in case of long-term production, therefore less common than the previous two methods.

6.2.4. European code provisions

As mentioned in Section 6.2.2, the design values of the basic variables introduced in Eurocodes are generally described in terms of representative values, which may be:

- the characteristic values, i.e. values with a prescribed or intended probability of being exceeded (i.e. fractile), commonly taken as 5%;

- the nominal values, which are treated as characteristic values for material properties and as design values for geometrical properties.

Such representative values should then be divided or multiplied by the appropriate partial factors to obtain the corresponding design values.

The design value for a variable related to the resistance as the material property X is defined as:

$$X_d = \eta \cdot \frac{X_k}{\gamma_m} \tag{6.18}$$

_____

Where X_k is the characteristic value, γ_m the partial safety factor related to the specific material property, and η is the mean value of the conversion function, which might be also implicitly be considered in the characteristic value. In particular, it should take into account volume and scale effects, effects of moisture and temperature, as well as any other relevant parameters.

The partial factor for resistance γ_M has in general two components:

$$\gamma_M = \gamma_m \cdot \gamma_{Rd} \tag{6.19}$$

where γ_m is referred to the uncertainty in the material properties, whereas γ_{Rd} represents the model uncertainty in structural resistance:

$$R_d = R\left\{\eta \frac{X_k}{\gamma_m}, a_d, \ldots\right\} / \gamma_{Rd} \tag{6.20}$$

Numerical values of model uncertainty γ_{Rd} depends on particular conditions and should be derived from previous experience and available experimental data. In particular, the resistance factor γ_{Rd} depends on the construction materials and behavior of the structural member.

As far as the material properties are concerned, the characteristic and design values commonly refer to the values of 5% and 0.1% fractiles, respectively.

In case of Lognormal distribution, commonly considered for random variables describing the material and geometrical properties, the following expression might be used to derive the characteristic and design values of a generic variable with the given probability distribution:

$$X_k = \mu_X \cdot \exp(u_{0.05} \cdot w_X) \tag{6.21}$$

$$X_d = \mu_X \exp(u_p \cdot w_X) \tag{6.22}$$

_____

Where $u_{0.05}$ and u_p are the 5%-fractile and p-fractile of a standardized random variable with a Normal distribution, respectively. For design values of material properties:

$$p = \phi(-\alpha_R \cdot \beta) \tag{6.23}$$

It results that the partial safety factor for the generic variable associated with the material properties is computed as:

$$\gamma_m = \frac{X_k}{X_d} \tag{6.24}$$

Annex D of Eurocode 0(European Committee for Standardization (CEN), 2002) defines further specifications in case the design is assisted by either numerical values or results of proper experimental tests.

Among the different types of tests, category b) of D3 represents those tests carried to obtain specific material properties using specified testing procedures, for instance to test new materials.

For the derivation from tests of the design values for a material property, a model parameter or a resistance should be carried out in one of the following ways:

- by assessing a characteristic value, which is then divided by a partial factor and possibly multiplied (if necessary) by an explicit conversion factor;

- by direct determination of the design value.

In general, the first method is preferred, provided that the partial factor is determined from the normal design procedure. Furthermore, the derivation of the characteristic value from tests should take into account: (i) the scatter of data tests; (ii) statistical uncertainty associated with the number of tests; (iii) prior statistical knowledge.

When evaluating test results, the behavior of test specimens and failure modes should be compared with theoretical predictions. Moreover, the evaluation of test results should be based on statistical methods, with the use of available statistical information about the type of distribution to be used and its associated parameters.

_____

Concerning the statistical determination of a single property, which might represent a resistance of a product or a property contributing to the resistance of a product, detailed procedure is shown in Section D7 of the Annex D of Eurocode 0.

The following assumptions are made:

- all variables follow either Normal or Lognormal distribution;

- there is no prior knowledge about the value of the mean.

In general, Lognormal distribution is preferred for resistance and geometrical variables for the advantage that no negative values can occur.

With Lognormal distribution, the design value can be computed from the characteristic value as:

$$X_d = \eta \cdot \frac{X_k}{\gamma_m} = \frac{\eta}{\gamma_m} \cdot \exp(m_y - k_n \cdot s_y)$$

(6.25)

It should be noted that the procedure follows the coverage method (as presented in Section 6.2.3). The estimations of mean and standard deviation of the test results are computed as:

$$m_y = \frac{1}{n} \cdot \sum_{i=1}^{n} \ln(x_i)$$

(6.26)

$$s_y = \sqrt{\frac{1}{n-1} \cdot \sum_{i=1}^{n} \left(\ln(x_i) - m_y \right)^2}$$

(6.27)

Appropriate value of γ_m should be taken according to the field of application of the test results.

_____

6.3. STATISTICAL DISTRIBUTION OF THE KEY MATERIAL PROPERTIES

6.3.1. The key material properties for WAAM stainless steel

Considering the specific case of WAAM 308LSi stainless steel element as characterized in Section 4, the following variables are considered for structural design applications:

- f_y : yielding stress, corresponding to $R_{p,02}$ from experimental tests;

- f_t : ultimate tensile strength, corresponding to *UTS* from experimental tests;

- E : Young's modulus.

While values of yielding and ultimate tensile strength are commonly considered random variables also for traditionally-manufactured stainless steel structural elements, additional considerations upon Young's modulus should be made for WAAM-produced elements. Indeed, as also considered in Section 4.3, the Young's modulus cannot be considered as a deterministic value for WAAM-produced stainless steel, as it is affected by a certain variability, and additionally is highly influenced on the direction of the element with respect to the printing deposition.

6.3.2. Best-fit statistical distributions

From the experimental results on WAAM stainless steel as presented in Section 4, a statistical analysis of the yielding and ultimate stress is carried out deriving the best-fit distribution of Normal, Weibull and Lognormal according to the maximum likelihood estimators. The distributions are estimated on the results from the tensile tests on machined specimens (presented in Section 4.3). Indeed, the tests on machined specimens provide basic information on the material properties having the material itself as the only source of uncertainty.

Figures 6.2, 6.3 and 6.4 provide a comparison between experimental and best-fit cumulative distribution functions (CDF) and probability density functions (PDF) as obtained for yielding stress (estimate as 0.2% proof stress), ultimate tensile strength and Young's modulus. The distributions have been estimated differentiating the three main orientations investigated, i.e.

_____

_____

transversal (T), longitudinal (L) and diagonal (D). The mean values (μ), standard deviations (σ) and coefficients of variation (w) of the best-fit distributions are summarized in Table 6.1.
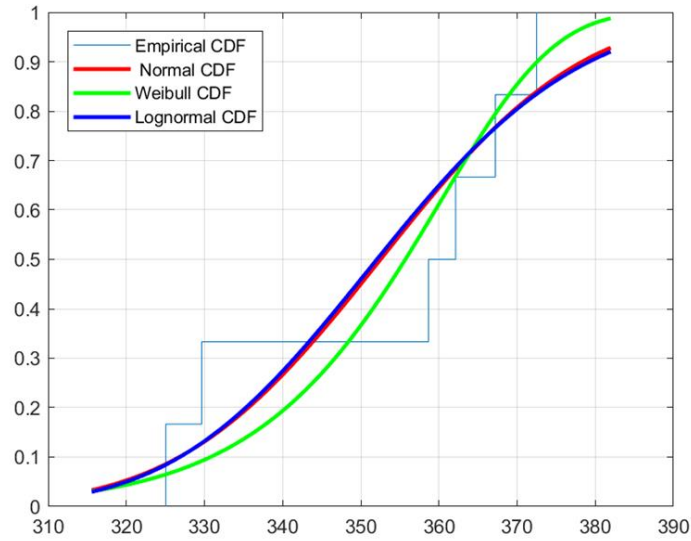
(a)
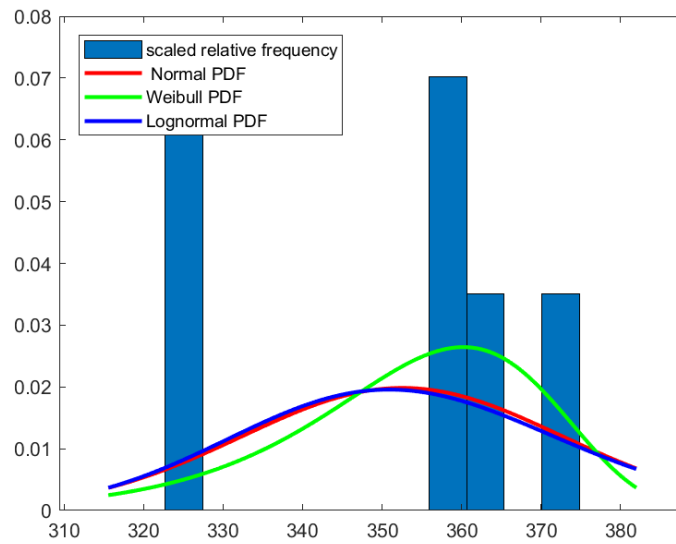
(b)

_____
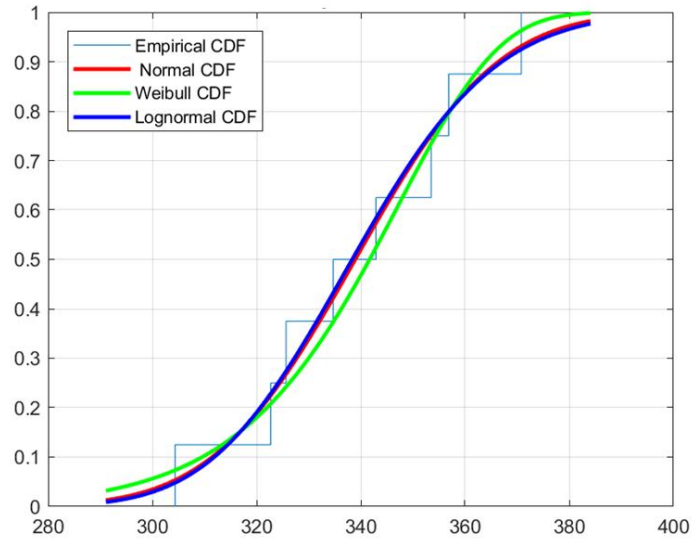
(c)
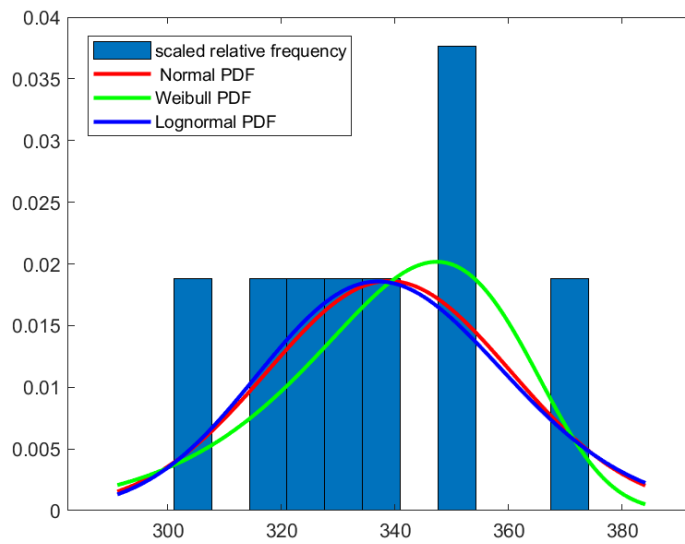
(d)
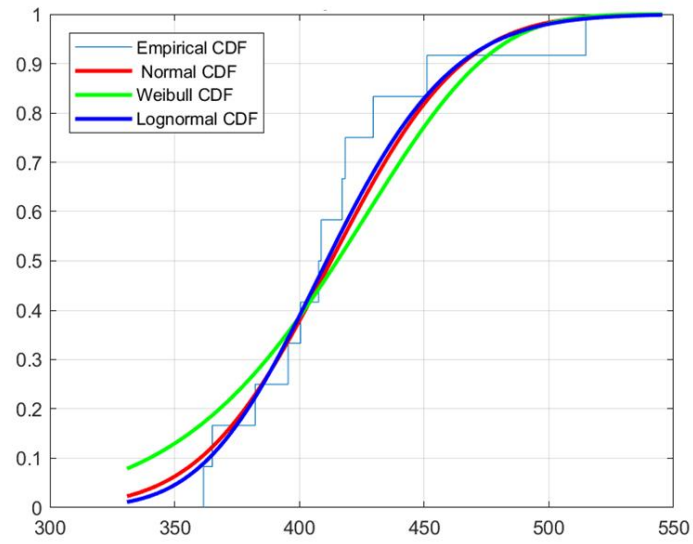
(e)
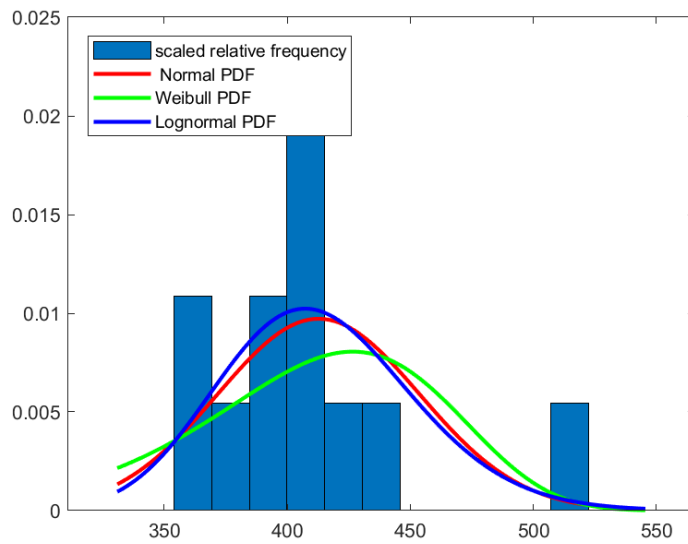
(f)

Figure 6.2: Statistical distributions of yielding stress values: (a) CDF and (b) PDF for specimens T; (c) CDF and (d) PDF for specimens L; (e) CDF and (f) PDF for specimens D.
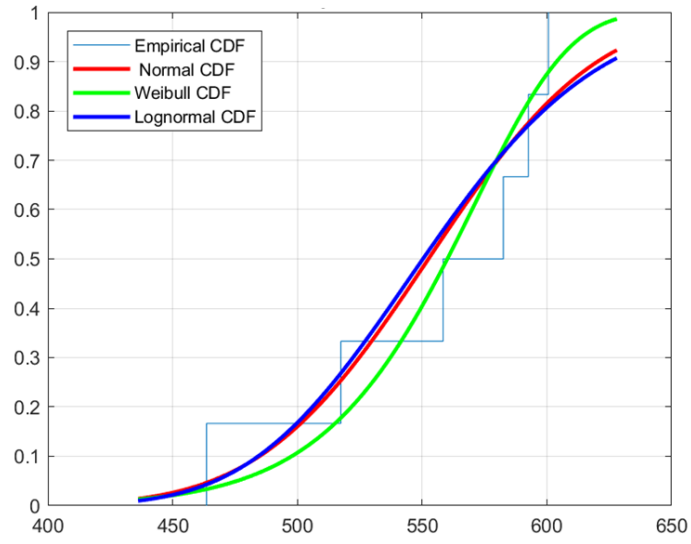
(a)
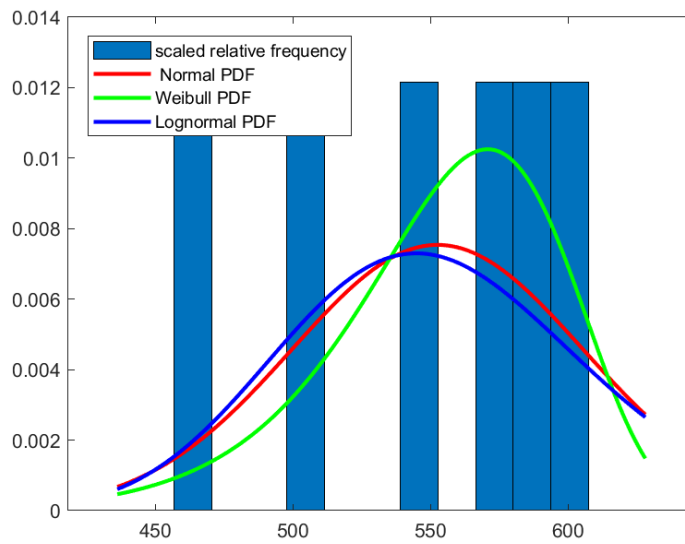
(b)
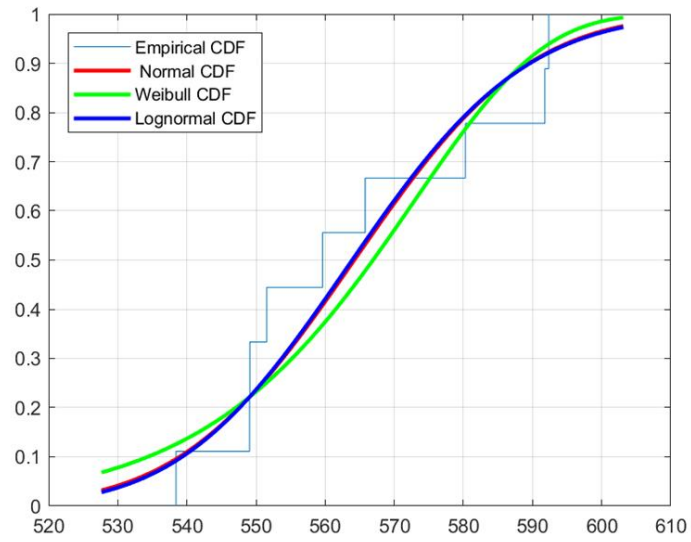
(c)
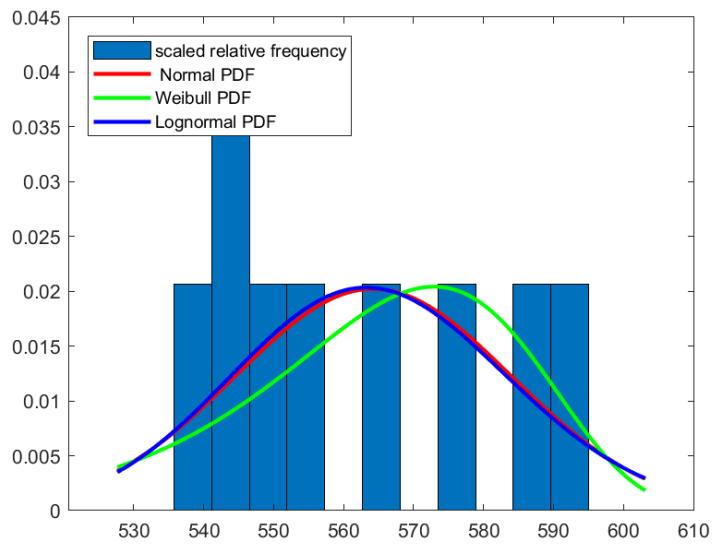
(d)
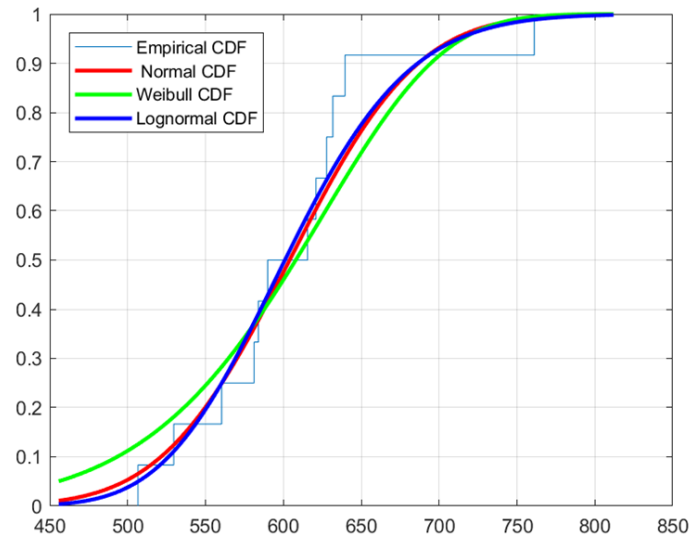
(e)
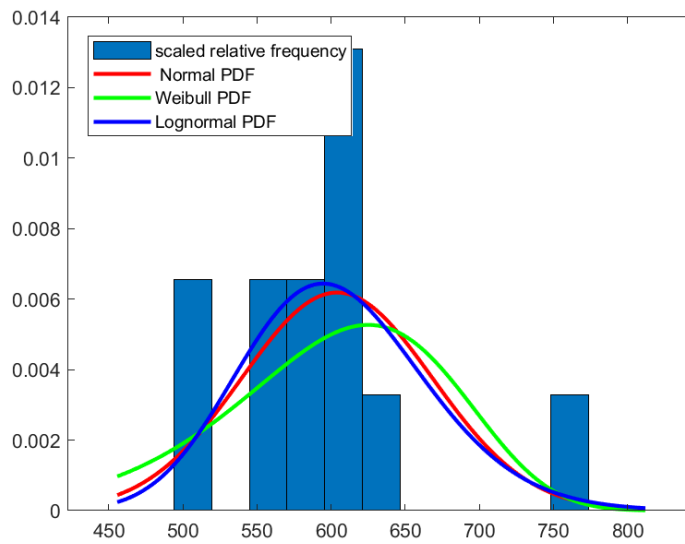
(f)

Figure 6.3: Statistical distributions of ultimate tensile strength values: (a) CDF and (b) PDF for specimens T; (c) CDF and (d) PDF for specimens L; (e) CDF and (f) PDF for specimens D.
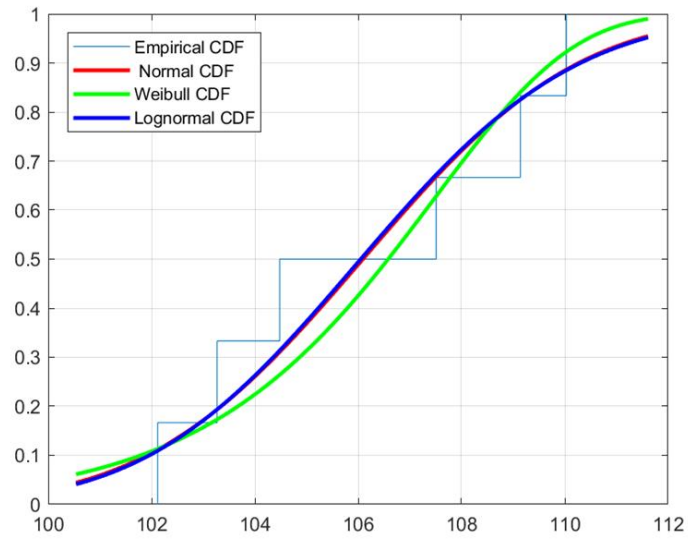
(a)
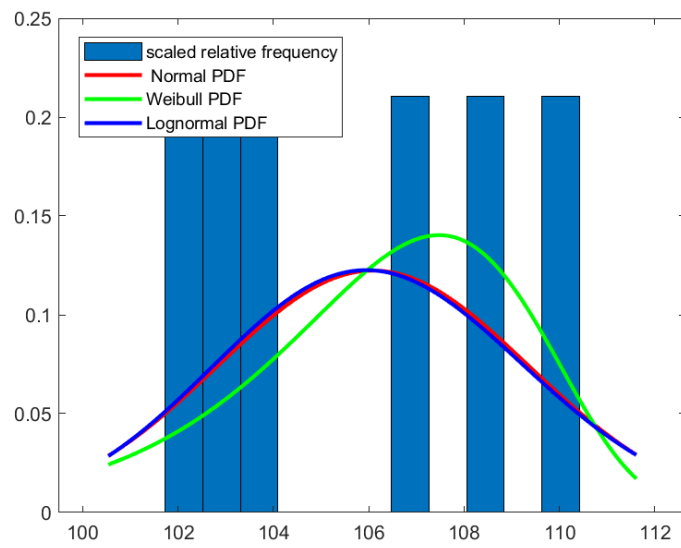
(b)
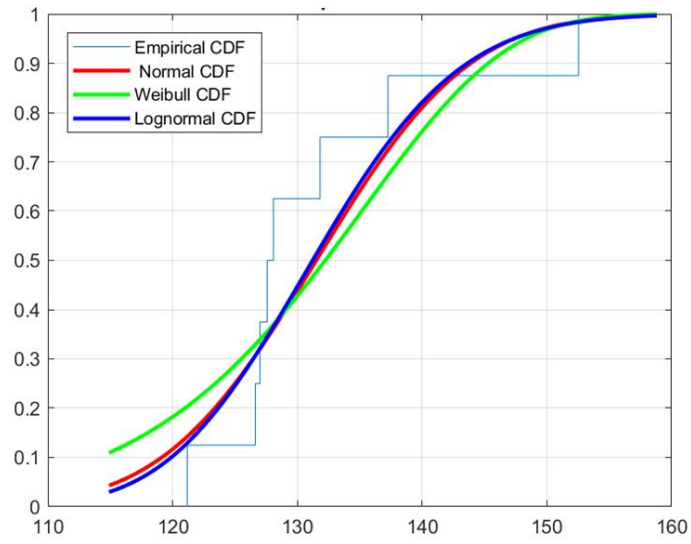
(c)
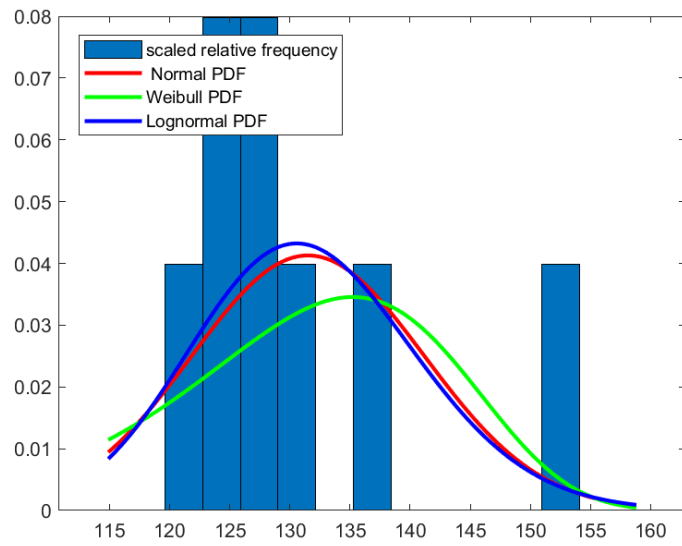
(d)
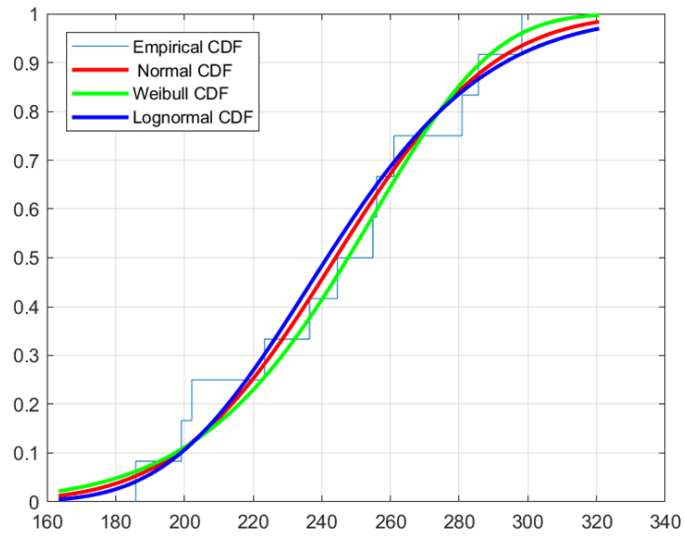
(e)
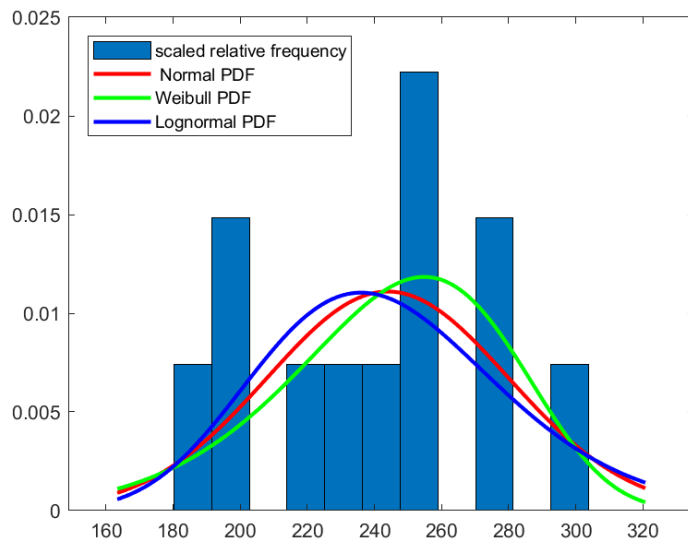
(f)

Figure 6.4: Statistical distributions of Young's modulus values: (a) CDF and (b) PDF for specimens T; (c) CDF and (d) PDF for specimens L; (e) CDF and (f) PDF for specimens D.

Table 6.1: Mean and standard deviation of Normal, Lognormal and Weibull best fit statistical distributions of the mechanical properties of WAAM stainless steel.

		NORMAL			WEIBULL			LOGNORMAL		
		μ_N [MPa]	σ_N [MPa]	w_N [-]	μ_W [MPa]	σ_W [MPa]	w_W [-]	μ_L [MPa]	σ_L [MPa]	w_L [-]
Yielding stress	T	352.54	20.11	0.057	353.24	17.02	0.048	352.65	20.47	0.058
	L	338.94	21.44	0.063	338.69	21.98	0.065	339.04	21.58	0.064
	D	412.71	41.05	0.099	409.59	52.26	0.128	412.83	39.43	0.096
		μ_N [MPa]	σ_N [MPa]	w_N [-]	μ_W [MPa]	σ_W [MPa]	w_W [-]	μ_L [MPa]	σ_L [MPa]	w_L [-]
Ultimate tensile strength	T	552.53	52.91	0.096	554.49	42.77	0.077	553.07	55.33	0.100
	L	564.22	19.73	0.035	563.64	22.22	0.039	564.25	19.64	0.035
	D	604.04	64.48	0.107	599.66	79.58	0.133	604.24	62.77	0.104
		μ_N [GPa]	σ_N [GPa]	w_N [-]	μ_W [GPa]	σ_W [GPa]	w_W [-]	μ_L [GPa]	σ_L [GPa]	w_L [-]
Young's modulus	T	106.09	3.26	0.031	106.08	3.26	0.031	106.10	3.26	0.031
	L	131.51	9.66	0.073	130.71	12.49	0.096	131.55	9.29	0.071
	D	244.00	35.95	0.147	244.18	35.12	0.144	244.29	37.17	0.152

It should be noted that the dimension of the samples size, although small, is in accordance with the minimum recommended dimension according to Annexes C and D of Eurocode 0 to perform calibration from experiments, as long as specific values of correction factors (as reported in the provisions) are adopted. The choice of the distribution models has been made according to the indications provided in Annex C and D of Eurocode 0 for strength data.

Overall, it should be noted that the coefficients of variation for both yielding stress and ultimate strength of all three distributions are within 2% and 10%, and in line with ranges obtained for traditionally-manufactured steel elements used in construction (Ballio & Mazzolani, 1979).

Table 6.2 provides the results of Kolmogorov-Smirnov test in terms of coefficient KS (Massey, 1951) of the best-fit distributions evaluated from maximum likelihood estimators for the experimental data. The obtained KS values range between 0.12 to 0.29. The critical values for $\alpha=0.05$ are: 0.519 for T specimens, 0.454 for L specimens and 0.375 for D specimens.

Overall, the results provide lower values than the critical, thus suggesting that all three distributions provide a good fit with the experimental results. Among the three distributions, the Lognormal distributions provide slightly smaller values of coefficient KS (the average KS value for the Lognormal distributions is around 0.2).

Thus, in the next section the Lognormal distributions will be considered to calibrate the design values. This is also in accordance with the recommendations provided in Eurocode 0 for calibration of design values for strength.

Table 6.2: Kolmogorov-Smirnov test of the Normal, Weibull and Lognormal best fit statistical distributions.

		Kolmogorov-Smirnov test		
		KS_N [-]	KS_W [-]	KS_L [-]
Yielding stress	T	0.2863	0.2432	0.2923
	L	0.1265	0.1329	0.1294
	D	0.1951	0.2248	0.1756
Ultimate tensile strength	T	0.2147	0.2265	0.2248
	L	0.1838	0.1934	0.1822
	D	0.2072	0.2512	0.1906
Young's modulus	T	0.1895	0.2360	0.1863
	L	0.2638	0.2639	0.2595
	D	0.1277	0.1285	0.1393

_____

6.4. DESIGN VALUES OF YIELDING AND ULTIMATE STRESSES

6.4.1. Calibration based on the statistical distributions

From best-fit statistical distributions as evaluated in Section 6.3, the fractiles corresponding to the characteristic and design values of yielding and ultimate stresses have been computed. From their ratio, the estimation of the partial factor of safety is evaluated as well.

According to the fundamental principles of reliability analysis as presented in Eurocode 0 and described in Section 6.2, the following fractiles of the random variable associated to the strength parameters are considered:

- 5%-percentile of the distribution, corresponding to the characteristic value;

- 0.1%-percentile of the distribution, corresponding to the design value.

It should be noted that the material partial safety factor for yielding stress γ_{m1} is to be compared with the value of partial factor recommended in Eurocode 3 (EN1993:1-4) for resistance of cross-sections to excessive yielding realized in stainless steel, equal to $\gamma_{M0}=1.10$. Similarly, the material partial safety factor calibrated on the ultimate tensile strength γ_{m2} should be compared to the partial factor recommended in Eurocode 3 for resistance of cross-sections in tension to fracture realized in stainless steel, equal to $\gamma_{M2}=1.25$.

6.4.2. Calibration according to Eurocode 0

As reported in Section 6.2.4, the European standard provisions (European Committee for Standardization (CEN), 2002) give a simplified formulation to evaluate the characteristic value of a population of samples ("design from samples", Annex D). Considering a Lognormal distribution, the formulation is the following:

$$X_k = \exp(m_y - k_n \cdot s_y) \tag{6.28}$$

where m_y and s_y are respectively the estimations of mean value and standard deviation taken from the Lognormal distribution of samples, while k_n is a calibrated coefficient which takes into

_____

account the numbers of samples in the population and the type of distribution considered. For a Lognormal distribution, the values of coefficient k_n as suggested by Eurocode 0 are equal to: 2.18 for specimens T (6 samples), 2.00 for specimens L (8 samples) and 1.89 for specimens D (12 samples).

Annex C of Eurocode 0 provides also the formulation to compute the design value of the material property considered, based on the type of distribution and the probability of failure chosen for the design purposes. In the present case, the evaluations have been performed considering a probability of having a more unfavorable value of 10^{-3}, typically assumed when dealing with ultimate limit states, and corresponding to a target reliability index β equal to 3.8.

Therefore, the design value can be evaluated with the following expression:

$$X_d = \mu_X \cdot \exp(-\alpha_R \cdot \beta \cdot w_X) \qquad (6.29)$$

Where μ_X and w_X are the mean and coefficient of variation of the distribution considered, and α_R is the FORM sensitivity factor, usually taken equal to 0.8 for design resistances.

Thus, the partial factor for safety of the considered material property can be estimated as the ratio between the computed characteristic and design values as follows:

$$\gamma_m = \frac{X_k}{X_d} \qquad (6.30)$$

6.4.3. Comparison of the results from calibration

Table 6.3 provides an overview of the results of calibration according to Eurocode 0, compared with the values of fractiles as evaluated from statistical distribution of the experimental results, as from Section 6.3.

Table 6.3: Overview of results of calibration of design values for WAAM stainless steel.

		5% and 0.1% fractiles from statistical distribution			Characteristic value, design value and safety factors according to EC0			EC3 recommendations for partial safety factors
		$f_{y,5\%}$	$f_{y,0.1\%}$	$f_{y,5\%}/f_{y,0.1\%}$	f_{yk}	f_{yd}	γ_{m1}	
Yielding stress [MPa]	T	321	296	1.08	310	301	1.03	1.10
	L	305	279	1.09	297	283	1.05	
	D	353	309	1.14	343	309	1.11	
		$f_{t,5\%}$	$f_{t,0.1\%}$	$f_{t,5\%}/f_{t,0.1\%}$	f_{tk}	f_{td}	γ_{m2}	
Ultimate tensile strength [MPa]	T	469	408	1.15	443	424	1.05	1.25
	L	533	508	1.05	532	517	1.03	
	D	509	441	1.16	494	443	1.12	

In general, the results indicate a good correspondence between the values of 5% and 0.1% fractiles from the statistical distributions and the characteristic and design values as obtained according to Eurocode 0. In detail, the characteristic values calibrated according to Eurocode 0 are overall lower than the actual 5% fractile taken from the Lognormal distribution which best fits the experimental data. This is due to the fact that for small sample sizes, the use of large values of k_n coefficient results in a characteristic value that corresponds to a fractile smaller than the 5% one. Consequently, in this case the characteristic values get closer to the design values and therefore the corresponding partial safety factors tend to reduce.

The anisotropic behavior with respect to the specimen's orientation is also evidenced by the calibrated characteristic and design values and corresponding partial factors. In particular, as expected, the values of the partial factors (for both yielding and ultimate stress) along the diagonal direction tend to be larger. In any case, the values of partial safety factors suggested by Eurocode 3 are in general, excluding the yielding stress along direction D, larger than those obtained in this study.

6.4.4. Considerations upon Young's modulus

Specific considerations on Young's modulus values are necessary to account for both the large anisotropy along the different orientations and for the intrinsic large variability of the parameter.

_____

Indeed, standard Young's modulus values of stainless steel material exhibit a quite reduced variability that is commonly neglected in the design phase.

For this aim, specific fractiles (namely 0.1%, 5%, 50%, 95% and 99.9% fractiles) have been evaluated from the best-fit statistical distributions considering the three orientations (Table 6.4). The lower-bound and upper-bound fractiles are provided to account for different design requirements for structural elements. Indeed, based on the type of member and the applied load condition, it would be advised in certain cases to have either higher or lower value of Young's modulus to stay on the safe side. Such values represent the extremes to be considered based on the statistical distribution calibrated from experimental data. Clearly, the 0.1% and 99.9% values correspond to the "tail" of the distribution, associated to a very low probability of occurrence. Nonetheless, in specific structural design cases it might be advisable to adopt such extreme values for safer considerations.

Table 6.4: Overview of results of distribution of Young's modulus for WAAM stainless steel.

		Fractiles from statistical distribution				
		$E_{0.1\%}$	$E_{5\%}$	$E_{50\%}$	$E_{95\%}$	$E_{99.9\%}$
Young's modulus [MPa]	T	97	101	106	112	116
	L	106	117	132	148	163
	D	154	190	244	314	388

The values reported in Table 6.4 clearly evidence the anisotropic behavior of Young's modulus with respect to the orientation of the specimen (T, L and D) and intrinsic variability which therefore should be taken into account during the design phase.

_____

6.5. SUMMARY OF SECTION 6

In order to provide first guidelines for the structural design of WAAM stainless steel planar elements, calibration of the design values of the key material properties has been carried out. The procedure referred to as "design from experiments" is reported in Annex D of Eurocode 0. In particular, statistical interpretation of the key material properties (yielding stress, ultimate tensile strength and Young's modulus) has been performed for the three main directions investigated experimentally (T, L and D).

From this, the following considerations can be drawn:

-   For all quantities considered along all directions, the distribution model that best fits the experimental data is the Lognormal, from which the definition of the fractiles for characteristic and design values have been evaluated.

-   The procedure presented in Eurocode 0 provided lower estimations of the characteristic and design values of the material properties with respect to the actual fractiles from the statistical distributions (5% and 0.1% respectively), due to the limited amount of experimental data available.

-   The design values of yielding stress for the three directions vary from 285 MPa to 310 MPa, while those of ultimate tensile strength vary from 425 MPa to 520 MPa. For both parameters, high anisotropic behavior is evaluated and should therefore be considered in the structural design phase.

-   The calibrated partial safety factors for yielding stress vary from 1.03 to 1.11 (in line with the provisions in Eurocode 3 for stainless steel structural elements), and those for ultimate tensile strength from 1.05 to 1.12 (lower than the one suggested in Eurocode 3).

-   Ad-hoc lower and upper bound fractiles of Young's modulus for the three directions have been calibrated for different structural design purposes.

_____

7. Explorations on the topology optimization of WAAM stainless steel planar elements

7.1. OVERVIEW

The WAAM orthotropic material model calibrated in Section 5 can be exploited in topology optimization algorithms to study optimal layouts depending upon the relative printing direction.

Among different structural optimization procedures, a topology optimization (TO) algorithm has been adapted to the design of WAAM planar elements. The algorithm takes into account the particular features of the printed plates (as studied in the previous sections), especially with reference to the variation of stiffness with respect to the relative orientation to the printing direction.

Section 7.2 presents an overview of the TO theory applied to AM processes. Section 7.3 presents an overview of results of simultaneous design of topology and printing orientation of WAAM-produced elements.

_____

7.2. TOPOLOGY OPTIMIZATION ALGORITHM FOR WAAM PLANAR ELEMENTS

7.2.1. Topology optimization theory

Topology optimization (TO) is a powerful design tool to sketch lightweight structural components (Christensen & Klarbring, 2008). TO distributes a prescribed amount of material with the goal of minimizing an objective function, given a set of constraints. The design variable is the point-wise "density" of the material that takes values in the range]0,1] to affect the elastic properties of the material through a suitable interpolation law.

To achieve pure 0-1 solutions, i.e. structures made by "full material" and "void", some methods could be envisaged. Among them, the so-called Solid Isotropic Model with Penalization (SIMP) (M. Zhou & Rozvany, 1991) is a power law interpolation of the elastic modulus that remarkably penalizes intermediate densities of the material. Indeed, it means that intermediate designs are penalized by using an alternative constitutive matrix in Hooke's law, in which the "effective" Young's modulus is $\rho^q E$ (ρ being the density and q the SIMP coefficient). The coefficient q guarantees that for values >1, the optimal solutions of ρ are for extreme values 0 and 1, as for the intermediate ones the stiffness is disproportionately low. Thus, it helps avoiding intermediate zones (not physically acceptable, especially for designs to 3D print).

7.2.2. Topology optimization and additive manufacturing

Lots of efforts are being made by the scientific community towards additive manufacturing (AM) and TO to leverage the full potential of their combined use (Feucht & Lange, 2019; Galjaard et al., 2015a; Li et al., 2020; J. Liu et al., 2018; Meng et al., 2020; Mirzendehdel et al., 2018; Saadlaoui et al., 2017; Zhang et al., 2017).

In many approaches of TO for AM, the build direction is mainly addressed with respect to possible overhang issues. In a layer-by-layer printing process, when the upper layer is not entirely supported by the lower one, additional supports may be requested to sustain overhangs and bridges. Recent literature work focused on the optimal design of supports in layer-by-layer

_____

_____

fabrication process (Allaire & Bogosel, 2018; M Bruggi et al., 2018), and on stage-dependent approaches for topology optimization (Allaire et al., 2017; Amir & Mass, 2018). In general, the build orientation is set a-priori in a topology optimization problem. In the work by Langelaar (Langelaar, 2018) simultaneous part and orientation optimization is performed to achieve optimal layouts that are self-supporting or need for limited amount of support. The recent contribution by Wang et al. (W. Wang et al., 2020) explores flexible fabrication beyond planar layer-by-layer deposition, by investigating the concurrent optimal design of a structure and its fabrication sequence.

The mechanical implications of the material orientation are of primary importance in special classes of optimization problems. Examples of this are topology optimization problems with oriented periodic microstructures (Allaire et al., 2019; Groen & Sigmund, 2018), and of composite optimization (Nikbakt et al., 2018). Among others, the work in (Nomura et al., 2015) addresses the simultaneous design of density and orientation of anisotropic material supporting both continuous and discrete orientation design. In (Peeters et al., 2015) the topology and the fiber angle distribution of two-dimensional composite structures are simultaneously optimized, also showing that different optimal shapes arise in case of quasi-isotropic material and composite laminate. The work in (Matteo Bruggi & Taliercio, 2015) investigates the optimal distribution and orientation of the fiber-reinforcement of strengthen plates adopting a SIMP-based approach, whereas the contribution in (Lee, Kim, & Yoon, 2019) presents an effective formulation for stress-constrained topology optimization using layer-wise theory for composite laminates (Lee, Kim, Kim, et al., 2019). The recent work in (Ranaivomiarana et al., 2019) performs concurrent optimization of spatial distribution and material orientation, by writing the compliance tensor of orthotropic two-dimensional media in terms of polar invariants (Vannucci, 2005) and performing a double minimization of the complementary energy. In all of the above-mentioned approaches, the orientation of the material is an unknown field. Indeed, it can take different values within the part.

7.2.3. The proposed TO algorithm for WAAM planar elements

WAM process commonly adopts a constant build orientation in the fabrication of the same part, with the aim of achieving high quality of the outcomes. On the other hand, as explored in the previous sections, the printing direction highly affects the mechanical response of the printed

_____

part, especially in terms of stiffness. Thus, in order to account for this specific characteristic, the formulated algorithm adopts as design variables not only the density field, but also the printing direction (Figure 7.1).

The algorithm is written as a displacement-constrained minimum weight formulation. The WAAM orthotropic material model as calibrated in Section 5 is adopted to account for the different behavior of the planar element based on the relative printing direction, i.e. the angle between the symmetry axes of the orthotropic alloy and the axes of the reference system of the part. The optimization problem is solved through sequential convex programming. The method is used to compute sensitivity with respect to the unknowns in an efficient way.
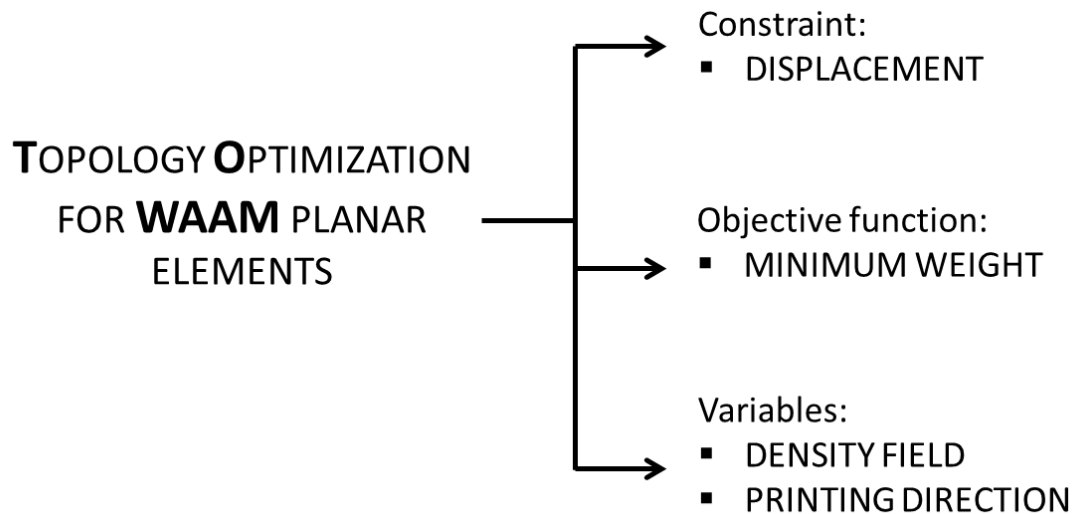
Figure 7.1: Conceptual flowchart of TO algorithm for WAAM elements.

_____

7.3. RESULTS ON THE SIMULTANEOUS DESIGN OF TOPOLOGY AND PRINTING ORIENTATION OF WAAM-PRODUCED ELEMENTS

7.3.1. Numerical implementation

The design of optimized structural elements for WAAM is formulated as a displacement-constrained minimum weight problem. Further details on the implementation can be found in (Bruggi et al., 2021).

The design examples presented include simulations performed for different sets of prescribed orientations. A displacement-constrained formulation allows investigating optimal layouts by enforcing requirements at the serviceability limit state. The amount of material needed to meet this requirement is an outcome of the problem. This is used to perform comparisons when different assumptions are made concerning the modeling/orientation of the WAAM material for the same example.

In the design examples presented the controlled displacement is the one at the loaded point along the direction of the applied force. The scalar product of the controlled displacement and the applied force provides the work of the external load at equilibrium, i.e. the compliance. Hence, the proposed problem is a compliance-constrained minimum weight problem, which is in turn equivalent to a classical weight-constrained minimum compliance problem. The same solution (up to scaling) is expected to arise when considering either problem (Achtziger, 1997), meaning that both formulations can be used to investigate the lightweight design of stiff structural elements.

The formulation for the simultaneous design of topology and orientation of the material is briefly presented hereafter.

A finite element discretization of a given design domain is operated, employing standard four-node displacement-based elements. A set of element-wise discrete design variables is considered. In the e-th of the n elements of the mesh, $0 \le \rho_e \le 1$ is a variable that controls the "density" of the orthotropic material. Additionally, the variable θ governs the orientation of the material (see Section 5). The angle θ is set to remain the same throughout the design domain because it is

_____

_____

assumed that the printing direction does not change during the fabrication process. The range $0 \leq \theta \leq 180°$ is used for the side constraints of this variable. It must be remarked that θ governs the (counterclockwise) rotation of the axis x_1 of the general reference system with respect to the axis of the material reference system. Assuming that the design domain is described in the general reference system Ox_1x_2, the orientation of the printed layers with respect to the axis x_1 is given by a (counterclockwise) rotation of this axis equal to $\alpha = 180° - \theta$, see Figure 7.2.
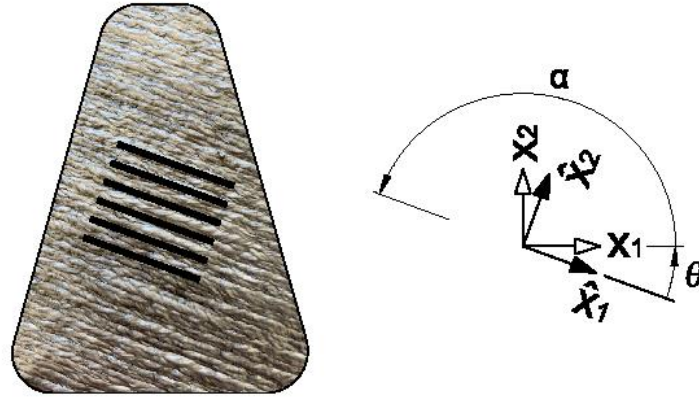
Figure 7.2: Orientation of the printed layers with respect to α.

The Solid Isotropic Material with Penalization (SIMP), extensively used in topology optimization (Bendsoe & Kikuchi, 1988), is modified to handle the orthotropic media as follows (Briccola & Bruggi, 2019; Lee, Kim, & Yoon, 2019). Due to the adopted finite element implementation, the direct form of the constitutive law is considered: $\sigma = C^{-1} \cdot \varepsilon$.

A problem for the simultaneous design of topology and orientation of the WAAM material can be stated as:

$$
\begin{cases}
\min_{0 < \rho_e \leq 1, 0 \leq \theta \leq 180°} w = \sum_{e=1}^{n} \rho_e \cdot W_{0,e} \\[2mm]
\text{s.t. } K(\rho,\theta) \cdot U = \left(\sum_{e=1}^{n} \rho_e^p \cdot K_{0,e}(\theta) \right) \cdot U = F \\[2mm]
u_a \leq u_{\lim}
\end{cases}
\tag{7.1}
$$

_____

In the above statement, the objective function is the weight of the structural element, which is computed through the sum of the element contributions $\rho_e \cdot W_{0,e}$, being $W_{0,e}$ the weight of one element for $\rho_e = 1$. The second equation prescribes the discrete equilibrium of the structural element. The global stiffness matrix $K(\rho, \theta)$ is computed by assembling the element contributions that account for the constitutive law (calibrated in Section 5). The element stiffness matrix can be conveniently written as $\rho_e^p \cdot K_{0,e}(\theta)$, where $K_{0,e}(\theta)$ refers to one element for $\rho_e = 1$. The load vector F allows to compute the nodal displacement vector U under the effect of a given point load acting along x_1 and x_2. The scalar quantity u_a stands for the displacement computed at the loaded node in the direction of the applied force. It may be written as:

$$u_a = L^T \cdot U \tag{7.2}$$

Where L is a vector made of zeros except for the entry referring to the relevant displacement degree of freedom of the loaded node, which takes unitary value. The third equation enforces a prescribed limit u_{lim} to u_a. $u_{lim} \geq u_0$ stands for the maximum displacement allowed at the serviceability limit state, where u_0 is the displacement computed for the design domain made of full material with layers oriented in the most favorable direction. Eq.7.1 can be used to explore more lightweight design by enforcing larger values of u_{lim}. This is equivalent to making an investigation by means of a volume-constrained minimum compliance problem with decreasing volume fraction (lower than 1).

For simplicity, a conventional linear filter (Borrvall & Petersson, 2001; Bourdin, 2001) is implemented on the element variables ρ_e to avoid potential issues related to the arising of mesh dependence and checkerboard patterns (Bendsøe & Sigmund, 2003). The new set of variables ρ_e is plotted for the design examples, to represent the physical "density" of the material in the elements.

The optimization problem in Eq.7.1 is solved via mathematical programming, adopting the Method of Moving Asymptotes (MMA) as minimizer (Svanberg, 1987). MMA is an iterative method that at each iteration provides the updated set of optimization unknowns, i.e. the current values of the element densities ρ_e and the value of the additional variable θ. A structured mesh using square finite elements is used to speed up the computation.

_____

7.3.2. Design examples on planar elements

A set of numerical simulations is presented. For each one of the considered examples, the optimal design achieved for the isotropic grade 304L stainless steel is taken as reference. It should be noted that, in order to properly adopt these results for WAAM applications, further studies related to the printing compatibility of these layouts with WAAM technique should be developed, including considerations on the overhangs, intersections and layer thickness.

At first, optimal solutions using the WAAM orthotropic material (as calibrated in Section 5) are sought by prescribing the direction of the printed layers with respect to the horizontal axis x_1. Figure 7.2 provides polar plots of the Young's modulus of the WAAM stainless steel for different values of the printing orientation, i.e. α=0°, 90°, 45°, 135°. In each diagram, the angular coordinate identifies the direction along which the apparent value of the elastic modulus is given with respect to x_1. The Young's modulus of the isotropic grade 304L stainless steel is reported for comparison.

The formulation of Eq. 7.1 is applied to define, simultaneously, the topology of the material and the direction of the printing layers which provides the most lightweight solution (under the same displacement constraint).

The procedure is initialized with $\rho_e = 1$ for all elements. The iterations stop when the maximum relative change in the value of the discrete design variables is less than 10^{-3}. Due to the non-convexity of the problem, several starting points were considered to assess the achieved solutions. Nonetheless, for all simulations presented, the tested starting guesses did not affect the achieved solutions, except for mirrored layouts (for which the convergence to either of them depends on the initialization of the procedure).

The first example is a cantilever beam with 80 cm x 40 cm rectangular domain (Figure 7.3a). The specimen is subjected to a vertical force $F = 8.33$ kN / mm (of thickness of the WAAM-printed plate), located at the mid-point of the right-hand side. The left-hand side is fully clamped. The allowed displacement is $u_{lim} = 4$ mm. A mesh of squared 0.5 cm x 0.5 cm elements is considered (for a total of 160 x 80 elements). The optimal design for isotropic grade 304L stainless steel (Figure 7.3b) results in a weight equal to $W = 36.34\%$.

(a)   (b)
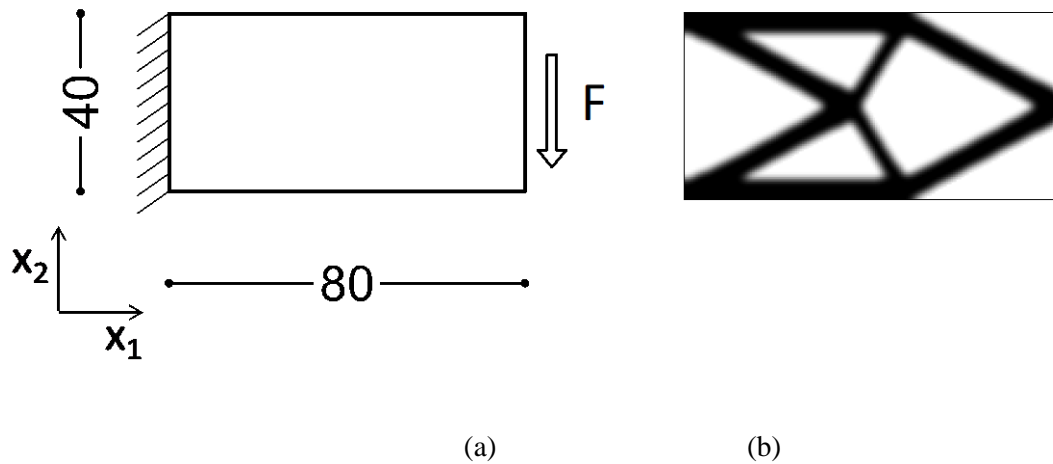
Figure 7.3: (a) Cantilever beam and (b) optimized design for isotropic grade 304L stainless steel.

The optimal design for WAAM orthotropic material for $\alpha = 0°$ (Figure 7.4a) has the same layout as the isotropic case, but an increase of around 15% in weight, equal to $W = 42.06\%$. A totally different layout results for $\alpha = 90°$ (Figure 7.4b), for which the size of the members remarkably increases with respect to the reference design (with a weight of $W = 51.64\%$). This is due to the smaller values of Young's modulus for WAAM orthotropic material model along longitudinal and transversal directions, which resulted in higher members size to enforce the displacement constraint. The optimal layout for $\alpha = 45°$ (Figure 7.4c) is affected by a slight lack of symmetry, due to the different values of Young's modulus for longitudinal and transversal directions (i.e. non-symmetric polar plot for 0° and 90°). Indeed, a mirrored solution is found for $\alpha = 135°$. For both solutions, the weight is equal to $W = 40.52\%$, around 11% more than the reference design.

(a)
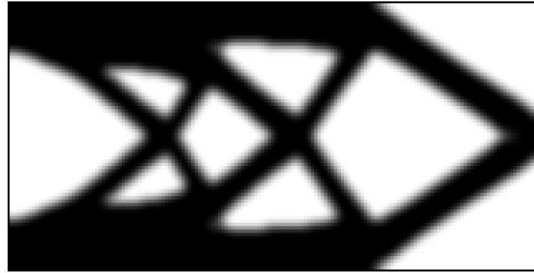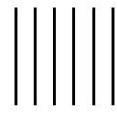
(b)
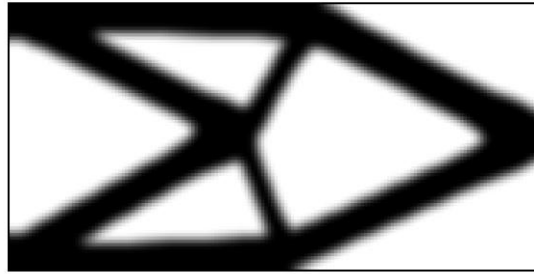
(c)

Figure 7.4: Optimized design of the cantilever beam for WAAM stainless steel: (a) 0°; (b) 90°; (c) 45°.

The simultaneous design of optimal layout and printing orientation found two mirrored solutions (depending on the initial guess to initialize the optimization). The weight at convergence is $W = 39.58\%$, only 9% more than the reference design. The orientation of the materials is $\alpha = 90 \pm 60.5°$ (Figure 7.5). For these solutions, the lack of symmetry is even more evident.
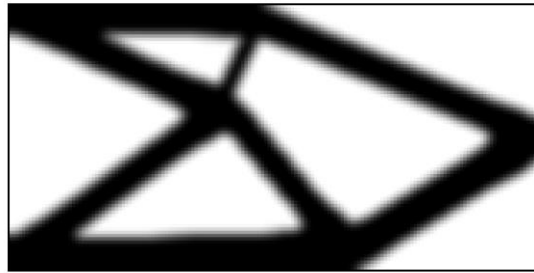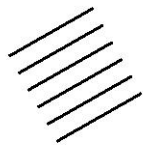
(a)

_____

(b)

Figure 7.5: Optimized layout and printing orientation of the cantilever beam for WAAM stainless steel: (a) 29.5°; (b) 150.5°.

Figure 7.6 presents a comparison of the reference optimal design for grade 304L isotropic material (blue dotted line) and the one achieved for WAAM orthotropic material for $\alpha = 150.5°$ (red line). Very little difference is found in terms of cross-sections, whereas the major difference lies upon the position of the three unrestrained and unloaded nodes of the truss-like structure, with consequent re-orientation of its members.
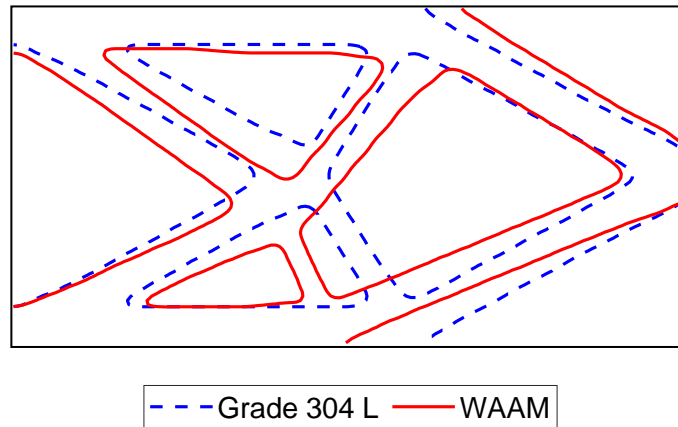
--- Grade 304 L —— WAAM

Figure 7.6: Comparison of the two optimal designs of the cantilever beam for isotropic grade 304L and WAAM stainless steel.

The second example is a simply-supported beam with 160 cm x 40 cm rectangular domain (Figure 7.7a). The specimen is subjected to a vertical force $F = 6.66$ kN/mm /of thickness of WAAM-printed plate) located at the mid-point of the upper side, whereas it is simply-supported at the extreme points of the lower side. The allowed displacement is $u_{lim} = 1$ mm. A mesh composed of squared 0.5 cm x 0.5 cm elements is used (i.e. a total of 320 x 80 elements is used).

The optimal design for grade 304L isotropic stainless steel (Figure 7.7b) is a truss-like structure with arcuated top chord. The total weight at convergence is $W = 37.96\%$.

(a)   (b)
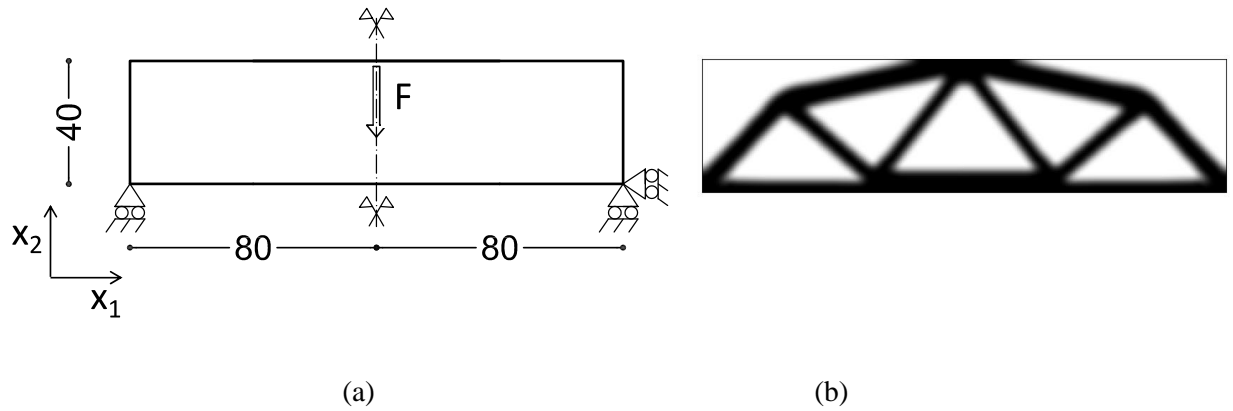
Figure 7.7: (a) Simply-supported beam and (b) optimized design for isotropic grade 304L stainless steel.

The solutions for $\alpha = 0°$ (Figure 7.8a) and $\alpha = 90°$ (Figure 7.8b) present the same number of elements as the reference design, but slightly higher weight ($W = 45.21\%$ and 51.02% respectively). The main difference in the design is that the top chord for both orientations is horizontal and both top and bottom chords are thicker, due to the lower values of Young's modulus at longitudinal and transversal directions with respect to traditionally-manufactured stainless steel.

The optimal design for $\alpha = 45°$ (Figure 7.8c) has a weight of $W = 41.93\%$, which is only 10% more than the reference design. The design presents an arcuated top chord, with higher number of members and loss of symmetry. A mirrored solution can be found for $\alpha = 135°$ (Figure 7.8d).

(a)

(b)

(c)

(d)
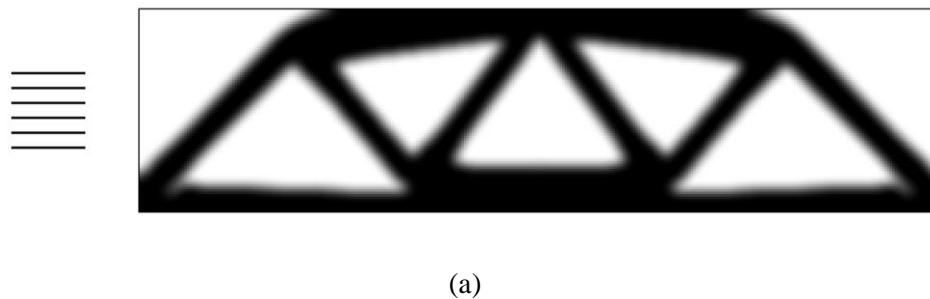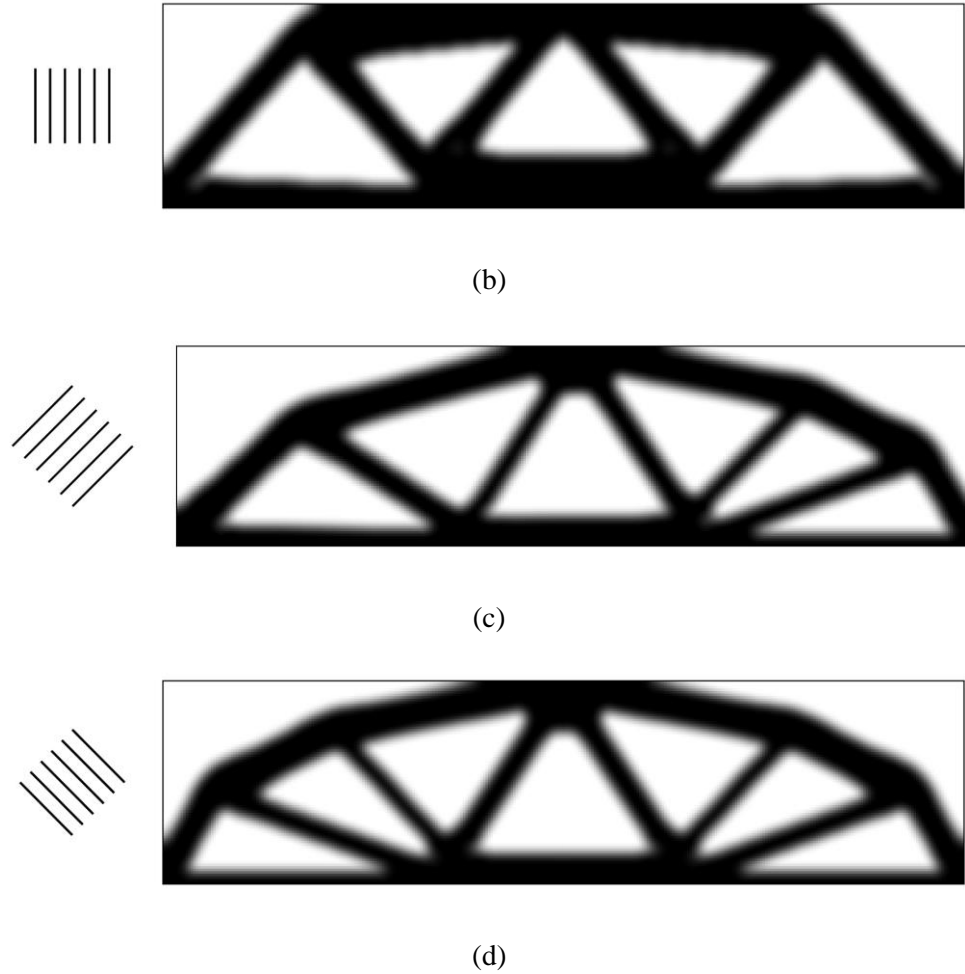
Figure 7.8: Optimized design of the simply-supported beam for WAAM stainless steel: (a) 0°; (b) 90°; (c) 45°; (d) 135°.

The simultaneous design of optimal layout and printing direction detected a minimum weight solution for $\alpha = 90 \pm 56.5°$ (Figure 7.9), with a weight of $W = 41.09\%$, around 8% more than the reference design. Again, in this case the loss of symmetry is even more visible.

(a)
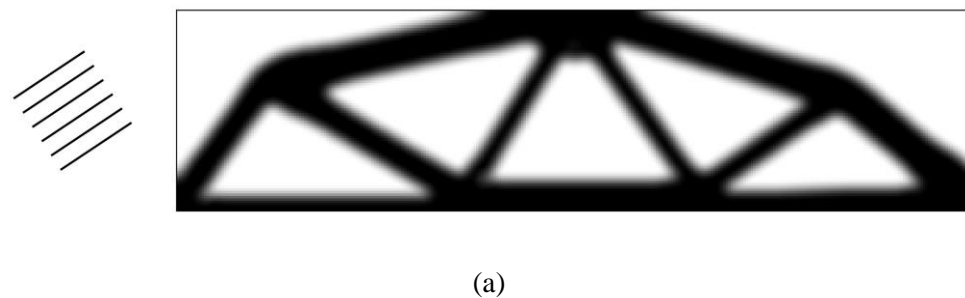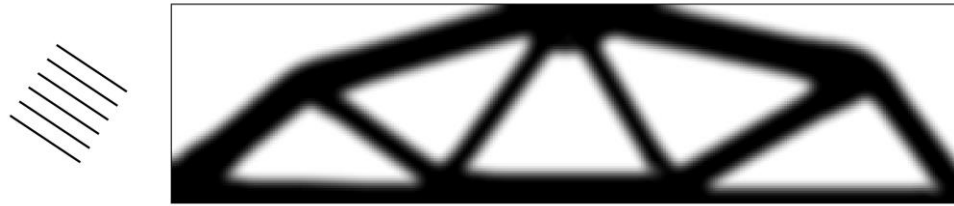
(b)

Figure 7.9: Optimized layout and printing orientation of the simply-supported beam for WAAM stainless steel: (a) 33.5°; (b) 146.5°.

Figure 7.10 compares the solutions found for the isotropic grade 304L stainless steel (blue dotted line) and the optimal design found for $\alpha = 146.5°$ (red line). Apart from the lack of symmetry for the latter design, the two solutions are quite similar in terms of topology. They slightly differ for the members size and the coordinates of the unrestrained and unloaded nodes (especially those of the top chord).
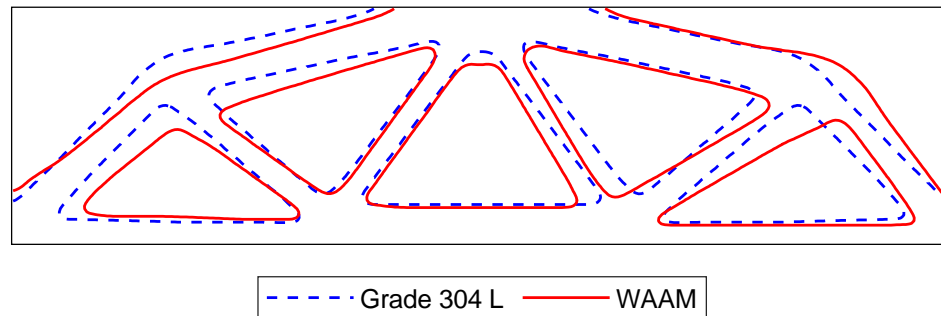
Figure 7.10: Comparison of the two optimal designs of the simply-supported beam for isotropic grade 304L and WAAM stainless steel.

Simultaneous design of layout and printed orientation is calculated also for a stricter displacement constraint, i.e. for $u_{lim} = 0.75$ mm. The minimum weight is achieved for orientations $\alpha = 90 \pm 54.5°$, only 2° of difference from the previous solution (Figure 7.11a). The same algorithm has been adopted for $u_{lim} = 0.60$ mm. In this case, the final layout is thicker and more branched than for the previous cases, and the optimal printed orientation is found at $\alpha = 90 \pm 48.5°$ (Figure 7.11b), with 8° difference from the solution with $u_{lim} = 1$ mm. Thus, the observed change in geometry is directly related with a non-negligible re-orientation of the printed layers.

(a)

(b)
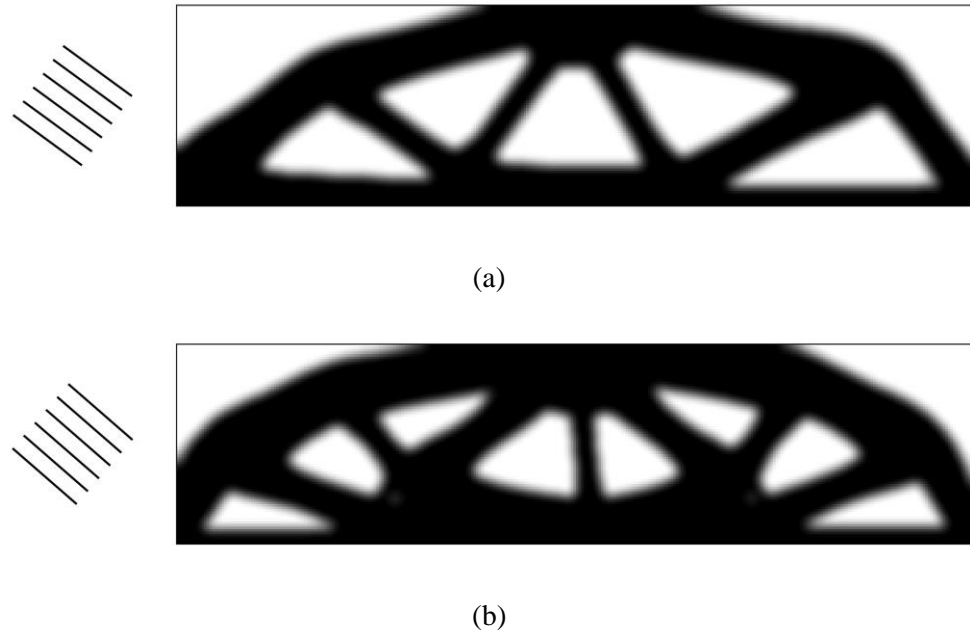
Figure 7.11: Optimized layout and printing orientation of the simply-supported beam for WAAM stainless steel: (a) u_{lim} = 0.75 mm; (b) u_{lim} = 0.60 mm.

7.3.3. Application of the results on a topologically-optimized I-type beam

The results from the 2D simply-supported beam are the starting point for a conscious optimization procedure applied to standardized steel members. For the case of a I-type European IPE beam, the optimized 2D simply-supported beam can be assumed at first approximation as the web of the IPE.

Among the different results presented in the previous section, some considerations need to be drawn to select the most suitable solution:

- The optimized layout printed at $\alpha = 90 \pm 56.5°$ corresponds to the highest reduction in volume (W = 41 %), with however severe asymmetry which might not be easy to implement in structural members;

- The optimized layouts printed at $\alpha = 45°$ and $\alpha = 135°$ have similar volume reduction as for the optimal solution, but results in asymmetric layout and arcuated upper chord, which is not structurally feasible to be applied for support purposes.

_____

Thus, a convenient solution is to adopt the optimized layout for printing orientation $\alpha = 0°$, which corresponds to almost 45% of volume with respect to the standard rectangular shape.

As far as the upper and lower flanges are concerned, the layout is optimized through traditional static analysis. Indeed, the two flanges are subjected to a bending moment acting towards the mid-point of the beam, which is absorbed through compression (of the upper flange) and tension (of the lower flange). Thus, in order to increase the stiffness, the two plates are optimized following a "feather-like" shape, with a quadratic distribution of width, having maximum dimension in the mid-point and minimized at the extremes. Furthermore, the printing orientation is set to maximize the stiffness, hence at 42°, corresponding to the direction of maximum Young's modulus (as presented in Section 5).

Figure 7.12 presents the first example of optimal layout based on a I-type European IPE 180 with 1:6 slenderness (i.e. length of 1080 mm). The web plate is designed with a 4-mm thickness, while the flanges with 8-mm thickness. The final design has a 50% weight reduction, comparable structural performances and higher architectural appeal with respect to the standard IPE 180. The main advantage of this result with respect to conventional manufacturing lies upon the possibility of fabricating the web and the flanges with different printing directions, thus enhancing the material stiffness while reducing the overall material use.

This example represents the possibility derived from advanced engineering of the printing orientation. Further explorations towards the realization of more complex shapes are currently under development.

Figure 7.12: Optimized I-type beam.

_____

_____

7.4. SUMMARY OF SECTION 7

The present section proposes an ad-hoc numerical procedure for the topology optimization (TO) of WAAM-produced planar elements. In particular, the procedure is based on traditional TO algorithms implemented for WAAM stainless steel, to account for the orthotropic nature (whose model has been calibrated in Section 5).

As such, a simultaneous layout optimization and printing orientation can be suitably estimated for planar elements.

The results evidence the influence of the printing orientation on the optimal layouts, with further volume reduction on suitable orientations.

The optimized solutions for 2D simply-supported beam are then applied for the case of a I-type beam. Indeed, the web corresponds to the most suitable solution of the 2D case, while the flanges are shaped based on traditional static analysis considerations.

The proposed tool can be conveniently used to save weight by adopting WAAM process to create customized optimal solutions for any design domain, load conditions and restraint configurations. Further explorations on more complex shapes are currently under development.

_____

8. Comparison of the results with current literature review

8.1. OVERVIEW

The research interest on Wire-and-Arc Additive Manufacturing technology is growing exponentially, although still limited to few application fields. In the last few years, researchers have tried to characterize the WAAM alloys in terms of mechanical and microstructural analyses. Very recently, the interest has been growing towards possible correlations of the specific mechanical properties and the microstructural features of the printed outcomes. However, still limited work has been done to fully comprehend and assess the features of WAAM material, especially referring to stainless steel.

Section 8.2 presents an overview of the results present in literature devoted to the characterization of the anisotropic behavior of WAAM stainless steel. Section 8.3 presents few works devoted to the characterization of the geometrical irregularities of WAAM pieces, while Section 8.4 addresses some design procedures proposed by the researchers at Imperial College London for the verification of WAAM-produced structures.

_____

8.2. COMPARISON ON THE MATERIAL PROPERTIES OF WAAM STAINLESS STEEL PLATES

In the last few years, some researchers focused on the microstructural and mechanical features of WAAM-produced steel, which resulted in a marked anisotropy inherent in the produced pieces.

Rafieazad et al. (Rafieazad et al., 2019) studied low-carbon low-alloy steel in terms of microstructural analysis and tensile strength, along two different directions with respect to the deposition layers (either parallel, also referred to as longitudinal, or perpendicular, also referred to as transversal). Ghaffari et al. (Ghaffari et al., 2019) presented the whole stress-strain behavior of low-carbon low-alloy steel produced with WAAM, which resulted in lower elongation at rupture for specimens oriented transversally. Similar results were also presented by Moore et al. (Moore et al., 2019) on steel and stainless steel specimens. In detail, the specimens oriented perpendicular to the deposition layers (transversally) showed lower performances both in terms of hardness, strengths and deformations. Other studies focused on the mechanical behavior of high strength steels in terms of different strain evolution and tensile strength of specimens taken along the two perpendicular directions with respect to the deposition layers (Sun et al., 2020; Yildiz et al., 2020). As far as stainless steel is concerned, Ji et al. (Ji et al., 2017) presented microstructural and mechanical features of 304L steel specimens taken along the two perpendicular directions. Gordon et al. (Gordon et al., 2018) also reported the Young's modulus values for each direction, suggesting an orthotropic elastic behavior of WAAM-produced stainless steel specimens. Very recently, Kyvelou et al. (Kyvelou et al., 2020) presented the results of a microstructural and mechanical characterization of WAAM-produced stainless steel along three different directions, longitudinal (parallel), transversal (perpendicular) and diagonal at 45° with respect to the deposition layers. From them, a marked anisotropic behavior in terms of both stiffness and strength has been registered, confirming the need for proper characterization of the anisotropic mechanical behavior of WAAM-produced stainless steel material.

Table 8.1 summarizes the main mechanical parameters of stainless steel specimens realized with different printing processes and tested at different orientations towards the layer deposition.

Only two papers reported Young's modulus data (Gordon et al., 2018; Kyvelou et al., 2020). In particular, Gordon et al. (Gordon et al., 2018) presented a comparable value both for the L and T direction of about 135 GPa, consistent with the results of the present study. The same considerations can be applied also for the other DED processes reported, even if it is worth

_____

mentioning that in one case (Griffith et al., 2000), also reported in (Ge et al., 2018), a significant anisotropy was found between L and T orientation, being the T one the most penalized, as for the present work. Only Kyvelou et al. (Kyvelou et al., 2020) presented the results for all three directions (L, T and D).

Overall, it can be noted that both 0.2% proof stress and ultimate tensile strength of the WAAM-produced 304L steel is on average higher than the standard requested for the wrought material. The strong difference is represented by the value of the Young's modulus, higher for the D specimens while consistently lower than the one required by the standards in the case of L and T specimens.

Table 8.1: Summary of 304L stainless steel tensile properties from literature review (Ge et al., 2018; Gordon et al., 2018; Griffith et al., 2000; Haden et al., 2017; Ji et al., 2017; Kyvelou et al., 2020), classified according to the type of the process. In the table, LENS stands for Laser Engineered Net Shaped, LMD for Laser Metal Deposition, L-DED Laser-based Direct Energy Deposition.

	Process type	Specimen orientation	E [GPa]	$R_{p0.2}$ [MPa]	UTS [MPa]	$A_{\%}$ [%]	Ref.
WAAM	GMAW	L	126.80	356.02	559.52	25.55	Present work (Section 4)
		T	104.84	351.47	513.14	21.41	
		D	240.86	419.62	607.51	21.88	
	GMAW	L	139	296	524	/	(Gordon et al., 2018)
		T	132	306	499	/	
	GTAW	L	/	231	622	88	(Ji et al., 2017)
		T	/	235	678	57	
	GMAW	L	/	356	612	/	(Haden et al., 2017)
	GMAW	L	143	356	575	40	(Kyvelou et al., 2020)
		T	140	338	554	40	

		D	220	407	626	40	
Other DED	LENS	L	/	448	710	59	(Ge et al., 2018)
		T	/	324	655	70	
	L-DED	L	/	337	609	48	(Ge et al., 2018; Griffith et al., 2000)
		T	/	314	606	56	
	LMD	L	/	337	609	48	(Griffith et al., 2000; Ji et al., 2017)
		T	/	314	606	56	
Wrought	/	/	200	190 - 230	500 - 540	/	(EC3:1-4)
	/	/	195	195 - 205	520	/	(AS/NZS 4673)
	/	/	193.1	247.2 - 275.8	551.6 - 620.6	/	(SEI/ASCE 08-02)

_____

8.3. COMPARISON ON THE GEOMETRICAL IRREGULARITIES OF WAAM STAINLESS STEEL PLATES

WAAM-produced pieces usually require machining to erase the inherent surface roughness and geometrical irregularities, depending on their end applications. Indeed, most of the research on the characterization of WAAM technology refers to machined specimens only.

However, for applications in the construction industry, the adoption of as-built WAAM-produced large scale structural elements would allow for on-site productions and low-cost solutions ready to be implemented in the market.

Kyvelou et al. (Kyvelou et al., 2020) addressed the need for proper characterization of the geometrical irregularities and their influence in the mechanical behavior of WAAM-produced elements. In detail, the measurements of the distribution of thickness along the length of as-built coupons at different orientations with respect to the printing direction were taken with laser scanning acquisition. The results confirmed that the longitudinal specimens were characterized by a more uniform distribution of cross-sections, since their relative orientation is parallel to the deposition layers. On the other hand, transversal coupons presented the highest standard deviation values of thickness distribution.

Rodrigues et al. (Rodrigues et al., 2019) performed a wide experimental investigation on high-strength low-alloy steel (HSLA) by performing different tests on parts produced with different WAAM process parameters. From the macroscopic inspection, it resulted that the samples realized with higher heat input have less surface waviness, because of the good wettability of the layers over the previously deposited ones.

Therefore, the geometrical irregularities proper of WAAM process are highly affected by the process parameters adopted. This suggests the need of detailed investigations for an optimized process that allows for lower geometrical discrepancies of the as-built pieces.

8.4. COMPARISON ON THE DESIGN CONSIDERATIONS OF WAAM STAINLESS STEEL

When designing a WAAM-produced structure or element, it is crucial to first assess the design approach to follow. Buchanan and Gardner addressed this issue in particular with reference to the levels of anisotropy, geometric imperfections and residual stresses proper of WAAM outcomes which are not commonly taken into considerations by existing structural design methods (Buchanan & Gardner, 2019).

One solution is the design by advanced analysis, as adopted for the case of the first metal 3D-printed footbridge, i.e. the MX3D Bridge (Gardner et al., 2020). Indeed, the research group from Imperial College of London performed structural verification by advanced analysis, since the complex geometry of the bridge required the development of a sophisticated geometrically and materially non-linear finite element model as part of the structural verification. This approach, referred to as the "digital twin", allows to perform detailed analyses with reference to both the inherent geometrical aspects (in terms of cross-sectional variability) and proper mechanical properties of the as-built specimens from experimental tests (see Section 3.3).

As an alternative to the advanced modelling approach, a simplified approach based on the existing structural design methods can be adopted (see Section 3.4). Kyvelou et al. (Kyvelou et al., 2020) proposed first design values of the key material properties of WAAM-produced stainless steel planar elements with comparison between machined and as-built coupons. For both types of specimens, the two-stage Ramberg-Osgood expression has been calibrated with reference to the experimental results of specimens taken along three main directions (L, T and D). The mechanical characterization of as-built coupons has been estimated considering effective cross-sections taken from volume measurements, and then compared with detailed measures on the geometrical irregularities from surface roughness with laser scanner acquisition. The effective mechanical parameters (i.e. taken from the tensile tests on as-built specimens) were compared with those taken from machined specimens, and their difference evidenced a reduction in the mechanical parameters for as-built specimens. The same approach has been followed for the present study as well (see Section 3.4).

Table 8.2 reports the ratio for material properties of as-built to machined material from the work by (Kyvelou et al., 2020) with reference to the present work. The results present little lower discrepancy for the case of the experiments presented in Section 4 with respect to those carried out at Imperial College of London. This might be due to: (i) different cooling strategies adopted,

188

_____

(ii) different thickness of the printed plates from which the samples have been extracted. Thus, further investigations on the matter are suggested.

Table 8.2: Summary of effective to machined mechanical properties for WAAM-produced 304L stainless steel.

	Specimen orientation	E_{eff}/E [GPa]	$R_{p0.2,eff}/R_{p,02}$ [MPa]	UTS_{eff}/UTS [MPa]	$A_{\%,eff}/A_{\%}$ [%]
Present work (Section 4)	L	1.02	0.97	0.98	0.85
	T	1.14	0.92	1.01	0.83
(Kyvelou et al., 2020)	L	0.95	0.94	0.96	0.89
	T	0.65	0.77	0.81	0.40
	D	0.88	0.85	0.91	0.70

8.5. SUMMARY OF SECTION 8

The overview of the results from literature review addressed some important remarks:

- Concerning the evaluation of the mechanical properties of WAAM-produced stainless steel, there is still limited work focusing on the anisotropic behavior of the material. Moreover, the few researchers addressing this aspect did not consider the diagonal direction D (at 45° from the printed layers), with the exception of (Kyvelou et al., 2020), whose results confirmed the ones of the present work (as presented in Section 4).

- As far as the geometrical characterization of the inherent irregularities and surface roughness is concerned, only two researchers addressed this issue so far. They both agreed in a need of proper evaluation of the geometrical features of WAAM-produced elements, which might affect their mechanical response.

- Two design procedures have been proposed by the research group of Imperial College London with reference to WAAM-produced stainless steel structures. One refers to the implementation of a "digital twin" to account for both geometrical and material nonlinearities and features proper of the WAAM process. The second one proposes instead a simplified approach by estimating the effective mechanical properties of as-built elements (by adopting effective cross-sections taken from volume measurements and verified through laser scanner). This latter has also been adopted successfully for the present work.

The comparison with current literature review shows the need for further investigation of specific aspects of WAAM-produced structural members, for direct applications in the construction field.

PART B: Wire-and-Arc Additive Manufacturing stainless steel – dot-by-dot printing

9. Introduction to Part B

9.1. BACKGROUND ON DOT-BY-DOT PRINTING

As presented in Part A, the first explorations of WAAM applications in construction were realized with the so-called "*continuous printing*" strategy, through the realization of planar elements with deposition of successive layers of welded metal.

Very recently, a new printing strategy referred to as "*dot-by-dot printing*" has been studied to realize rod-like and lattice elements, through the deposition of successive drops of welded material to realize rods. This innovative strategy could be applied for the realization of lattice structures and diagrid geometries. Moreover, current research is investigating the application of the printed rods as steel reinforcement for innovative concrete structures, either 3D-printed or realized with shotcrete technique (Kloft et al., 2020)

Nonetheless, given the novelty of the printing strategy, at the current state of the art there is no literature work on the mechanical, geometrical and microstructural characterization of the printed samples.

9.2. OBJECTIVES OF PART B

Part B of the doctoral thesis focuses on the so-called "*dot-by-dot printing*" technology of WAAM process as developed by MX3D adopted to create 3D-printed stainless steel structural elements, as for the case of the "Cucuyo" project (*MX3D Webpage*), proof-of-concept of the possibilities of this strategy to create innovative metal lattice structures. The *dot-by-dot printing* strategy consists in fabricating rod-like elements through successive deposition of drops of welded material.

Given the lack of experimental results on the mechanical properties of dot-by-dot rods, it becomes crucial to first investigate the mechanical and geometrical characterization of the printed samples, from which deriving the first guidelines for structural design applications.

From the experimental results, ad-hoc computational design can be developed to realize lattice and diagrid structural elements following topology optimization principles.

9.3. ORGANIZATION OF THE TEXT

The second part of the doctoral thesis presents first studies related to WAAM dot-by-dot printing (Part B).

Section 10 presents an overview of WAAM dot-by-dot printing and the related design issues. Section 11 presents the first results from the experimental characterization of WAAM stainless steel rod-like elements, from the geometrical and mechanical point of view. From these, the design values for structural design of diagrid elements are calibrated in Section 12. Then, the first application of dot-by-dot printing for the realization of a metal 3D printed diagrid column is presented in Section 13. As the dot-by-dot printing strategy is at its pioneering stage, no literature review is reported at the moment on this specific topic.

10. The dot-by-dot printing process

10.1. OVERVIEW

The dot-by-dot printing strategy is an alternative printing solution for WAAM elements to create rods and diagrid elements. As for the continuous printing (presented in part A), the dot-by-dot process presents some design issues to be addressed, in terms of geometrical irregularities and different mechanical properties with respect to the traditionally-manufactured base material.

The present chapter provides an insight on Wire-and-Arc Additive Manufacturing dot-by-dot process (Section 10.2) and the specific design issues related to WAAM dot-by-dot rod-like elements (Section 10.3). The considered approach adopted in this work is presented in Section 10.4.

Figure 10.1: Example of dot-by-dot printing process (*The Method Case*).

10.2. THE PRINTING PROCESS

The dot-by-dot printing strategy is an innovative (and still unexplored) WAAM technique to deposit dots of welding metal on a discontinuous process along one axis (Joosten, 2015; Van Bolderen, 2017). The printed outcome results in a one-dimension rod-like element, having constant nominal diameter (as governed by the welding dot) and longitudinal main axis. The specimens considered have been manufactured by MX3D using a commercially available standard stainless steel welding wire grade ER308LSi (1 mm diameter) supplied by *Oerlikon*. The printing parameters are listed in Table 10.1.

Table 10.1: Printing process parameters.

Process parameters	Details	Value
Deposition power	Current	100 - 140 A
	Arc voltage	18 - 21 V
Speed	Welding spot	0.5 - 1 s
	Wire feed rate	2 - 4 m/min
Distance and angle	Rod diameter	3- 7 mm
	Electrode to layer angle	90°
Wire	Wire grade	ER 308LSi
	Wire diameter	1 mm
Shield gas	Shield gas type	98% Ar, 2%CO_2
	Shield gas flow rate	10-20 L/min

10.3. DESIGN ISSUES OF WAAM DOT-BY-DOT PRINTING

As for the WAAM-produced planar elements studied in part A, the dot-by-dot rods are characterized by their inherent geometrical irregularities, proper of the printed process, and specific mechanical properties which differ from the base material. Therefore, also for the dot-by-dot printed elements both issues need to be properly taken into account and fully characterized for structural design purposes.

However, differently from the WAAM-produced continuously printed plates, the printed rods are characterized by a one-dimension geometry, thus the tests on the machined parts are quite challenging. Moreover, the printed outcomes from this process are expected to be used in their as-built conditions, i.e. without machining.

For these reasons, the design approach for the rod-like elements is devoted to address the effective mechanical properties of the as-built printed outcomes. On the other hand, the one-dimensional geometry of the rods addresses another fundamental issue, which is related to the behavior under compression of the elements. Indeed, given the slender nature of the rods and their irregular geometries, it is crucial to study the buckling behavior of the printed outcomes with reference to the reference code provisions.

Thus, the mechanical characterization (as presented in Section 11) is guided by a first study of the geometrical irregularities of the as-built rods, in terms of cross-section distribution and lack of straightness. From them, the results from both tensile and compression tests are interpreted with reference to the effective mechanical properties of WAAM dot-by-dot stainless steel rods and global imperfection factors.

10.3.1. Inherent geometrical irregularities of WAAM-produced rod elements

Dot-by-dot printed elements are developed along the main axis through successive points of welded material. This results in 1D elements (commonly referred to as "rods") of constant nominal diameter which is directly related to the drop of welding metal. Usually the nominal diameter of the dot-by-dot rods is of 4 to 8 mm. However, with the same principle as the surface roughness generated by the layer-by-layer deposition (as studied in Part A), for dot-by-dot printed rods the successive deposition of drops of welding metal causes a variation of diameter

along the height of the rod which is of the order of around 0.5 mm. Additionally, the deposition process induces also some lack of straightness which should also be studied (Figure 10.2).

Figure 10.2: Close-up views of the surface irregularities proper of WAAM-produced rod elements.

With regards of rod elements realized with dot-by-dot printing strategy, the deposition of successive drops of welded metal results in a non-uniform circular cross-section and non-straight longitudinal axis (formed by the polyline connecting the centroids of each circular cross-section) (Figure 10.3).

The nominal geometry of the digital model is a uniform full cylinder with straight longitudinal axis (coincident with axis z of the cylindrical coordinate system). The geometry is described by the nominal rod length (L_n=250 mm) and the nominal cross-sectional diameter (d_n=6 mm).

However, due to the intrinsic imperfections derived by the specific printing process, the outcome is a solid element with non-uniform circular cross-section varying along its length ($d_{real}=d_{real}(z)$) and non-straight longitudinal axis. At a generic height z_i, the centroid of the cross-section is $c_{real} = c_{real}(z)$.
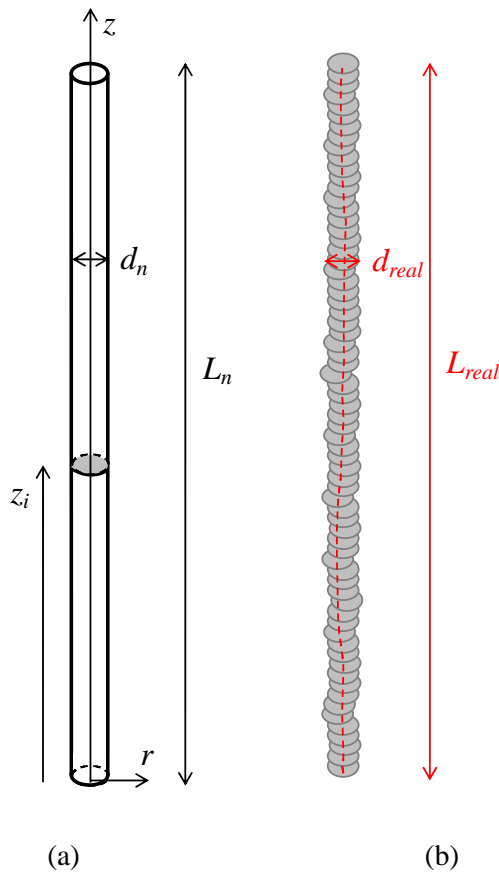
Figure 10.3: Digital model (a) and corresponding printed element (b) of a WAAM-produced rod element.

10.3.2. Anisotropic behavior of WAAM-produced rod elements

As for the continuously-printed WAAM plates (presented in Part A), the possible anisotropic behavior is evaluated also for dot-by-dot printed specimens, for which different inclinations of the rods with respect to the vertical longitudinal axis have been considered.

The rods have been produced in three orientations: (i) with the longitudinal axis aligned along the vertical direction, coincident with the printing direction; (ii) with the longitudinal axis inclined by an angle of 10° with respect to the vertical direction and (iii) with the longitudinal axis inclined by an angle of 45° with respect to the vertical direction (Figure 10.4).
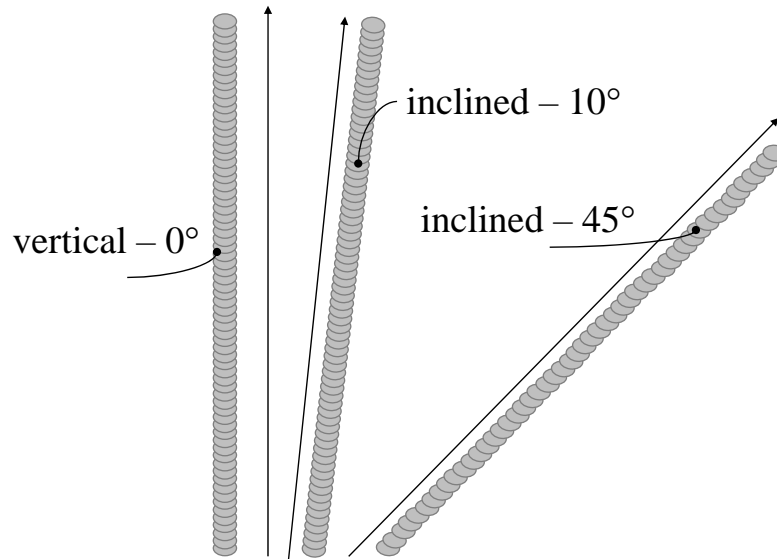
Figure 10.4: Graphical representation of the rod elements printed with three different orientations: vertical at 0° (aligned with the vertical direction of deposition), inclined at 10° and 45° (from the vertical direction of deposition).

_____

10.4.   THE CONSIDERED APPROACH

With reference to the approach adopted in part A for continuously-printed WAAM plates (presented in Section 3), the same considerations have been applied to the dot-by-dot WAAM rods.

The simplified approach adopted for WAAM plates (studied in part A) is transposed for the WAAM rods. The design approach adopted in the study is devoted to separate the two sources of uncertainties (i.e. the one related to the geometrical irregularities and the one proper of the inherent material behavior) from the experimental characterization, and treat them separately to draw design provisions for structural engineering applications.

Indeed, the effective mechanical properties of the printed elements are estimated from the general information on the diameter and cross-sectional area taken from the geometrical characterization of the specimens (Figure 10.5). Detailed studies on the cross-section variability and lack of straightness are also carried out for future works based on advanced modelling approaches.

The mechanical tests are interpreted assuming a constant effective cross-sectional area (as presented in Section 3.4) determined through volume-based measures (Figure 10.5).
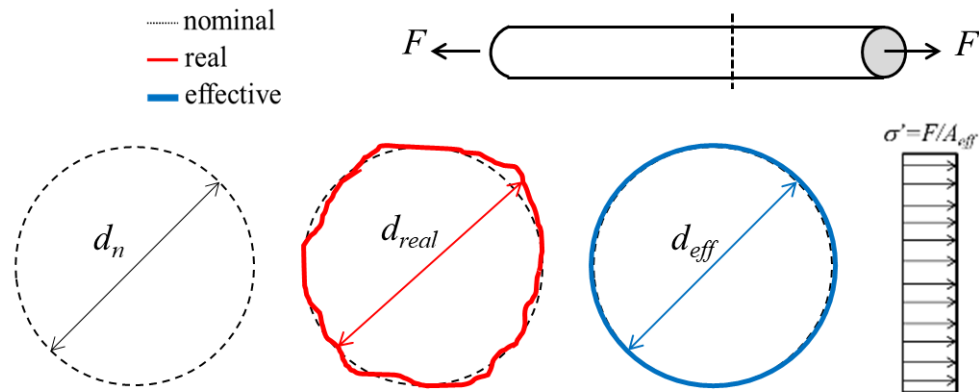
Figure 10.5: Nominal, real and effective thickness for WAAM rod specimen.

These results could then be used to draw general interpretations on the buckling behavior of the printed rods. Nonetheless, more detailed approaches involving 3D scan models of the geometrical imperfections and advanced structural analysis would be required to draw a more detailed interpretation of the overall mechanical behavior (Figure 10.6).
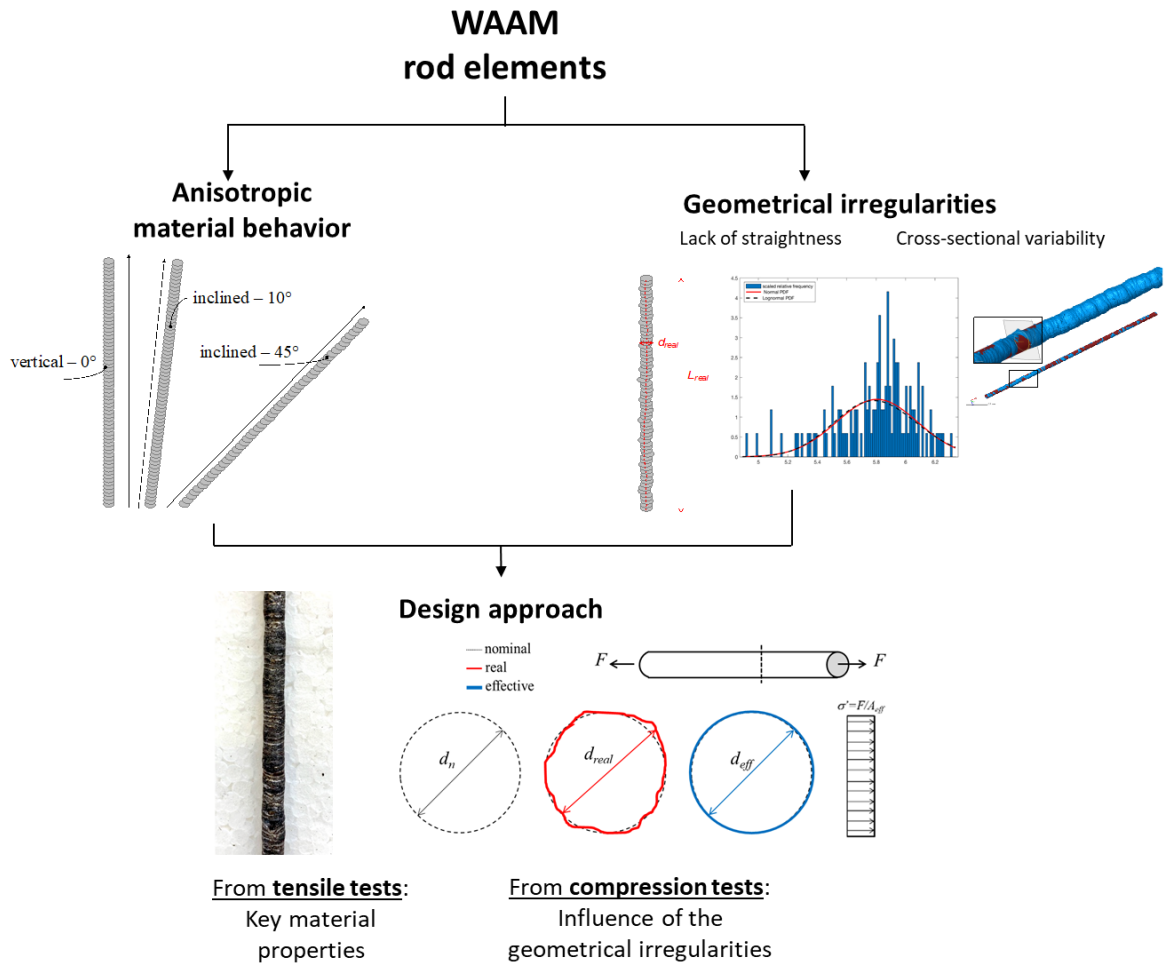
Figure 10.6: Conceptual flowchart of the proposed design approach for WAAM rod elements.

_____

10.5. SUMMARY OF SECTION 10

The chapter briefly introduces the Wire-and-Arc Additive Manufacturing process for dot-by-dot printing of rod elements. The specific printing process parameters adopted to realize the specimens for experimental characterization (as presented in Section 11) have been described. Then, the main design issues for WAAM dot-by-dot rods are addressed, in terms of both geometrical irregularities and different mechanical behavior.

As for the WAAM-produced plates (studied in part A), the same simplified design approach is adopted to estimate the effective mechanical parameters of as-built rods, considering an equivalent constant cross-section from which the main material parameters are derived. Then, the geometrical irregularities are assessed with specific measures and considered for future advanced modelling. The slender nature of the rods suggests the need of proper characterization of also the buckling behavior under compression, which should be studied as well.

11. Experimental characterization of WAAM stainless steel rods

11.1. OVERVIEW

In order to study the overall experimental characterization of WAAM-produced dot-by-dot rod elements, first studies on the geometrical and mechanical characterization have been performed.

Detailed investigation on the inherent geometrical irregularities in terms of cross-sectional variation and lack of straightness has been analyzed through 3D scan acquisition of one rod. Then, general information on the effective cross-sectional area of the rods tested has been acquired through manual and volume measurements (Section 11.3).

Mechanical characterization has been performed through both tensile and compression tests on 6-mm diameter full circular rods (Section 11.4).

_____

11.2.   GEOMETRICAL CHARACTERIZATION ON DOT-BY-DOT RODS

11.2.1. Measurements and equipment

In order to fully characterize the inherent geometrical irregularities of WAAM dot-by-dot rods, detailed and global investigations have been performed through different types of measures.

A detailed investigation on the cross-sectional distribution and lack of straightness proper of dot-by-dot WAAM process has been performed on one specific specimen using 3D scanning technique. The specimen was printed straight (0° angle from vertical direction). From the 3D model, a total of 120 cross-sections along the length of the specimen have been extracted, from which information regarding the cross-sectional diameter and centroid has been analyzed.

The instrument adopted for the 3D scan acquisition is a structured-light projection Artec Spider 3D scanner (*Artec 3D Webpage*), as adopted for the continuously-printed WAAM specimens (presented in Part A). The 3D model of the scanned rod specimen consists of around 40 millions triangular elements, with a medium points spacing of about 0.10 mm. Figure 11.1 shows a view of the entire mesh (blue model) and a zoom of it. The mesh is compared with a uniform cylinder having the dimensions of the digital model used as input in the printing process (red model).
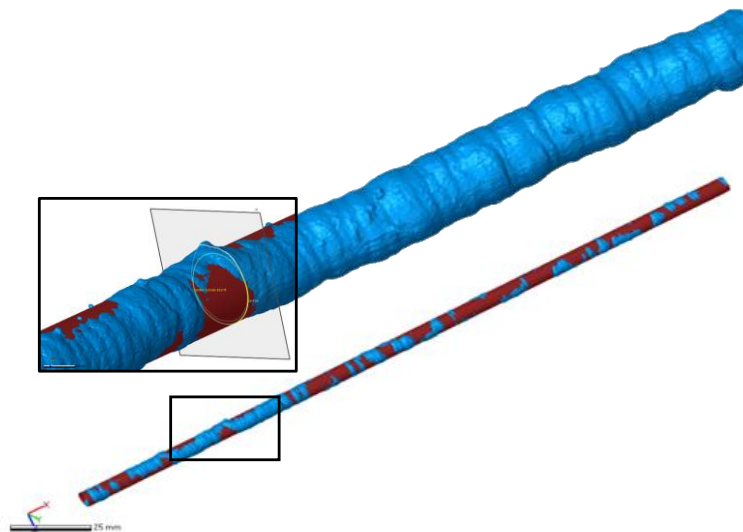
Figure 11.1: 3D model of one dotted 1D specimen and a zoom of it.

The global investigation was carried out on all rods tested both in tensile and compression. The effective cross-sectional area A_{eff} of the specimens has been characterized by means of volume measurements, based on the Archimedes' principle (Gardner et al., 2019; Laghi et al., 2020a), as also adopted in Part A.

11.2.2. Cross-sectional distribution

Given the inherent geometrical variability of the WAAM-produced rods, high-precision 3D scanning acquisition was adopted to evaluate the distribution of cross-sections with respect to the digital input. Indeed, the rods were realized having a full circular cross-section of nominal diameter equal to 6 mm.

Figure 11.2 shows the distribution of the diameter in terms of cumulative frequency (Figure 11.2a) and frequency distribution (Figure 11.2b) as evaluated on 120 cross-sections of the 3D-scan model (in terms of relative frequency scaled to have a unitary bars' area). Both Gaussian Normal and Lognormal distributions seem to fit well the empirical distribution of the diameters measured.
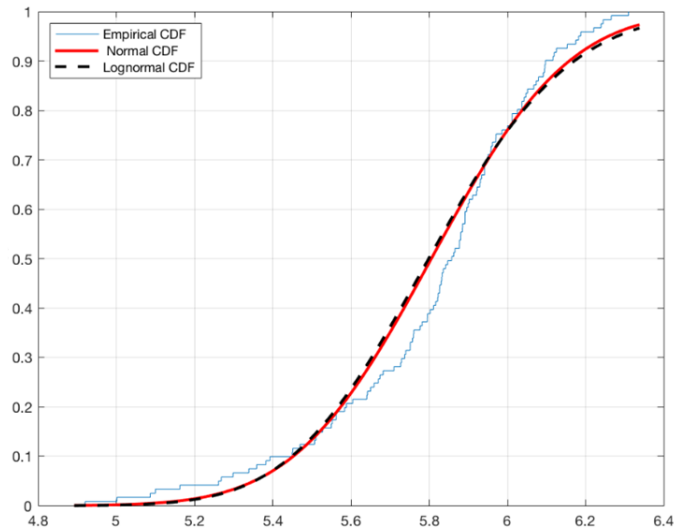
(a)
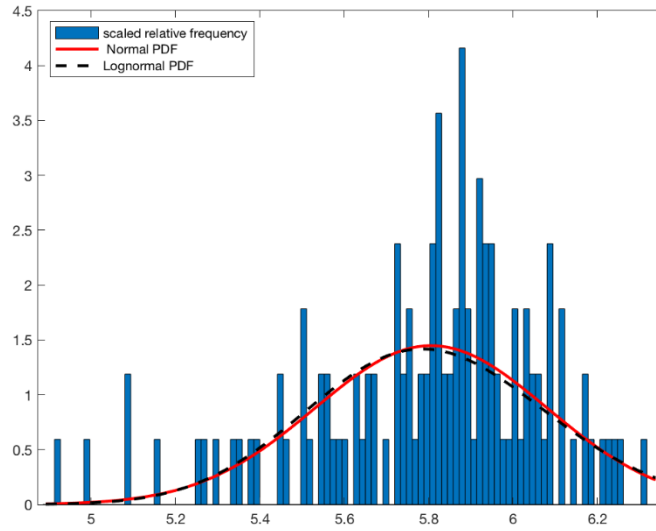
(b)

Figure 11.2: (a) Empirical cumulative distribution and (b) frequency distribution of diameters of a WAAM-produced rod.

The average diameter from the analysis of the 3D scan acquisition is equal to 5.81 mm, resulting in a discrepancy with respect to the nominal value of 3%. The standard deviation results equal to 0.28. The KS test for the Normal and Lognormal distributions provided a coefficient of 0.114 and 0.124, respectively. Thus, the Normal distribution has been considered to best fit the experimental data.

Table 11.1: Statistical parameters of the best-fit distribution of diameter along the 3D-scanned specimen.

Specimen Type	Measurement type	Distribution type	μ_t [mm]	σ_t [mm]
dot-0	3D scanning	Normal	5.80	0.28
		Lognormal	5.80	0.28

In order to correctly interpret the results of the mechanical tests, a volume-equivalent effective cross-section has been considered as the resistant effective area adopted to compute the effective stresses from tensile tests, according to the procedure adopted also for the as-built planar specimens presented in Part A. The values of the effective cross-sectional area have been taken from volume measurements according to Archimedes' principle, according to the design procedure explained in Section 10.4, and also adopted in Part A. The average value of the effective diameter taken over the 40 specimens is 5.80 ± 0.27 mm, substantially equal to the average diameter obtained from 3D scan acquisition (equal to 5.81 mm). It should also be noted that the difference between the effective diameter and the nominal one is in the order of 3% of the nominal value.

11.2.3. Lack-of-straightness

From the 120 cross-sections taken on the 3D model, information regarding the lack of straightness of WAAM-produced rods has been investigated as well. In detail, from each cross-section, the coordinates of the centroid have been extracted both on Cartesian coordinate system (x, y, z) and cylindrical coordinate system (r, θ, z). Figure 11.3 presents the distribution of centroids forming the real longitudinal axis compared to the straight nominal one. Table 11.2 reports maximum, minimum and mean values of coordinates of the centroids measured. A maximum discrepancy of 1.10 mm has been registered on one cross-section, although on average the variation of straightness is of 0.46 mm, corresponding to 0.18% of the total length of the rod.

_____
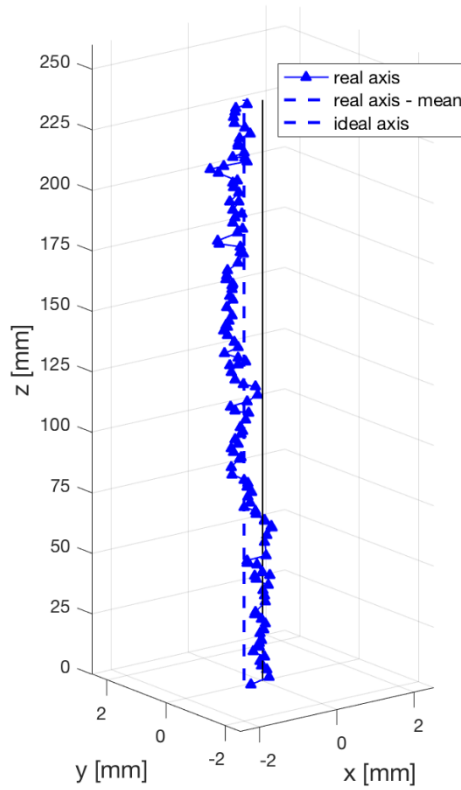
Figure 11.3: Study of straightness of longitudinal axis for a WAAM-produced rod.

Table 11.2: Lack of straightness for a WAAM-produced rod.

Longitudinal axis	$c_{real,x}$ [mm]	$c_{real,y}$ [mm]	$\lvert c_{real,r} \rvert$ [mm]	$c_{real,x}/L$ [%]	$c_{real,y}/L$ [%]	$\lvert c_{real,r} \rvert /L$ [%]
max	0.48	0.84	1.10	0.19	0.33	0.43
min	-0.74	-0.34	0.04	-0.29	-0.13	0.01
μ	**-0.29**	**0.25**	**0.46**	**-0.11**	**0.10**	**0.18**
COV	**0.88**	**0.91**	**0.49**	**/**	**/**	**/**

Figure 11.4 shows the distribution of the centroids in terms of cumulative frequency (Figure 11.4a) and frequency distribution (Figure 11.4b) as evaluated on 120 cross-sections of the 3D scan model (in terms of relative frequency scaled to have a unitary bars' area). In this case, the Normal distribution seem to fit better the empirical distribution of the centroids measured.
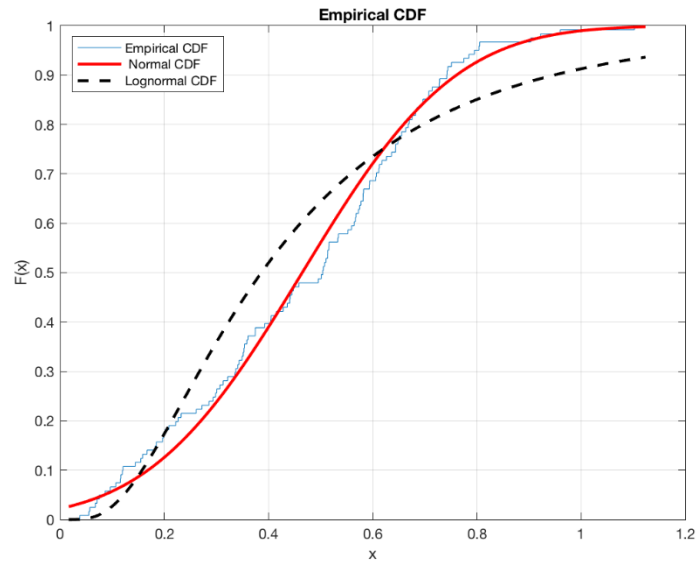
(a)
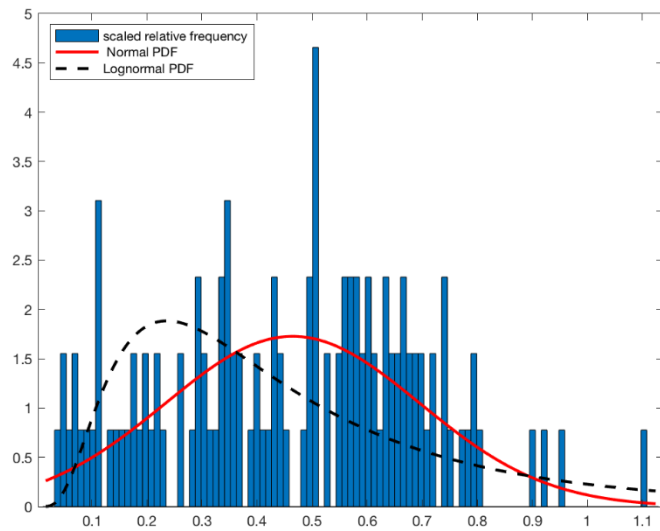
(b)

Figure 11.4: (a) Empirical cumulative distribution and (b) frequency distribution of centroids of a WAAM-produced rod.

_____

11.3. MECHANICAL CHARACTERIZATION ON DOT-BY-DOT RODS

11.3.1. Measurements and set-up

Both tensile and compressive tests have been performed on a Universal testing machine of 500 kN load capacity at the Structural Engineering labs of University of Bologna.

The specimens tested under tension have been tested in displacement-control with a velocity of 2 MPa/sec. Two types of monitoring systems have been adopted to evaluate the strains: a linear deformometer of nominal dimension of 50 mm, to detect the linear deformation of the specimens up to yielding, and an optical-based system referred to as Digital Image Correlation (DIC), to acquire the full strain field during the whole test until failure (Figure 11.5a).

The specimens tested under compression have been tested in displacement-control with a initial velocity of 0.2 mm/min, with an unloading after 6-mm displacement at 0.4 mm/min, and re-loading at 0.2 mm/min until 12-mm displacement. The rods were constrained with a hinge-clamped configuration. Since the purpose of the compression tests is to evaluate the buckling strength at different slenderness values, no additional monitoring systems were adopted (Figure 11.5c).

(a) (b) (c)

Figure 11.5: (a) Tensile test set-up; (b) typical tensile rupture; (c) typical compression/buckling

_____

failure (specimen of aspect ratio around 0.7).

11.3.2. Tensile tests

The tensile tests were performed on a total of 39 specimens (10 specimens printed at 0° from vertical direction, 10 inclined at 10° and 9 inclined at 45°). Figures 11.6 and 11.7 present the whole engineering stress-strain curve of WAAM-produced rods tested under monotonic tensile action and a zoom of them. Overall, for all three orientations considered the variations in tensile response is quite high within each single orientation. Specimens straight and slightly inclined (at 0° and 10° from vertical) present ultimate stress values around 600 MPa and ultimate deformations on average around 40%. On the other hand, specimens with higher inclination (45° from vertical) present ultimate stress values lower than 500 MPa and ultimate deformation values around 30%. All three orientations have important post-yielding hardening behavior until rupture. From a closer look at the first part of the tensile tests (before 1% deformation) (Figure 11.7), the yielding stress values are around 200-250 MPa for all three orientations.
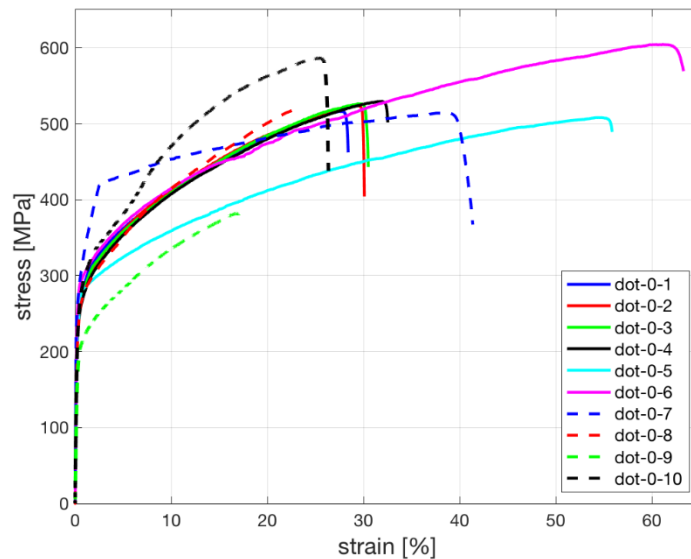
(a)

_____
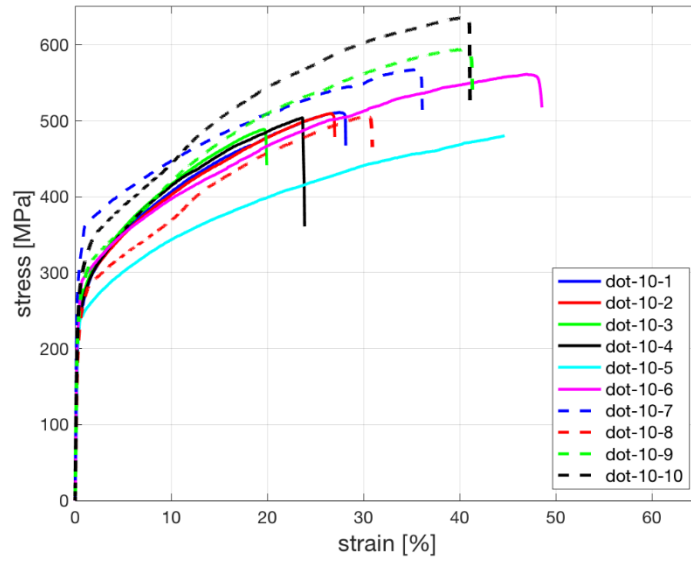
(b)
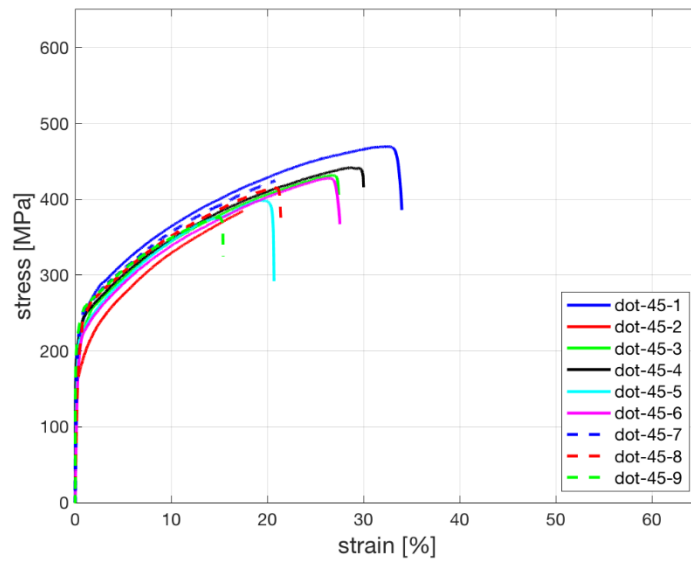
(c)

Figure 11.6: Stress-strain curves for tensile tests on dotted rods: (a) straight specimens (0°), (b) specimens inclined at 10° and (c) inclined at 45°.
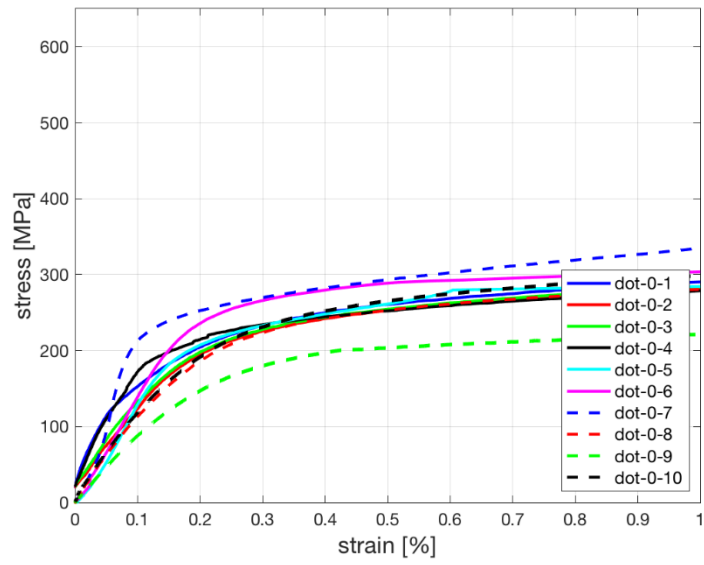
(a)
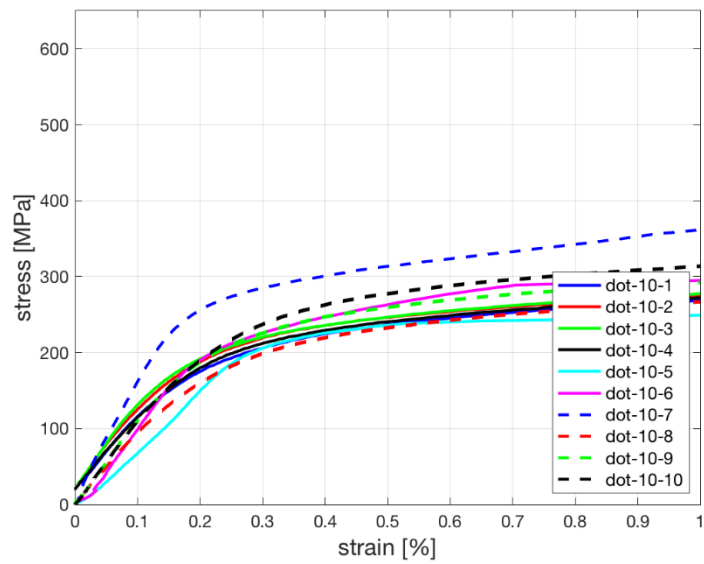
(b)
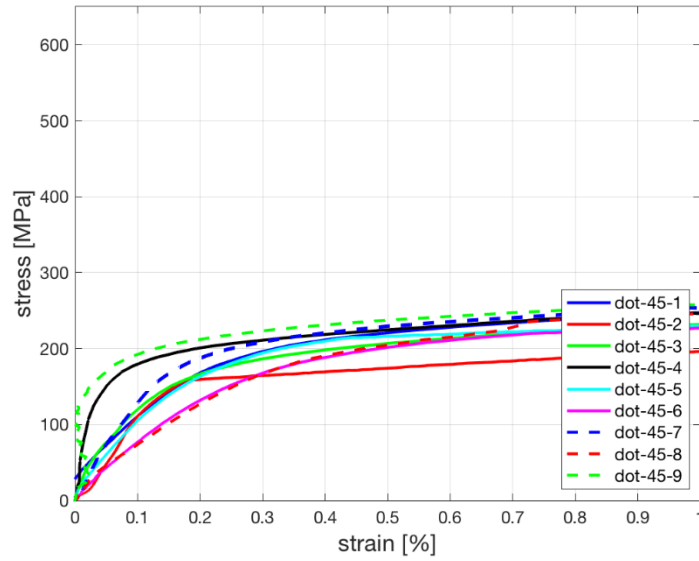
(c)

Figure 11.7: Zoom of stress-strain curves (at deformations <1%) for tensile tests on dotted rods: (a) straight specimens (0°), (b) specimens inclined at 10° and (c) inclined at 45°.

Table 11.3 collects the main mechanical parameters in terms of Young's modulus (*E*), 0.2% proof stress ($R_{p,02}$), ultimate tensile strength (*UTS*), elongation at rupture ($A_{\%}$) and yield to tensile strength ratio ($R_{p0.2}/UTS$).

Table 11.3: Mechanical parameters from tensile tests on dotted rods.

Specimen type	Printing direction	Specimen ID	E [GPa]	$R_{p0.2}$ [MPa]	UTS [MPa]	$A_{\%}$ [%]	$R_{p0.2}/UTS$ [-]
dot	0°	dot-0	133 ± 27	243 ± 20	524 ± 56	35 ± 14	**0.47** ± 0.03
	10°	dot-10	108 ± 19	247 ± 21	536 ± 49	34 ± 9	**0.46** ± 0.03
	45°	dot-45	98 ± 28	208 ± 20	419 ± 29	24 ± 6	**0.50** ± 0.06

_____

11.3.3. Discussion on the key material properties

Figure 11.8 compares the key mechanical properties for the three orientations investigated on dot-by-dot rods. Reference to traditional values of the key mechanical properties of 304L stainless steel according to European building code (EC3:1-4) is also provided.

Overall, the three orientations do not seem to have marked difference among them, even though a slight reduction in all mechanical properties is registered from straight to slightly inclined (10°) till considerably inclined (45°) specimens. Comparing the values from dot-by-dot specimens to traditionally-manufactured 304L steel, the main discrepancy is evidenced for Young's modulus, for which 30% to 50% of reduction is registered for dot-by-dot specimens. These values are in line with those of machined specimens cut transversally (T) as presented in Part A, with exception for the 0.2% proof stress, for which the dot-by-dot specimens resulted in lower values.
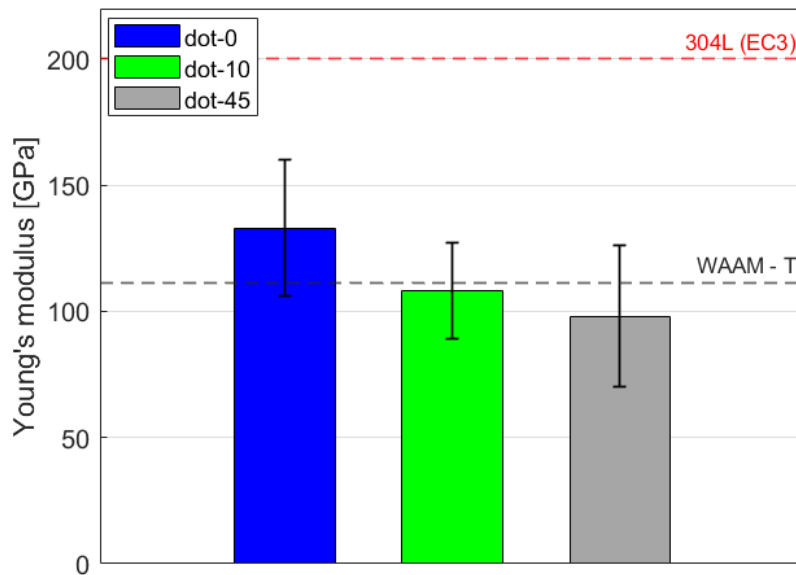
(a)
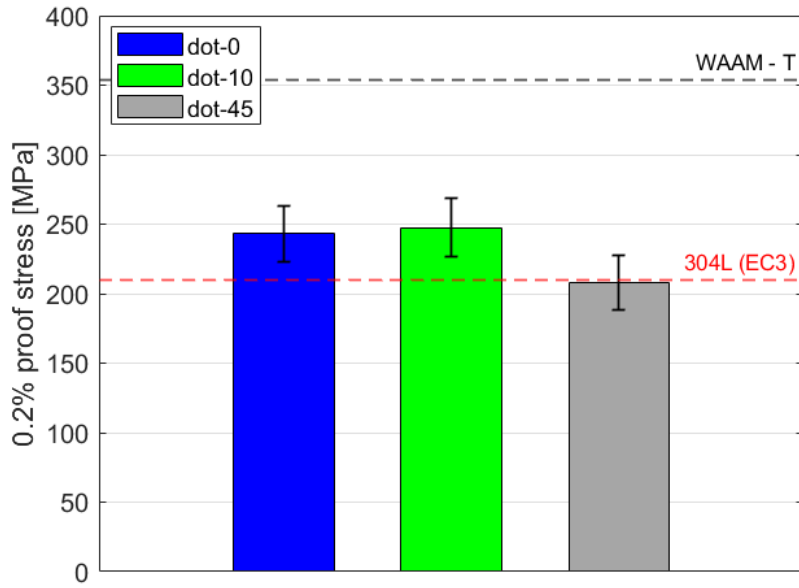
(b)
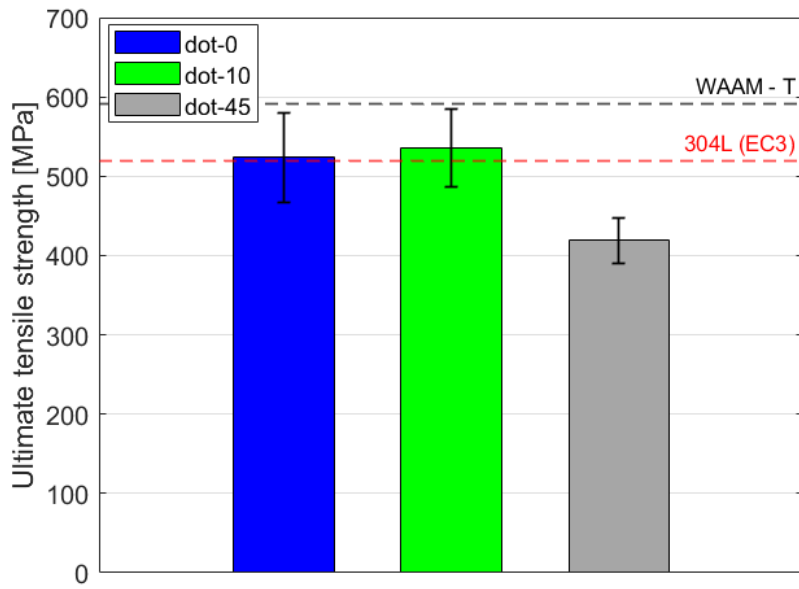
(c)
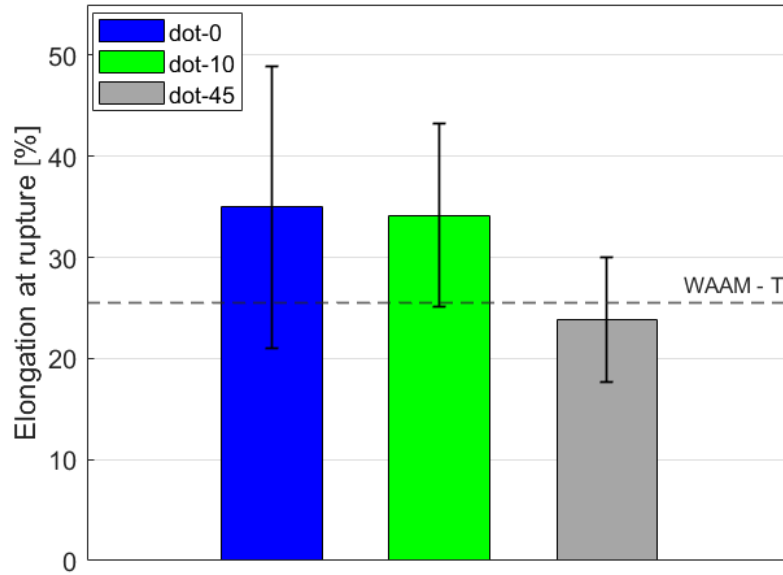
(d)

Figure 11.8: Results of the tensile tests on WAAM dot-by-dot rods printed at different angles: (a) 0.2% proof stress; (b) ultimate tensile strength; (c) Young's modulus; (d) elongation at rupture.

Table 11.4 reports the relative ratios of the main mechanical parameters with respect to the printing inclination. The values evidence a detrimental effect of the printing inclination on the mechanical response of the WAAM-produced rods. Indeed, the higher the printing angle, the higher the reduction in the material property with respect to the straight printing configuration (at 0°). This aspect should be further analyzed, with specific experimental tests and correlations with the microstructure and fracture analysis. These latter aspects are currently under development and will be presented in a specifically devoted research article.

Table 11.4: Relative ratios of the main mechanical properties with respect to the specimen's printing inclination.

Relative ratio	E [-]	$R_{p0.2}$ [-]	UTS [-]	$A_{\%}$ [-]	YS/UTS [-]
10° / 0°	0.78	0.98	1.00	1.00	0.98
45° / 0°	0.69	0.82	0.78	0.64	1.06

11.3.4. Compression tests

Compression tests have been performed on rods printed vertically (0° from vertical direction) and at 10° inclination from vertical. A total of 30 specimens have been tested, with different lengths L (slenderness ratios $\lambda=i/L_{eff}$ from 0.30 to 1.70, with i equal to the cross-section radius of gyration and L_{eff} the effective length based on the end-constraints). In detail, 4 categories of slenderness were tested: (1) 8 specimens at $\lambda = 0.30$ (very stub), (2) 11 specimens at $\lambda = 0.85$ (stub), (3) 2 specimes at $\lambda = 1.35$ (slender), (4) 9 specimens at $\lambda = 1.70$ (very slender).

The values of critical Eulerian force have been evaluated as:

$$N_{cr} = \pi^2 \frac{EJ}{L_{eff}^{\,2}} \qquad\qquad (11.1)$$

The effective length has been evaluated as: $L_{eff} = K \cdot L$ where K is the effective length factor accounting for the end-constraint of the member. For the compression tests presented, previous estimation on the K factor has been carried out through a series of compression tests with the same test set-up on uniform cylindrical S275 steel rods of 250 mm length and 6-mm diameter full circular cross-section. From these first tests, the K factor resulted to be equal to 0.74. It should be noted that for perfectly clamped-hinged end constraints the K factor is equal to 0.71. Thus, the end-constraint configuration adopted can be considered at first approximation as hinged-clamped.

The plastic force has been evaluated considering the effective cross-sectional area A_{eff} taken from volume-based measurements (and also used for the tensile tests). The average 0.2% proof stress value for dot-by-dot straight (0°) specimens has been considered. The specimens with smallest slenderness ratio (i.e. stub rods of $\lambda=0.30$) registered ultimate force values (N_u) higher than their corresponding mean plastic force. This might be due to the double uncertainty correlated with the estimation of the plastic force: (i) in the value of the effective cross-sectional area, and (ii) in the estimation of the yielding stress in compression taken as the $R_{p,02}$ value estimated from tensile tests. Table 11.5 collects the mean results based on four main groups of specimens, divided into their slenderness ratio λ. It also presents the values of the characteristic ultimate force ($N_{u,k}$), evaluated as the mean value minus two standard deviations, according to the recommendations provided by the European Convention for Constructional Steelwork (ECCS) (European Convention For Constructional Steelwork, 1976). The results are also reported in Figure 11.9.

Table 11.5: Results from compression tests on dotted rods.

Specimen type	L_m [mm]	λ_m [-]	$N_{cr,m}$ [kN]	$N_{u,m}$ [kN]	$N_{u,k}$ [kN]
dot – 0°	43.12	0.28	83.99	8.83	8.71
	127.63	0.87	8.66	4.57	3.24
	192.00	1.38	3.07	2.79	2.79
	255.17	1.67	2.53	1.50	0.91
dot – 10°	42.78	0.32	68.01	8.75	8.37
	105.33	0.82	9.87	4.82	3.73
	199.06	1.50	2.91	3.40	3.40
	232.51	1.81	1.87	1.61	1.05
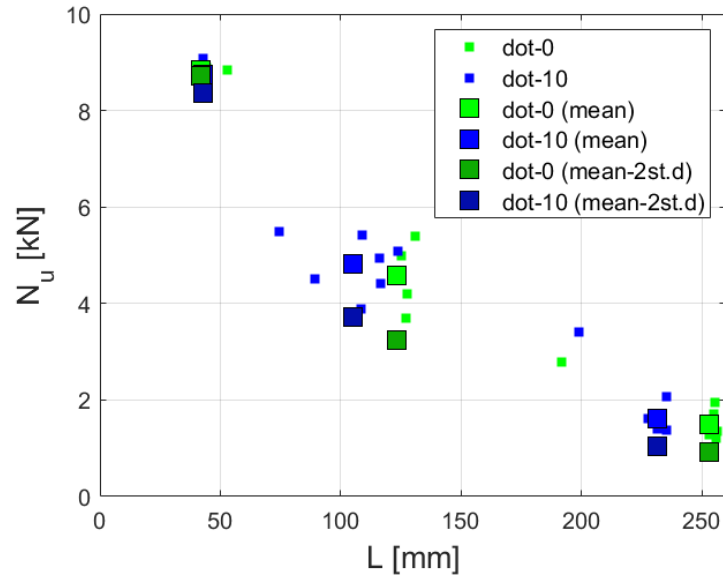
Figure 11.9: Compression results of dot-by-dot specimens.

11.4. SUMMARY OF SECTION 11

From the results on the experimental characterization of WAAM-produced stainless steel rod-like elements, some important results have been evidenced:

- In order to geometrically characterize the rods, detailed measurements on the diameter distribution (influenced by the surface roughness of the as-built specimens) resulted in an effective diameter of 5.80 mm, with 3% discrepancy from the nominal value (of 6 mm). Non-negligible lack of straightness is also estimated of the order of 0.18% of the total length of the rod.

- Given the one-dimensional nature of the rods, the key material properties were derived on as-built specimens only. From the tensile tests, it appeared that the mechanical behavior of dot-by-dot printed specimens is remarkably different with respect to the one of continuously-printed specimens (presented in part A). In detail, the former ones are characterized by values of Young's modulus of the order of the T direction for continuously-printed plates (around 101 GPa). Moreover, a marked hardening behavior is registered, with strength ratio lower than 0.50. The printing direction slightly affects the mechanical response, with a significant reduction in strength and stiffness with the increase of the printing angle from the vertical direction.

- First investigation on the buckling resistance of rods has been carried out through compression tests on rods with different slenderness values.

The results provide first investigations, which are currently under development. Further studies are aimed at including also microstructural and fractographic analyses.

These first results on the mechanical characterization of dot-by-dot rods suggest the need of proper studies devoted to this particular WAAM process, which results in different response with respect to the continuous printing strategy (presented in part A). Nonetheless, the experimental results can be used as first estimation of the design values for dot-by-dot printing.

12. Design guidelines for WAAM stainless steel rods

12.1. OVERVIEW

As for the WAAM-produced plates presented in part A, the results from the experimental characterization of WAAM-produced stainless steel rods suggest the need for proper calibration of the key material properties (in terms of yielding stress, ultimate tensile stress and Young's modulus) for the structural design of WAAM-produced stainless steel rods, with considerations regarding the different inclination of the element with respect to the vertical printing direction.

Therefore, the present chapter illustrates a first calibration of the design mechanical properties and partial factors of safety of WAAM-produced stainless steel elements for structural purposes. Section 12.2 presents the first results from the statistical distributions of the key material properties, from which the design values and partial factors of safety are calibrated (Section 12.3).

12.2. STATISTICAL DISTRIBUTION

Similarly to the case of WAAM-produced plates (presented in Section 6), the following variables are considered for structural design applications of WAAM-produced rods:

- f_y : yielding stress, corresponding to $R_{p,02}$ from experimental tests;

- f_t : ultimate tensile strength, corresponding to *UTS* from experimental tests;

- E : Young's modulus.

From the experimental results on WAAM-produced stainless steel as presented in Section 11, a statistical analysis of the yielding and ultimate stress is carried out deriving the best-fit distribution of Normal, Weibull and Lognormal according to the maximum likelihood estimators. The distributions are estimated on the results from the tensile tests on as-built rods (presented in Section 11.3). The key material properties are obtained as effective values, considering a uniform effective cross-section along the length of the rod.

Figures 12.1, 12.2 and 12.3 provide a comparison between experimental and best-fit cumulative distribution functions (CDF) and probability density functions (PDF) as obtained for yielding stress (estimate as 0.2% proof stress), ultimate tensile strength and Young's modulus. The distributions have been estimated differentiating the three main inclinations investigated, i.e. straight (0°), inclined at 10° and at 45°. The mean values (μ), standard deviations (σ) and coefficients of variation (w) of the best-fit distributions are summarized in Table 12.1.
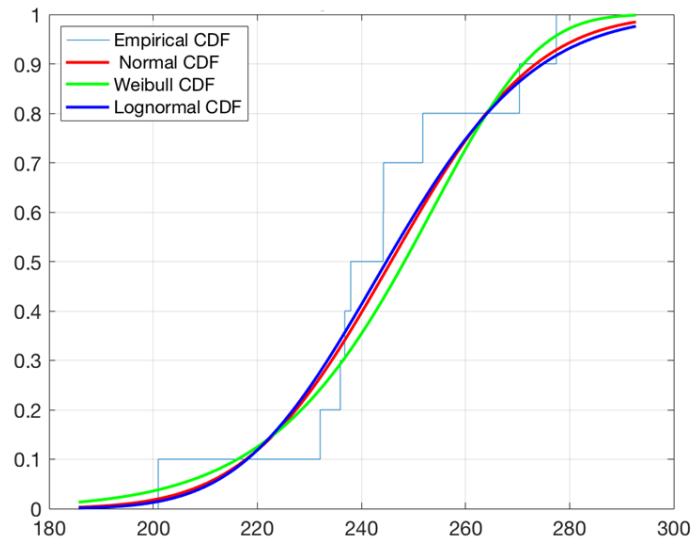
(a)
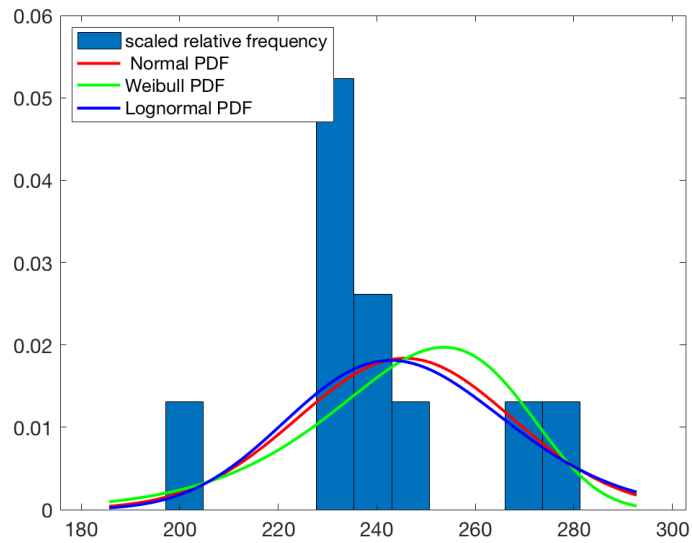
(b)
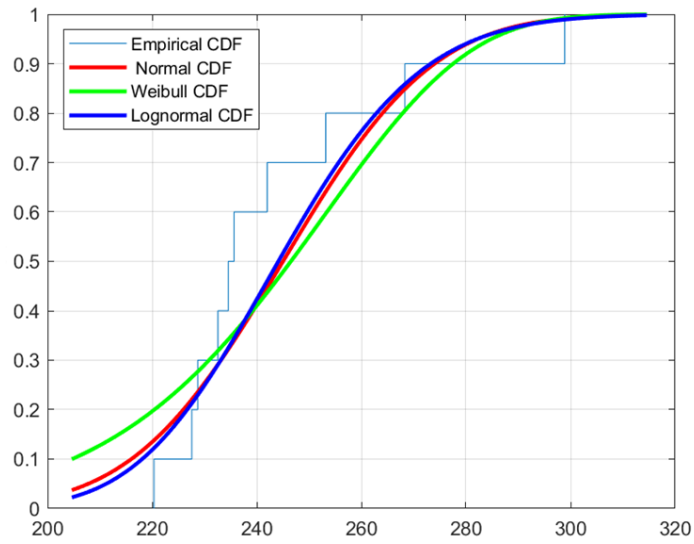
(c)
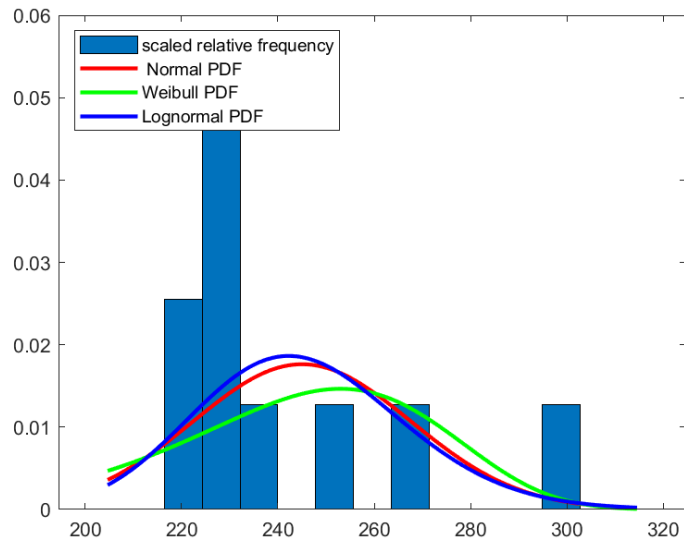
(d)
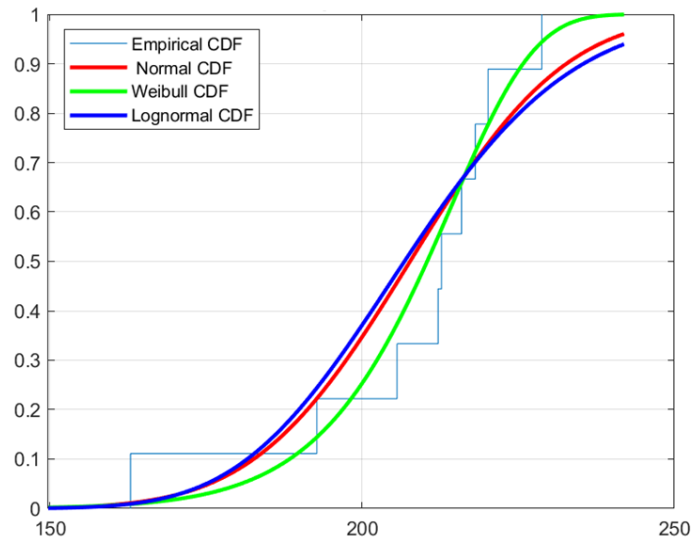
(e)
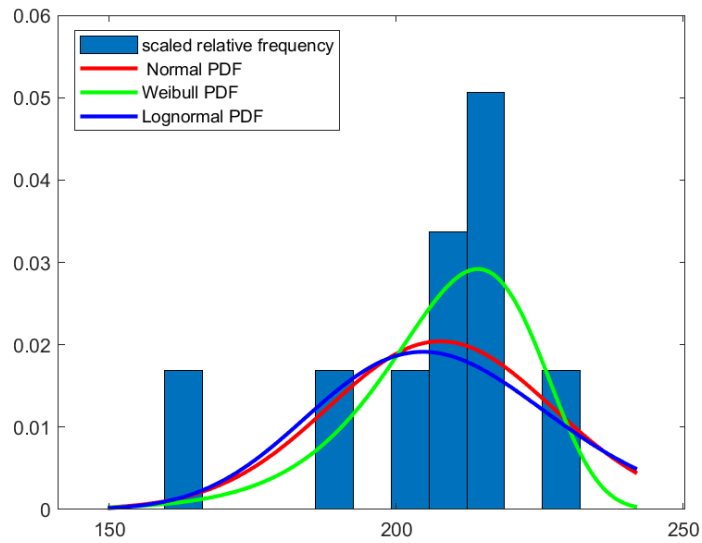
(f)

Figure 12.1: Statistical distributions of yielding stress values: (a) CDF and (b) PDF for specimens at 0°; (c) CDF and (d) PDF for specimens at 10°; (e) CDF and (f) PDF for specimens at 45°.

(a)

(b)
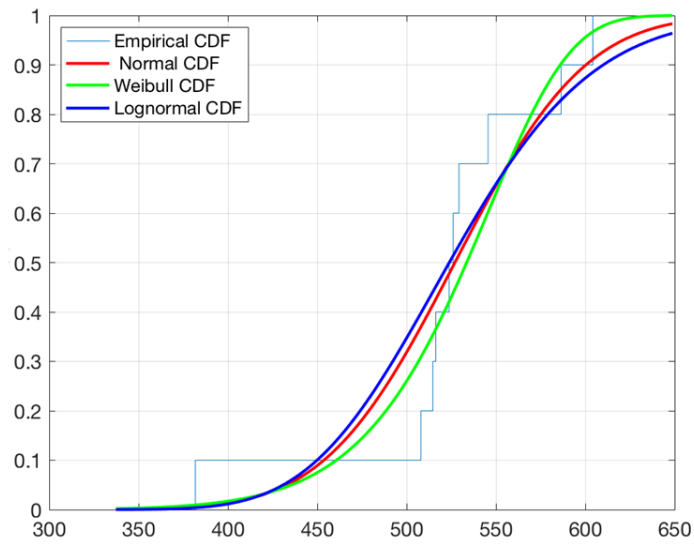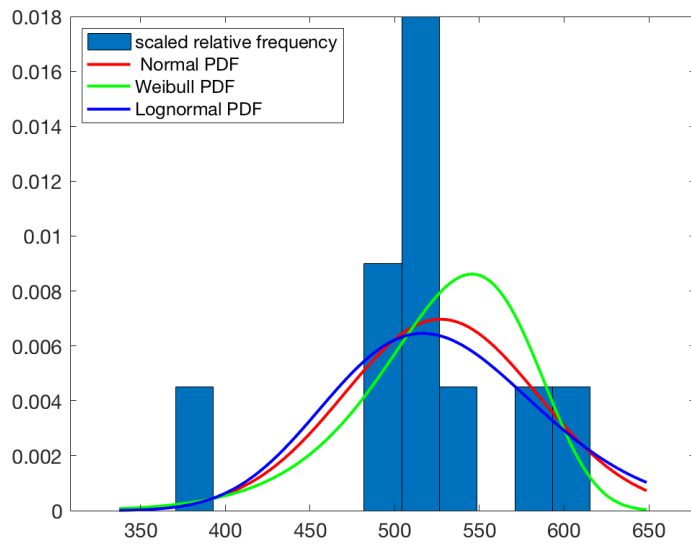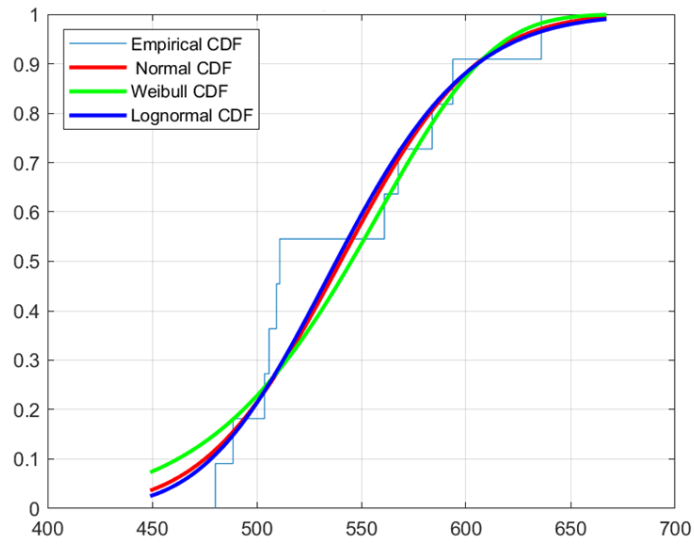
(c)
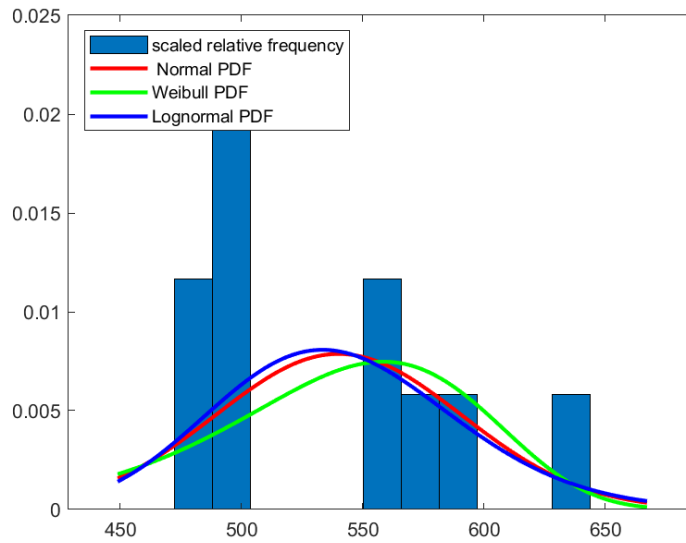
(d)
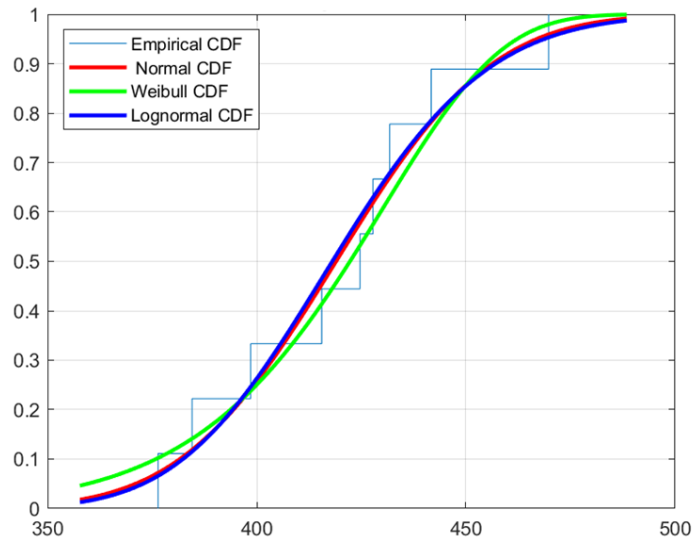
(e)
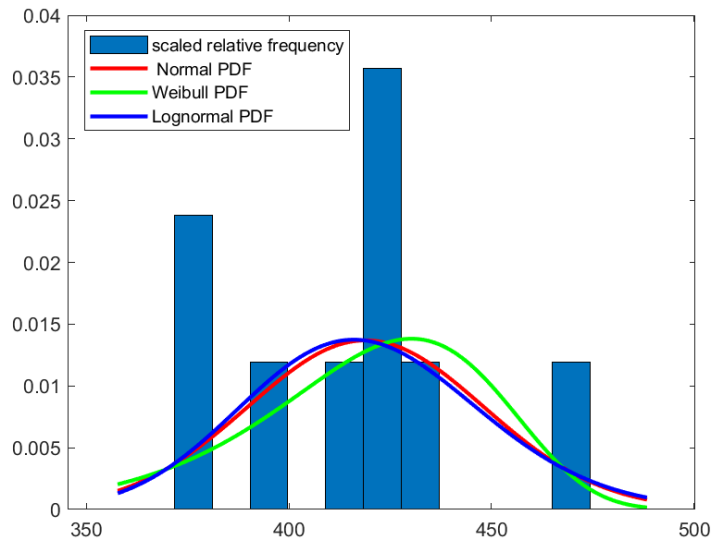
(f)

Figure 12.2: Statistical distributions of ultimate tensile strength values: (a) CDF and (b) PDF for specimens at 0°; (c) CDF and (d) PDF for specimens at 10°; (e) CDF and (f) PDF for specimens at 45°.
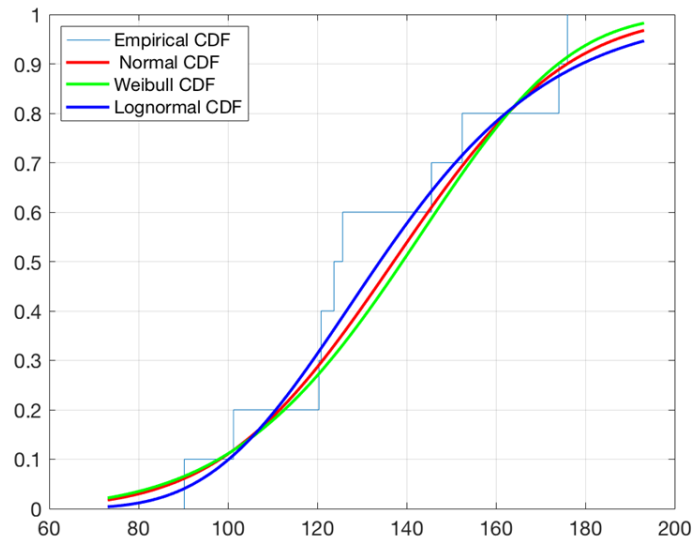
(a)
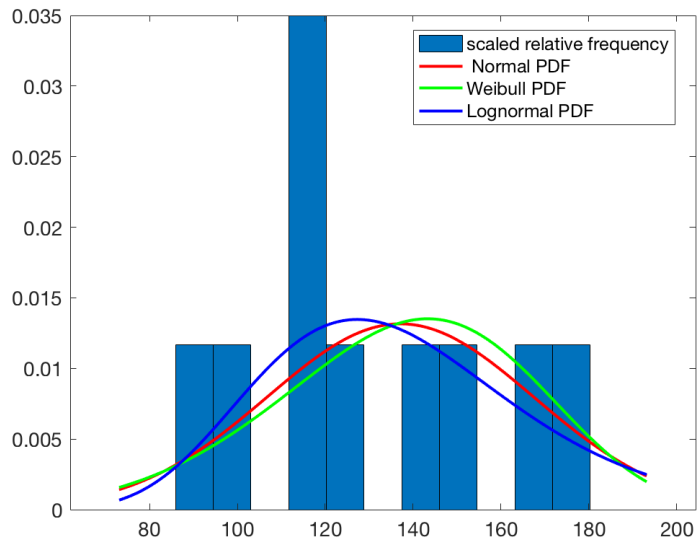
(b)
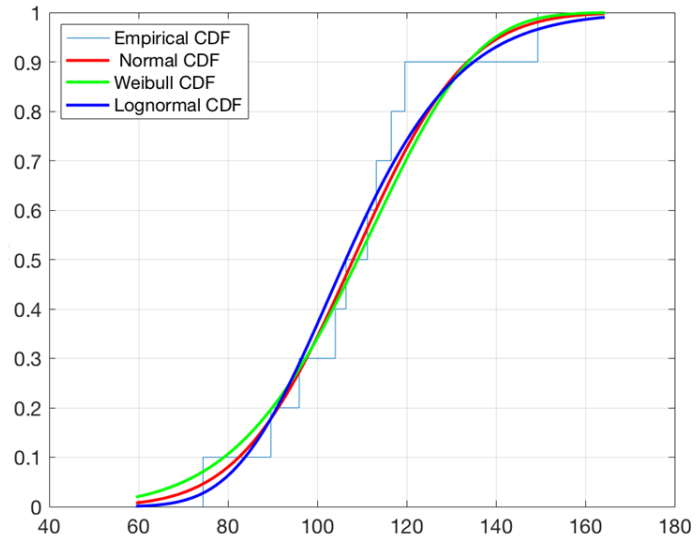
(c)
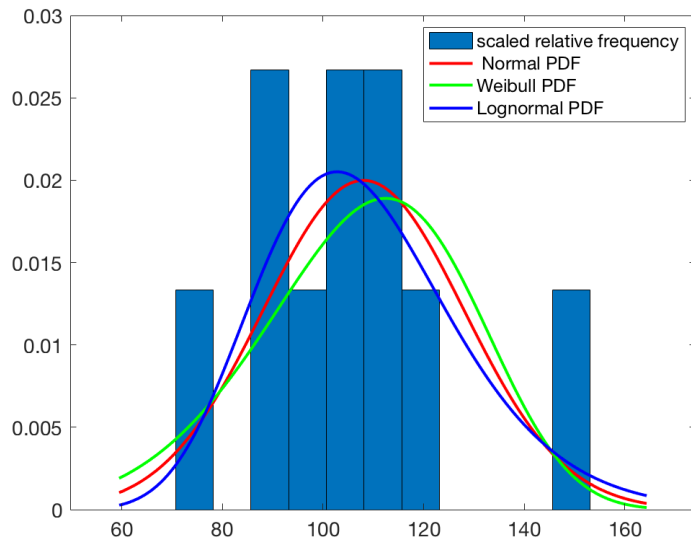
(d)
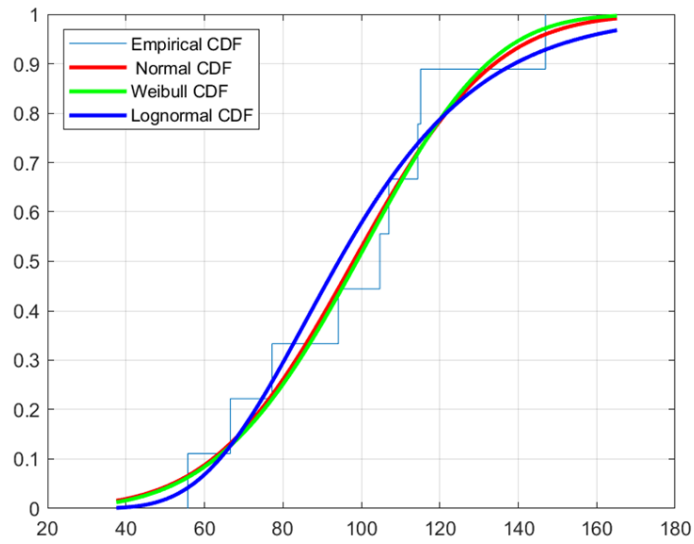
(e)
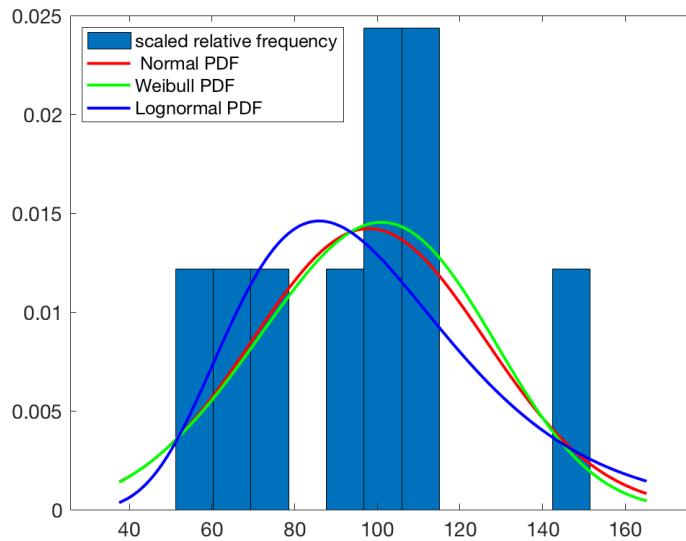
(f)

Figure 12.3: Statistical distributions of Young's modulus values: (a) CDF and (b) PDF for specimens at 0°; (c) CDF and (d) PDF for specimens at 10°; (e) CDF and (f) PDF for specimens at 45°.

Table 12.1: Mean and standard deviation of Normal, Log-normal and Weibull best fit statistical

distributions of the mechanical properties of WAAM 308LSi stainless steel rods.

		NORMAL			WEIBULL			LOGNORMAL		
		μ_N [MPa]	σ_N [MPa]	w_N [-]	μ_W [MPa]	σ_W [MPa]	w_W [-]	μ_L [MPa]	σ_L [MPa]	w_L [-]
Yielding stress	0°	243.18	21.12	0.09	245.52	22.01	0.09	245.81	22.24	0.09
	10°	245.01	22.62	0.09	243.31	28.92	0.12	245.08	21.61	0.09
	45°	207.69	19.54	0.09	208.41	15.08	0.07	207.85	21.11	0.10
		μ_N [MPa]	σ_N [MPa]	w_N [-]	μ_W [MPa]	σ_W [MPa]	w_W [-]	μ_L [MPa]	σ_L [MPa]	w_L [-]
Ultimate tensile strength	0°	527.05	57.22	0.11	527.45	50.12	0.10	527.61	62.90	0.12
	10°	540.10	50.69	0.09	538.48	57.25	0.11	540.31	49.92	0.09
	45°	418.97	29.14	0.07	418.09	31.77	0.08	419.06	29.20	0.07
		μ_N [GPa]	σ_N [GPa]	w_N [-]	μ_W [GPa]	σ_W [GPa]	w_W [-]	μ_L [GPa]	σ_L [GPa]	w_L [-]
Young's modulus	0°	137.12	30.32	0.22	137.31	29.45	0.21	137.50	31.59	0.23
	10°	108.05	19.96	0.18	107.56	21.26	0.20	108.26	20.31	0.19
	45°	97.99	28.06	0.29	98.08	26.71	0.27	98.67	30.66	0.31

It should be noted that the dimension of the samples size, although small, is in accordance with the minimum recommended dimension according to Annexes C and D of Eurocode 0 (EN 1990) to perform calibration from experiments, as long as specific values of correction factors (as reported in the provisions) are adopted. The choice of the distribution models has been made according to the indications provided in Annex C and D of Eurocode 0 for strength data.

Overall, it should be noted that the coefficients of variation for both yielding stress and ultimate strength of all three distributions are within 2% and 10%, and in line with ranges obtained for traditionally-manufactured steel elements used in construction (Ballio & Mazzolani, 1979).

Table 12.2 provides the results of Kolmogorov-Smirnov test in terms of coefficient KS (Massey, 1951) of the best-fit distributions evaluated from maximum likelihood estimators for the

experimental data. The obtained KS values range between 0.15 to 0.30. The critical values for α=0.05 are: 0.409 for specimens at 0° and 10°, 0.430 for specimens at 45°.

Overall, the results provide lower values than the critical, thus suggesting that all three distributions provide a good fit with the experimental results. No clear trend is visible for the three distributions.

Thus, according to the recommendations provided by Eurocode 0, in the next section the Lognormal distributions will be considered to calibrate the design values.

Table 12.2: Kolmogorov-Smirnov test of the Normal, Lognormal and Weibull best fit statistical distributions.

		Kolmogorov-Smirnov test		
		KS_N [-]	KS_W [-]	KS_L [-]
Yielding stress	0°	0.175	0.211	0.187
	10°	0.210	0.220	0.201
	45°	0.258	0.217	0.267
Ultimate tensile strength	0°	0.279	0.218	0.307
	10°	0.265	0.264	0.257
	45°	0.279	0.218	0.307
Young's modulus	0°	0.193	0.157	0.215
	10°	0.181	0.165	0.204
	45°	0.193	0.215	0.157

_____

12.3.   CALIBRATION OF DESIGN VALUES AND PARTIAL FACTORS OF KEY MATERIAL PROPERTIES

12.3.1. Calibration based on the statistical distributions

As for the case of WAAM plates calibrated in part A, the fractiles corresponding to the characteristic and design values of yielding and ultimate stresses have been computed from best-fit statistical distribution (Section 12.2).

In accordance with the structural reliability theory and the recommendations presented in Eurocode 0, the following fractiles of the random variable associated to the strength parameters are considered:

-   5%-percentile of the distribution, corresponding to the characteristic value;

-   0.1%-percentile of the distribution, corresponding to the design value.

The same partial safety factors as calibrated for WAAM plates studied in part A (presented in Section 6) are considered for dot-by-dot rods as well: the material partial safety factor for yielding stress γ_{m1} is to be compared with the value of partial factor recommended in Eurocode 3 sections to excessive yielding realized in stainless steel, equal to γ_{M0}=1.10. Similarly, the material partial safety factor calibrated on the ultimate tensile strength γ_{m2} should be compared to the partial factor recommended in Eurocode 3 (EN1993:1-4) for resistance of cross-sections in tension to fracture realized in stainless steel, equal to γ_{M2}=1.25.

12.3.2. Calibration according to Eurocode 0

Along with the statistical distributions, the calibration of characteristic and design values is also performed according to Eurocode 0 formulation "design from samples" of Annex D (as already presented in Section 6.4). For a Lognormal distribution, the values of coefficient k_n as suggested by (European Committee for Standardization (CEN), 2002) are equal to: 1.92 for specimens at 0° and 10° (10 samples), 1.96 for specimens at 45° (9 samples).

12.3.3. Comparison of the results from calibration

Table 12.3 provides an overview of the results of calibration according to Eurocode 0 (European Committee for Standardization (CEN), 2002), compared with the values of fractiles as evaluated from statistical distribution of the experimental results, as from Section 12.2.

Table 12.3: Overview of results of calibration of design values for WAAM stainless steel rods.

		5% and 0.1% fractiles from statistical distribution			Characteristic value, design value and safety factors according to EC0 (EN 1990)			EC3 recommendations for partial safety factors (EN 1993:1-4)
		$f_{y,5\%}$	$f_{y,0.1\%}$	$f_{y,5\%}/f_{y,0.1\%}$	f_{yk}	f_{yd}	γ_{m1}	
Yielding stress [MPa]	0°	207.86	182.83	1.14	204.51	186.76	1.10	
	10°	211.99	187.45	1.13	209.26	189.70	1.10	1.10
	45°	175.87	152.64	1.15	169.55	156.03	1.09	
		$f_{t,5\%}$	$f_{t,0.1\%}$	$f_{t,5\%}/f_{t,0.1\%}$	f_{tk}	f_{td}	γ_{m2}	
Ultimate tensile strength [MPa]	0°	433.65	367.21	1.18	410.91	371.49	1.11	
	10°	464.13	408.01	1.14	446.48	403.77	1.11	1.25
	45°	373.68	339.06	1.10	364.76	339.11	1.08	

As for the case of WAAM plates presented in part A, also for dot-by-dot printing rods the results indicate in general a good correspondence between the values of 5% and 0.1% fractiles from the statistical distributions and the characteristic and design values as obtained according to Eurocode 0. In detail, the characteristic values calibrated according to Eurocode 0 are overall lower than the actual 5% fractile taken from the Lognormal distribution which best fits the experimental data. This is due to the fact that for small sample sizes, the use of large values of k_n coefficient results in a characteristic value that corresponds to a fractile smaller than the 5% one. Consequently, in this case the characteristic values get closer to the design values and therefore the corresponding partial safety factors tend to reduce.

The influence on the inclination of the rods is also evidenced by the calibrated characteristic and design values and corresponding partial factors. In particular, as expected, the values for 45°-inclined rods are much lower than for the case of 10°-inclined and straight ones. One of the reasons might be due to the higher geometrical irregularities presented in the more inclined rods.

12.3.4. Considerations upon Young's modulus

Also for dot-by-dot printed rods, Young's modulus values are in general affected by non-negligible variability which should be considered. For this aim, specific fractiles (namely 0.1%, 5%, 50%, 95% and 99.9% fractiles) have been evaluated from the best-fit statistical distributions considering the three orientations (Table 12.4). The lower-bound and upper-bound fractiles are provided to account for different design requirements for structural elements. Indeed, based on the type of member and the applied load condition, it would be advised in certain cases to have either higher or lower value of Young's modulus to stay on the safe side. As for the case of the continuous printing strategy (reported in Part A), these values should be taken as extremes (or "tails") of the calibrated statistical distribution.

Table 12.4: Overview of results of distribution of Young's modulus for WAAM stainless steel rods.

		Fractiles from statistical distribution				
		$E_{0.1\%}$	$E_{5\%}$	$E_{50\%}$	$E_{95\%}$	$E_{99.9\%}$
Young's modulus [GPa]	0°	68.39	94.22	137.50	200.65	276.46
	10°	61.20	79.51	108.26	147.40	191.49
	45°	41.03	61.18	98.67	155.95	234.02

The results clearly evidence the influence on the inclination of dot-by-dot WAAM rods in the Young's modulus values which should be taken into account during the design phase.

_____

12.4. SUMMARY OF SECTION 12

The present Section provides the first results on the calibration of design values and partial safety factors of the key material properties of WAAM-produced dot-by-dot rods realized in stainless steel.

From this, the following considerations can be drawn:

- For all quantities considered along all three inclinations (i.e. 0°, 10° and 45° from vertical), the distribution model that best fits the experimental data is the Log-normal, from which the definition of the fractiles for characteristic and design values are evaluated.

- The procedure presented in Eurocode 0 provided lower estimations of the characteristic but higher of the design values for the key material properties with respect to the actual fractiles from the statistical distributions (5% and 0.1% respectively). Reasonings of this might be due to the limited amount of experimental data available.

- The design values of yielding stress for the three inclinations vary from 150 MPa to 190 MPa, well lower than the one calibrated for WAAM-produced plates (Section 5). The design values of ultimate tensile strength vary from 365 MPa to 465 MPa, slightly lower than then one calibrated for WAAM-produced plates (Section 6). For both parameters, high discrepancy between the investigated inclinations is evaluated and should therefore be considered in the structural design phase.

- The calibrated partial safety factors for yielding stress vary from 1.10 to 1.15 (slightly higher than the provisions in Eurocode 3 for stainless steel structural elements), and those for ultimate tensile strength from 1.10 to 1.18 (slightly lower than the one suggested in Eurocode 3).

- Ad-hoc lower and upper bound fractiles of Young's modulus for the three inclinations have been calibrated for different structural design purposes.

13. Computational design of WAAM diagrid elements

13.1. OVERVIEW

The present Section illustrates the computational design process (from the concept to the final design) of a WAAM-produced diagrid column.

The conceptual design has been guided by solutions found in the scientific and technical literature (Section 13.2) dealing with the problem of determining the optimal shape of a structural element subjected to compression. The parametric design phase, presented in Section 13.3, has been carried out in two steps, namely the global shape design and the topological design, and takes into account the manufacturing constraints and the material properties of the adopted WAAM process, thus allowing to obtain the final design ready to be 3D-printed without the need of further iterations.

The structural performances of the final design (Sections 13.4 and 13.5) are evaluated by means of finite element analysis comparing the stress levels with that of a benchmark solution.

The final design is then fabricated (Section 13.6) half-scaled and presented in several important exhibitions.

_____

13.2. HISTORICAL PRECEDENTS OF COLUMNS WITH OPTIMAL SHAPE

Since Galileo Galilei's investigations on "equistrong beams" in the 17th century, several researchers have been dedicated an effort on determining the "most efficient shape" of an element, intended as the configuration of minimum weight ensuring the same safety factor under certain applied loads and restraint conditions. The shape of the equistrong rod under a compressive force is found in the Euler's problem. In 1960 Keller (Keller, 1960) solved the problem of determining the shape of a column with the largest critical buckling load, of a given length and volume. The results show that the strongest column is not uniform but tapered, being thicker at its center and thinner at its ends. Indeed, appropriately tapering a column of circular cross-section increases its critical buckling load by one-third over that of a uniform column. The analytical equation of the along-the height variation of the cross section area of the strongest column has a quadratic sinusoidal form (Keller, 1960). Such a column with variable cross section has a weight reduced by 13% of that of a uniform full cylindrical column having the same buckling load (Bejan, 2000).

In addition to the theoretical studies related to the strongest beam, more practical-oriented research has been carried out since the early 20th century to obtain efficient structural solutions for tall and slender structures, such as nuclear cooling towers or water towers. In particular, hyperboidal thin shell structures are characterized by excellent aerodynamic, strength and stability properties. The remarkable Russian engineer Vladimir Shukov, who designed and realized the hyperboloidal water tower for the 1896 industrial exhibition in Nizhny Novgorod, is recognized as the pioneer of hyperboloidal structures. More recent examples of hyperboloidal structures are the McDonnell Plantarium roof in St. Louis, the Brasilia Cathedral and the Kobe Port tower (Bektas, 2017). As hyperboloid structures are doubly curved, their simultaneous curvature in opposite directions leads to high resistance against buckling. Furthermore, given their anticlastic curvature, they are able to carry the same load with less amount of material with respect to traditional cylindrical shapes (Beckh, 2015; Krivoshapko, 2002).

The two families of optimal shapes for a column subjected to compression, namely the "sinusoidal-like" and the "hyperbolic-like", have been considered in this study as selection criterion to identify the global geometrical shape of the diagrid column in the first step of the parametric design process (see Section 13.3). Figure 13.1 conceptually explains the merging of the "sinusoidal-like" and "hyperdoloic-like" shapes towards the the final designed shape.

_____
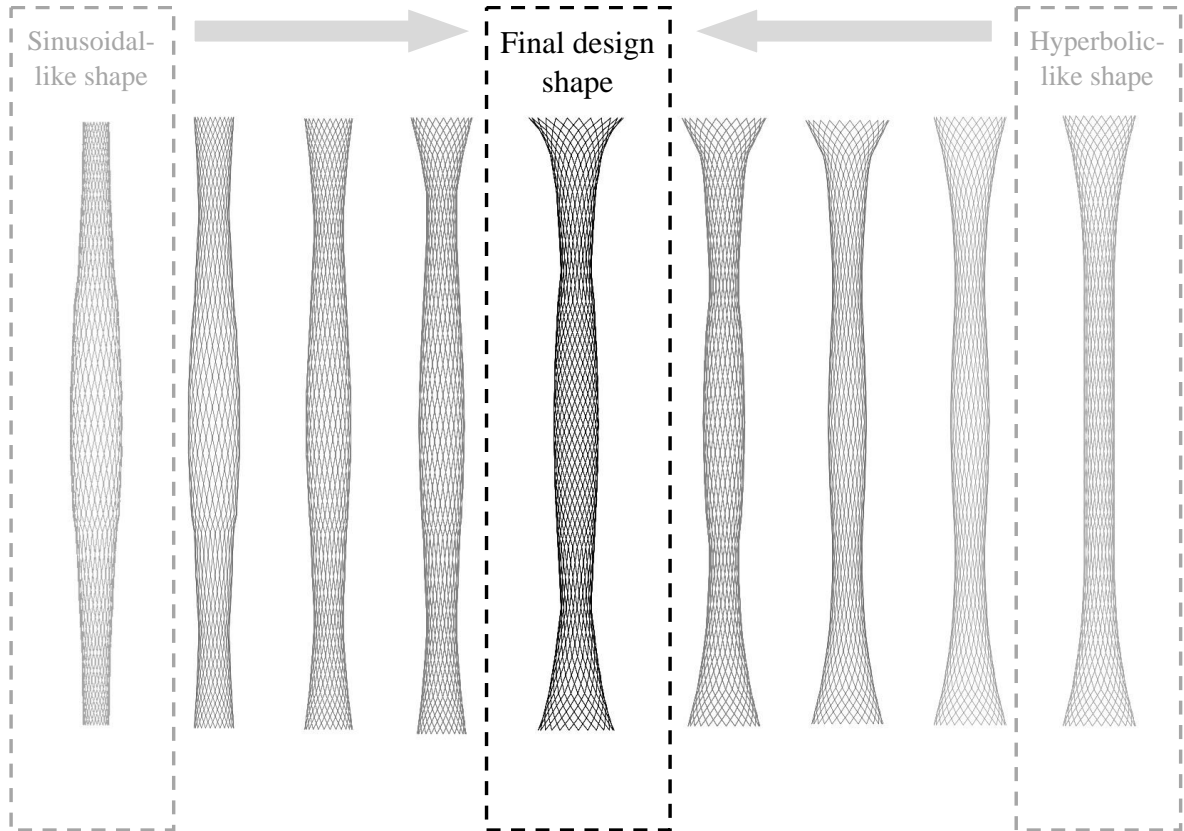
Figure 13.1: Path towards the shape of a diagrid column.

_____

13.3.   THE PARAMETRIC DESIGN ALGORITHM

The computational design flow is articulated in different phases (Figure 13.2), from the set of the initial geometry (phase 1) to the parametric design algorithm (phase 2 and 3) towards the final design. In detail, the parametric design phases are the global shape design (phase 2) and the topological design (phase 3). In both parametric design phases, a parametric design algorithm has been implemented by means of *Grasshopper* (www.grasshopper3d.com) program in *Rhinoceros5* (www.rhino3d.com) software environment, widely used for parametric design purposes since it allows to perform advanced algorithm-aided design and structural analyses directly on CAD drawings through a real-time iterative procedure to the final design. The two plug-ins used for the purpose of the present work are *Karamba3D* (www.karamba3d.com) and *Galapagos* (built-in feature of *Grasshopper*): the first one, in particular, is a plug-in able to perform non-linear structural analysis of beam and shell models; the second one, instead, solves optimization problems making use of genetic algorithms to generate a population of different solutions based on the problem at hand.

The objective of both global and topological design is to determine the structural configuration (defined in a parametric form) of minimum weight satisfying a target structural requirement under additional constraints. In each design step, specific geometrical parameters are chosen as the design variables, while the remaining ones are set to constant values. The final configuration at the end of each design step is selected among the ones generated by the genetic algorithm according to a selection criterion. The structural requirements are verified through linear static analyses by computing the utilization factors (U_i) of each structural member and verifying U_i <1.0. Indeed, the utilization factor, according to Eurocodes, is computed as the ratio between the design actions and the corresponding resistances for a given limit state, and the acceptable design should satisfy the threshold of utilization factor of 100%.

In this case, the utilization factor is calculated as $U = \dfrac{N_{Ed}}{N_{Rd}} + \dfrac{M_{y,Ed}}{M_{y,Rd}} + \dfrac{M_{z,Ed}}{M_{z,Rd}}$, where N_{Ed}, $M_{y,Ed}$ and $M_{z,Ed}$ are respectively the axial force and bending moments along directions y and z due to the applied loads, while N_{Rd}, $M_{y,Rd}$ and $M_{z,Rd}$ are the corresponding resisting values.
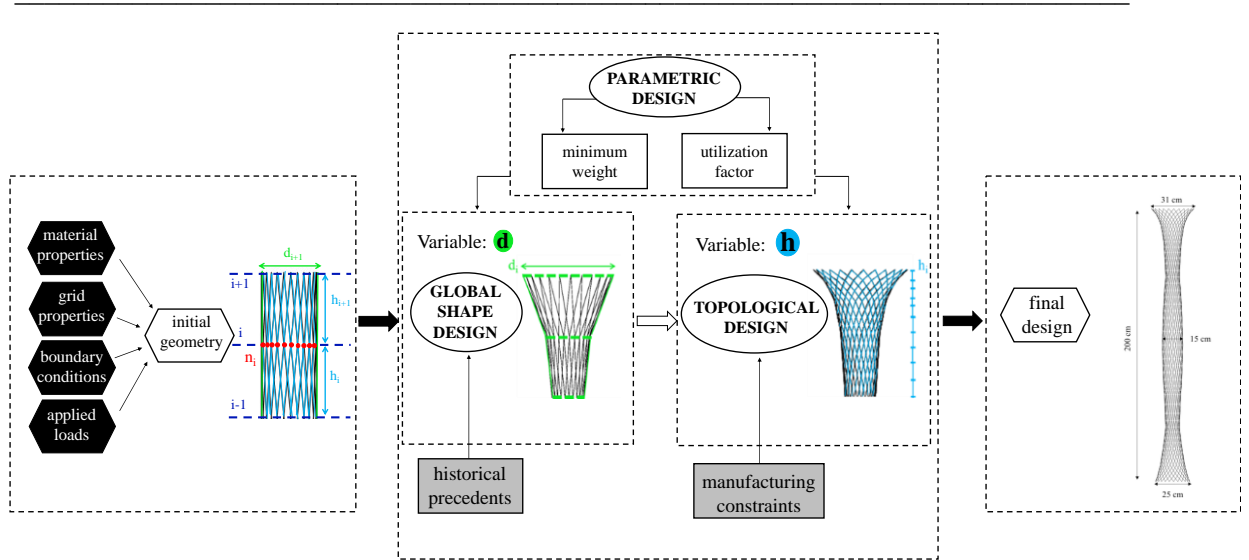
Figure 13.2: Computational design flowchart.

The first phase consists in the creation of a parametric model considering the following inputs: (i) material properties, (ii) grid properties, (iii) boundary conditions and (iv) applied loads. Based on the specific inputs, an initial geometrical configuration is generated in a parametric form. The parametrization allows to control both the global shape and the topology acting on some of the parameters (Figure 13.3). In the specific case, the selected geometry is a non-uniform cylindrical diagrid tube described by the following set of parameters (Figure 13.3a): number of control sections N along the column height (z_i indicates the vertical coordinate of the i-th cross-section), the outer diameter d, the section spacing h (corresponding to the distance between two consecutive control sections) and the number of control points n (from which at each control section the diagonal elements are generated). At the i-th control section it is thus possible to associate specific values of parameters d_i, h_i, n_i.

In phase 2 (global shape design) the GA variable (i.e. variable of the genetic algorithm) is the outer diameter d, governing the external shape of the column. Among the population of allowable solutions found through the algorithm, the selection criterion for the final global shape is based on the "merging" of the two best shapes: the sinusoidal-like and the hyperbolic-like (Figure 13.3b).

In phase 3 (topological design), the GA variable is the section spacing h, governing the length of the diagonal elements, hence the topology of the diagrid. Among the population of allowable solutions found through the genetic algorithm, the selection criterion for the final topology is

_____

based upon the manufacturing constraints proper of the process, in terms of maximum allowable rod lengths l and angle of inclination (θ) of the diagonal elements (Figure 13.3c).

For both phases, the "fitness value" of the GA (genetic algorithm) corresponds to the minimization of the mean utilization factor, as performed through *Karamba3D* component (*Karamba3D,* n.d.)

t the end of the computational design, the result of the final design is provided in terms of a set of values of the geometrical parameters (*d, h, n*) for each control section of the column.
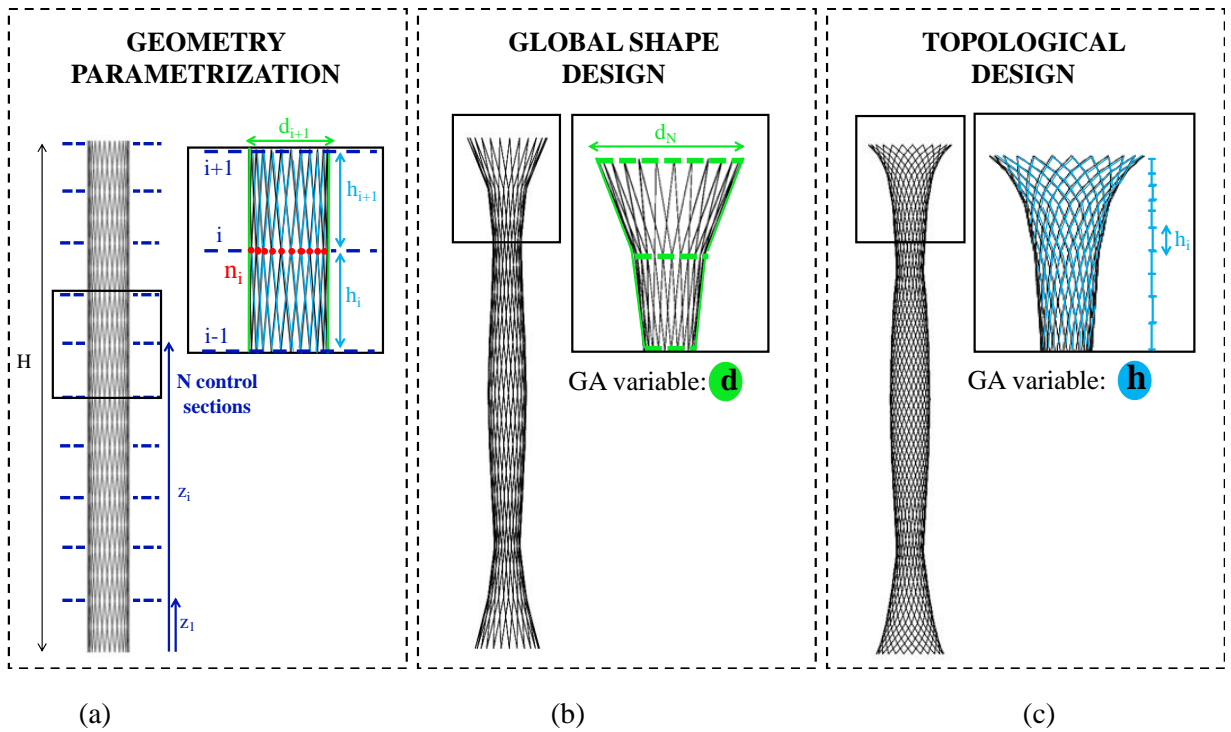
Figure 13.3: Phases of the parametric design: (a) parametrization of the geometry; (b) global shape design; (c) topological design.

_____

13.4.   DESIGN OF THE DIAGRID COLUMN AND ITS GLOBAL PERFORMANCES

A 2 m-high WAAM diagrid column has been designed according to the parametric design algorithm presented in Section 13.3. The design is a half-scaled structure representative of a 4-m high column. The assumed initial geometrical configuration at phase 1 is characterized by a constant diameter d=15 cm at all control sections. The inclined rods of the diagrid have a 6-mm diameter. The design is developed considering a reference vertical load of 25 kN applied at the top of the column. The applied vertical load corresponds to the resultant of distributed loads simulating the loads (dead plus live) applied on top of a porticos-like structure. It is assumed that the 1:1 scaled column would withstand the loads applied on an influence area corresponding to a 5-m column spacing. The column is considered clamped at the base, while the top is free to translate and rotate (cantilever condition). The mechanical properties of the rods (Young's modulus, tensile and compression capacity) are taken from the results of the experimental tests on dot-by-dot WAAM specimens described in Section 9.

In phase 2 (global shape design), the sections spacing h and number of control points n have been set constant and equal to 20 cm and 25 at each section, respectively. The along-the-height distribution of the external diameter $d_i(z_i)$ at each control section defines the global shape of the diagrid. The values d_i have been obtained from the population of allowable solutions coming from the genetic algorithm, according to the shape criterion, as a linear combination of the two "optimal shape functions". The values of d_i vary from 10 cm to 31 cm with an average value of 16 cm (Figure 13.4a).

In phase 3 (topological design), the number of control points n has been set constant and equal to 25 at each section, while the distribution of external diameter $d_i(z_i)$ is based upon the result of phase 2. The cross-section spacing $h_i(z_i)$ defines the global topology of the diagrid. The values h_i have been determined from the population of allowable solutions coming from the generic algorithm and accounting for the manufacturing constraints: maximum rod lengths $l \leq 100$ mm and maximum angle $\theta \leq 30°$ (Figure 13.4b). In particular, by changing the section spacing h, a higher number of control sections N resulted to define the final design while following the manufacturing constraints. Figure 10.4b compares the initial topology (having 10 control sections and constant cross-section spacing h equal to 20 cm) with the final one (having 35 control sections and cross-section spacing h_i varying from 4 to 10 cm). The final diagrid column is presented in Figure 13.4c.

_____

_____

(a)   (b)   (c)
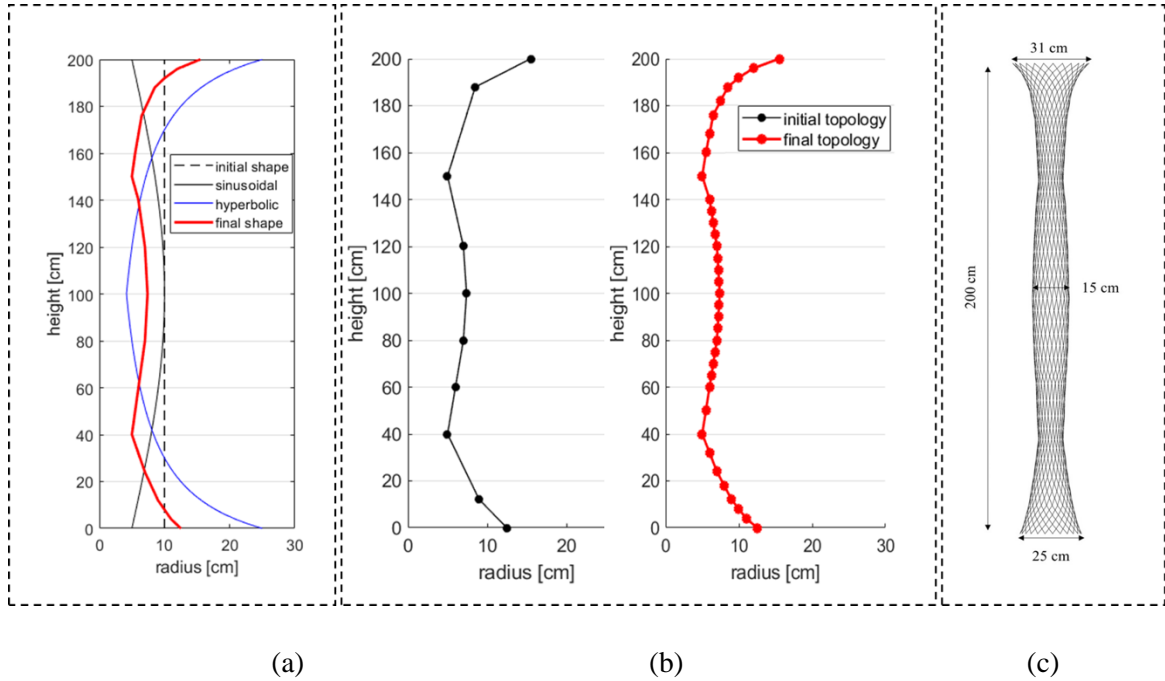
Figure 13.4: Diagrid parametric design: (a) global shape design; (b) topological design; (c) the final design.

For the sake of comparison, a uniform (constant diameter along the height) cylindrical diagrid column has been also designed. The equivalent cylindrical diagrid column is characterized by the following geometrical parameters: constant outer diameter (d=20 cm), constant sections spacing (h=20 cm) and constant number of control points (n=30). The rods have a 6-mm diameter. The cylindrical diagrid column has been designed to have maximum utilization factor $U_i \leq 100\%$ under the same vertical load of 25 kN.

The structural performances of the two diagrid columns have been evaluated by means of FE analyses carried out with the commercial software SAP2000 (www.csiamerica.com/sap2000). In particular, linear static analyses have been conducted with the purpose of evaluating the stresses in the diagrid members due to a constant vertical load of 25 kN. Each rod is modelled with a unique beam element having circular cross-section of 6 mm diameter. The total vertical load is applied through concentrated vertical forces applied at the top nodes.

A rigid hoop (not present in the original design) is added at the level of the top nodes of the two columns in order to limit the bending stresses at the top and account for practical issues of load application, thus ensuring better structural performances. The top horizontal hoop is not part of

_____

the computational design as the manufacturing constraints proper of the studied WAAM dot-by-dot printing strategy do not allow to print horizontal elements. However, it could be easily manufactured separately (even using more traditional techniques) and then welded after the completion of the column.

In order to evaluate the effectiveness of the proposed solution with respect to the uniform cylinder, two global performance indices have been introduced: the weight ratio (weight of the final design divided by the weight of the uniform cylinder) and the average utilization ratio (mean utilization factor of the final design divided by the mean utilization factor of the uniform cylinder). The mean utilization factor corresponds to the average value of the utilization factor along all members.

Table 13.1 reports and compares the two designs in terms of weight and utilization factor. The values of the weight ratio (0.88) and utilization ratio (0.72) indicate that the proposed solution is more efficient than the cylindrical column in terms of both amount of material and average utilization. It is worth noticing that the utilization factors of both solutions have a large variability from the minimum to the maximum values, which will be further discussed in the next section.

Table 13.1: Global performances of the two solutions in terms of weight ratio and utilization factors.

	Weight (W)		Utilization factor (U)			
	W	$W_{final} / W_{uniform}$	U_{min}	U_{max}	U_{mean}	$U_{mean,final} / U_{mean,uniform}$
Uniform cylinder	26.87 kg	0.88	29%	86%	68%	0.72
Final design	23.66 kg		14%	75%	49%	

_____

13.5. EFFECTS OF THE COMPUTATIONAL DESIGN ON THE STRUCTURAL PERFORMANCES OF THE DIAGRID COLUMN

In this section the structural behavior of the two compared solutions is analyzed. In general, for both solutions, the absence of horizontal hoops at the level of the control sections determines the presence of an unbalanced component (outward "centrifugal" force as depicted in Figure 13.5) of the internal actions at the intersection of two rods responsible for secondary bending moments which substantially increase the stresses in the diagonal rods. This behavior is known in the structural engineering design of tall buildings (Mele et al., 2014; Montuori et al., 2014; Moon et al., 2007; W. Zhou et al., 2016) which make use of structural diagrid, such as 30 St. Mary Axe in London (Figure 13.6). Indeed, most of the diagrid-based designs in architecture include horizontal elements (working as "hoops") to contain and prevent the previously mentioned unbalanced forces. However, there are few examples (as it is the case of the QIPCO Tower in Doha, the Prada Ayoama building in Tokyo and of the Oakland Arena) in which the structure performs without any horizontal hoop closing the diagrid (Figure 13.6b).
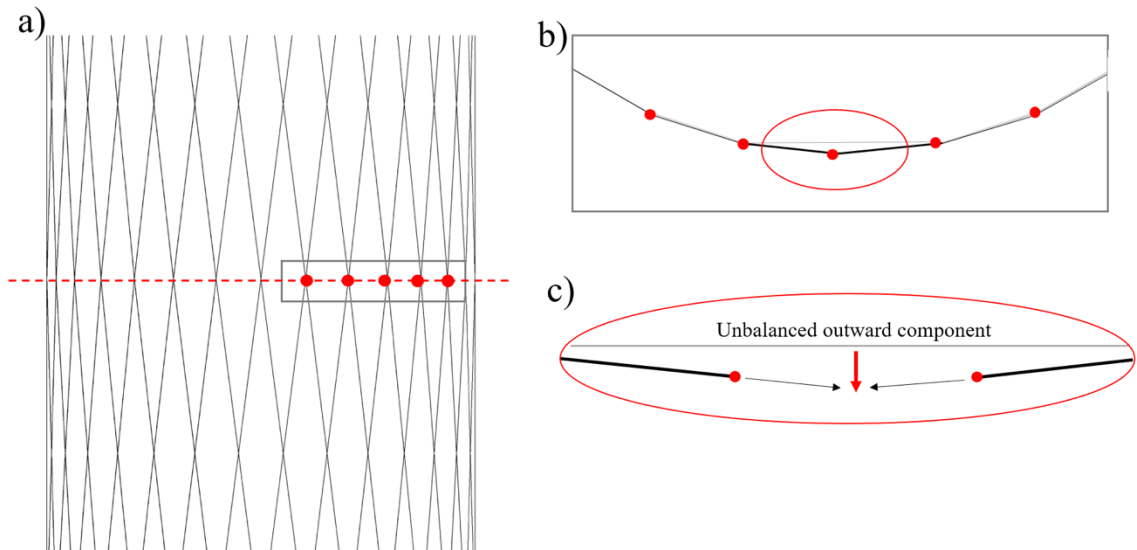
Figure 13.5: Geometrical considerations on unbalanced "centrifugal" actions on the diagrid column: (a) side view; (b) plane view; (c) close-up.

_____

(a)   (b)

Figure 13.6: Typical examples of diagrid structures applied to tall buildings: (a) 30 St. Mary Axe; (b) QIPCO Tower.

Figure 13.7 represents the bending moment diagrams and the distributions of the utilization factors along the height of the two compared solutions. The uniform cylinder presents an almost symmetrical (with respect to the mid-height) along-the-height distribution of the bending moments and utilization factors with maximum values around the mid height and minimum values at the top and bottom portions. This reduction in bending moment (and utilization factor) is due to restraining effects provided by the upper hoop and the base connection.

On the other hand, the final design results in a non-symmetrical along-the-height distribution of bending moments and utilization factors, due to the continuously changing curvature associated to the global shape partially contrasting the "centrifugal" outward actions due to the absence of horizontal hoops as evidenced in Figure 13.5. Overall, the peak values of bending moments (and utilization factors) are lower than those of the uniform cylinder.

Figures 13.8a and b present the cumulative graphs and relative frequency histograms of the utilization factors for the two designs. The comparison between the cumulative graphs clearly shows that the final design leads to reduced values of the utilization factors. For the case of the uniform cylinder column, the histogram of the relative frequency shows that the U values are

_____

grouped into two main ranges, one around 0.3-0.4 and one around 0.7-0.9, with a peak in the range of 0.8-0.9. On the other hand, for the final design the U values are more uniformly distributed with values between 0.2 and 0.8.

This result suggests future possibilities for more efficient designs of the diagrid column, towards a more uniform along-the-height distribution of utilization factors. This could be done in principle by changing the thickness of the rods. However, at the current state of art of WAAM applications it is not a feasible solution for the dot-by-dot printing strategy.
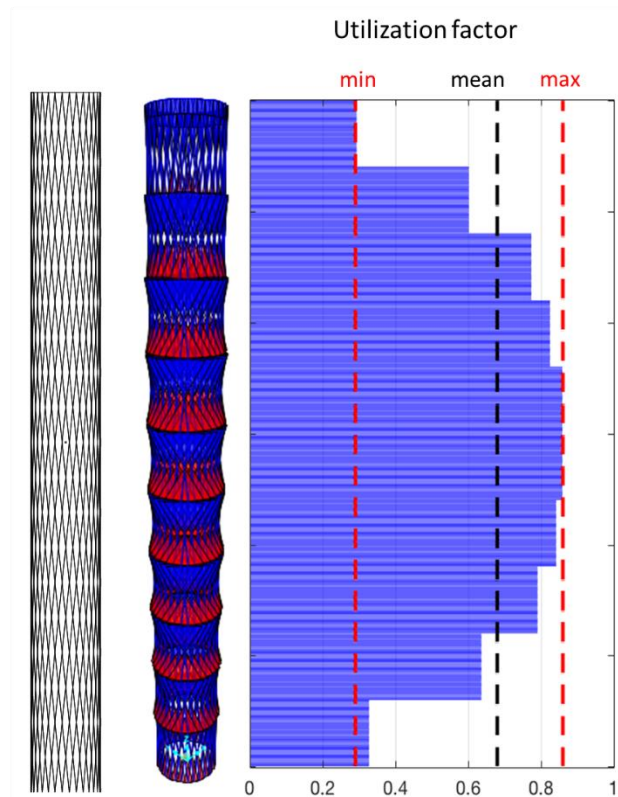
(a)
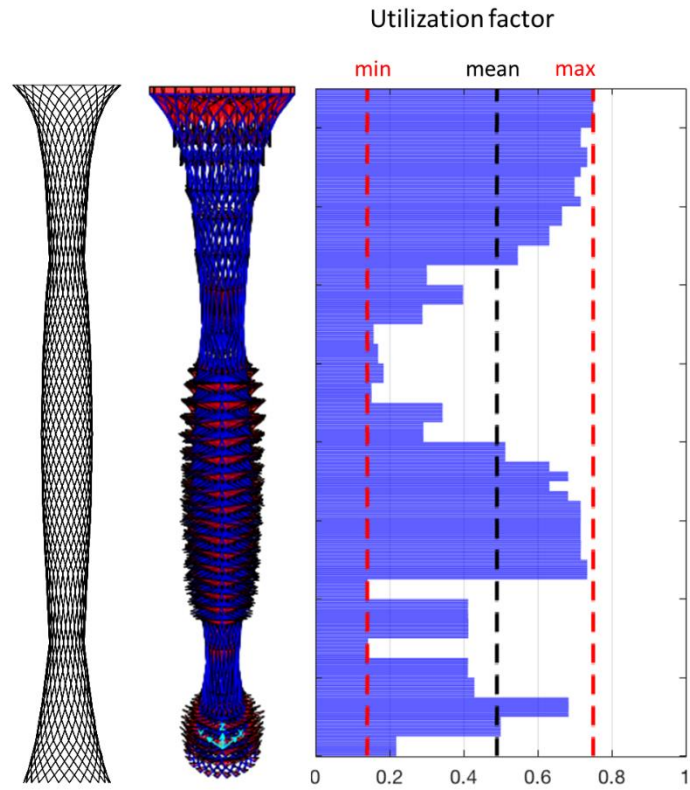
(b)

Figure 13.7: Results from structural analysis in terms of bending moment diagram and utilization factor: (a) uniform cylinder; (b) final design.
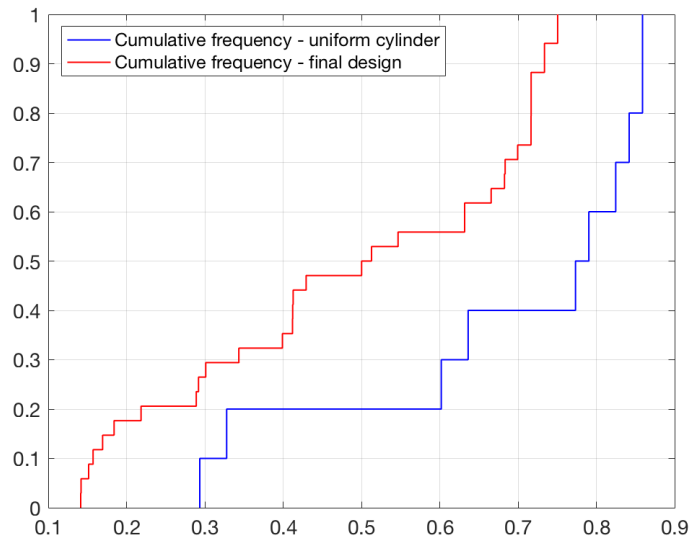
(a)
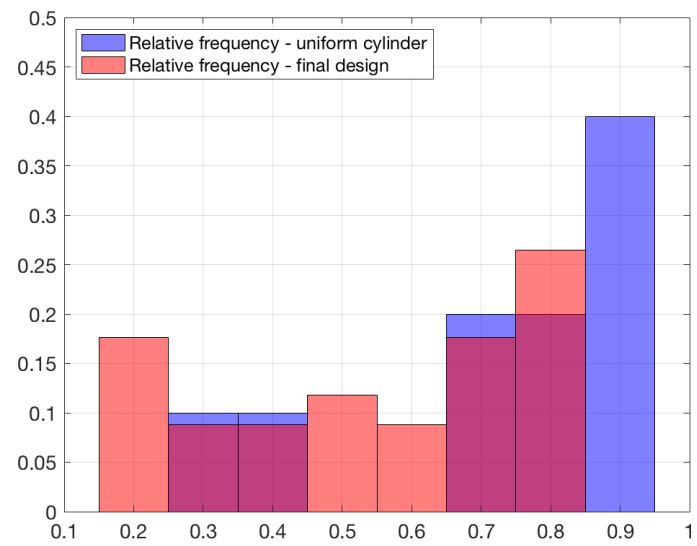
(b)

Figure 13.8: Distribution of the utilization factors for the two compared solutions; (a) cumulative frequency graph (b) histograms of relative frequency.

_____

13.6. FABRICATION

The final stage of the research consisted in the fabrication of the diagrid column as per the final design, using the WAAM technology adopted by MX3D (Figure 13.9).

The column has been manufactured at the MX3D facilities in Amsterdam using the same process parameters as the ones adopted to realize the specimens tested (see Section 10). Table 13.2 provides the fabrication parameters in terms of effective layer height, printing time and actual weight.

Table 13.2: Fabrication parameters.

Fabrication parameters	Value
Layer height	0.95 mm – 1.15 mm
Printing time	60 – 70 hours
Printed weight	26.50 kg
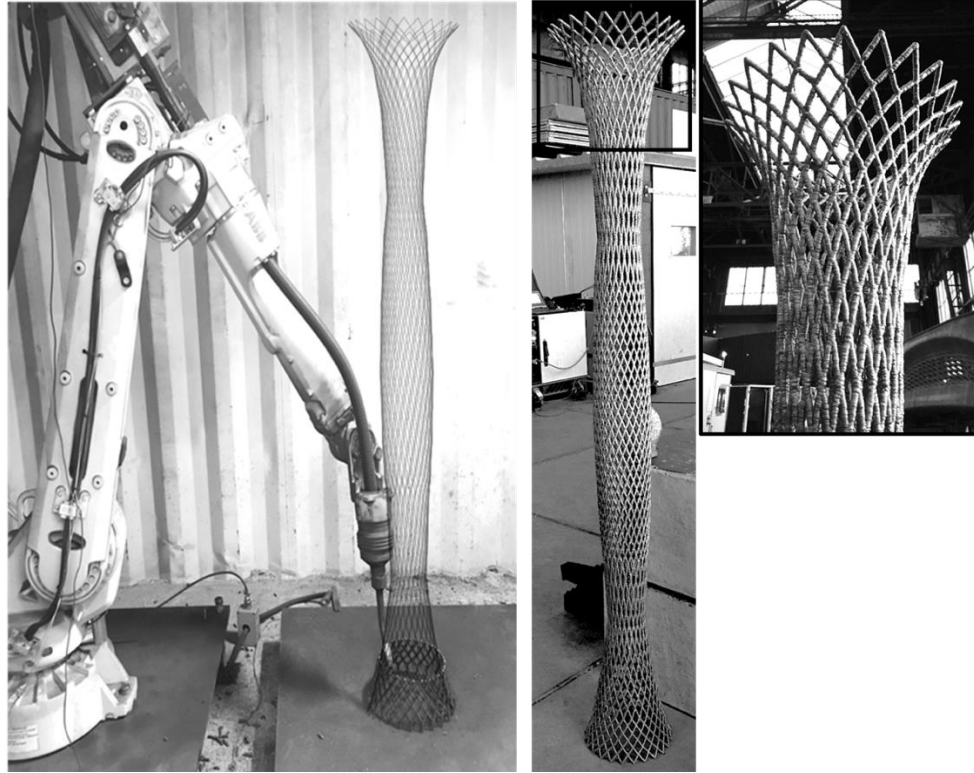
(a)

(b)

Figure 13.9: (a) Manufacturing of the designed diagrid column through WAAM process; (b) zoom of the top part.

_____

The printed outcome has been presented at "The Big 5- International Building and Construction" show, held in Dubai from November 25th till November 28th 2018, as a showcase of the possibilities offered by metal 3D printing to create innovative forms and aesthetically appealing structures. The final outcome has also been presented in "Formnext" Exhibition in Frankfurt on November 20th-22nd 2019.

The tree-like shape of the final diagrid column is particularly suitable for support of outdoor lightweight structures, such as tree-houses (Figure 13.10).

Further studies related to the investigation of the structural integrity of the nodal intersections of the dot-by-dot diagrid structure are currently under development.

Figure 13.10: Application of the designed diagrid column as support for tree-houses.

_____

13.7.   SUMMARY OF SECTION 13

The present Section presents the computational design and fabrication of a diagrid column realized in WAAM stainless steel.

The design has been realized through ad-hoc parametric design procedure, from historical precedents on optimized shapes for buckling-resistant columns, accounting for both the specific mechanical properties of WAAM dot-by-dot rods (from Section 11) as well as the manufacturing constraints proper of the dot-by-dot printing technique (from Section 10).

The final design has been also verified through structural analysis and the performances compared with the case of a cylinder shape. The results confirm the better performances of the final design, compared with a cylinder shape of the same weight.

The final design has then been fabricated and presented in important exhibitions on the possibilities of Additive Manufacturing in construction.

Further studies related to the investigation of the structural integrity of the nodal intersections of the dot-by-dot diagrid structure are currently under development.

PART C: New technologies and future developments

14. Introduction to Part C

14.1. BACKGROUND

Over the last decade, major interest has been devoted on the application of robotic innovations in construction, especially concerning aerospace and mechanical engineering field. As far as structural engineering is concerned, the main issue regards the large dimensions of the elements to be realized by means of Additive Manufacturing process, which bring to limitations in the process parameters to be adopted, as well as in a lower precision of the overall result.

Within the design framework of the civil, architecture and mechanical fields, there is growing interest in Free Form Design (FFD) and structural optimization, to model and design elements with optimized shapes according to their performances, with minimum amount of material use.

The realization of such complex morphologies is possible thanks to the technological innovation that brought to a production revolution with the use of 3D printing in the manufacturing sectors.

With reference to the construction industry, the principal research project in the international framework can be grouped in 3 categories: (i) automation construction with pre-shaped elements (Termes project, Harvard, NCCR Digital Fabrication, ETH Zurich); (ii) 3D printing of full houses (Huashang Tendga studio, WASP project); (iii) advanced 3D printing systems (MX3D Bridge). Nonetheless, none of the above mentioned projects explores the integration of efficient forms with additive manufacturing, nor allows for the construction of free-form elements directly on site.

Recent work done by Cranfield University along with Foster and Partners in LASIMM Project (www.lasimm.eu) outlines a huge potential of WAAM technique in moving from Computer-Aided Design into production with advanced all-in-one machines able to produce large scale finished engineering structures. Further research in the application of robotic advancements in the construction field has been done over the years by the Gramazio Kohler Research center at ETH Zurich (http://gramaziokohler.arch.ethz.ch/web/e/forschung/index.html), focusing on additive digital fabrication techniques used to build non-standardized architectural components.

However, an issue still unresolved in the application of WAAM in the structural engineering field is the difficulty in producing on-site engineering elements, as the robotic arms currently adopted for these applications are 6-axes robots with considerable dimensions and weight, thus unlikely to be used at the construction site.

Therefore, the need to develop a smart robotic system of small dimensions, able to print the structural elements while moving on them, inspired by the spiders that move on their web while creating it, would be a major step toward automatic on-site construction using WAAM technologies.

14.2. OBJECTIVES OF PART C

Part C of the doctoral thesis focuses on new technologies and future perspectives of WAAM applications in construction.

New construction processes and solutions can be envisaged, which make use of robotic devices able to move on the structure while 3D printing it, without any scaffoldings or human support. These advancements of automation in construction would pave the way to realize mega-structures and to build in harsh non-human environments, even in space.

Additionally, in order to accurately control the quality of the printing process, especially in construction fields where the human presence is not possible, it becomes crucial to study real-time monitoring systems and techniques.

_____

14.3.   ORGANIZATION OF THE TEXT

From the basic knowledge on the Wire-and-Arc Additive Manufacturing process, new technologies and possibilities related to the construction industry could be envisaged.

In Section 15 a new mobile 3D-printing technology has been proposed and patented by the research team at University of Bologna. The technology consists in a mobile 3D-printing robotic device with integrated motion, able to move along the structure while 3D printing it. The research has reached a TRL-3 stage, with the realization of a prototype demonstrator.

In Section 16 an innovative integrated monitoring system is proposed. The system allows to monitor real-time the WAAM process through image-based devices, to capture the quality of the printing during its realization.

_____

15. Mobile 3D-printing system

15.1. OVERVIEW

The present Section illustrates the concept of an interdisciplinary research project carried out at University of Bologna to realize a mobile integrated 3D-printing system able to move along the structure while 3D printing on it.

The research has been articulated in different parts and activities, carried out by the departments of Architecture, Structural Engineering, Additive Manufacturing and Robotics. The final outcome is a prototype demonstrator able to move while 3D print in polymer (PA12 material). The idea has patent protection in Italy, with possibility to extension internationally.

_____

15.2.   MOBILE 3D-PRINTING ROBOTIC DEVICE

At the end of 2017, an interdisciplinary research group has been established at University of Bologna to explore the possibilities offered by Additive Manufacturing technologies for the construction industry. The first year of activities has been devoted to the research project Autor3dicolari (https://autor3dicolari.com/), aimed at the development of a novel mobile 3D printing technology for the auto-construction of spatial steel truss structures.

The limitations of the actually available technologies clearly revealed the need of an interdisciplinary research effort able to integrate issues of architectural and structural design with constraints and possibilities offered by new construction procedures based on the development of ad-hoc robotized Additive Manufacturing technologies. The composition of the team reflects such needs since it includes researchers dealing with structural design and modelling, mechanics of materials, imaging and robotics.

The ultimate goal has been the development a new mobile Additive Manufacturing technology through a circular integration of (i) Architecture, (ii) Structural Engineering, (iii) Additive Manufacturing and (iv) Robotics. From a conceptual/methodological point of view, the project has cyclically and iteratively gone over the following main five steps with increasing level of accuracy:

1. Architectural design: definition of the geometry of the spatial structure. The design can be accomplished through topological optimization tools (see Section 7) or computational design algorithms (see Section 13).

2. Robot kinematics: on the basis of the outcome of step 1, and by taking into account the constraints imposed by the printing process, the kinematics of the robotic printer has been defined in order to assure the desired mobility on the structure and the dexterity required for the printing operation. The robotic kinematics has been validated by means of numerical simulations. Obviously, the kinematic complexity of the robot, in terms of number of degrees of freedom, strongly depended on the designed structure and therefore a refining process based on a modification of the geometry defined at step 1 and aiming at an optimization of the robotic device has been applied.

3. Printing head: the printing technique (material selection and related deposition strategy) of the mobile printer has been selected in order to be compatible with geometrical requirements (from step 1) and kinematics (of step 2).

_____

_____

4. Robot mechanical design: once the kinematic structure of the mobile printer has been defined and validated, its mechanical design has been performed. In this phase, the load due to the printing head and the velocities required by the printing process have been the specifications that, together with the mechanical stiffness necessary for obtaining given precisions, led the choice of the mechanical structure and materials, motors sizing, etc. The goal was the optimization of the overall weight of the robot.

5. Structural design: once the geometrical properties of the structure, loads imposed by the robot, mechanical properties of the printed material are defined (steps 1-3), a structural analysis should be carried out. This analysis would verify the structural performances of the system both in its final configuration and during construction. This would encompass appropriate design loads (live loads, dead loads, loads imposed by the robots), inherent geometrical imperfection (associated to the printing process), construction sequence (staged construction), specific mechanical properties of the printed material. At higher level of project definition a full probabilistic reliability analysis of the structure should be developed with reference to different levels of limit states (such as ultimate and serviceability).

The research project has been articulated into Phases (A, B and C), while the activities (tasks) have been carried out by autonomous research lines, interacting with each other to share advancements and results. The initial Phase A-Principles has been aimed at investigating the fundamental aspects necessary for the development of the innovative technology. Then, In Phase B- Integration the results of the single lines of research have been integrated with the purpose of delivering a protocol (know-how) for the development of the new technology. The final Phase C- Proof of concept has delivered the first prototype of the printing robot. Three lines of research have been established: (i) Material characterization research line (referred to as M research line), (ii) structural Design & Optimization research line (referred to as D&O research line), (iii) Robotized printer line (referred to as R research line).

The final outcome of the *Auto-r3dicolari* project consisted in a prototype demonstrator of the mobile 3D printing robotic device, with an integrated gripping system within the printed element. The invention consists of an integrated gripping system for mobile 3D printing of free-form elements. In detail, the gripping system allows the robotic device to move along the element while 3D printing it.

_____

_____

The gripping system is realized to allow the 3D printing of tubular elements by means of a mobile robotic device able to 3D print while moving on the printing element. The robotic device is gripped at the printing element through a system composed by two wings and a rack placed at the four sides of the tubular section. This system is part of the geometry of the section to be printed. It is considered to be realized with the same material as the tubular element, polymer-based or metal-based. The system allows the printing of tubular elements with section of any shape, minimum dimensions of 134 x 134 mm and maximum dimensions of 170 x 316 mm. Theoretically, the gripping system is intended for the realization of tubular elements with infinite length (Figure 15.1).

The system is composed of two wings and combined with a rack used as "rail" to build within the geometry of the element to be 3D printed. The robotic device can move along the element through a cogwheel which seizes the 3D printed rack. It allows for the 3D printing of elements of any shape in terms of cross-section and thickness, and ideally infinite length.

The mobile 3D printing robotic system with integrated gripping allows to create 3D printed elements with theoretically any shape and geometry, and infinite longitudinal development. It can be used for the on-site 3D print of tubular components for the mechanical, aerospace or structural field.
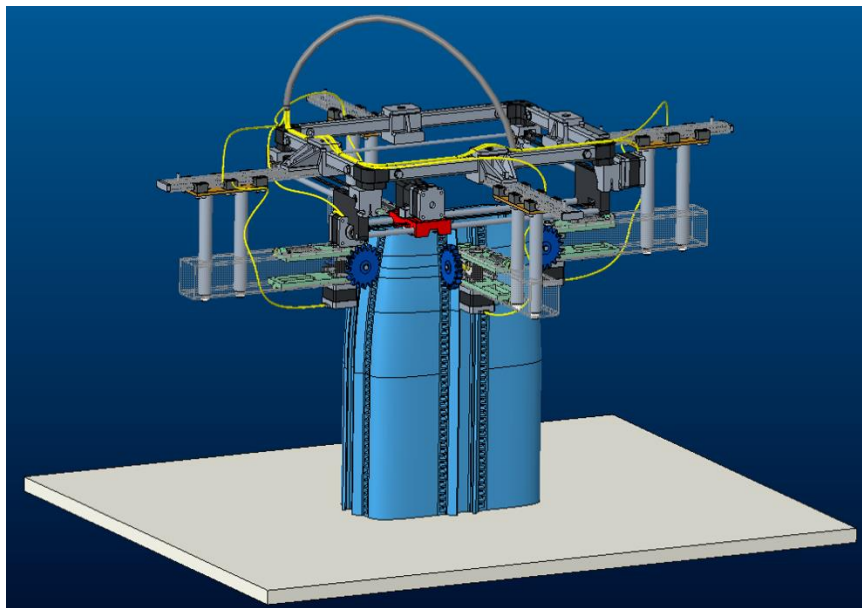
Figure 15.1: Mobile 3D printing robot system with integrated motion.

_____

_____

The current stage of development is a proof of concept (TRL – 3) demonstrated through a prototype demonstrator using a plastic material (PA12). The prototype demonstrator is able to print a 3D geometry with convex cross-sectional shape and longitudinal axis (Figure 15.2).

The next steps of development will include the adaptation to different geometrical shapes and materials, as well as the integration of a real-time control system to monitor the printing process.

The innovative solution has patent protection in Italy, with possibility to extend internationally (Patent number: 102020000024109) "Stampante tridimensionale, relative procedimento per la realizzazione di un oggetto stampato ed oggetto così ottenuto".
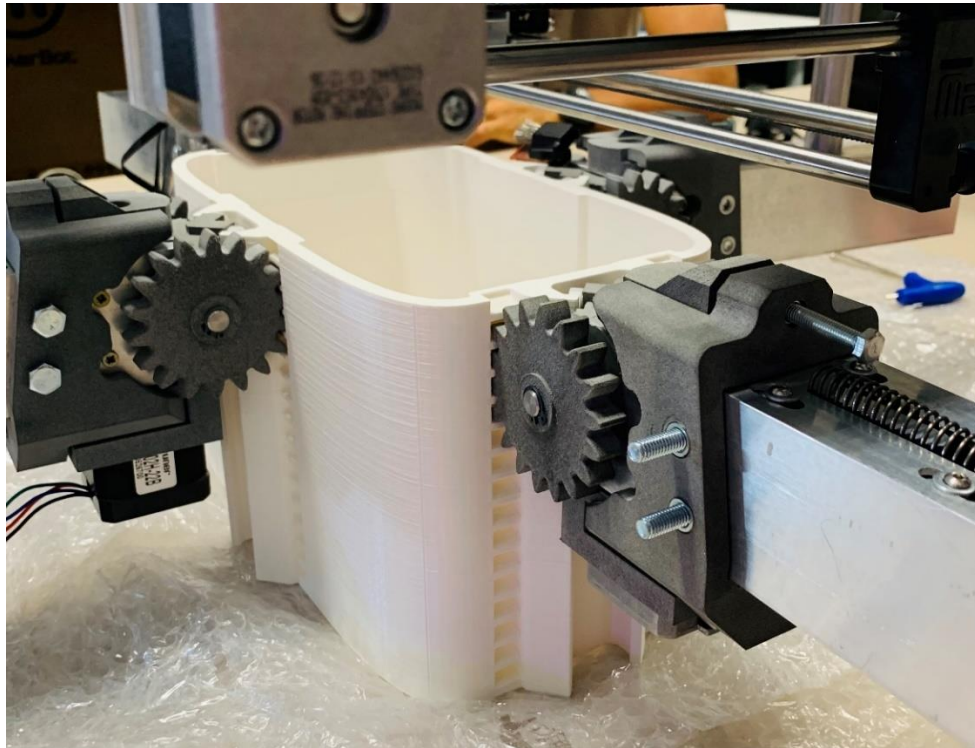
Figure 15.2: Prototype demonstrator of the proposed technology.

The long-term vision of this technology is the adoption of a swarm-system of mobile 3D printing robots able to move along the structure while 3D printing it, and fabricate geometries with several orders of magnitudes higher than the devices. This solution could be applied to create mega-structures, as the visionary "city domes" which could cover entire cities in harsh environments (Figure 15.3). Furthermore, the technology would be suitable to realize structures in non-human environments, such as extra-terrestrial places.

_____

Figure 15.3: Visionary concept of the "swarms" of mobile 3D printing robots to realize large domes.

_____

15.3.   SUMMARY OF SECTION 15

In the present Section, new construction applications for Additive Manufacturing processes are presented.

The proposed research is based on an interdisciplinary project carried out at University of Bologna (*Auto-r3(d)icolari* project) and consisted in the development of a new robotic device able to move along the structure while 3D printing it. This new mobile 3D-printing robot could be used to realized innovative forms and geometries, with several orders of magnitude of dimensions with respect to those of the printing device. The idea has been developed up to the realization of a prototype demonstrator. The mobile 3D-printing robot has also been patented in Italy, with possibility of extension internationally. This new construction solution could be expanded through the coordination of a "swarm" of mobile 3D-printing devices which could ideally be used to create mega-structures.

These new developments would pave the way towards a new generation of construction processes and technologies for the realization of new structures, also in harsh and non-human environments.

_____

16. Future perspectives towards an integrated monitoring system

16.1. OVERVIEW

This Section illustrates the future perspective in WAAM process, through the integration of a real-time monitoring system to acquire useful information on the quality and the performances of the printing process.

The long-term vision of this research is the possibility to control and monitor the printing process also in harsh and non-human environments.

_____

16.2. INTEGRATED REAL-TIME MONITORING SYSTEM

The first investigations on Additive Manufacturing technologies in construction revealed the need for interdisciplinary research to provide new processes, faster printing, quality assurance and more data on mechanical properties before AM could realize its full potential in the construction industry.

With reference to Wire-and-Arc Additive Manufacturing (WAAM), a recent survey on the material properties of the printed outcomes (Xu et al., 2018) shows that the repeatability of geometrical features and mechanical properties of the outcomes is not yet satisfactory since their relationships with the printing parameters (such as current and voltage, welding speed, wire diameter and wide feed rate, nozzle-to-bead distance, preheat temperature and gas flow rate) are, generally, highly non-linear and not yet fully understood. Indeed, a deeper understanding of the mutual relationships between printing parameters, thermal history and geometrical and mechanical properties of the outcomes would allow to reduce the process uncertainties, thus increasing the quality of the result. At the moment, the uncertain quality of the final product constitutes the main barrier to the adoption of WAAM by manufactures.

Hence a proper metrology, i.e. the science and act of measuring, is required not only from a technological confidence point of view but also due to the market pull for consistent and reliable performances.

As such, MX3D realized a smart monitoring system ("Smart Bridge" project) in collaboration with Autodesk for real-time monitoring of the performances of the MX3D Bridge once it will be placed in Amsterdam city center (Figure 16.1).

_____
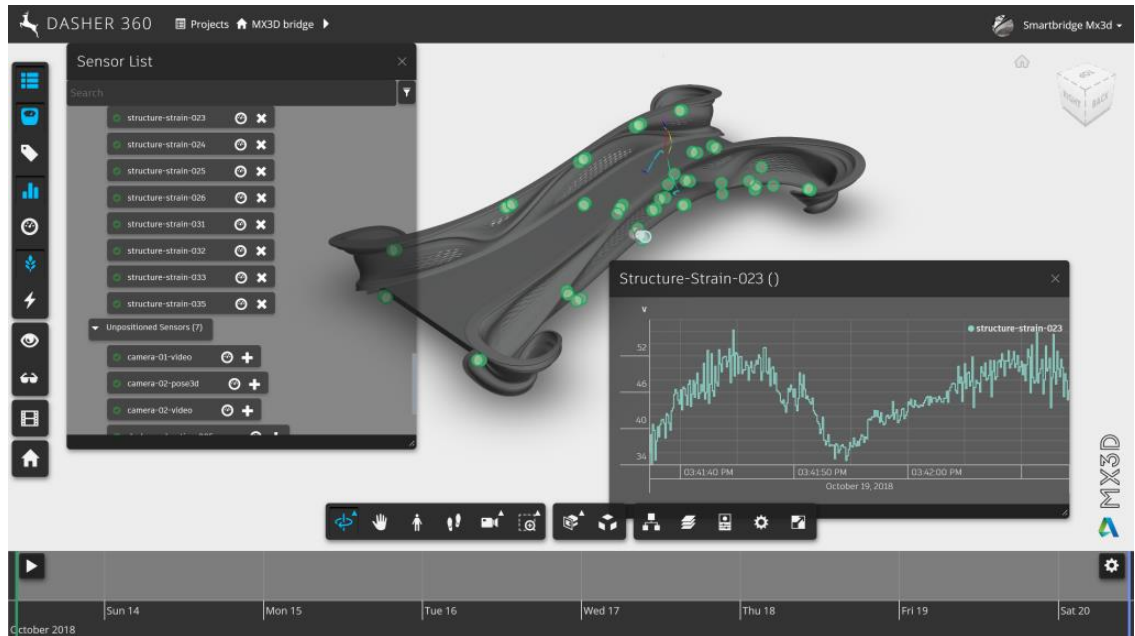
Figure 16.1: MX3D "Smart Bridge" project in collaboration with Autodesk (*"Smart Bridge" Project*).

Hence, the future developments of the WAAM technology is the integration of real-time monitoring system, based on the use of existing image-based monitoring technologies (e.g. high speed CCD cameras, thermal cameras, X-ray tomography) for on-line control of WAAM manufacturing processes. The monitoring system will be able to characterize the process thermal-history, to detect structural and microstructural defects in AM parts and to provide information on the process-generated internal network of pores and surface roughness. Both visible light and thermal images will be acquired and processed. The monitoring system could be conceived as a network of cameras and devices (some of them possibly embedded in the printing tool through robotized arms) so that the process could be monitored from different points of view. It could include also a Closed-loop Control System, with one or more feedbacks between its outputs (data measured by cameras and sensor) and inputs coming from digital models. To do so, a complex control software is required to acquire data in real-time (using fast image filtering algorithms to improve images quality, resolution, reduce noise) and to integrate them with the input models that control the process from both a thermal and geometrical point of view (3D CAD model). The images processing part relies on super resolution methods based on the overlapping of images taken from multiple viewpoints. The knowledge about the structure of the objects of interest represents a good a-priori information to drive the reconstruction and to limit the effect of low resolution devices involved in the monitoring process.

_____

The innovative monitoring system would be used to enhance the inherent precision of the manufacturing process through an optimal fine-tuning of the nominal deposition parameters, such as wire feed rate, heat input and travel speed. Also, during this first phase, the closed-loop system would be used to set-up correction strategies/algorithms for real-time "compensation of deviations" of layer-upon-layer deposition through a small variation in the values of printing parameters. During operational conditions, the use of the monitoring system could be tested with the purpose of delivering a protocol for on-line process and product quality control. After the training phase, during ordinary operational conditions, the same monitoring system could be used for the automatic continuous and real-time control of the production, thus not requiring to interrupt the work and the human presence for visual inspection.

A first example of real-time monitoring system for WAAM production is the "MaxQ" developed by RAMLAB (*RAMLAB*, n.d.), to automate the printing production, quality inspection and certification process. In detail, the system automatically controls the interpass temperature, detects anomalies and defects, and corrects the produced geometry.

From a scientific point of view, the innovation potential of the innovative monitoring system could impact both the scientific communities of Imaging Science and Material Science. From an industrial point of view, the results could impact the industry of Additive Manufacturing and more in general the construction industry and control of welding processes.

At long term, the real-time monitoring system could be integrated into a next-generation of mobile robots with integrated 3D printers for automatic and adaptive on-site constructions and repairing with no need of human interventions.

_____

16.3. SUMMARY OF SECTION 16

In the present Section, new possibilities related to the integration of real-time monitoring system has been proposed.

As such, the proposed integrated monitoring system would be able to capture the quality of the printing process through real-time monitoring with the use of image-based devices.

These new developments would allow to increase the quality of the WAAM printing process, allowing for a smart real-time monitoring during the printing phase, thus ensuring a high quality of the printed outcome.

This application could lead to future applications on large scale structures, for which a high level of precision and accuracy of the printing process is requested.

_____

17. Conclusions

17.1. SUMMARY OF WORK

The study presented in this dissertation is focused on the application of an innovative metal 3D printing technique, referred to as Wire-and-Arc Additive Manufacturing (WAAM) in the construction field. The scope of the study was to define the main characteristics of the WAAM-produced parts to derive first design guidelines for structural applications, and explore new possibilities for innovative structural elements and construction processes.

The study has been divided in three parts: Part A, Part B and Part C.

Part A was devoted to study the so-called *continuous* printing process, consisting in the deposition of layer upon layer of welded material in continuous, to realize planar elements. The first part of the study has been focused on the definition of the suitable design approach for this process, based on its inherent issues and specifics. Then, a wide experimental activity has been carried out to define the microstructural features, the mechanical properties and geometrical irregularities of the printed outcomes. From these results, an ad-hoc orthotropic material model has been calibrated in order to describe the anisotropic behaviour of the printed plates. The experimental material properties have also been used to derive first design guidelines, through the calibration of design values and partial safety factors of WAAM-produced plates according to European standard provisions for steel structures. Then, first explorations on new structural forms through the development of ad-hoc topological optimization algorithms were proposed.

Part B was devoted to study the so-called *dot-by-dot* printing process, consisting in the deposition of successive drops of welded material, to realize rod-like and lattice elements. The first part of the study has been focused on the definition of the design issues of this printing process, to take into account in the definition of the design approach, as already defined from Part A. Then, a first experimental work has been carried out to define the mechanical properties and geometrical features of the rod-like samples. From these results, the calibration of the design values and partial safety factors defined the first guidelines for structural design applications, following the procedure adopted in Part A. Then, from the experimental results, an ad-hoc computational design procedure has been adopted to design and fabricate the first metal 3D-printed diagrid column.

_____

Part C was devoted to explore new technologies and future perspectives for applications of 3D printing technologies in construction, in terms of new construction processes and integrated monitoring systems.

_____

17.2.   SUMMARY OF FINDINGS

17.2.1. Main findings of Part A

The main findings from Part A are summarized as follows:

-   The design approach considered for the application of WAAM continuous printing in steel structures is based on the simplified semi-probabilistic approach commonly adopted for traditional structures (as recommended from European code provisions). The approach is redefined based on the specific issues of the WAAM-produced parts, in terms of geometrical irregularities and anisotropic behavior, which should be considered in the design phase.

-   The experimental tests were carried out on 308LSi stainless steel printed samples cut along three directions with respect to the printed layers (longitudinal, i.e. parallel to the printed layers, transversal, i.e. perpendicular to them, and diagonal, i.e. at 45°). The results revealed a marked anisotropy of the key material properties (as computed from tensile tests on machined specimens cut along different printing directions). The anisotropic nature has been confirmed also by the microstructure, characterized by an orthotropic grain growth and crystalline orientation influenced by the layer-by-layer deposition. Young's modulus and Poisson's ratios are the parameters most influenced by the anisotropic behavior, with high variations depending on the relative printing direction of the samples. The geometrical irregularities, in terms of surface roughness and thickness variation, slightly influence the mechanical response of the as-built specimens, especially in terms of Young's modulus and elongation at rupture.

-   The elastic parameters defined from experiments were adopted to calibrate an orthotropic material model to acquire the full elastic behavior of the WAAM-produced plates. From the calibrated model, the highest values of Young's modulus are registered for a direction θ of around ±42°, for an average value of 245 GPa, more than 20% higher than the standard value adopted for stainless steel material. The highest values of shear modulus are registered for a direction θ of ±90°, for an average value of 150 GPa, almost double the standard value adopted for stainless steel material.

-   The first design guidelines were drawn in terms of calibration of the design values and partial safety factors for the key material properties. Statistical analysis and calibration procedures according to Annex D of Eurocode 0 have been performed on the three main

_____

_____

printing directions investigated experimentally, to characterize the anisotropic behavior of the printed material. The results confirm values of partial safety factors in line with the recommendations for stainless steel structures according to Eurocode 3. Additional considerations were made for Young's modulus, for which ad-hoc calibration has been performed even though traditionally the value has defined as deterministic.

- From the orthotropic material model, ad-hoc topological optimization algorithms have been implemented, to simultaneously optimize both the layout and the printing orientation of the printed element, in order to maximize the structural performances (in terms of stiffness) with minimum amount of material use. The optimization procedure has been applied for standard 2D cases, then extended for the case study of a I-type beam.

17.2.2. Main findings of Part B

The main findings from Part B are summarized as follows:

- As for the continuous printing, also for dot-by-dot printing strategy first the definition of the main design issues has been studied, in terms of geometrical irregularities and mechanical influence of the printing inclination of the rods. The same design approach has been applied as for Part A.

- Tensile tests were performed on 308LSi rods printed with three different inclinations (0°, 10° and 45° from vertical direction). The results evidenced a decrease in the mechanical properties with increasing inclinations of the rods. Overall, with reference to the results on the continuously printed along T direction, the mechanical properties of the rods follow the same trend, with slight difference in yielding values, for which the 0.2% proof stress has been registered of around 250 MPa. The geometrical characterization has been carried out in terms of definition of the diameter distribution of the rods as well as their lack of straightness. Compression tests were performed on rods printed at 0° and 10°. The results suggest some important influence of the geometrical irregularities in the buckling behavior of the slender rods.

- The first design guidelines were drawn in terms of calibration of the key design values and partial safety factors, according to the procedure adopted in Part A. The results

_____

_____

confirmed quite good mechanical performances, with slightly higher values of partial safety factors with respect to the continuous printing.

- An ad-hoc computational design procedure has been proposed and adopted to design and fabricate the first 3D-printed metal diagrid column. The final design resulted in higher structural performances with respect to the traditional cylindrical shape, with additional aesthetic appeal, suitable for high-impact architectural applications.

17.2.3. Main findings of Part C

The main findings from Part C are summarized as follows:

- Among the new technologies for innovative construction processes with the use of Additive Manufacturing technology, a mobile 3D-printing robotic system has been proposed. The device is the outcome of an interdisciplinary research project (*Auto-r3(d)icolari*) carried out with the departments of Structural Engineering, Architecture, Additive Manufacturing and Robotics. The final result is a prototype demonstrator of the idea, able to move along the printed part with an integrated system while 3d print it. The idea has patent protection in Italy, which could be extended internationally.

- Future perspectives towards an improvement of WAAM process is the integration of real-time monitoring system, able to control the printing process and solve any possible issues during printing, without ideally the need of human presence.

_____

_____

17.3. FUTURE RESEARCH WORK

Future developments of this study include, but are not limited to:

- Integration of additional experimental tests, to define the fatigue resistance and impact resistance of WAAM-produced parts.

- Definition of appropriate design guidelines, based on the specific issues of the printing process and on the experimental results.

- Definition of a new generation of optimized structural members, realized with WAAM, through the exploitation of ad-hoc algorithms to reduce the material use and increase the overall efficiency of the elements, while ensuring high structural performances.

- Extension of the mobile 3D-printing robotic system for other printing materials and processes, such as WAAM.

- Equipment of WAAM printing devices with integrated real-time monitoring systems, to increase the quality of the printing process and define printing standards to widen the application of this technology in other sectors.

References

Achtziger, W. (1997). Topology optimization of discrete structures. In *Topology optimization in structural mechanics* (pp. 57–100). Springer.

Addis, W. (2007). *Building: 3000 years of design engineering and construction.* London: Phaidon.

Adriaenssens, S., Block, P., Veenendaal, D., & Williams, C. (2014). *Shell structures for architecture: form finding and optimization*. Routledge.

AIRMESH Pavilion. (n.d.).

Alan Turing Institute to Turn the World's First 3D Printed Steel Bridge Into a "Living Laboratory" for Research. (n.d.). Retrieved June 23, 2020, from https://www.turing.ac.uk/news/alan-turing-institute-turn-worlds-first-3d-printed-steel-bridge-living-laboratory-research

Allaire, G., & Bogosel, B. (2018). Optimizing supports for additive manufacturing. *Structural and Multidisciplinary Optimization*, *58*(6), 2493–2515.

Allaire, G., Dapogny, C., Estevez, R., Faure, A., & Michailidis, G. (2017). Structural optimization under overhang constraints imposed by additive manufacturing technologies. *Journal of Computational Physics*, *351*, 295–328.

Allaire, G., Geoffroy-Donders, P., & Pantz, O. (2019). Topology optimization of modulated and oriented periodic microstructures by the homogenization method. *Computers & Mathematics with Applications*, *78*(7), 2197–2229.

Amir, O., & Mass, Y. (2018). Topology optimization for staged construction. *Structural and Multidisciplinary Optimization*, *57*(4), 1679–1694.

ANSI/AWS A5.9-93: Specification for bare stainless steel welding electrodes and rods. (1993). American Welding Society.

Artec 3D webpage. (n.d.). https://www.artec3d.com

ARUP - Additive Manufacturing. (n.d.). Retrieved July 10, 2020, from https://www.arup.com/projects/additive-manufacturing

AS/NZS 4673: Cold-formed stainless steel structures. (2001). Australian/New Zealand Standards.

ASTM. (2010). *ASTM F 2792-10 Standard Terminology for Additive Manufacturing Technologies*. American Society for Testing and Materials, ASTM International.

ASTM A276-16. (2016). Standard Specification for Stainless Steel Bars and Shapes. *ASTM International*, 1–8. https://doi.org/10.1520/A0276

ASTM International. (2012). *ISO/ASTM 52900: 2015: Standard Terminology for Additive Manufacturing Technologies - General Principles - Terminology*.

ASTM International. (2017). E3 Preparation of Metallographic Specimens. *Annual Book of ASTM Standards*, *11*(Reapproved 2017), 1–17. https://doi.org/10.1520/E0003-11R17.1

References

_____

Attaran, M. (2017). The rise of 3-D printing: The advantages of additive manufacturing over traditional manufacturing. *Business Horizons*. https://doi.org/10.1016/j.bushor.2017.05.011

Bae, H. R., Grandhi, R. V., & Canfield, R. A. (2004). Epistemic uncertainty quantification techniques including evidence theory for large-scale structures. *Computers and Structures*. https://doi.org/10.1016/j.compstruc.2004.03.014

Ballio, G., & Mazzolani, F. M. (1979). *Strutture in acciaio*. Arnoldo Mondadori Editore.

Basak, A., & Das, S. (2016). Epitaxy and Microstructure Evolution in Metal Additive Manufacturing. *Annual Review of Materials Research*, *46*(1), 125–149. https://doi.org/10.1146/annurev-matsci-070115-031728

Beckh, M. (2015). *Hyperbolic structures: Shukhov's lattice towers-forerunners of modern lightweight construction*. John Wiley & Sons.

Bejan, A. (2000). *Shape and structure, from engineering to nature*. Cambridge University Press.

Bektas, S. (2017). Design of hyperboloid structures. *Journal of Architectural Research and Development*, *1*(2).

Bendsoe, M. P., & Kikuchi, N. (1988). *Generating optimal topologies in structural design using a homogenization method*.

Bendsøe, M., & Sigmund, O. (2003). *Topology optimization - theory, methods and applications*. Springer EUA, New York.

Borrvall, T., & Petersson, J. (2001). Topology optimization using regularized intermediate density control. *Computer Methods in Applied Mechanics and Engineering*, *190*(37–38), 4911–4928.

Bourdin, B. (2001). Filters in topology optimization. *International Journal for Numerical Methods in Engineering*, *50*(9), 2143–2158.

Bourne, R., & Bourne, R. (2010). ImageJ. *Fundamentals of Digital Imaging in Medicine*, *9*(7), 185–188. https://doi.org/10.1007/978-1-84882-087-6_9

Briccola, D., & Bruggi, M. (2019). Analysis of 3D linear elastic masonry-like structures through the API of a finite element software. *Advances in Engineering Software*, *133*, 60–75.

Bruggi, M, Parolini, N., Regazzoni, F., & Verani, M. (2018). Topology optimization with a time-integral cost functional. *Finite Elements in Analysis and Design*, *140*, 11–22.

Bruggi, Matteo, Laghi, V., & Trombetti, T. (2021). Simultaneous design of the topology and the build orientation of Wire-and-Arc Additively Manufactured structural elements. *Computers and Structures*, *242*, 106370. https://doi.org/10.1016/j.compstruc.2020.106370

Bruggi, Matteo, & Taliercio, A. (2015). Optimal strengthening of concrete plates with unidirectional fiber-reinforcing layers. *International Journal of Solids and Structures*, *67*, 311–325.

Buchanan, C., & Gardner, L. (2019). Metal 3D printing in construction: A review of methods, research, applications, opportunities and challenges. *Engineering Structures*, *180*(November 2018), 332–348. https://doi.org/10.1016/j.engstruct.2018.11.045

_____

References

Buchanan, Craig, Matilainen, V. P., Salminen, A., & Gardner, L. (2017). Structural performance of additive manufactured metallic material and cross-sections. *Journal of Constructional Steel Research*, *136*(April), 35–48. https://doi.org/10.1016/j.jcsr.2017.05.002

Carpo, M. (2013). *The digital turn in architecture 1992-2012*. John Wiley & Sons.

Christensen, P. W., & Klarbring, A. (2008). *An introduction to structural optimization* (Vol. 153). Springer Science & Business Media.

Committee, A. H. (n.d.). *ASM Handbook, Volume 1: Properties and Selection: Irons, Steels, and High-Performance Alloys*.

Courtney, T. H. (2005). *Mechanical behavior of materials*. Waveland Press.

Dieter, G. E., & Bacon, D. J. (1986). *Mechanical metallurgy*. McGraw-hill.

Dinovitzer, M., Chen, X., Laliberte, J., Huang, X., & Frei, H. (2019). Effect of wire and arc additive manufacturing (WAAM) process parameters on bead geometry and microstructure. *Additive Manufacturing*, *26*(December 2018), 138–146. https://doi.org/10.1016/j.addma.2018.12.013

European Committee for Standardization (CEN). (2002). *EN 1990: Eurocode 0 - Basis of Structural Design*.

European Committee for Standardization (CEN). (2015). *EN 1993 1-4: Eurocode 3 - Design of steel structures, part 1-4: General rules, supplementary rules for stainless steel*. European Committee for Standardization (CEN).

European Convention For Constructional Steelwork. (1976). Manual on Stability of Steel Structures. *22*, 328.

Everton, S. K., Hirsch, M., Stavroulakis, P. I., Leach, R. K., & Clare, A. T. (2016). Review of in-situ process monitoring and in-situ metrology for metal additive manufacturing. *Materials and Design*, *95*, 431–445. https://doi.org/10.1016/j.matdes.2016.01.099

Feucht, T., & Lange, J. (2019). 3-d-printing with steel: Additive manufacturing of connection elements. *Advances in Engineering Materials, Structures and Systems: Innovations, Mechanics and Applications - Proceedings of the 7th International Conference on Structural Engineering, Mechanics and Computation, 2019*, *Lmd*, 419–424. https://doi.org/10.1201/9780429426506-75

Galjaard, S., Hofman, S., & Ren, S. (2015a). *Optimizing Structural Building Elements in Metal by using Additive Manufacturing*. August.

Galjaard, S., Hofman, S., & Ren, S. (2015b). New Opportunities to Optimize Structural Designs in Metal by Using Additive Manufacturing. In P. Block, J. Knippers, N. J. Mitra, & W. Wang (Eds.), *Advances in Architectural Geometry 2014* (pp. 79–93). Springer International Publishing.

Gardner, L., Kyvelou, P., & Buchanan, C. (2019). *Testing of wire and arc additively manufactured tubular sections*. 978–981. https://doi.org/10.3850/978-981-11-0745-0

Gardner, L., Kyvelou, P., Herbert, G., & Buchanan, C. (2020). Testing and initial verification of the world's first metal 3D printed bridge. *Journal of Constructional Steel Research*, *172*. https://doi.org/10.1016/j.jcsr.2020.106233

References

_____

Ge, J., Lin, J., Chen, Y., Lei, Y., & Fu, H. (2018). Characterization of wire arc additive manufacturing 2Cr13 part: Process stability, microstructural evolution, and tensile properties. *Journal of Alloys and Compounds*, *748*, 911–921. https://doi.org/10.1016/j.jallcom.2018.03.222

Ghaffari, M., Vahedi Nemani, A., Rafieazad, M., & Nasiri, A. (2019). Effect of Solidification Defects and HAZ Softening on the Anisotropic Mechanical Properties of a Wire Arc Additive-Manufactured Low-Carbon Low-Alloy Steel Part. *Jom*, *71*(11), 4215–4224. https://doi.org/10.1007/s11837-019-03773-5

Giannatsis, J., & Dedoussis, V. (2009). Additive fabrication technologies applied to medicine and health care: A review. *International Journal of Advanced Manufacturing Technology*, *40*(1–2), 116–127. https://doi.org/10.1007/s00170-007-1308-1

Gordon, J. V., Haden, C. V., Nied, H. F., Vinci, R. P., & Harlow, D. G. (2018). Fatigue crack growth anisotropy, texture and residual stress in austenitic steel made by wire and arc additive manufacturing. *Materials Science and Engineering A*, *724*(March), 431–438. https://doi.org/10.1016/j.msea.2018.03.075

Grasshopper. (n.d.). www.grasshopper3d.com

Griffith, M. L., Ensz, M. T., Puskar, J. D., Robino, C. V., Brooks, J. A., Phillibert, J. A., Smugeresky, J. E., & Hofmeister, W. H. (2000). Understanding the microstructure and properties of components fabricated by laser engineered net shaping (LENS). *MRS Online Proceedings Library Archive2*, *625*. https://doi.org/10.1111/jfb.12029

Groen, J. P., & Sigmund, O. (2018). Homogenization-based topology optimization for high-resolution manufacturable microstructures. *International Journal for Numerical Methods in Engineering*, *113*(8), 1148–1163.

Guan, K., Wang, Z., Gao, M., Li, X., & Zeng, X. (2013). Effects of processing parameters on tensile properties of selective laser melted 304 stainless steel. *Materials and Design*, *50*, 581–586. https://doi.org/10.1016/j.matdes.2013.03.056

Haden, C. V., Zeng, G., Carter, F. M., Ruhl, C., Krick, B. A., & Harlow, D. G. (2017). Wire and arc additive manufactured steel: Tensile and wear properties. *Additive Manufacturing*, *16*, 115–123. https://doi.org/10.1016/j.addma.2017.05.010

Hejripour, F., Binesh, F., Hebel, M., & Aidun, D. K. (2019). Thermal modeling and characterization of wire arc additive manufactured duplex stainless steel. *Journal of Materials Processing Technology*, *272*(May), 58–71. https://doi.org/10.1016/j.jmatprotec.2019.05.003

Holicky, M. (2009). *Reliability analysis for structural design*. SUN press.

Hovig, E. W., Azar, A. S., Grytten, F., Sørby, K., & Andreassen, E. (2018). Determination of anisotropic mechanical properties for materials processed by laser powder bed fusion. *Advances in Materials Science and Engineering*, *2018*. https://doi.org/10.1155/2018/7650303

Hutchinson, B. (2015). Critical assessment 16: Anisotropy in metals. *Materials Science and Technology (United Kingdom)*, *31*(12), 1393–1401. https://doi.org/10.1179/1743284715Y.0000000118

ISO. (2012). *BSI Standards Publication Geometrical product specifications (GPS) — Surface texture : Areal Part 2 : Terms , definitions and surface*.

_____

References

_____

ISO 2394 - General principles on reliability for structures. (1998).

Ji, L., Lu, J., Liu, C., Jing, C., Fan, H., & Ma, S. (2017). Microstructure and mechanical properties of 304L steel fabricated by arc additive manufacturing. *MATEC Web of Conferences*, *128*. https://doi.org/10.1051/matecconf/201712803006

Joosten, S. K. (2015). *Printing a stainless steel bridge: an exploration of structural properties of stainless steel additive manufactured for civil engineering purposes*. University of Technology Delft.

Karamba3D. (n.d.). www.karamba3d.com

Kaw, A. K. (2005). *Mechanics of composite materials*. CRC press.

Keller, J. B. (1960). The shape of the strongest column. *Archive for Rational Mechanics and Analysis*, *5*(1), 275–285. https://doi.org/10.1007/BF00252909

Khoshnevis, B. (2004). Automated construction by contour crafting - Related robotics and information technologies. *Automation in Construction*. https://doi.org/10.1016/j.autcon.2003.08.012

Kim, I. S., Son, K. J., Yang, Y. S., & Yaragada, P. K. D. V. (2003). Sensitivity analysis for process parameters in GMA welding processes using a factorial design method. *International Journal of Machine Tools and Manufacture*, *43*(8), 763–769. https://doi.org/10.1016/S0890-6955(03)00054-3

Kloft, H., Empelmann, M., Hack, N., Herrmann, E., & Lowke, D. (2020). Reinforcement strategies for 3D-concrete-printing . *Civil Engineering Design*, *2*(4), 131–139. https://doi.org/10.1002/cend.202000022

Kou, S. (2003). Post-solidification phase transformations. In *Welding Metallurgy*. https://doi.org/10.1002/0471434027.ch9

Krivoshapko, S. N. (2002). Static, vibration, and buckling analyses and applications to one-sheet hyperboloidal shells of revolution. *Applied Mechanics Reviews*, *55*(3), 241–269. https://doi.org/10.1115/1.1470479

Kyvelou, P., Slack, H., Mountanou, D. D., Wadee, M. A., Britton, T. Ben, Buchanan, C., & Gardner, L. (2020). Mechanical and microstructural testing of wire and arc additively manufactured sheet material. *Materials & Design*, 108675. https://doi.org/10.1016/J.MATDES.2020.108675

Laghi, V., Palermo, M., Tonelli, L., Gasparini, G., Ceschini, L., & Trombetti, T. (2020). Tensile properties and microstructural features of 304L austenitic stainless steel produced by wire-and-arc additive manufacturing. *International Journal of Advanced Manufacturing Technology*, *106*(9–10). https://doi.org/10.1007/s00170-019-04868-8

Laghi, V., Palermo, M., Gasparini, G., Girelli, V. A., & Trombetti, T. (2019). Geometrical characterization of Wire-and-Arc Additive Manufactured steel elements. *VBRI Press Advanced Materials Letters*, *10*(10), 695–699.

Laghi, V., Palermo, M., Gasparini, G., Girelli, V. A., & Trombetti, T. (2021). On the influence of the geometrical irregularities in the mechanical response of Wire-and-Arc Additively Manufactured planar elements. *Journal of Constructional Steel Research*.

Laghi, V., Palermo, M., Gasparini, G., Girelli, V. A., & Trombetti, T. (2020b). Experimental results for

_____

structural design of Wire-and-Arc Additive Manufactured stainless steel members. *Journal of Constructional Steel Research*, *167*. https://doi.org/10.1016/j.jcsr.2019.105858

Laghi, V., Tonelli, L., Palermo, M., Bruggi, M., Sola, R., Ceschini, L., & Trombetti, T. (2021). Orthotropic elastic model for Wire-and-Arc Additively Manufactured stainless steel. *Additive Manufacturing*.

Langelaar, M. (2018). Combined optimization of part topology, support structure layout and build orientation for additive manufacturing. *Structural and Multidisciplinary Optimization*, *57*(5), 1985–2004.

Ledbetter, H. M. (1984). Monocrystal-Polycrystal Elastic Constants of a Stainless Steel. *Physica Status Solidi (A)*, *85*(1), 89–96. https://doi.org/10.1002/pssa.2210850111

Ledbetter, H. M. (1985). Predicted monocrystal elastic constants of 304-type stainless steel. *Physica B+C*, *128*(1), 1–4. https://doi.org/https://doi.org/10.1016/0378-4363(85)90076-2

Lee, J. W., Kim, J. J., Kim, H. S., & Yoon, G. H. (2019). Application of a layerwise theory for efficient topology optimization of laminate structure. *Journal of Mechanical Science and Technology*, *33*(2), 711–719.

Lee, J. W., Kim, J. J., & Yoon, G. H. (2019). Stress constraint topology optimization using layerwise theory for composite laminates. *Composite Structures*, *226*, 111184.

Lewandowski, J. J., & Seifi, M. (2016). Metal Additive Manufacturing: A Review of Mechanical Properties. *Annual Review of Materials Research*, *46*(1), 151–186. https://doi.org/10.1146/annurev-matsci-070115-032024

Li, S., Yuan, S., Zhu, J., Wang, C., Li, J., & Zhang, W. (2020). Additive manufacturing-driven design optimization: Building direction and structural topology. *Additive Manufacturing*, *36*(June), 101406. https://doi.org/10.1016/j.addma.2020.101406

Liu, J., Gaynor, A. T., Chen, S., Kang, Z., Suresh, K., Takezawa, A., Li, L., Kato, J., Tang, J., Wang, C. C. L., Cheng, L., Liang, X., & To, A. C. (2018). Current and future trends in topology optimization for additive manufacturing. *Structural and Multidisciplinary Optimization*, *57*(6), 2457–2483. https://doi.org/10.1007/s00158-018-1994-3

Liu, M., Liu, H., Wang, D., Liu, B., Shi, Y., Li, F., Gong, Y., Li, L., Li, L., & Zhang, W. (2019). Effect of nanodiamond concentration and the current density of the electrolyte on the texture and mechanical properties of Ni/Nanodiamond composite coatings produced by electrodeposition. *Materials*, *12*(7). https://doi.org/10.3390/ma12071105

Massey, F. J. J. (1951). The Kolmogorov-Smirnov Test for Goodness of Fit. *Journal of the American Statistical Association*, *46*(253), 68–78. https://doi.org/10.1080/01621459.1951.10500769

Mele, E., Toreno, M., Brandonisio, G., & De Luca, A. (2014). Diagrid structures for tall buildings: case studies and design considerations. *The Structural Design of Tall and Special Buildings*, *23*(July 2014), 124–145. https://doi.org/10.1002/tal

Meng, L., Zhang, W., Quan, D., Shi, G., Tang, L., Hou, Y., Breitkopf, P., Zhu, J., & Gao, T. (2020). From Topology Optimization Design to Additive Manufacturing: Today's Success and Tomorrow's Roadmap. *Archives of Computational Methods in Engineering*, *27*(3), 805–830. https://doi.org/10.1007/s11831-019-09331-1

Metallic materials — Tensile testing — Part 1: Method of test at room temperature Matériaux métalliques — Essai de traction — Partie 1: Méthode d'essai à température ambiante COPYRIGHT PROTECTED DOCUMENT. (2009). In *Iso 6892-1*. http://files.instrument.com.cn/FilesCenter/20090913/200991371610112081.pdf

Mirzendehdel, A. M., Rankouhi, B., & Suresh, K. (2018). Strength-based topology optimization for anisotropic parts. *Additive Manufacturing*. https://doi.org/10.1016/j.addma.2017.11.007

Montuori, G. M., Mele, E., Brandonisio, G., & De Luca, A. (2014). Geometrical patterns for diagrid buildings: Exploring alternative design strategies from the structural point of view. *Engineering Structures*, *71*, 112–127. https://doi.org/10.1016/j.engstruct.2014.04.017

Moon, K. S., Connor, J. J., & Fernandez, J. E. (2007). Diagrid structural systems for tall buildings: Characteristics and methodology for preliminary design. *Structural Design of Tall and Special Buildings*, *16*(2), 205–230. https://doi.org/10.1002/tal.311

Moore, P., Addison, A., & Nowak-Coventry, M. (2019). Mechanical properties of wire plus arc additive manufactured steel and stainless steel structures. *Welding in the World*, *63*(6), 1521–1530. https://doi.org/10.1007/s40194-019-00775-4

Morozov, E. V., & Vasiliev, V. V. (2003). Determination of the shear modulus of orthotropic materials from off-axis tension tests. *Composite Structures*, *62*(3–4), 379–382. https://doi.org/10.1016/j.compstruct.2003.09.008

MX3D - Takenaka connector. (n.d.).

MX3D Webpage. (n.d.). www.mx3d.com

Niendorf, T., Leuders, S., Riemer, A., Richard, H. A., Tröster, T., & Schwarze, D. (2013). Highly anisotropic steel processed by selective laser melting. *Metallurgical and Materials Transactions B: Process Metallurgy and Materials Processing Science*, *44*(4), 794–796. https://doi.org/10.1007/s11663-013-9875-z

Nikbakt, S., Kamarian, S., & Shakeri, M. (2018). A review on optimization of composite structures Part I: Laminated composites. *Composite Structures*, *195*, 158–185.

Nomura, T., Dede, E. M., Lee, J., Yamasaki, S., Matsumori, T., Kawamoto, A., & Kikuchi, N. (2015). General topology optimization method with continuous and discrete orientation design using isoparametric projection. *International Journal for Numerical Methods in Engineering*, *101*(8), 571–605.

Oerlikon. (n.d.). https://www.oerlikon.com/en/

Okita, T., Kawabata, T., Murayama, H., Nishino, N., & Aichi, M. (2019). A new concept of digital twin of artifact systems: Synthesizing monitoring/inspections, physical/numerical models, and social system models. *Procedia CIRP*, *79*, 667–672. https://doi.org/10.1016/j.procir.2019.02.048

Peeters, D., van Baalen, D., & Abdallah, M. (2015). Combining topology and lamination parameter optimisation. *Structural and Multidisciplinary Optimization*, *52*(1), 105–120.

Rafieazad, M., Ghaffari, M., Vahedi Nemani, A., & Nasiri, A. (2019). Microstructural evolution and mechanical properties of a low-carbon low-alloy steel produced by wire arc additive manufacturing. *International Journal of Advanced Manufacturing Technology*, *105*(5–6), 2121–

2134. https://doi.org/10.1007/s00170-019-04393-8

RAMLAB. (n.d.).

Ranaivomiarana, N., Irisarri, F.-X., Bettebghor, D., & Desmorat, B. (2019). Concurrent optimization of material spatial distribution and material anisotropy repartition for two-dimensional structures. *Continuum Mechanics and Thermodynamics*, *31*(1), 133–146.

Raspall, F., Banon, C., & Tay, J. C. (2019). AIRTABLE. Stainless steel printing for functional space frames. *Computer-Aided Architectural Design Research in Asia (CAADRIA) 2019*, *1*, 113–122.

Rhinoceros 5. (n.d.). www.rhino3d.com

Rodrigues, T. A., Duarte, V., Avila, J. A., Santos, T. G., Miranda, R. M., & Oliveira, J. P. (2019). Wire and arc additive manufacturing of HSLA steel: Effect of thermal cycles on microstructure and mechanical properties. *Additive Manufacturing*, *27*(March), 440–450. https://doi.org/10.1016/j.addma.2019.03.029

Saadlaoui, Y., Milan, J. L., Rossi, J. M., & Chabrand, P. (2017). Topology optimization and additive manufacturing: Comparison of conception methods using industrial codes. In *Journal of Manufacturing Systems*. https://doi.org/10.1016/j.jmsy.2017.03.006

Saikia, P., Joseph, A., Rane, R., Saikia, B. K., & Mukherjee, S. (2013). Role of substrate and deposition conditions on the texture evolution of titanium nitride thin film on bare and plasma-nitrided high-speed steel. *Journal of Theoretical and Applied Physics*, *7*(1), 66. https://doi.org/10.1186/2251-7235-7-66

Sames, W. J., List, F. A., Pannala, S., Dehoff, R. R., & Babu, S. S. (2016). The metallurgy and processing science of metal additive manufacturing. *International Materials Reviews*, *61*(5), 315–360. https://doi.org/10.1080/09506608.2015.1116649

SAP2000. (n.d.). www.csiamerica.com/products/sap2000

SEI/ASCE 08-02: Specification for the design of cold-formed stainless steel structural members. (1991). American Society of Civil Engineers.

Skiba, T., Baufeld, B., & Van Der Biest, O. (2009). Microstructure and mechanical properties of stainless steel component manufactured by shaped metal deposition. *ISIJ International*, *49*(10), 1588–1591. https://doi.org/10.2355/isijinternational.49.1588

"Smart Bridge" project. (n.d.). https://mx3d.com/projects/smart-bridge/

Snijder, A. H., van der Linden, L. P. L., Goulas, C., Louter, C., & Nijsse, R. (2020). The glass swing: a vector active structure made of glass struts and 3D-printed steel nodes. *Glass Structures and Engineering*, *5*(1), 99–116. https://doi.org/10.1007/s40940-019-00110-9

Song, B., Zhao, X., Li, S., Han, C., Wei, Q., Wen, S., Liu, J., & Shi, Y. (2015). Differences in microstructure and properties between selective laser melting and traditional manufacturing for fabrication of metal parts: A review. *Frontiers of Mechanical Engineering*, *10*(2), 111–125. https://doi.org/10.1007/s11465-015-0341-2

Song, Y., Yan, Y., Zhang, R., Xu, D., & Wang, F. (2002). Manufacture of the die of an automobile deck part based on rapid prototyping and rapid tooling technology. *Journal of Materials Processing*

Technology. https://doi.org/10.1016/S0924-0136(01)01165-7

Staab, G. (2015). *Laminar composites*. Butterworth-Heinemann.

Strauß, H., & Knaack, U. (2016). Additive Manufacturing for Future Facades: The potential of 3D printed parts for the building envelope. *Journal of Facade Design and Engineering*, *3*(3–4), 225–235. https://doi.org/10.3233/fde-150042

Sun, L., Jiang, F., Huang, R., Yuan, D., Guo, C., & Wang, J. (2020). Anisotropic mechanical properties and deformation behavior of low-carbon high-strength steel component fabricated by wire and arc additive manufacturing. *Materials Science and Engineering A*, *787*(February), 139514. https://doi.org/10.1016/j.msea.2020.139514

Svanberg, K. (1987). The method of moving asymptotes—a new method for structural optimization. *International Journal for Numerical Methods in Engineering*, *24*(2), 359–373. https://doi.org/10.1002/nme.1620240207

Taliercio, A. (2020). *Introduzione alla meccanica dei solidi*. Società Editrice Esculapio.

The Method Case. (n.d.). https://www.themethodcase.com/mx3d-metal-joris-laarman-lab/

Thomas, C. L., Gaffney, T. M., Kaza, S., & Lee, C. H. (1998). Rapid prototyping of large scale aerospace structures. *1996 IEEE Aerospace Applications Conference*, 219–230.

Uziel, A. (2016). Looking at large-scale, arc-based Additive Manufacturing. *Welding Journal*, *4*.

Van Bolderen, G. S. (2017). *Exploration of stability of 3D-printed steel members*. University of Technology Delft.

Vander Voort, G. F., Lucas, G. M., & Manilova, E. P. (2004). Metallography and microstructures of stainless steels and maraging steels. *Materials Park, OH: ASM International*, 670–700.

Vannucci, P. (2005). Plane anisotropy by the polar method. *Meccanica*, *40*(4–6), 437–454.

Vannucci, P. (2018). The Polar Formalism. In *Anisotropic Elasticity* (pp. 131–244). Springer.

Wang, L., Xue, J., & Wang, Q. (2019). Correlation between arc mode, microstructure, and mechanical properties during wire arc additive manufacturing of 316L stainless steel. *Materials Science and Engineering A*, *751*(February), 183–190. https://doi.org/10.1016/j.msea.2019.02.078

Wang, W., Munro, D., Wang, C. C. L., van Keulen, F., & Wu, J. (2020). Space-time topology optimization for additive manufacturing. *Structural and Multidisciplinary Optimization*, *61*(1), 1–18.

Williams, S. W., Martina, F., Addison, A. C., Ding, J., Pardal, G., & Colegrove, P. (2016). Wire + Arc additive manufacturing. *Materials Science and Technology (United Kingdom)*, *32*(7), 641–647. https://doi.org/10.1179/1743284715Y.0000000073

Wong, K. V., & Hernandez, A. (2012). A Review of Additive Manufacturing. *ISRN Mechanical Engineering*, *2012*, 1–10. https://doi.org/10.5402/2012/208760

Wu, W., Xue, J., Wang, L., Zhang, Z., Hu, Y., & Dong, C. (2019). Forming process, microstructure, and mechanical properties of thin-walled 316L stainless steel using speed-cold-welding additive

_____

manufacturing. *Metals*, *9*(1). https://doi.org/10.3390/met9010109

Xu, X., Ganguly, S., Ding, J., Guo, S., Williams, S., & Martina, F. (2018). Microstructural evolution and mechanical properties of maraging steel produced by wire + arc additive manufacture process. *Materials Characterization*, *143*(October 2017), 152–162. https://doi.org/10.1016/j.matchar.2017.12.002

Yap, C. Y., Chua, C. K., Dong, Z. L., Liu, Z. H., Zhang, D. Q., Loh, L. E., & Sing, S. L. (2015). Review of selective laser melting: Materials and applications. *Applied Physics Reviews*, *2*(4), 041101. https://doi.org/10.1063/1.4935926

Yildiz, A. S., Davut, K., Koc, B., & Yilmaz, O. (2020). *Wire arc additive manufacturing of high-strength low alloy steels : study of process parameters and their influence on the bead geometry and mechanical characteristics*.

Yilmaz, O., & Ugla, A. A. (2017). Microstructure characterization of SS308LSi components manufactured by GTAW-based additive manufacturing: shaped metal deposition using pulsed current arc. *International Journal of Advanced Manufacturing Technology*, *89*(1–4), 13–25. https://doi.org/10.1007/s00170-016-9053-y

Zhang, P., Liu, J., & To, A. C. (2017). Role of anisotropic properties on topology optimization of additive manufactured load bearing structures. *Scripta Materialia*. https://doi.org/10.1016/j.scriptamat.2016.10.021

Zhou, M., & Rozvany, G. I. N. (1991). The COC algorithm, Part II: Topological, geometrical and generalized shape optimization. *Computer Methods in Applied Mechanics and Engineering*, *89*(1–3), 309–336.

Zhou, W., Cao, Z., & Zhang, J. (2016). Experiment and analysis on reinforced concrete spatial connection in diagrid tube. *Structural Design of Tall and Special Buildings*, *25*(4), 179–192. https://doi.org/10.1002/tal.1234